2017

# Application of an improved video-based depth inversion technique to a macrotidal sandy beach

Bergsma, Erwin Willem Johan

# APPLICATION OF AN IMPROVED VIDEO-BASED DEPTH INVERSION TECHNIQUE TO A MACROTIDAL SANDY BEACH

by

ERWIN WILLEM JOHAN BERGSMA

A thesis submitted to Plymouth University
in partial fulfilment for the degree of

DOCTOR OF PHILOSOPHY


Plymouth University
Faculty of Science and Engineering
School of Marine Science and Engineering

August 2016

# Acknowledgements

The initial title of the PhD *Morphodynamic modelling of macro-tidal beaches* suggests numerical modelling, well that is not what this work is about. Things evolve and so it is with the PhD. Guidance, or advise as Daniel said several times, is provided along the way by the supervisory team: Daniel Conley as Director of Studies, Mark Davidson and Tim O'Hare. My search of bottom/morphological data to model a macro-tidal beach lead to Daniels suggestion to apply a video-based depth inversion technique. A suggestion with large consequences. The vast majority of the PhD I have worked on the depth estimation technique *cBathy*. Endless weekly discussions with Daniel, Mark and Tim led to a much better understanding and significant improvements of cBathy in macro-tidal environments. The rest is history and a stand-alone camera system is developed since. The depth estimation technique *cBathy* is mainly developed and supplied by Rob Holman via Deltares. Rob, although your contribution to my work seems small, you gave me insight in and showed me how cBathy works!

One of most enjoyable parts of the PhD-track were the fieldwork experiences. Short campaigns such as the storm surveys with, in particular, Pedro 'Luis' Almeida, Tim Poate and Gerd Masselink. I have learned a great bit from you guys in the field if it comes to LiDAR, dedication and commitment to collect the best dataset possible: Never sit still there is always something to improve. Pedro, you were one of my best friends in Plymouth and I have enjoyed working in the field with you in particular. Our last campaign together in Vietnam was an absolute winner and keep up the good work! The Monthly surveys at Porthtowan are memorable. Christopher, Hugo, Stokes shared the first year with me. I enjoyed that time a lot with nice discussions, visiting band practises, staying over in Truro, lunch at the *Filling Station* and the joined quad-bike washing. Big-foot Sam was my second partner in crime. Radio 2 changed to Radio 1 but that was no problem with Sam's quality vocals. In the beginning, Sam's lovely British accent seems like a real tongue twister but when you get used to it, it is okay. On the contrary, my Dutch accent was not always as clear as it should be. I won't forget: Offshore, Porthtowan, North, South. Enjoyed it a lot guys!

The Coastal Processes Research Group at Plymouth is a nice group doing some pretty nice science. It is a team to stay in Plymouth for. The many PhD-students in the group made resulted in a vibrant ambiance in the Marine building. All the friends from the former 2nd, now 3rd floor, thanks a lot for the nice moments, the football session between the real scientist and the Engineers, fieldworks, diners, BBQ's and pub visits with Carlos, Olivier, Davide, Pedro and Paula, Kris, Kit, Claire, Thomas, Guio, Javier, Sam and Thom. [Too] many coffee breaks, beers, pool sessions and stone-oven pizze were shared with the little one, Guio. Little in size,

big in thought, voice and kicking butts. One thing Guio, do not roll the quad-bike over in the mud ;). I will never forget one word: *Malakas*. The greatest Malaka of all is Thomas who was my house-mate in Plymouth for around 2.5 years. Sorry mate, my best memory is beating a Greek 5-0 in Tavli. Well, okay, and the home-made Greek yoghurt, bread and awesome coffee machine were also nice. Finish your PhD and we meet up to laugh about those days in beautiful Plymouth. Olivier, cacahuète, get in shape! Shoot on goal properly [actually Pedro too ;-)]. Thanks for the good moments in surveys, walks around Plymouth, letting me stay at your place and football sessions. Also, I will make sure there are enough toilets at the Bath Half Marathon next year.

A large part of the writing-up I have spent in Porto, Portugal. Writing up at FEUP of the University of Porto was a great opportunity to get to know new people and another research environment. Mario and later Victor, thanks mates for the good times! Remember, only play table football with mixed teams.

In Porto I stayed with you, Andreia, and your Mum. I want to thank you for all the caring, love and support during this time. In the beginning it was hard, partially due to the greatest loss in your live. However, live is cyclic and after a low comes a high. A new period in the Açores lies in front of you and I am sure that many adventures will follow. Take those adventures with both hands, be passionate with all your heart and live your life, hopefully together. You are beautiful.

Leaving the country you grew up in, isn't always easy. You cannot see friends and family on a regular basis. I experienced this a few times with funerals and when my little [he is getting big though] nephew was born prematurely. Not being able to be there in the moment is not nice and rather frustrating but I would like you to remember that all of you have a special place in my heart, family is important to me and I will always support you wherever I am in the world and wherever you are. I am very lucky that I have some nice family members that *are always right* so a single *right* consult is enough for advice with nice values. Johan and Ria there are few people that change lives and you did. You both encouraged me to continue studying, work hard and achieve goals. Living abroad didn't help to keep frequent contact but I am sure, when I am in the Netherlands, I will pass by!

Bath, United Kingdom,
8 August 2016,
Erwin W. J. Bergsma

# Authors declaration

At no time during the registration for the degree of Doctor of Philosophy has the author been registered for any other University award without prior agreement of the Graduate Sub-Committee. Work submitted for this research degree at Plymouth University has not formed part of any other degree either at Plymouth University or at another establishment.

Relevant scientific seminars and conferences were regularly attended at which work was presented. One paper have been accepted for publication in refereed journals.

**Publications:**

**Bergsma, E.W.J, Conley, D.C., Davidson, M.A. & O'Hare T.J.** *Video-based near shore bathymetry estimation in macro-tidal environments* 2016, Marine Geology volume 374 pp. 31-41

**Bergsma, E.W.J, Conley, D.C., Davidson, M.A. & O'Hare T.J.** *cBathy under storm conditions; a storm impact and recovery assessment of Porthtowan beach, UK* submitted

**Posters and conference presentations:**

**AGU** AGU Fall meeting 2015, San Francisco, United States of America; Poster presentation: *High Spatio-Temporal Resolution Video-Based Depth Estimation under Extreme Storm Conditions in a Macro Tidal Environment* December 2015.

**ARGUS Workshop** Workshop within the Argus community for Argus developers and users 2014, Delft, The Netherlands; Oral presentation: *An Assessment Of Video-Based Bathymetry Estimation in a Macro-Tidal Environment* September 2014.

**ICCE** International Conference on Coastal Engineering 2014, Seoul, Korea; Oral presentation: *An Assessment Of Video-Based Bathymetry Estimation in a Macro-Tidal Environment* June 2014.

**Invited oral presentations:**

**FEUP** Faculdade de Engenharia da Universidade do Porto Hydraulic Engineering Seminar 2016, Porto, Portugal; Oral presentation: *Coastal video imagery, video-based depth estimations to observe storm impact and recovery* April 2016.

**PCO** Plymouth Coastal Observatory, annual stakeholders meeting 2015, Newton Abbot, United Kingdom; Oral presentation: *Depth estimation using video cameras in the South-West* October 2015.

Word count for the main body of this thesis: **43331**

**Signed:** _____

**Date:** _____

# Abstract

Erwin Willem Johan Bergsma

## Application of an improved video-based depth inversion technique to a macrotidal sandy beach

Storm conditions are considered *the* dominating erosional mechanism for the coastal zone. Morphological changes during storms are hard to measure due to energetic environmental conditions. Surveys are therefore mostly executed right after a storm on a local scale over a single or few storms [days to weeks]. The impact of a single storm might depend on the preceding sequence of storms. Here, a video camera system is deployed in the South-West of England at the beach of Porthtowan to observe and assess short-term storm impact and long-term recovery. The morphological change is observed with a state-of-the-art video-based depth estimation tool that is based on the linear dispersion relationship between depth and wave celerity (cBathy). This work shows the first application of this depth estimation tool in a highly energetic macrotidal environment. Within this application two sources of first-order inaccuracies are identified: 1) camera related issues on the camera boundaries and 2) fixed pixel location for all tidal elevations. These systematic inaccuracies are overcome by 1) an adaptive pixel collection scheme and camera boundary solution and 2) freely moving pixels. The solutions together result in a maximum RMS-error reduction of 60%. *From October 2013 to February 2015 depths are hourly estimated during daylight.* This period included, the 2013-2014 winter season which was the most energetic winter since wave records began. Inter-tidal beach surveys show 200 $m^3/m$ erosion while the sub-tidal video derived bathymetries show a sediment loss of around 20 $m^3/m$. At the same time the sub-tidal (outer) bar changes from 3D to linear due to a significant increase in alongshore wave power during storm conditions. Complex-EOF based storm-by-storm impact reveals that the individual storm impact at Porthtowan can be described as a combined function of storm-integrated incident offshore wave power [P] and disequilibrium [$\mathbf{\Delta\Omega}$] and that the tidal range has limited effect on the storm impact. The inter- and sub-tidal domain together gain volume over the 2013-2014 winter and the two domains show an interactive inverse behaviour indicating sediment exchange during relatively calm summer conditions. The inter-tidal domain shows accelerated accretion during more energetic conditions in fall 2014. The outer bar slowly migrated onshore until more energetic wave conditions activate the sub-tidal storm deposits and 3 dimensionality is reintroduced. The inter-tidal beach shows full recovery in November 2014, 8 months after the stormy winter.

# Contents

**Author's declaration** **v**

**1 Introduction** **16**

1.1 Context . . . . . 16

1.2 Objectives, approach and research questions . . . . . 17

1.2.1 General aim and objectives . . . . . 17

1.2.2 Research questions . . . . . 18

1.2.3 Approach . . . . . 19

1.3 Thesis outline . . . . . 19

**2 Background and Literature review** **21**

2.1 Conceptual beach morphology . . . . . 22

2.1.1 Wave-related changes in a conceptual model . . . . . 23

2.1.2 Wave and tide based conceptual model . . . . . 26

2.1.3 Near-shore bar morphology . . . . . 28

2.1.4 Storm Morphology . . . . . 32

2.2 Video-based coastal monitoring . . . . . 35

2.2.1 Argus systems . . . . . 35

2.2.2 Multiple cameras per camera system . . . . . 36

2.2.3 Inter-tidal topography estimation through video-imagery . . . . . 36

2.2.4 Sub-tidal depth estimations through video-imagery . . . . . 37

**3 Methods** **42**

3.1 Introduction . . . . . 42

3.2 Study site: Porthtowan . . . . . 42

3.3 Topography and bathymetry data collection . . . . . 48

3.4 Camera system at Porthtowan . . . . . 50

3.4.1 Video-based depth estimation technique . . . . . 51

3.4.2 cBathy settings at Porthtowan . . . . . 55

3.5 Momentary coastline . . . . . 57

3.6 Disequilibrium modelling of the momentary coastline . . . . . 58

3.7 Sub-tidal bar extraction . . . . . 62

3.7.1 Application at Porthtowan . . . . . 64

3.8 Empirical Orthogonal Functions . . . . . 66

3.8.1 Ordinary and Complex Empirical Orthogonal Functions . . . . . 67

3.9 Application of the methods . . . . . 71

**4 Video-based depth estimation in a Macro-Tidal environment** **73**

4.1 Introduction . . . . . 73

4.1.1 Environmental conditions . . . . . 73

4.2 Using multiple cameras in a cBathy domain . . . . . 74

4.2.1 Camera boundary issue . . . . . 75

4.2.2 Camera movement and adaptive collection scheme . . . . . 78

4.3 Performance in a macro-tidal environment . . . . . 81

4.3.1 cBathy in a macro-tidal environment . . . . . 81

4.3.2 Accuracy assessment . . . . . 84

4.4 Floating pixel modification . . . . . 87

4.5 Performance with modifications . . . . . 89

4.5.1 Improved accuracy . . . . . 90
4.6 The effect of the Kalman filter . . . . . 93
4.7 Discussion . . . . . 97
4.7.1 Potential effects at other sites . . . . . 98
4.7.2 Relation between wave height and accuracy . . . . . 100
4.7.3 Offshore extent of cBathy . . . . . 102
4.8 Conclusions . . . . . 104

**5 Observations of storm impact and recovery winter 2013-2014 105**

5.1 Introduction . . . . . 105
5.2 Overall storm impact and recovery October 2013 to December 2014 . . . . . 106
5.3 Sectioned storm impact winter season 2013-2014 . . . . . 107
5.3.1 Wave conditions and storm identification . . . . . 108
5.3.2 Time-frame selection . . . . . 109
5.3.3 October to December 2013 . . . . . 110
5.3.4 December 2013 to end-January 2014 . . . . . 110
5.3.5 End-January to mid-February 2014 . . . . . 112
5.3.6 mid-February to mid-March . . . . . 115
5.3.7 Observation of storm deposits . . . . . 117
5.4 Recovery over the remainder of 2014 . . . . . 120
5.4.1 Recovery wave conditions . . . . . 120
5.4.2 March to May 2014 . . . . . 120
5.4.3 May to September 2014 . . . . . 123
5.4.4 September to early-December 2014 . . . . . 125
5.5 Inter- and sub-tidal interaction . . . . . 129
5.6 Sub-tidal bar behaviour at Porthtowan [2013-2015] . . . . . 131
5.7 Discussion . . . . . 137

5.7.1 Long-term perspective of winter 2013-2014 . . . . . 137
5.7.2 Alongshore wave power and three dimensionality . . . . . 138
5.8 Conclusions . . . . . 139

**6 The application of EOFs to video-based bathymetries 141**

6.1 Introduction . . . . . 141
6.2 Application of EOFs at Porthtowan . . . . . 142
6.2.1 Input dataset and modal confidence . . . . . 142
6.2.2 Spatial amplitude and phase patterns . . . . . 144
6.2.3 Spatial pattern variation due to phase shift . . . . . 146
6.2.4 Alongshore average behaviour . . . . . 146
6.3 Results . . . . . 153
6.3.1 Temporal results and volume estimation . . . . . 153
6.3.2 Hourly wave power versus morphology . . . . . 157
6.4 Discussion . . . . . 159
6.4.1 Storm impact . . . . . 159
6.4.2 Recovery over the remainder of 2014 . . . . . 166
6.5 Conclusions . . . . . 169

**7 Discussion and conclusions 171**

7.1 Synthesis . . . . . 171
7.2 Reflection on the research questions . . . . . 173
7.2.1 Hourly video-based bathymetric data collection . . . . . 173
7.2.2 Storm impact and recovery . . . . . 175
7.3 Suggestions for Future Research . . . . . 181
7.4 Conclusions . . . . . 183
7.4.1 Video-based bathymetry estimation . . . . . 183
7.4.2 Storm impact and recovery . . . . . 184

**A Sinusoidal Least Square fitting** **185**

**B Tidal prediction routine** **187**

**C Validation of the reconstruction procedure** **189**

C.0.1 Progressive wave test . . . . . 191

C.0.2 Filtering with EOFS . . . . . 193

**D Alongshore wave power** **197**

**List of references** **199**

# List of Figures


2.1 Schematic representation of the used coastal definitions in this work. . . . . 21

2.2 Conceptual model covering wave-dominated beach changes [modified from Wright & Short (1984)]. . . . . 24

2.3 Conceptual beach classification model to predict beach morphology based on the dimensionless fall velocity [$\Omega$] and relative tidal range [RTR] [modified from Masselink & Short (1993)]. . . . . 27

2.4 Conceptual beach classification model to predict beach morphology based on the dimensionless fall velocity [$\Omega$] and relative tidal range [RTR] for the United Kingdom [modified from Scott et al. (2011)]. . . . . 28

2.5 a) examples of nearshore bar configurations. b) upper and middle panel: two conceptual template-forcing mechanisms for bar formation [modified from (Komar 1999)], lower panel represents velocities under a standing wave [modified from (Holthuijsen 2007)]. . . . . 29

3.1 Historical photographs of Porthtowan (*Porth Tewyn*) 1880-2010 . . . . . 43

3.2 Map overview of the region around Porthtowan and Perranporth. . . . . 44

3.3 Beach classification following (Masselink & Short 1993), Relative Tidal Range (RTR) versus dimensionless fall velocity $\Omega$. a) represents the period from January to June and b) covers July to December. . . . . 45

3.4 Wave rose from the Perranporth wave buoy data Numbers around the circle indicate incoming wave angle and the radial bands correspond to the wave heights [0-6 m] . . . . . 46

3.5 Tidal constituents and amplitudes derived from pressure transducer data. . . . . 47

3.6 a) Residual tidal elevation signal [measured - reconstructed] in blue, atmospheric pressure data in grey and the inverse barometric effect in red. b) represents the over ($>0$) and under-prediction ($<0$) of the tidal elevation after the inclusion of the inverse barometric effect . . . . . 48

3.7 Typical survey domains for the topography [blue] and bathymetry [red] measurements . . . . . 49

3.8 Measured bathymetry (10 April 2014) with the overlaying lines indicate the different regions for the further analysis; inter-tidal (green), sub-tidal bar region (yellow) and offshore region (purple). . . . . 50

3.9 a) Camera footprint per camera for the video system at Porthtowan with 4 cameras overlaying satellite imagery and b) camera footprints over a surveyed bathymetry together with the earlier defined regions. . . . . 52

3.10 Temporal decay in faith of an estimate [prior] presented in percentage considering a **new** estimate with a certain depth estimation error [$h_{error}$] . . . . . 55

3.11 Momentary coastline principle in this work [modified from (TAW 2002)]. . . . . 58

3.12 Example of disequilibrium modelling results using the wave data as presented in Section 3.2. a) instantaneous dimensionless fall velocity in grey and weighted dimensionless fall velocity in orange. b) disequilibrium in grey and the time integrated disequilibrium in orange [a proxy for DLT10 if $k=0$]. c) final model results of DLT10 with $k=2$ following Wright et al. (1985) in grey and DST13 in orange. . . . . 60

3.13 Example of the bar-line identification after de-trending an arbitrary bathymetry. The left figure represent a bathymetry estimate and at the right the base profile is subtracted from the depth estimate. . . . . 63

3.14 Base bathymetry on the left and cross shore profile on the right. The red line is the mean profile and the blue line is the base profile that is used to construct the base bathymetry. . . . . 65

3.15 Example of the bar-line identification after de-trending an arbitrary bathymetry. The left figure represent a bathymetry estimate and at the right the base profile is subtracted from the depth estimate. . . . . 66

3.16 Estimated bar positions [white asterisks] and the bar lines in red for the same example as in Figure 3.15 . . . . . 67

4.1 Estimated depths on an arbitrary day with the camera boundaries(lines) . . . . . 75

4.2 Difference between the survey (10 April 2014) and estimates (9 april 2014). (a) represents the difference between the survey and a single estimate (18:00) and (b) is the difference between the survey and the daily Kalman filtered result. The black lines represent the camera boundaries. . . . . 76

4.3 Difference between the survey (10 April 2014) and estimates (9 April 2014). (a) represents the difference between the survey and a single estimate (18:00) without the solution and (b) shows the difference between the survey and the same single estimate (18:00) with the camera boundary solution. The black lines represent the camera boundaries. . . . . 77

4.4 Adjustment of the camera footprint after modified data collection scheme. a) overview of the camera footprint, b) Coverage number of cameras over the whole domain c) re-initiation of a camera boundary between to equally important cameras 79

4.5 On the left side respectively the bathymetry estimate on the 10th of April 2014 (a), the difference to the survey (c) and two cross sections (e) (at 100m and 300m) are shown. On the right side respectively the bathymetry estimate (b), the difference to the survey (d) and two cross sections (f) (at 100m and 300m) on 17 April 2014 are presented. . . . . 82

4.6 a) and b) represent the estimated depth plotted against the surveyed depth for respectively the estimates on the 10th of April 2014 and 17th of April 2014. c) and d) show the corresponding probability distribution for both estimate dates. . 85

4.7 RMS error compared to wave height and tidal range. Red line is represents a linear regression with $r^2 = 0.295$ and is significant ($p = 0.024$) at the 95% confidence interval. Grey patch indicates the domain of the macro tidal range ($TR > 4$). . . 86

4.8 a) Schematic representation of the pixel movement and contraction/expansion of a patch of pixels. b) Horizontal pixel movement during largest spring tide at Porthtowan. Grey dot indicates the position of the camera system . . . . . 88

4.9 On the left panel respectively a renewed bathymetry estimate using the modifications on the 10th of April 2014 (a) and two cross sections (c) at X=100 meters and X=300 meters. On the right is the renewed bathymetry estimate (b) on 17 April 2014 and the corresponding cross sections (d) at X=100 and X=300 . . . . 89

4.10 a) and b) represent the estimated depth plotted against the surveyed depth for respectively the estimates on the 10th of April 2014 and 17th of April 2014. c) and d) show the corresponding probability distribution for both estimate dates. . 91

4.11 a) and b) represent the estimated depth plotted against the surveyed depth for respectively the estimates using a daily Kalman Filter and a long-term Kalman Filter. c) and d) show the corresponding probability distribution for both applications. . . . . 95

4.12 The untimate comparision between the measured bathymetry in a) and estimated bathymetry in b) under the largest tidal range conditions at Porthtowan. c) represents the difference over the domain and d) shows cross shore profiles at Y = 100 m and Y = 300 m. . . . . 96

4.13 RMS error for modified cBathy over the whole domain against wave height and tidal range. a) represent the RMS error for cBathy without all modifications, b) shows the RMS error with the modifications and c) shows the reduction in percentage of the RMS error between the a) and b). . . . . 98

4.14 Horizontal pixel displacement (log scale) as function of the tidal range and ratio d/h (d = distance from the camera and h = camera height) . . . . . 99

4.15 Accuracy values versus wave height; trends and extrapolation. a) RMS error, b) the mean error ($\mu$), c) the standard deviation ($\sigma$) and d) $|\Delta Z| < 0.4$ m for mulitple depth estimates. . . . . 101

4.16 Annual mean wave height [$\bar{H}_s$] and corresponding depth of closure from 2008 to 2015. . . . . 103

5.1 Measured [black line] and modelled [orange line] momentary coastline with underlying wave power from October 2013 to December 2014. . . . . 106

5.2 Wave conditions during the winter 2013-2014. Wave height and period, red and green line represent respectively the 1% and 5% exceedance threshold. . . . . 108

5.3 Inter-tidal beach survey 7 October 2013 (a) and 6 December 2013 (b). The red is mean sea level, the yellow line represents the lower boundary for the momentary coastline and the black dashed line is the calculated cross shore position of the momentary coastline. c) the difference between the two surveys dates and d) measured and modelled momentary coastline. e) and f) represent the most accurate depth estimation within a few days of the inter-tidal beach surveys . . . 111

5.4 Inter-tidal beach survey 6 December 2013 (a) and 30 January 2014 (b). The red is mean sea level, the yellow line represents the lower boundary for the momentary coastline and the black dashed line is the calculated cross shore position of the momentary coastline. c) the difference between the two surveys dates and d) measured and modelled momentary coastline. e) and f) represent the most accurate depth estimation within a few days of the inter-tidal beach surveys . . . 113

5.5 Inter-tidal beach survey 30 January 2014 (a) and 17 February 2014 (b). The red is mean sea level, the yellow line represents the lower boundary for the momentary coastline and the black dashed line is the calculated cross shore position of the momentary coastline. c) the difference between the two surveys dates and d) measured and modelled momentary coastline. e) and f) represent the most accurate depth estimation within a few days of the inter-tidal beach surveys . . . 114

5.6 Inter-tidal beach survey 17 February 2014 (a) and 19 March 2014 (b). The red is mean sea level, the yellow line represents the lower boundary for the momentary coastline and the black dashed line is the calculated cross shore position of the momentary coastline. c) the difference between the two surveys dates and d) measured and modelled momentary coastline. e) and f) represent the most accurate depth estimation within a few days of the inter-tidal beach surveys . . . 116

5.7 Inter-tidal beach survey 7 October 2013 (a) and 17 February 2014 (b). The red is mean sea level, the yellow line represents the lower boundary for the momentary coastline and the black dashed line is the calculated cross shore position of the momentary coastline. c) and d) represent the most accurate depth estimation within a few days of the inter-tidal beach survey. e) and f) are the difference plots for respectively the inter-tidal beach surveys [e)] and video-based depth estimations [f)]. . . . . 119

5.8 Wave conditions [grey] and tidal range [orange] during the recovery period. The red dashed line represents the 1% exceedance and the green dashed line is the line of 5% exceendance . . . . . 120

5.9 Inter-tidal beach survey 19 March 2014 (a) and 14 May 2014 (b). The red is mean sea level, the yellow line represents the lower boundary for the momentary coastline and the black dashed line is the calculated cross shore position of the momentary coastline. c) the difference between the two surveys dates and d) measured and modelled momentary coastline. e) and f) represent the most accurate depth estimation within a few days of the inter-tidal beach surveys . . . 122

5.10 Inter-tidal beach survey 14 May 2014 (a) and 13 September 2014 (b). The red is mean sea level, the yellow line represents the lower boundary for the momentary coastline and the black dashed line is the calculated cross shore position of the momentary coastline. c) the difference between the two surveys dates and d) measured and modelled momentary coastline. e) and f) represent the most accurate depth estimation within a few days of the inter-tidal beach surveys . . . 124

5.11 Inter-tidal beach survey 13 September 2014 (a) and 5 December 2014 (b). The red is mean sea level, the yellow line represents the lower boundary for the momentary coastline and the black dashed line is the calculated cross shore position of the momentary coastline. c) the difference between the two surveys dates and d) measured and modelled momentary coastline. e) and f) represent the most accurate depth estimation within a few days of the inter-tidal beach surveys . . . 126

5.12 Inter-tidal beach survey 7 October 2013 (a) and 5 December 2014 (b). The red is mean sea level, the yellow line represents the lower boundary for the momentary coastline and the black dashed line is the calculated cross shore position of the momentary coastline. c) and d) represent the most accurate depth estimation within a few days of the inter-tidal beach survey. e) and f) are the difference plots for respectively the inter-tidal beach surveys [e)] and video-based depth estimations [f)]. . . . . 128

5.13 Cumulative volumetric change per meter shoreline from November 2013 to February 2015 . . . . . 129

5.14 The blue line represents the wave power over time, the black line is the daily mean cross shore sub-tidal bar position over time with the grey patch indicating the standard deviation of the bars.The orange line represents a mean cross shore bar position over a period between surveys . . . . . 131

5.15 a) A three dimensional example of the bar detection b) A linear example of the bar detection . . . . . 133

5.16 The blue line represents the wave power and the black line represents a continuous proxy for bar three dimensionality, the orange line is a mean over a period between surveys. . . . . 134

5.17 An example bathymetry estimate mid-August that indicates the geometry problem at this time and the artificial increase in three-dimensionality. . . . . 134

5.18 Representative example bar detections a) 20 October 2013, b) 25 April 2014, c) 31 May 2014, d) 5 September 2014, e) 27 November 2014 and f) 30 December 2014136

5.19 Measured [black curve] and modelled [orange curve] momentary coastline presented together with the wave power [grey curve] over a period from 2008 to mid-2015. . . . . 137

5.20 Alongshore wave power at Porthtowan . . . . . 139

6.1 a) Mean bathymetry is subtracted from the input matrix $A$. All the variation found in the EOF modes varies around this mean bathymetry. b) Monte Carlo simulation analysis to assess the statistical relevance of the EOF modes for the Porthtowan depth estimates dataset. The blue dots represent the found eigenvalue per EOF mode, the lines indicate the 99%, 95% and 50% confidence interval. . . 143

6.2 Two most dominant modes at Porthtowan. a) and c) represent the spatial amplitude and the b) and d) show the corresponding spatial phases. . . . . 144

6.3 Spatial EOF modes with phase shift, a) $1^{st}$ mode + $\pi$ shift, b) $2^{nd}$ mode + $\pi$ shift, c) $1^{st}$ mode + $\frac{3\pi}{4}$ shift, d) $2^{nd}$ mode + $\frac{3\pi}{4}$ shift, e) $1^{st}$ mode + $\frac{\pi}{2}$ shift, f) $2^{nd}$ mode + $\frac{\pi}{2}$ shift . . . . . 147

6.4 Spatial EOF modes with phase shift, a) $1^{st}$ mode + $\frac{\pi}{4}$ shift, b) $2^{nd}$ mode + $\frac{\pi}{4}$ shift, c) $1^{st}$ mode + 0 shift, d) $2^{nd}$ mode + 0 shift, e) $1^{st}$ mode $-\frac{\pi}{4}$ shift, f) $2^{nd}$ mode $-\frac{\pi}{4}$ shift . . . . . 148

6.5 Spatial EOF modes with phase shift, a) $1^{st}$ mode $-\frac{\pi}{2}$ shift, b) $2^{nd}$ mode $-\frac{\pi}{2}$ shift, c) $1^{st}$ mode $-\frac{3\pi}{4}$ shift, d) $2^{nd}$ mode $-\frac{3\pi}{4}$ shift, e) $1^{st}$ mode $-\pi$ shift, f) $2^{nd}$ mode $-\pi$ shift . . . . . 149

6.6 Alongshore average EOF mode profiles with different (artificial) temporal phase shifts. a) represents the first EOF mode and b) corresponds to the second EOF mode. The mean profile (black line) is plotted in the bottom of a) and b) with the minimum and maximum impact of the EOF modes before multiplication with the temporal amplitude. . . . . 150

6.7 a) Represents the amplitude (blue) and phase (grey) of the first EOF mode. b) Represents the amplitude (blue) and phase (grey) of the second EOF mode. . . 154

6.8 a) Time stack of the alongshore average profile [combination of spatial amplitude and phase and temporal amplitude and phase] corresponding to the first EOF mode [42.4% of the variance]. b) Modelled disequilibrium as described in Section 5.2 - c) Time stack of the alongshore average profile [combination of spatial amplitude and phase and temporal amplitude and phase] corresponding to the second EOF mode [15.35% of the variance] . . . . . 155

6.9 Cumulative volume per EOF-mode and for the inter-tidal beach survey. . . . . 156

6.10 Orange line represents the normalised integrated disequilibrium based on wave data. Black line is the normalised momentary coastline of the inter-tidal beach surveys. The blue and purple line are the volume change for respectively the first and second EOF mode, integrated over time for the whole camera domain. All data are normalised over the time frame 2008 - 2015 . . . . . 157

6.11 Instantaneous $\Delta V$ against instantaneous wave power [MWh/m] . . . . . 158

6.12 Accumulative wave power over a storm potted against storm duration in hours. 160

6.13 $\Delta V$ over a storm against the corresponding storm duration. . . . . 160

6.14 a) $\Delta V$ over a storm against the corresponding maximum wave power during the storm. b) $\Delta V$ over a storm against the corresponding accumulative wave power. . 161

6.15 a) $\Delta V$ over a storm against mean dimensionless fall velocity [$\Omega$] over the storms. b) $\Delta V$ over a storm against the corresponding disequilibrium $\Delta\Omega$. . . . . 162

6.16 a) $\Delta V$ over a storm the corresponding time-integrated disequilibrium during the storm. b) $\Delta V$ over a storm against the corresponding time-integrated disequilibrium stress over the storm. . . . . 163

6.17 a) $\Delta V$ over a storm against the corresponding tidal elevation at maximum storm power. b) $\Delta V$ over a storm against the corresponding mean tidal range during the storm. . . . . 164

6.18 Storm impact (a) and instant $\Delta V$ (b) in time over the period covering winter 2013-2014 . . . . . 165

6.19 Recovery [March to November/December 2014] and subsequent erosion [December 2014 - February 2015] for the inter- and sub-tidal beach. Grey solid line is the wave power [corresponding to the left y-axis], the blue line represents the EOF derived volume, the black dashed line is the measured momentary coastline with the astrisks indicating the survey date and the orange line represents the modelled time-integrated disequilibrium. . . . . 167

C.1 Resulting four components of a complex EOF analysis using Horel (1984), Ruessink et al. (2000). In the top two plots, the black line is the real part and the blue line represents the imaginary part of the solution. The four bottom plots are the temporal multipliers. . . . . 190

C.2 Reconstruction test combining the four components of a complex EOF analysis using Horel (1984), Ruessink et al. (2000). . . . . 191

C.3 Progressive wave test with a) an ordinary EOF analysis and b) a complex EOF analysis. For both the input, two EOF components and reconstruction is shown. 192

C.4 Progressive wave test including noise using a complex EOF analysis. Two EOF components and reconstruction are shown. . . . . 193

C.5 Black line is real part and blue line is imaginary part. 2 Components case without noise; shows that the first EOF gets 100% of the input . . . . . 195

C.6 Black line is real part and Blue line is imaginary part. If we introduce Gaussian White noise to the data we see that the EOF system is capable of extracting the input component without noise. EOFs could be used to as a filtering technique . 196

D.1 Wave height ($H_s$), period ($T_p$), direction relative to shore normal ($\theta$), wave power (P) and alongshore wave power ($P_y$) at Porthtowan . . . . . 198

# List of Tables

3.1 Overview of Porthtowan specific settings for cBathy . . . . . 56

4.1 Tide range and day-average wave conditions during **surveys** and estimates . . . . 74

4.2 Accuracy values: Root Mean Square error (RMSE), $R^2$ and the mean error ($\mu$), standard deviation ($\sigma$) for $\Delta Z$ for the neap and spring tide case. The RMS error is divided in the whole domain [All], the inter-tidal area [IT], the sub-tidal area [ST], sub-tidal bar domain [ST bar] and the offshore domain [Off]. For the RMS error the error percentage of the local depth is presented between brackets. . . . 86

4.3 Accuracy values: Root Mean Square error (RMSE), $R^2$ and the mean error ($\mu$), standard deviation ($\sigma$) for $\Delta Z$ for the original (orange), floating pixel (gray) and floating pixel with camera boundary solution (blue). The RMS error is divided in the whole domain [All], the inter-tidal area [IT], the sub-tidal area [ST], sub-tidal bar domain [ST bar] and the offshore domain [Off]. For the RMS error the error percentage of the local depth is presented between brackets. . . . . 92

4.4 Root mean square errors for all zones and accuracy values: $R^2$ and the mean ($\mu$), standard deviation ($\sigma$) for $\Delta Z$ for daily Kalman filtered depth estimates using the floating pixel and camera boundary solution (blue) and long-term (months) Kalman filtered depth estimates using the floating pixel and camera boundary solution (white). . . . . 94

6.1 Overview of the morphological behaviour per mode per change in phase shift $\psi$ . 152

# Chapter 1

# Introduction

## 1.1 Context

Globally changing environmental conditions are believed to result in intensifying weather conditions, e.g. an increasing trend in wind speeds is observed from 1850 to 2010 (Dobrynin et al. 2012). Ultimately, intensifying weather conditions lead to more energetic, rougher, wave conditions (Dodet et al. 2010, Wang et al. 2012, Dobrynin et al. 2012, Woolf & Wolf 2013). As waves dissipate their energy in the coastal zone, resulting in sediment transport, one can expect coastal zones to experience more erosive wave conditions and change the overall dynamic beach states due to changing incident wave conditions. The former leaves the coastal zone more vulnerable to coastal flooding during severe storms. Adaptation to, and mitigation against, the increased severe conditions requires in depth understanding of the impact such storms have on the coastal zone (Masselink & van Heteren 2014). Coco et al. (2014) and Masselink et al. (2015) both mention the lack of qualitative and appropriate observational storm response datasets to develop, calibrate and validate [numerical] models to predict storm impact. Also, Ranasinghe et al. (2013) shows that field observations are rarely sufficient to numerically predict future storm impact. Recent developments of video-based depth estimation (Plant et al. 2008) and (Holman et al. 2013) can fill the identified data-gap.

Holman et al. (2013) shows that depths are estimated with a typical accuracy in the order of 10s of centimetres. This accuracy depends to a large extent on the wave conditions - the bias increases if the wave height increases. Nonetheless, these depth estimates are obtained under quasi-ideal circumstances, e.g. micro tidal environment and moderate waves. The depth estimation technique is promising but has never been tested under more energetic wave con-

ditions and larger tidal ranges. Here, the depth estimation method of Holman et al. (2013) is applied to macro-tidal environment and generally highly energetic wave climate over a period from October 2013 to December 2014. Ultimately, the depth estimation technique is assessed during the extreme winter of 2013-2014, which contained one of the most extreme clusters of storms ever measured in Western Europe (Masselink et al. 2015, Castelle et al. 2015).

The morphological impact of storms is often assessed using inter-tidal beach surveying over a single storm event or a small number of subsequent storms (Coco et al. 2014). The inter-tidal beach surveys provide knowledge on the volume of sediment loss from the beach but not where this sediment is transported to. Qualitatively, Plant et al. (2006) and Gallagher et al. (1998) show the rapid seaward transport of sediment during energetic [erosive] wave conditions and slow landwards transport during calmer [accretive] wave conditions. These observations often coincide with respectively straightening and re-introducing three dimensionality of the outer bar (Price & Ruessink 2011). The depth inversion technique will allow for a storm-by-storm impact analysis and assess the storm-impact contribution of individual parameters such as tidal range, dis-equilibrium and storm clustering (Birkemeier et al. 1999, Ferreira 2005, Splinter et al. 2014). Coco et al. (2014) and Masselink et al. (2015) mention the lack of storm impact and recovery datasets that have a sufficient offshore extent to track the offshore sediment deposition during storms, subsequent slower recovery and the inter-action between sub-tidal bars and recovery of the inter-tidal beach.

## 1.2 Objectives, approach and research questions

### 1.2.1 General aim and objectives

This work aims to apply and improve the new video-based depth inversion technique (Holman et al. 2013) and access storm impact and recovery of Porthtowan beach, using the video-based depth estimations, following the above identified research gaps and context. The storm-impact specific aim is to quantify sediment loss, storm deposits, the interaction between the inter- and sub-tidal zone and a storm-by-storm impact assessment to assess effects of, for example, tidal range and wave power on the impact of individual storms. In order to fulfil these aims we derived three main assessment objectives:

1. Assess the applicability of Holman et al. (2013) and obtain high spatial [O(100-1000 m)] and temporal [daily to hourly] video-based bathymetry estimations at the macro-tidal study site,

2. Assess storm impact [2013-2014 winter season] and quantify the relationships between the volumetric impact of individual storms and environmental parameters such as wave power, tidal elevation and tidal range at the macro-tidal study site,
3. Assess the [long-term] storm impact and recovery of the 2013-2014 winter season in terms of coastal strength and sub-tidal bar dynamics.

### 1.2.2 Research questions

The objectives are accompanied by research questions which are divided in two sub-sections: the video-based depth estimations and, secondly, the storm impact. The former focusses on the applicability of the depth estimation tool in macro-tidal environments. The depth estimation tool has not been applied in environments with large tidal range prior to this work. In addition, the effect/limitations of multiple cameras on the depth estimation are currently unknown, especially on the camera boundaries as the field of views of cameras overlap. Research questions related to the application of a video-based depth estimation technique in a macro-tidal environment that are targeted are:

1. What are the restrictions of video-based depth estimations in a multi camera domain?
2. How accurate are video-based depth estimations (Holman et al. 2013) in macro-tidal environments?
3. What is the effect of bathymetry assimilation through a Kalman Filter?

The storm impact and subsequent recovery is analysed using inter-tidal beach surveys and the video-based depth estimations. The inter-tidal beach surveys have been collected since 2008 and provide the long-term impact of the winter 2013-2014 through a momentary coastline analysis. The seasonal storm impact is analysed using the inter- and sub-tidal bed level elevations. Ultimately the sub-tidal video-based depth estimations are used for the storm-by-storm analysis. Morphological modes [through Empirical Orthogonal Functions] are derived for the storm-by-storm analysis. Research question regarding these analyses are:

1. What is the impact of the 2013-2014 winter season and does the beach recover in the remainder of 2014?
2. How does the volumetric change over individual storms relate to the corresponding storm duration, wave power, tidal elevation and tidal range?

3. Is the inter-tidal beach erosion due to the 2013-2014 winter unusual over year-long time scales?

4. How does the cross-shore migration and three dimensionality of the bar relate to occurring storms and subsequent recovery?

### 1.2.3 Approach

A three step overall approach is applied to achieve all the objectives and associated research questions: 1) bathymetry information collection [Chapter 4], 2) Observation of the 2013-2014 winter season storm impact (volumetric changes and bar morphology) and subsequent recovery over the remainder of 2014 [Chapter 5] and 3) the assessment of a storm-by-storm impact [Chapter 6].

## 1.3 Thesis outline

**This Chapter** the introduction gives the context of this research, states the objectives and introduces research questions per objective.

**Chapter 2; Background and Literature review** gives the necessary background to understand and have a perception of general applications/processes that are investigated in this work and cover at the same time the current state-of-the-art.

**Chapter 3; Methods** introduces all the methods used during the investigation of the objectives and answering of the research questions. The chapter contains descriptions of the collection of data [wave, tidal and bed level data], beach state, momentary coastline, sub-tidal bar detection/extraction and Empirical Orthogonal Functions [EOFs].

**Chapter 4; Video-based depth estimation in a Macro-Tidal environment** deals with the application, accuracy assessment and improvement of the video-based depth estimations.

**Chapter 5; Observations of storm impact and recovery winter 2013-2014** describes the storm impact over the 2013-2014 winter season and the recovery in the remainder of 2014 in terms of volume changes over the inter-tidal beach domain, momentary coastline and video-based depth estimations. The storm impact is placed in a year-long perspective.

**Chapter 6; The application of EOFs to video-based bathymetries** presents the EOF-filtering and extraction of principle EOF modes that represent morphological change. These principle modes are utilised to assess the storm by storm volumetric impact and compare those results to wave power, tidal range and elevation, disequilibrium and disequilibrium stress.

**Chapter 7; Discussion and conclusions** discusses the main new findings for each objective and ultimately answers the research questions one by one. Further research suggestions are stated here. The final section of the Chapter enumerates the final conclusions of this work.

# Chapter 2

# Background and Literature review

In this Chapter the background material and current state of knowledge relating to the study is discussed. Here we focus on three topics: 1) general beach morphology, 2) video-based coastal monitoring and 3) storms in relation to coastal impact.

### Coastal definitions

Coastal definitions come in many forms. Depending on the application or research topics, certain zones are more highlighted than others. The coastal definitions used in this work are schematically presented in Figure 2.1.

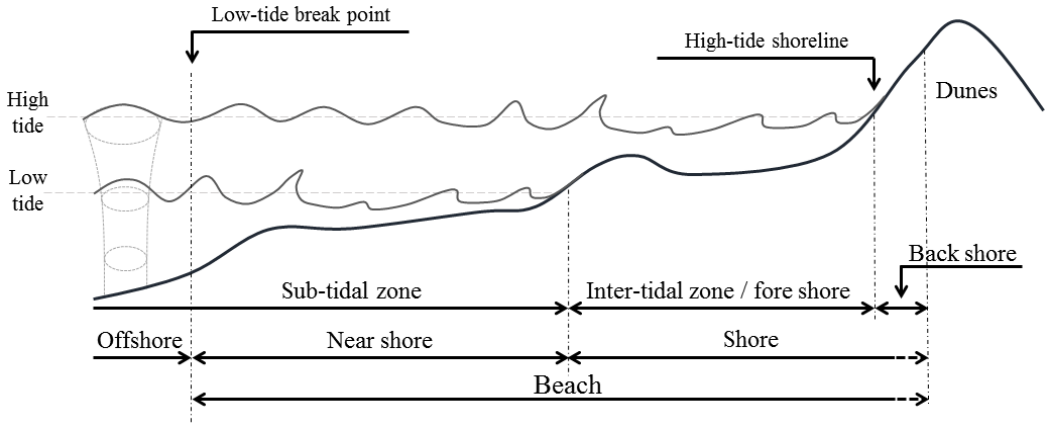


Figure 2.1: Schematic representation of the used coastal definitions in this work.

Here, the offshore domain is the outer edge of the surf zone at low-tide. Only a small part of the offshore domain is shown in Figure 2.1 as the waves are already in shallow water [particle

motion indicator in light grey]. The domain to the right of the offshore edge in Figure 2.1 represents the beach. the beach is considered the domain covering from the sub-tidal zone to the dunes. The beach domain is divided in two shore zones; near shore and shore. The near shore is considered the part of the beach that is always sub-merged and therefore "sub-tidal". Shore contains the inter-tidal zone/fore shore and the back shore and reaches to the dunes.

## 2.1 Conceptual beach morphology

Coastal morphology is in essence a function of all interrelated processes such as the local environmental forcing [waves and tides] and resulting coastal hydrodynamics, bathymetry, coastline geology and sediment availability. General coastal morphology can be divided into five main parts according to Davies (1980); 1) highly tide dominated coasts, 2) low tide dominated coasts, 3) mix energy tide dominated coasts, 4) mixed energy wave dominated coasts and 5) wave dominated coasts. It is the ratio between the mean wave height and mean tidal range that determines to some extent what regime the coastal system experiences. As a general division between the two extremes [fully tide or wave dominated] one could say that tide dominated coasts contain larger estuaries, larger deltas and tidal inlets while the wave dominated coastal zones are typically characterised by long uninterrupted coastlines [with smaller scale 3D features such as bars]. The mixed-energy to wave dominated environments are relevant to this work considering the study site and those will be described in a conceptual manner in this section.

In wave-dominated coastal environments, sediment transport is predominantly generated by incident waves and can be sub-divided into two processes; bed-load and suspended-load sediment transport. Waves are depth limited in intermediate and shallow water and this results in a bottom shear stress. For the bed-load transport this stress moves sediment without entraining it in the water column. For the suspended load transport, the shear stress entrains sediment in the water column and those entrained sediments are transported by wave generated currents before settling down to the bottom. Shields (1936) found from experimental data that sediment transport occurs when a critical threshold value of the bottom shear stress is exceeded. The threshold value for the sediment to move is strongly related to the sediment properties like density and grain diameter. Wave-induced bottom shear stresses are believed to be a function of the wave-induced orbital velocity at the bottom. This means that in order to move sediments, the orbital motions of incident waves have to "feel" the bottom. As the waves propagate into shallower waters and eventually break the bottom shear stress increases, resulting in more sediment transport and morphodynamics. Hallmeier (1981) sub-divided the beach zone in an

upper shore-face where sediment transport is measurable and a lower shore-face where sediment transport occasionally occurs during, for example, storms. Hallmeier (1981) separates the upper and lower shore-face by the depth of closure. The depth of closure represents the depth at a certain cross shore position of limited morphological change at the offshore boundary of the upper shore-face. The upper shore is discussed in the following Sections 2.1.1, 2.1.2 and 2.1.3, the storm impact and sediment transport further offshore will be discussed in Section 2.1.4.

### 2.1.1 Wave-related changes in a conceptual model

The section above illustrates the sediment transport due to waves in the near-shore and inter-tidal zone. These zones together are commonly referred to as the littoral zone. The beach morphology of the littoral zone under varying wave climates is often described through a conceptual beach state model by Wright & Short (1984). The conceptual beach state model consists of six beach states where the beach state normally ranges from; 1) dissipative, 2)-5) intermediate and 6) reflective as shown in Figure 2.2. The intermediate beach states are respectively Longshore Bar Through [LBT], Rhythmic Bar and Beach [RBB], Transverse Bar and Beach [TBB] and Ridge and Runnel or Low Tide Terrace [LTT]. The dissipative beach state is characterised by a gentle slope and incident waves are mostly spilling breakers, while the reflective beach has a steep slope and surging breakers. The dissipative and reflective beach states are relatively featureless [in comparison to the intermediate states] and are well distinguishable by the surf-zone scaling factor epsilon (2.1). The surf scaling factor can be seen as an indicator of the relative importance of reflection and dissipation.

$$\varepsilon = \frac{2\pi^2 H_b}{gT^2 \tan^2 \beta} \tag{2.1}$$

In this expression $\varepsilon$ is the surf zone scaling factor, $H_b$ represents the breaker wave height, $g$ is the gravitational acceleration, $T$ represents the wave period and $\beta$ is the beach slope. Reflective wave conditions are dominant if $\varepsilon < 2.5$ and for $\varepsilon > 20$ dissipative conditions prevail. If the surf scaling factor is in between the two extremes, both reflection and dissipation occurs and this relates to intermediate beach states as presented in Figure 2.2. The two extreme beach states are well defined by the surf zone scaling factor but the intermediate states less so. An alternative dimensionless factor is therefore linked to the beach state by Wright & Short (1984) namely the dimensionless fall velocity (Nayak 1970, Dean 1973).

$$\Omega = \frac{\mathrm{H_b}}{w_\mathrm{s}\mathrm{T}} \tag{2.2}$$

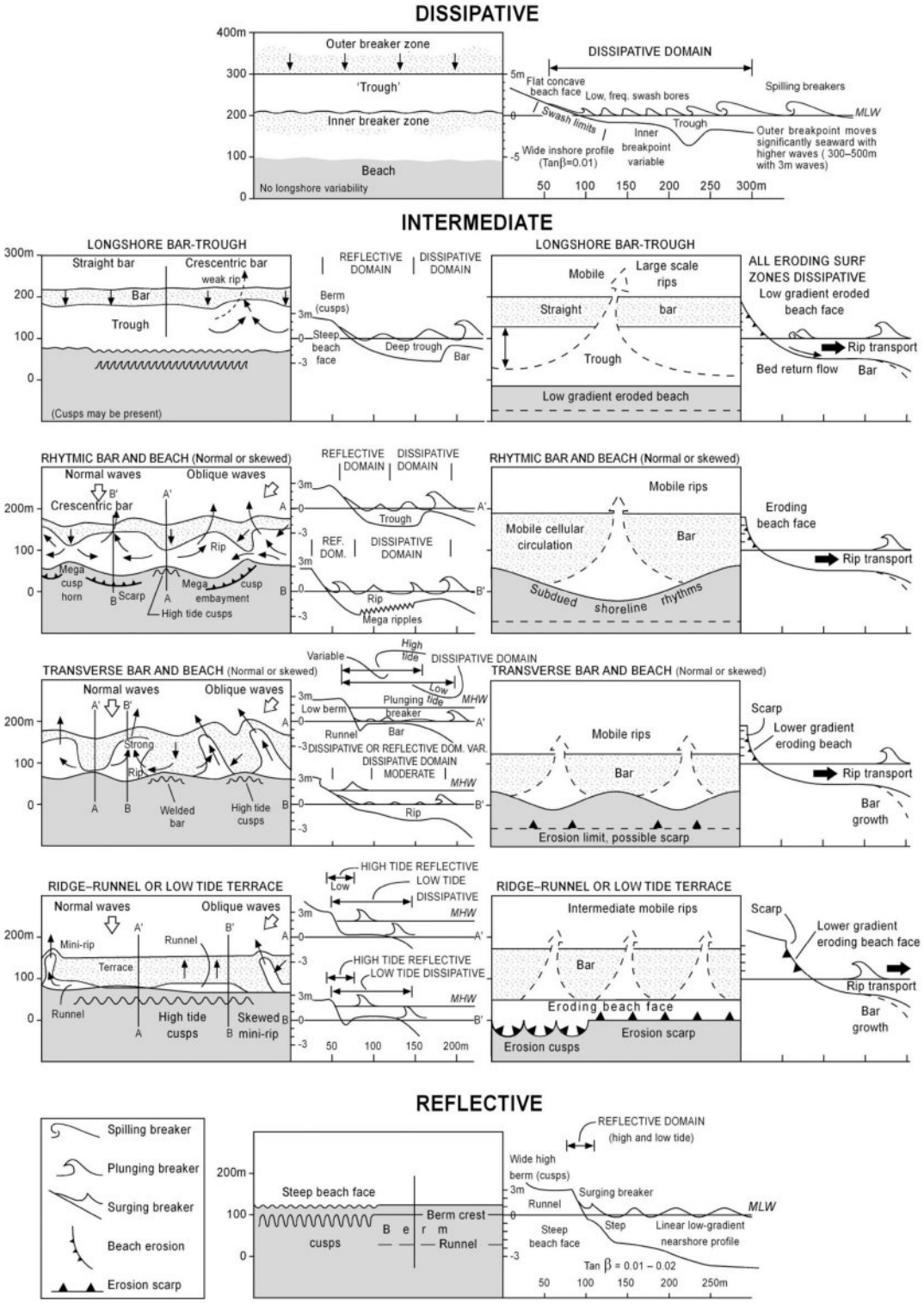


Figure 2.2: Conceptual model covering wave-dominated beach changes [modified from Wright & Short (1984)].

Here, $H_b$ is the breaker wave height, $w_s$ represents fall velocity and $T$ is the wave period. The dimensionless fall velocity provides an approximate indicator for the beach state. If $\Omega$ exceeds a value of 5.5 the beach is in a dissipative regime and if $\Omega$ is smaller than 1.5 the beach state is considered reflective. For the intermediate beaches an approximate value for $\Omega$ indicates: LBT [$\Omega \approx 5$], RBB [$\Omega \approx 4$], TBB [$\Omega \approx 3$] and LTT [$\Omega \approx 2$]. Figure 2.2 provides an overview of the beach states in accretive mode [left – down-state] and erosive mode [right – up-state]. Generally, one should see the accretive mode as going from dissipative to reflective and vice versa for the erosive mode. The dissipative state is relatively featureless with a gentle beach slope. The low gradient of the beach means that dissipative beaches are often linked to limited wave run-up and high infra-gravity energy. The first intermediate alongshore bar-trough state shows a linear or slightly crescentic bar. The bar migrates onshore towards the next accretive mode [RBB] and coincides with a more crescentic bar [higher three dimensionality]. As the beach shows more accretion in the Transverse Bar and Beach state the three dimensional crescentic bar is welding with the shore. The orientation of the transverse bars and thus the rip channels is related to the dominant wave conditions. Welding of the bar to shore continues as a beach moves to the next state of LTT. The rip channels decrease in size and associated rip currents generally reduce in strength. Three dimensionality decreases as the bar is welding to the shore. The upper part of the beach becomes steeper and steeper while the inter-tidal domain shows a flat terrace that is dry during low tide. At the point that the bar is completely welded, the beach state is basically considered reflective. The reflective state is more related to the steepest profile and wave run-up is maximum. During the accretive stages of the beach states, more and more sediment is brought to shore and the upper part of the beach becomes steeper. The erosive state experiences an inverse process. This conceptual model is especially valid for medium to high energetic wave regimes with limited micro-tidal ranges.

### Predicting beach state change

After Wright & Short (1984) identified and classified the beach states they aimed to describe the change of beaches between the different beach states. In Wright & Short (1984) they briefly considered change between beach states and in Wright et al. (1985) a predictive empirical model for beach state change was introduced. Wright et al. (1985) argued that just the instantaneous values for $\Omega$ poorly represent the actual state of the beach; e.g. a beach requires time to change state. Therefore, they introduced a predictive model that was based on the concept that if the dimensionless fall velocity was in disequilibrium, change towards another beach state should occur. The disequilibrium term [$\Delta\Omega$] captures the difference between the equilibrium

dimensionless fall velocity [$\bar{\bar{\Omega}}_{eq}$] and the instantaneous dimensionless fall velocity [$\Omega$] as presented in (2.3).

$$\Delta\Omega = \bar{\bar{\Omega}}_{eq} - \Omega \tag{2.3}$$

The equilibrium dimensionless fall velocity [$\bar{\bar{\Omega}}_{eq}$] must include recent historic information considering that the instantaneous values for beach state do not perfectly identify beach state. The equilibrium dimensionless fall velocity therefore contains recent historic information about the beach state in the form of recent antecedent values for $\Omega$ following (2.4).

$$\bar{\bar{\Omega}}_{eq} = \left[\sum_{j=1}^{D} 10^{-j/\Phi}\right]^{-1} \sum_{j=1}^{D} \Omega_j 10^{-j/\Phi} \tag{2.4}$$

in which $D$ is the number of days prior to the observation, $\phi$ represents time in days that the weighting factor decreases to 10% prior to the observation date. $\phi$ is mostly explained as a memory-decay: a large value of $\phi$ [100s of days] represents seasonal behaviour while smaller values for $\phi$ [days] indicate a more storm change behaviour. This disequilibrium concept is nowadays used to model and predict beach changes numerically. While current applications do not necessarily focus on beach state, they have been successfully applied to shore line position (Davidson et al. 2013), bar three dimensionality (Stokes et al. 2015) and sediment grain size (Prodger et al. 2016). This disequilibrium modelling is further explained in the methods in Section 3.6.

### 2.1.2 Wave and tide based conceptual model

One large drawback of the conceptual model described above is the absence of tidal regimes. The conceptual model is mainly derived for micro-tidal wave-dominated coastal environments. This conceptual model was therefore extended with a tidal range indicator a few years later (Masselink & Short 1993). The tidal range is introduced in the form of a relative tidal range [RTR] as shown in (2.5).

$$\mathrm{RTR} = \frac{\mathrm{MSR}}{\mathrm{H_b}} \tag{2.5}$$

wherein RTR represents Relative Tidal Range, MSR represents the Mean Spring Tidal Range and $H_b$ is the wave height at breaking. The relative tidal range is presented against the dimensionless fall velocity in Figure 2.3 with the associated beach states. For the dimensionless

fall velocity, the same separation is applied; 1) dissipative, 2) intermediate and 3) reflective. The relative tidal range is also divided in three subsections, RTR from 0 to 3 represents mostly representing barred beaches, RTR from 3 to 15 indicates low tide terrace and low tide bar/rip. A transition into tide-dominated coasts/tidal flats is associated with relative tidal ranges that exceed a value of 15.

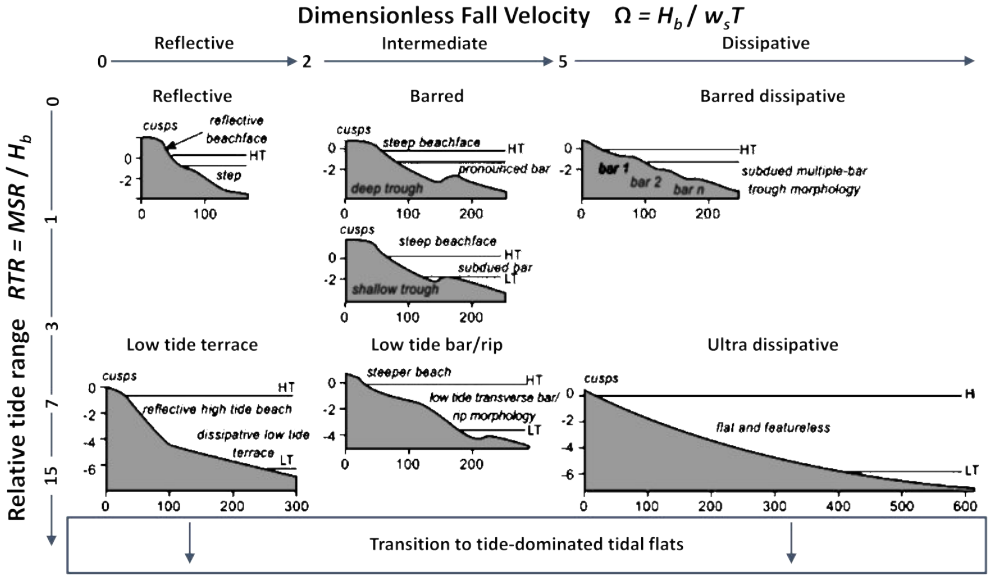


Figure 2.3: Conceptual beach classification model to predict beach morphology based on the dimensionless fall velocity [Ω] and relative tidal range [RTR] [modified from Masselink & Short (1993)].

When $RTR < 3$ the tidal effects are relatively insignificant, while for RTR greater than 15 the tidal effects dominate morphological processes. The dissipative, intermediate and reflected beach states like Wright & Short (1984) occur when the RTR is smaller than 3. A RTR greater than 3 but smaller than 15 indicates that the wave and tidal processes are important (mixed tide-wave processes). To incorporate the mixed wave-tide processes, three additional states are introduced: 1) the low tide terrace beach state [$\Omega < 2$ and $3 <$ RTR $< 15$], 2) low tide bar/rip [$2 < \Omega < 5$ and $3 <$ RTR $< 7$] and 3) ultra dissipative [$\Omega > 5$ and $3 <$ RTR $< 15$].

### UK beach classification model

The two mentioned conceptual beach models are both widely used. However, Wright & Short (1984)'s model was developed for the coast of New South Wales, Australia and Masselink & Short (1993) extended this model with RTR for all the 10685 beach systems in Australia. Beach classification models are mostly based on large temporal/spatial data sets and most applicable

in the environment where they are collected in. From this perspective, Scott et al. (2011) introduced a morphological beach classification based on the two previous conceptual models for the United Kingdom, as presented in Figure 2.4

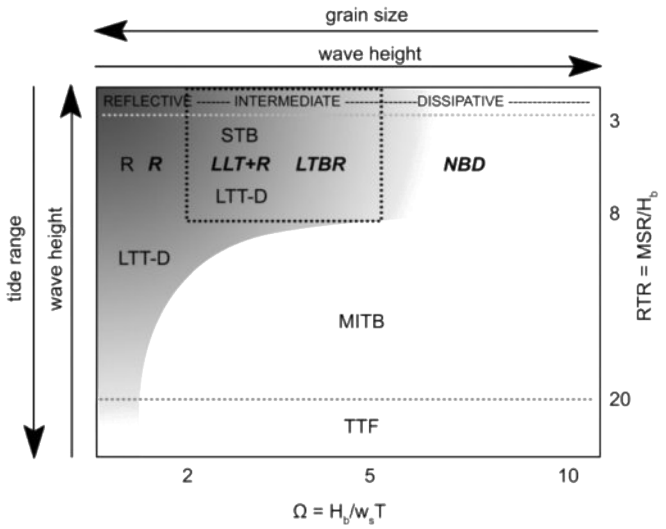


Figure 2.4: Conceptual beach classification model to predict beach morphology based on the dimensionless fall velocity [Ω] and relative tidal range [RTR] for the United Kingdom [modified from Scott et al. (2011)].

The conceptual beach classification model for the United Kingdom contains a key difference: a total set of 9 beach states that are separated on wave energy. The 9 beach states that are incorporated are 1) Reflective, low energy [R(LE)], 2) Reflective, high energy [R(HE)], 3) Linear sub-tidal barred [STB], 4) Low-tide terrace / non-barred dissipative, low energy [LTT-D(LE)], 5) Low-tide terrace and rip [LTT+R], 6) Low-tide bar rip [LTBR], 7) Non-barred dissipative, high energy [NBD(HE)], 8) Multi inter-tidal barred [MITB] and 9) Transition to tidal flats [TTF]. Compared to Masselink & Short (1993), Scott et al. (2011) found that there is a distinguishable difference between beach states by the absolute wave energy. The RTR in Scott et al. (2011) for the transition to tidal flats is significantly higher [20 over 15].

### 2.1.3 Near-shore bar morphology

The conceptual beach models show that beaches can be planar but for all the intermediate states contain bars and troughs. These bar systems are an illustration of gradients in hydrodynamics and sediment transport. Typical examples of near-shore bar configurations are presented in Figure 2.5a and contains transverse bars, crescentic bars, straight alongshore bars and multiple bar [double, triple, etc.] systems.

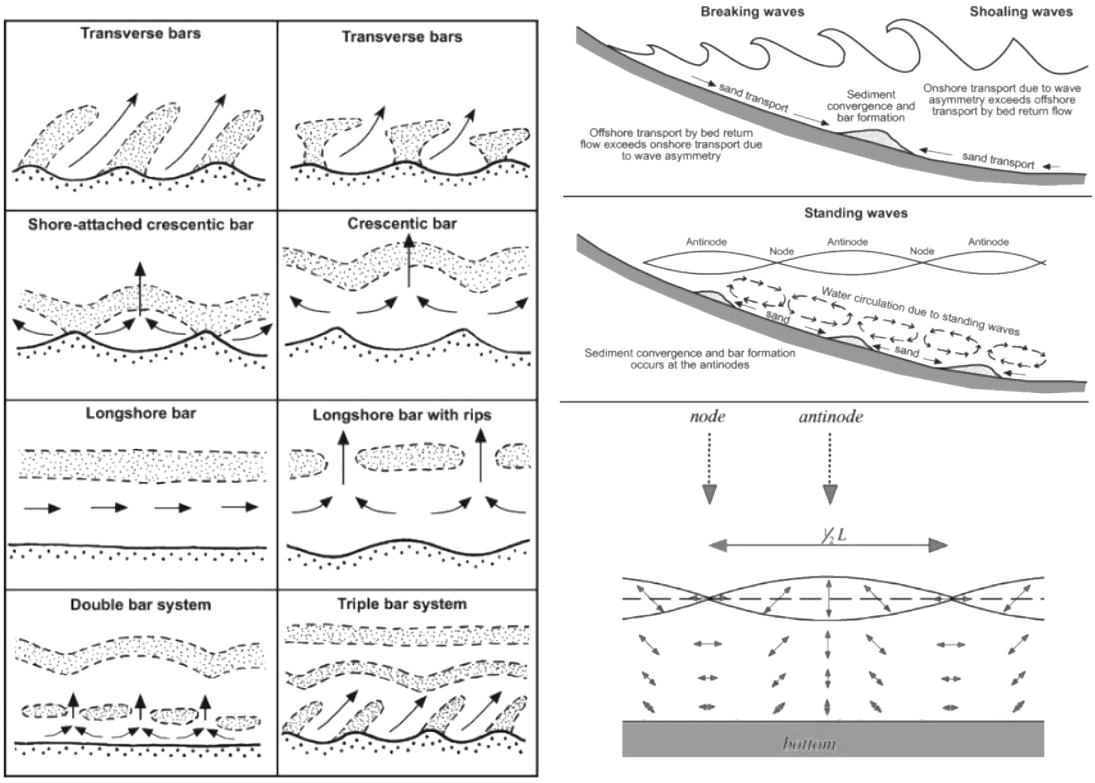


(a) (b)

Figure 2.5: a) examples of nearshore bar configurations. b) upper and middle panel: two conceptual template-forcing mechanisms for bar formation [modified from (Komar 1999)], lower panel represents velocities under a standing wave [modified from (Holthuijsen 2007)].

The sub-tidal bar configurations presented in Figure 2.5a are similar to the earlier shown beach state patterns in Wright & Short (1984). The formation and evolution of these linear and more three-dimensional features is a complex matter and has been subject to research for decades without a clear consensus. Generally, two streams of *belief* are described in literature: 1) template forcing and 2) self-organizing free patterns. The template forcing follows the principle that near-shore morphology is formed and forced to follow a certain template, for example a hydrodynamic template such as standing wave patterns [imprinted on the seabed]. Self-organisation contains the principle of feed-back interaction between the morphology and the local hydrodynamics.

**Template forcing** Template forcing is the typical text-book description of bar formation and follows an explainable theory of a forcing that imprints it spatial gradients on the seabed.

Template forcing of the near-shore morphology can generally be divided in two subdivisions; 1) (partial) standing long-wave patterns and 2) wave break point related mechanism. The (partial) standing wave approach takes infra-gravity related processes as the source for bar formation [for example due to edge-waves Bowen & Inman (1971), Holman & Bowen (1982)]. Second order drift velocities from the standing long waves result in recirculation cells where the anti-node [as indicatively shown in the lower two plots in Figure 2.5b] have been associated to bar formation (Carter et al. 1973). When suspended load sediment transport is dominant, bars form near the anti-nodes. In case bed load sediment transport prevails, bars form in the vicinity of the nodal points under fully standing (Bowen & Inman 1971) and partially standing waves (O'Hare & Davies 1993).

Another typical hydrodynamic template is the breaker point theory wherein bars form around the break point. The breaker point is determined as the location of the depth at which waves break. The breaker wave height [at the breaking point] is linked to the breaker depth through a breaker index $\gamma$ as shown in (2.6). Breaker point mechanisms typically involve bar formation through gradients in processes that occur in the near surroundings of the wave breaking point. An example of such theory is the formation of the bar around the breaker point through the convergence of two wave generated currents: 1) wave asymmetry in the offshore results in an onshore directed sediment transport and 2) the return flow under breaking waves in the near-shore zone (Dyhr-Nielsen & Sørensen 1970).

$$h_b = \gamma H_b \tag{2.6}$$

in which $h_b$ is the depth at wave breaking, $\gamma$ represents the breaker index and $H_b$ is the breaker wave height. (2.6) shows the linear relation between the breaker wave height and the water depth at wave breaking. Wave breaking of regenerated broken waves means the existence of multiple breaker points and leads to more complex [multiple bar] features (Wijnberg & Kroon 2002). The linear relation between the water depth and wave height also means that the breaker point position in the near-shore zone is also controlled by the wave height. For example, during a storm increased wave heights are commonly measured which results, following the breaker point theory, in an offshore migration of the sub-tidal bar.

**Self-organisation** Self-organisation of the near-shore zone is a traditional challenger of the template forcing approach. Self-organisation incorporates feedback between hydrodynamic processes and morphology changes. The key difference to the template forcing is that self-organisation allows the morphology affect the hydrodynamics while the forcing template assumes that the

hydrodynamic conditions overrule this morphological feedback to the hydrodynamics (Coco & Murray 2007). While the template forcing, in the case of edge waves, can be solved analytically (Chen & Guza 1998), self-organisation cannot, and self-organisation is therefore mostly studied using morphological numerical models. This means that the numerical model (based on physics, mass balance and momentum equations) are executed with varying boundary conditions. The application of these numerical models is relatively recent and started with linear models [amongst others Hino (1974)]. Linearisation of the mass balance and momentum equation only allows small perturbations of the seabed and therefore only represents initial bar developments. The most pronounced bar development is then assumed to be the final configuration. Non-linear models like, for example, Delft3D were introduced to study the initiation of single (Reniers et al. 2004) and double (Smit et al. 2008) bar systems through self-organisation. The interaction, self-organised or template forced, between the inner and outer bar has been investigated more recently (Castelle et al. 2010a, Price 2013). Castelle et al. (2010a) shows the thin line between self-organisation and template forcing. For example, the outer bar might be formed by self-organisation but then seems to dictate the inner bar morphology [which is a template]. This example shows the difficulty of identifying the driving mechanism, template forcing versus self-organisation.

### Observations of bar dynamics

Observing evolving bar morphology requires an intensive survey campaigns of bathymetry measurements such as in Birkemeier et al. (1989) and Plant et al. (1999). One of the few long-term sub-tidal bar measurements are obtained at DUCK, USA. Over 16-years more than 400 surveys were collected. Plant et al. (1999) used this dataset to determine a long-term mean cross shore profile and describe the bar behaviour as the variation of the bed around this mean cross shore profile. Plant et al. (1999) found that the bars at DUCK are cyclic on an inter-annual basis. Besides the experiments at DUCK, survey campaigns that capture sub-tidal bar dynamics are mostly carried out over relatively short time. Alternatively, Lippmann & Holman (1989) deployed video imagery at DUCK, NC to observe wave breaking over the bar and essentially estimating bar position in that way. The video imagery generally covers a large domain and longer time-scales. Evolving sub-tidal bar structures are observed this way on kilometre spatial scale and year temporal scale. The disadvantage of this method is that the waves have to break over the bar to be visible in the video imagery. Also, the breaking point over the bar depends on the elevation of the free surface, incident wave height and the bathymetry itself as pointed out by van Enckevort & Ruessink (2001). To highlight this, for non-saturated wave fields in

particular, the crest of the bar is often observed with the video-imagery seawards of the actual crest with a typical cross shore bias of O(10m). van Enckevort & Ruessink (2001) shows that the bias can be halved if occasional surveyed bathymetry information is available.

Long-term video-imagery datasets allowed for estimating the cross shore bar position over kilometres alongshore. This lead to analyses of bar migration and cyclic behaviour for alongshore uniform (van Enckevort & Ruessink 2003*a*) and non-uniform (van Enckevort & Ruessink 2003*b*) trends. In the combined studies they found migration rates between 0-10 m/day in seaward direction and 0-8 m/day landwards over seasonal time-scales with stronger resets during storm periods. Later van Enckevort et al. (2004) performed a more in depth analysis of template forcing versus self-organisation. They found that for the range of beaches considered, the template forcing concept did not hold considering the insignificant edge wave and alongshore variation in the crescentic features [while the template forcing predicts rhythmic features with similar wave lengths]. Plant et al. (2006) used bar estimation from video imagery to predict bar behaviour and links the mean cross shore position and variation around the mean to incident wave conditions. Plant et al. (2006) shows that bar behaviour is predictable through an empirical model that couples the incident wave conditions to the dynamics of the mean cross shore position and the standard deviation. The model was applied and extended in Australia (Splinter et al. 2011). Stokes et al. (2015) introduced dis-equilibrium modelling [presented above] to predict the mean position and standard deviation of the picked bar line through video imaging. Although the position of the sub-tidal bar is estimated with O(10m) accuracy that depends on the environmental conditions, this work can be extended to bar shape through novel developments in depth estimation techniques [as described in Section 2.2.4].

### 2.1.4 Storm Morphology

Storm conditions have the capability to induce sediment transport beyond the normal offshore boundary of the littoral zone. The increased wave conditions result in an offshore transport of sediments. As seen with the conceptual beach model, eroded sediment from the upper beach face is transported offshore making the beach move towards a more dissipative state (Wright et al. 1985). Self-organisation, as described above, is overwhelmed during highly energetic conditions (Coco & Murray 2007). Following the breaker point approach during storms [template overrules self-organisation] one could say that breaking point is further offshore during the storms and so the sub-tidal bar is likely to migrate seawards and often a linear storm bar further offshore with storm deposits is formed. Following the conceptual beach models, alongshore linear bars are mostly associated with an erosive [more energetic] state while crescentic and transverse bar are

generally associated with accretive conditions. Considering this, near shore sand bars should solely be dominated by wave height and period. Evidence was thought to be found in video observations of bar resets (from 3D to linear) over short times during storm events (Lippmann & Holman 1990, van Enckevort & Ruessink 2003*b*) . However, more recently, numerical studies (e.g. Calvete et al. (2005)) show that rip channel growth accelerates as the wave power increases. (Price & Ruessink 2011) analysed video derived bar configurations and showed that a reset event did not necessarily induced an up-state transition. In contrast, if the incident wave angle was small during the storm events, a down-state transition occurred and only when the wave angle was large ($\theta > 30°$) up-state transitions occurred. A numerical study by Garnier et al. (2013) shows for an idealised case using a 2DH morphological model that wave obliquity leads to straightening of the sandbar due to weakened intensity and down drift shifting of the rip-current as the wave angle increase. The investigated angles vary from 0 to 15 degrees and results illustrate down-state (up-state) transitions for small (larger) incident wave angle irrespectively if the initial condition is a straight or crescentic bar. Garnier et al. (2013) stresses that the threshold angle for up- or down-state transition is site and condition specific.

Highly energetic wave events (storms) can be seen as a dominating erosional mechanism for open beaches (Ferreira 2005, Almeida et al. 2012). Depending on the instant beach state and the environmental forcing [mainly waves] the beach erodes to a certain extent and fashion. Knowledge about potential storm impact, recovery and forecasting of the impact is important and demanded by society (Arceneaux & Stein 2006). However, considering the large degrees of freedom (e.g. geomorphological setting, antecedent conditions and sediment supply) make anticipation to storm erosion difficult (Coco et al. 2014). Although up-front knowledge of the coastal system is paramount in understanding storm impact on a coastal system and implementing adequate coastal management strategies (Ferreira 2005), this is much subject to the scale one adopts; for example the impact (and subsequent recovery) can vary significanlty from beach to beach on a regional scale (Masselink et al. 2015). Taking the extremely stormy 2013/2014 winter as an example, from the 38 investigated beaches around the North and South coast of South-West England in Scott et al. (2016), beaches volumes accreted (sheltered beaches), indicated temporal sediment loss (open beaches), rotation (embayed beaches) and showed permanent sediment loss (barrier beach). Scott et al. (2016) shows that after the storms the beach does not necessarily recovers during calm conditions (Komar 1999); highly energetic swell and (vital) increasing 3 dimensional morphology seems to drive on shore migration of sediment. The increase three dimensionality is creating a dynamic inter-action mechanism between the storm deposits and the inter-tidal beach.

**Storm impact and tidal elevation** The majority of storm impact research includes solely wave conditions or wave energy/power, as a measure for storm impact (Birkemeier et al. 1999, Harley et al. 2009, Splinter et al. 2014). However, these studies were conducted in micro-tidal environments. In recent work in macro-tidal areas, the tidal elevation and range (Coco et al. 2014, Masselink et al. 2015) is identified as a potential important factor in storm erosion. The tidal elevation at the moment of maximum storm strength is suspected to be a major driver behind storm erosion. However, clear evidence is not yet presented.

**Storm cluster or individual storm impact** The question of whether an individual storm or a cluster of storms has more impact and higher return frequency has been increasingly subject to research since the 1990s (Southgate 1995, Birkemeier et al. 1999). A general engineering approach is to take a single design storm with a certain return period. However, storm clusters [a sequence of small storms] have the potential to have a greater impact than a single extreme storm due to the limited recovery time between storms and unstable bed configurations that are likely to be remobilised (Birkemeier et al. 1999). Storms are mostly grouped/clustered if the available recovery time is considered insufficient for actual recovery to take place. The predefined recovery period seems quite vague and the periods quoted in literature vary substantially [2 weeks - 6 months (Birkemeier et al. 1999, Ferreira 2005, Splinter et al. 2014)]. The period of 6 months (Splinter et al. 2014) indicates that in that case the complete winter is seen as a cluster of storms. Morton et al. (1995) defines the recovery period as the time it takes a beach to fully recovered from a single storm before the next storm occurs. If the beach is not fully recovered before the next storm, these storms are considered a storm cluster.

The occurrence of storm clustering seems to vary significantly per application. The issue with assessing the impact of individual storms is that continuous data, or at least data before and after a storm, is only in few cases available (Birkemeier et al. 1999) but mostly unavailable (Splinter et al. 2014, Dissanayake et al. 2015b). Most numerical studies focus in the validation on a period with multiple storms. There are cases that storm clustering or sequencing is not affecting the individual impact (Coco et al. 2014, Splinter et al. 2014, Dissanayake et al. 2015a) while others find a memory and accumulation of storm impact per cluster (Ferreira 2005, Callaghan et al. 2008, Vousdoukas 2011).

## 2.2 Video-based coastal monitoring

Topographic coastal monitoring [e.g. beach morphology and sub-tidal bar morphology] can be carried out in various ways, for example, in-situ GPS measurements, echo sounding and remote sensing. The latter group consists of, for example, video-imagery, LiDAR and radar. Some techniques that are presented in this section, for example depth inversion, are widely applied across the different remote sensing instruments systems. In this section the focus is on optical methods with minor reference to other remote sensing techniques where appropriate.

### 2.2.1 Argus systems

Various research-based video camera systems exist that monitor the coastal zone, such as Argus (Holman et al. 1993), Cam-Era [`www.niwa.co.nz`], EVS [`http://www.svm.it`], Sirena (Nieto et al. 2010), COSMOS (Taborda & Silva 2012) and Kosta [`http://www.kostasystem.com`]. In this work, an *Argus* system is utilised that is operational at the study site. The Argus camera system has been developed over the last 30+ years by Oregon State University, in a later stage in cooperation with Deltares [data acquisition in Europe]. 10 years after the first timex images (long TIMe EXposure with ND-filter taken with a SLR camera) the first unmanned automated *Argus* station was deployed in 1992 (Holman et al. 1993). An extensive toolbox for post-processing images alongside hardware improvements makes the system robust. Nowadays, Argus systems are mainly used as a tool for research activities and coastal zone management (Davidson et al. 2007).

Typical primary products that are recorded at every Argus system are the snapshots, timex [mean pixel intensity over 10 minutes] and variance images. The images can be merged and projected on a horizontal plane with a real world [local] coordinate system (Holland et al. 1997). The timex images give a quantitative proxy of the cross shore position of the sub-tidal bar (Lippmann & Holman 1989), whereas the intensity maximum locates the preferential breaking of the waves over the sub-tidal bar crest. However, this cross shore position of the sub-tidal bar is strongly dependent on the instant tidal elevation of the water surface and the wave characteristics at the time the timex is taken (van Enckevort & Ruessink 2001). To overcome the tide dependency Holman & Stanley (2007) introduced day-long timex images. Datasets of the short and long timex images allow researchers, engineers and coastal zone managers to understand and assess the morphological variability and take actions accordingly. A secondary product that an Argus system can deliver is a so-called time-stack. Instead of the whole image, only selected pixels [in order to limit the required storage capacity] are stored for 1024 seconds at a frequency

of 2Hz (Lippmann & Holman 1991). Time-stack data has been used to determine the run-up, wave period, wave angle, directional wave spectrum, alongshore current and bathymetries.

### 2.2.2 Multiple cameras per camera system

Video camera systems that monitor the coastal zone typically consist of a sequence of multiple cameras to enlarge the field of view without great distortion or losing resolution. The orientation of the individual cameras in a group of cameras is such that there is overlap between the adjacent cameras. One can imagine on camera boundaries inter-camera issues might occur such as different pixel intensities or a slight shift in XY location due to distortion differences. For the primary Argus products (e.g. snapshots, Timex, rectification and IBM) interpolation between pixels on the camera boundaries is a sufficient solution. For example, images can be merged together and rectified on a horizontal plane with the Argus toolbox (Holland et al. 1997). Every camera has its own geometry and relates its pixels to the right position in the real-world. On the boundaries pixels from individual pixels from different cameras might think that they are on the same place and cover the same footprint but in reality there might be discrepancies due to e.g. distortion differences and slight camera movements. Holland et al. (1997) introduced a least-squares fit between pixel-sets from each camera onto a user-specified grid in the merging process to overcome this issue.

### 2.2.3 Inter-tidal topography estimation through video-imagery

Most of long-term beach survey datasets focus on the inter-tidal beach; as in datasets containing beach profiles e.g. (Larson & Kraus 1994, Wijnberg & Terwindt 1995, Lacey & Peck 1998) and three dimensional beach surveys. The main issue is that the vast majority of the surveys are carried out intermittently as in mostly monthly or bi-monthly. In addition, long-term datasets are rarely acquired in macro-tidal environments (Poate et al. 2014, Sénéchal et al. 2009). Video camera systems have been used to extend or infill existing datasets by obtaining inter-tidal elevations to supplement e.g. inter-tidal surveys (Kroon et al. 2008, Harley et al. 2011).

In order to get three dimensional information of the beach, following Plant & Holman (1997), knowledge of two variables is required: tidal elevation and Timex images. Timex images contain a local pixel intensity maximum that represents the shoreline. Due to the averaging of pixel intensities the shore line is detected more accurately than if snapshot imagery would be used. Plant & Holman (1997) developed a tool to track this local intensity maximum over time in the cross-shore direction and relates the cross-shore position to the known tidal elevation. In

this way, a contour map of the shoreline based on tidal elevation levels can be constructed. Aarninkhof et al. (2003) adopted this method and improved the accuracy after the introduction of colour images. The accuracy mainly increased due to the more distinct separation of the water line from beach though the RGB-colours.

### 2.2.4 Sub-tidal depth estimations through video-imagery

#### Breaker Intensity Model (BIM)

Similarly, to the inter-tidal beach mapper, maximum pixel intensities corresponding to wave breaking can be used to estimate two- and three-dimensional sub-tidal morphology. Bar locations have been identified by relating the maximum pixel intensity to wave dissipation and therefore the location of the bar (Lippmann & Holman 1989, 1990, van Enckevort & Ruessink 2001). This cross-shore location proxy of the sub-tidal bar made it possible to study the two-dimensional morphology of the sub-tidal bar over long time scales. Nevertheless, the aim is 3D information and thus a relationship between the pixel intensity and depth is required.

Local depth information can be obtained by coupling the pixel intensities to wave energy dissipation rates in relation to an underlying depth profile (Battjes & Janssen 1978). The pixel intensities represent to a large extent wave breaking and therefore wave energy dissipation. The pixel intensities show background illumination and persistent foam due to aerated rollers and the release of trapped air after wave breaking (Aarninkhof & Ruessink 2004). A filtering technique applied to the pixel intensities distils dissipation rates based on the wave rollers and thus wave breaking over a cross shore profile. The isolated pixel intensities related to roller dissipation are compared to the calculated dissipation rates through Battjes & Janssen (1978) and update the bed level estimation (Aarninkhof et al. 2005). This process is iterated until a bathymetry is found where the dissipation rates match within a pre-defined error range. Increased skill of the morphodynamic model [such as Delft3D] is found if this process is used simultaneously [*on the fly*] with a numerical model of the near-shore zone. Aarninkhof et al. (2005) shows that this technique has potential but a rather large absolute bias [O(1m)] between survey and estimate is found.

**BeachWizard** The breaker intensity model is extended through a system called BeachWizard (van Dongeren et al. 2008). BeachWizard (van Dongeren et al. 2008) deploys a Kalman filter (Kalman 1960) to combine depth estimation techniques where they perform best and update over time when a better estimate is found. For the breaker intensity model, XBeach is used

to match observed dissipation maps instead of Delft3D (as described in the original breaker intensity model). In principle, all types of depth estimations can be included in BeachWizard as long as the estimates have a corresponding error measure. In addition, inter-tidal topography estimates could be combined with the sub-tidal bathymetry estimates. However, at present there is no error measure for the inter-tidal shoreline mapper.

### Linear depth-inversion relation

Depth inversion is an indirect technique where modulations of the free water surface are used to determine depth through the linear dispersion relation for gravity waves as presented in (2.7).

$$c^2 = \frac{\sigma^2}{k^2} = \frac{g}{k}\tanh(kh) + \vec{U}^2 \tag{2.7}$$

wherein $c$ is wave celerity, $g$ is the gravitational acceleration, $k$ represents the wave number, $h$ is depth and $\vec{U}$ represents the mean current. $\vec{U}$ in the right-most term of the right-hand side of (2.7) is typically small compared to the phase speed of the wave in the direction of wave propagation. The low influence relative to the phase speed is confirmed with field measurements carried out by Merrifield & Guza (1990), Holland (2001). $\vec{U}$ in the right-most term of the right-hand side of (2.7) is therefore neglected. In absence of the mean current, the dispersion relation can be rearranged so that depth becomes a function of the wave celerity [$c = \sigma/k$ or $L/T$].

$$c^2 = \frac{\sigma^2}{k^2} = \frac{g}{k}\tanh(kh) \;\Leftrightarrow\; h = \frac{\tanh^{-1}\left(\frac{\sigma^2}{kg}\right)}{k} \tag{2.8}$$

This means that considering (2.8) the wave celerity in the form of wave length and period or wave number and frequency has to be sensed. One of the first known practical applications of estimating the sub-surface depths through depth inversion is from the Second World War in order to obtain near-shore depth information of enemy-held beaches (Williams 1946, Seiwell 1946, Coleman & Lundahl 1948). At the time, wave lengths (distance between two wave crests) and wave celerity (difference in position over time between two photographs) were determined manually from airborne photo imagery. Nowadays, depth inversion techniques are widely applied in a more automatic fashion such as shore-based optic sensors (Stockdon & Holman 2000), aerial optic, Infra-red imagery (Dugan et al. 1996, 2001), and X-band radar (Bell 1999).

### Non-linear depth-inversion relations

The presented linear approach is popular and can be solved explicitly but has drawbacks and sources of inaccuracies in the near shore. Catálan & Haller (2008) assigns inaccuracies to dispersive effects of the waves based on low frequency surface modulations (Tissier et al. 2015) and underestimation of the wave speeds through the linear dispersion relation in shallow waters (Svendsen et al. 1979, Stive 1984). Intriguingly, *no* improvements concerning the depth estimations are found when the low frequency modulations are accounted for in a video-based depth inversion (Tissier et al. 2015). This might well be related to the time-averaging of pixel intensities in most depth inversion methods and thus the averaging out the individual wave by wave interactions. The underestimation of the phase speed seems a larger issue. In shallow water $[kh < \pi/10]$ the linear dispersion relation reduces to a $c = \sqrt{gh}$. Empirical relationships were found in the surf zone by Svendsen & Hansen (1986) that show wave speeds are larger but still follow $\propto a\sqrt{gh}$ where $a$ represents a constant to be found. Stive (1984) found a consistent value for $a$ to be 1.3 and Stansby & Feng (2005) show in one laboratory test a variation in $a$ over the surf zone ranging from 1.06 to 1.32. From a large dataset of cross shore pressure sensors, Holland (2001) found that errors related to the application of the linear dispersion relation could exceed 50% of the local depth related to the offshore wave height. Earlier, Grilli (1998) arrived at a similar conclusion of errors around 50% to 70% through a numerical modelling exercise using a Boussinesq model. To overcome these inaccuracies Catálan & Haller (2008) tested a range of non-linear approaches in a laboratory setting and compared them to the linear dispersion approach. They found that the best preforming relations were the composite models of a modified linear dispersion relation shown in (2.9) (Booij 1981) and a further modified version of Booij (1981) for a wider range of water depths (Kirby & Dalrymple 1986).

$$c^2 = \frac{\sigma^2}{k^2} = \frac{g}{k}\tanh\left[k\left(h + \frac{H}{2}\right)\right] \tag{2.9}$$

wherein $c$ is wave celerity, $\sigma$ the wave frequency, $k$ wave number, $h$ is water depth and $H$ is the wave height. Catálan & Haller (2008) found a reduction of 64% in mean relative error by taking non-linear effects into account through a composite model. This shows that the non-linearity induces errors in shallow water but that it can (partially) be accounted for. However, accounting for non-linearity comes at a cost: the linear dispersion relation is explicit while non-linear approaches require an iterative procedure and near-shore wave height information. Wave heights are currently not, or are only poorly, estimated with video-cameras. To overcome this issue, numerical models are often used to provide the wave height (Misra et al. 2003).

Nonetheless, the application of non-linear depth inversion requires either in-situ wave data or a computational effort which is additional compared to the linear dispersion relation.

### Video-based depth inversions though the linear dispersion relation

To estimate depth through the linear dispersion relation without the incorporation of the wave height [as in (2.9)] only the wave celerity has to be approximated. The wave celerity consist of the wave number and frequency or wave length and period [$c = \sigma/k$ or $L/T$] and it is these parameters that can be obtained from video imagery. Williams (1946) measured the distance between successive wave crests from multiple photographs with a known time interval. This is known as the *space-lag* problem. However, for most camera systems each pixel is associated to a certain $X,Y$ position in the real world after geo-rectifying all the pixels. If you know the physical distance between the pixels and the time between two photographs is known, one can estimate the wave celerity as the ratio between the time and distance. This is known as a *time-lag* problem.

Here, the time-lag problem is described in two ways in 1) the time domain and 2) the spectral domain. Both approaches adopt the starting point that pixel intensities from video-imagery relate to propagating waves (Lippmann & Holman 1991). Examples of tackling the time-lag issue in the time domain are given in Bos (2006) and Almar et al. (2008). Almar et al. (2008) combines the space and time-lag approach. They adopt the assumption that the change in shape of the signal is limited over a short distance [O(10-40m)]. An optimal [$\Delta x$ with highest correlation] travelled distance $\Delta x_0$ of the wave over an arbitrary period $\Delta t$ is computed through an auto-correlation function. This results in a cross shore array of optimum values for $\Delta x$ which are then used to calculate the associated celerity $c = \Delta x_0/\Delta t$.

The time-lag approach in the spectral domain has firstly been demonstrated by Stockdon & Holman (2000) and is based on finding wave phase differences over a distance or the phase ramp between two points following [$k_x = d\phi/dx$ (Merrifield & Guza 1990)]. Stockdon & Holman (2000) transforms the time-varying pixel intensities into the frequency domain through a Fast Fourier Transform procedure. From the resulting normalised spectra, the cross spectral matrix with the complex conjugate is calculated. For a defined frequency band, the cross spectral matrix is used in a complex EOF analysis to find a propagating wave phase structure [or the wave phase ramp] of the most dominant frequency. Stockdon & Holman (2000) then target the difference in phase between the selected points to approximate the wave number. The RMS error of the application described in the paper to a planar beach at Duck in the United States is around 0.7 to 0.9 m. For more complex bathymetries the accuracy decays. Plant et al. (2008)

extended this technique by the use of multiple frequencies and a fit for each frequency between the observed wave phase ramps to a modelled wave phase ramp associated with a sinusoid. The depth estimation errors in Plant et al. (2008) were approximately halved in comparison to Stockdon & Holman (2000). Plant et al. (2008) forms the foundation for cBathy (Holman et al. 2013) in which the technique is further extended into two-dimensions and data assimilation through a Kalman filter is introduced. cBathy will be further explained in detail in Section 3.4.1.

# Chapter 3

# Methods

## 3.1 Introduction

In order to achieve the three general objectives of this work, data is collected at the study site and subsequently analysed. In this Chapter the study site and principal methods are described that are used throughout the work such as data collection and analysing techniques. The data collection comprises wave and tidal data, measured topography and bathymetry data and a video-based depth estimation technique. For the data analysis the principle techniques of the momentary coastline, sub-tidal bar detection and Empirical Orthogonal Functions are introduced here.

## 3.2 Study site: Porthtowan

The study site throughout this work is the beach at Porthtowan, a village in the South-West of England in the county of Cornwall. The name Porthtowan originates from *Porth Tewyn* in Cornish and translates to *cove of dunes*. Dunes have been present between the two rocky cliffs for at least 130 years as historic photographs back to 1880 show [Figure 3.1].

The most prosperous times of the village were in the Victorian era when Cornwall could profit from tin and copper mining. Copper mining activities at the North Cornwall coast started around 1750s. In the valley east of the village, remains of the Tywarnhayle mine [just visible in the top right corner of Figure 3.1] can be found. The cliffs and surrounding landscape in combination with the remains of the mines make this area a World Heritage Site.

Figure 3.1: Historical photographs of Porthtowan (*Porth Tewyn*) 1880-2010

The local economy declined [like the county of Cornwall in general] after the mining activities were decimated. Over the last few decades the main income generators are holiday makers and beach visitors in the summer. Furthermore, Porthtowan is known among [local] surfers for its consistent and powerful wave that breaks on the sub-tidal sandbar during low tide.

### Porthtowan beach and beach state dynamics

One enters the beach at the Southern part of the geologically constrained bay at the town of Porthtowan. The town and beach are separated by a small dune. During windy conditions, large quantities of sediment is blown from the dune into the down. The local community is activly involved liasing with the local authorities in maintaining the dunes and preventing. The high tide water level hardly reaches the dunes under normal conditions, only during storms (at high tide) the dunes are reached. Crossing the dunes from the town, one arrives at the main pocket beach of porthtowan. During mid to high tide the beaches are geologically constrained by the rocky cliffs creating 5 pocket beaches over the domain from Porthtowan to Chapel Porth. During low-tide, a single alongshore stretch of open beach at the foot of the rocky cliff appears, stretching from Porthtowan to Chapel Porth. The 5 m contour line West of Porthtowan and Chapel Porth in Figure 3.2 roughly indicates the stretch of exposed beach during spring low tide. Typically, the lower beach face exhibits a slope of approximately 0.015 whereas the upper beach face is steeper with a slope of 0.045. At the lower and upper part of the beach a grain size ($D_{50}$) of respectively 380 $\mu m$ and 410 $\mu m$ is found (Buscombe & Scott 2008, Poate et al. 2014).

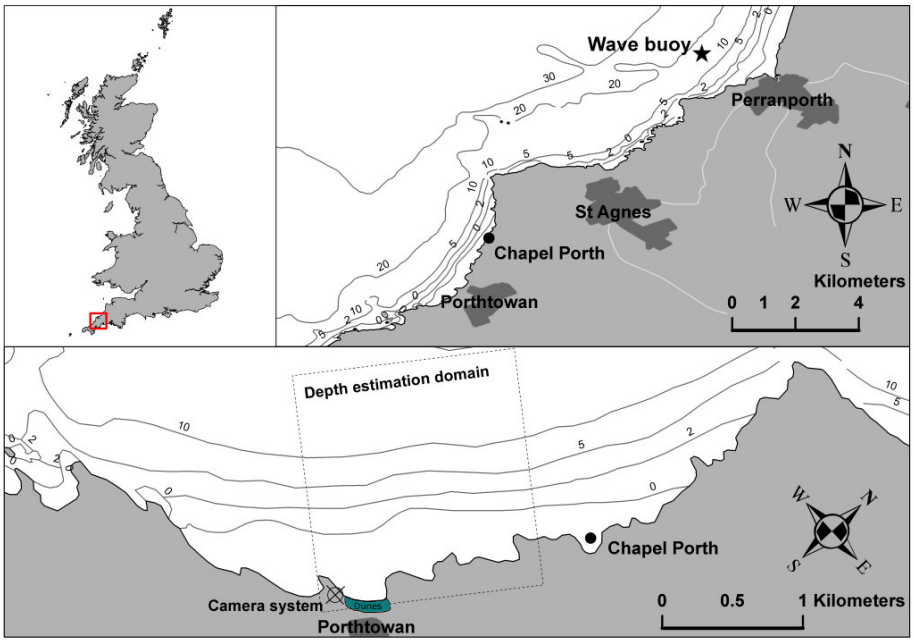


Figure 3.2: Map overview of the region around Porthtowan and Perranporth.

Following Section 2.1 using Masselink & Short (1993) together with local wave and tidal information, the inter-tidal beach at Porthtowan can be classified into two general beach states: 1) Low tide bar/rip and 2) barred beach. Figure 3.3 shows the dimensionless fall velocity ($\Omega$) against the relative tidal range (RTR) for all the data from 2008 to 2015. The data is separated in monthly sets and used to calculate monthly means, linear trend and standard deviation for the relative tidal range and dimensionless fall velocity. Figure 3.3 shows the monthly mean as a dot, the linear trend as the solid lines and the mean plus two standard deviations [in x and y direction] as the dashed lines. The solid line of the linear trend is curved considering the logarithmic y-axis. The standard deviation is plotted around the linear trend as a circle/ellipse [depending on the standard deviation of relative tidal range and dimensionless fall velocities]. Figure 3.3a shows curves for January [dark blue] until June [light green] and Figure 3.3b shows the data for July [yellow] to December [red/orange].

The mean spring tidal range at Porthtowan is 6 m and the mean fall velocity is 0.053 m/sec (Poate et al. 2014). Here, these values are kept constant to the mean values so the variation is only a function of the wave conditions [$H_b$ and $T_p$]. The results in Figure 3.3 indicate that during the more energetic months [November - March] the beach is likely to be in a more dissipative barred stage. The rest of the months the beach turns to the low tide bar/rip state considering Figure 3.3. The standard deviation of the summer months gives the indication that during those months the beach at Porthtowan is likely to be in a low tide terrace+rip state. The mean values

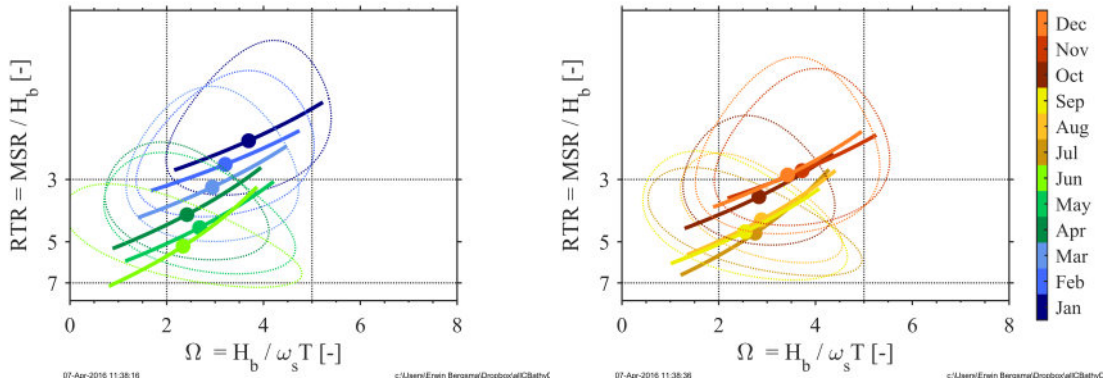


(a) (b)

Figure 3.3: Beach classification following (Masselink & Short 1993), Relative Tidal Range (RTR) versus dimensionless fall velocity Ω. a) represents the period from January to June and b) covers July to December.

of the ratio between Ω and RTR indicate that Porthtowan over the whole is an intermediate low-tide bar/rip state beach. This is in correspondence with earlier found beach states in the South-west of England (Scott et al. 2011).

### Waves at Porthtowan

In this work there are three sources for wave information: 1) wave buoy at Perranporth in intermediate waters [approx. 14 m water depth], 2) Sevenstones lightship in deep water [70 m water depth] and 3) a regional SWAN model output [only the output is available]. The buoy at Perranporth is situated around 1.6 km offshore from the coast. The wave data since mid-December 2006 is obtained with a Datawell Directional WaveRider Mk III buoy. A disadvantage of the wave buoy at Perranporth is the limited water depth at the location of the buoy. The majority of the waves recorded here are affected by the depth [e.g. shoaling or even depth-induced breaking during extreme storms]. During the extreme storms of 2013-2014, discussed in Chapter 5, the wave buoy came adrift and was badly damaged. During this period the SWAN model or the deeper, but more remote, Sevenstones lightship can provide wave information. The Sevenstones lightship is an offshore ship that is permanently anchored in around 70 m water depth. For the majority of the waves this means that they are measured without depth limiting effects.

Figure 3.4 shows percentile occurrence of the measured waves after the wave data is sectioned in directional and wave height bins in a) for the Perranporth wave buoy and b) for the SevenStones data. The values around the circle represent the incoming wave angle and the

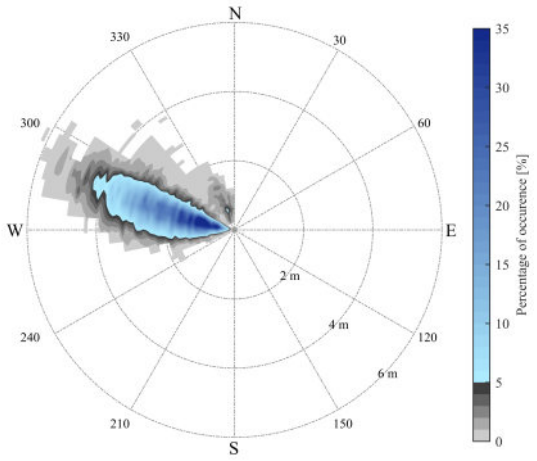


Figure 3.4: Wave rose from the Perranporth wave buoy data Numbers around the circle indicate incoming wave angle and the radial bands correspond to the wave heights [0-6 m]

radial grid indicates the wave heights [from 0 to 6 m]. The colour indicates the occurrence of a certain directional/wave height bin. Figure 3.4a,b show a fairly similar pattern. The majority of the waves comes from W-NW direction. The overall directional spreading is quite narrow as most of the waves arrive from between 260 and 300 degrees. The majority of the waves have a wave height in the range 0-2 m. This wave band contains swell and wind sea waves. A second, less distinguishable band of occurrence is observed between 340 and 0 degrees. The wave height is mostly between 0-1 m and these waves are more locally generated wind sea waves.

### Tides at Porthtowan

Tidal gauge data in the South-West of England, in particular the north coast of Cornwall, is not collected due to the absence of a substantial size port. The closest tidal gauge in the South is in Newlyn 30 km away and Ilfracombe around 130 km away to the North. However, the tidal elevation is well calculable from tidal constituents. The tidal constituents can be derived from water level elevations, preferably without the sea-swell waves. Here, the r-t tide model (Leffler & Jay 2009) has been used to extract tidal constituents and fore- and hind-cast temporal tidal elevations. The water level elevations were retrieved with a pressure transducer [PT] in the field over a period of 2 years [2008-2009] (Poate 2011). The pressure transducer was installed during spring low tide. As a consequence, the pressure transducer was exposed and dry during every spring low tide. The collected PT data is therefore intermittent which effects the determination of the tidal constituents in the r-t-tide model. The model assigns more importance to higher

harmonics that flatten-out the data gaps. In order to infill the data gaps a single sinusoid with the frequency of the M2 tide is fitted [following Appendix A] to the data over the period that the PT falls dry. The in-filled time-series is subsequently used to derive the tidal constituents. The resulting tidal constituents are presented in Figure 3.5.

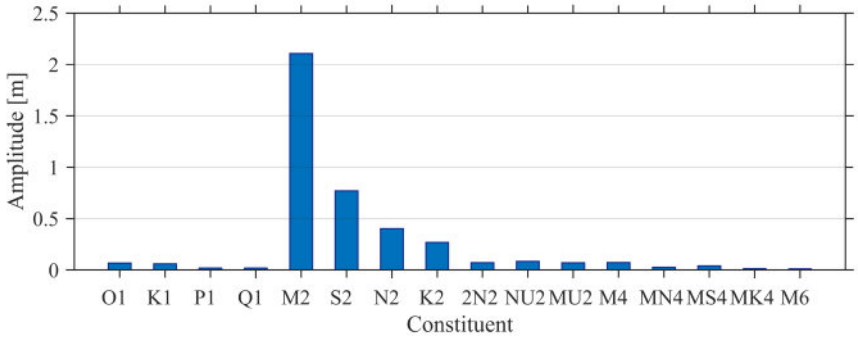


Figure 3.5: Tidal constituents and amplitudes derived from pressure transducer data.

Considering Figure 3.5, the largest most prominent constituent is the M2 component with an amplitude of 2.1 meters, followed by S2 (0.77 m), N2 (0.4 m) and K2 (0.3 m). This four components together result in 3.57 m amplitude, meaning an absolute maximum tidal range of 7.14 metres (bear in mind, the smaller components are not yet included).

**Atmospheric correction** The tidal signal can be reproduced for any point in time using the tidal constituents from Figure 3.5. Figure 3.5 shows that at Porthtowan the influence of the moon constituent [M2] dominates. When the temporal signal is reconstructed for any given point in time it does not include atmospheric pressure, wave and wind driven effects. The wave and wind effects are mostly local and hard to take into account. The atmospheric pressure is on a more regional scale and can be accounted for. The atmospheric pressure is directly related to increased water levels if the atmospheric pressure is low and lowered water levels if the atmospheric pressure is high. This relation between atmospheric pressure and water level response is generally referred to as the inverse barometric effect. Figure 3.6a shows the residual signal [measured - reconstructed] in blue. The atmospheric pressure is displayed in grey and in red the corresponding inverse barometric pressure effect is shown.

Atmospheric pressure data is measured half-hourly nearby at Perranporth. Figure 3.6a shows that in our dataset the relation between the residual surface elevation signal is strongly related to the inverse barometric effect. Figure 3.6b shows the error in tidal elevation after the inclusion of the barometric effect. The mean error is around 1.4 cm and 68% of the tidal elevation predictions within 11 cm.

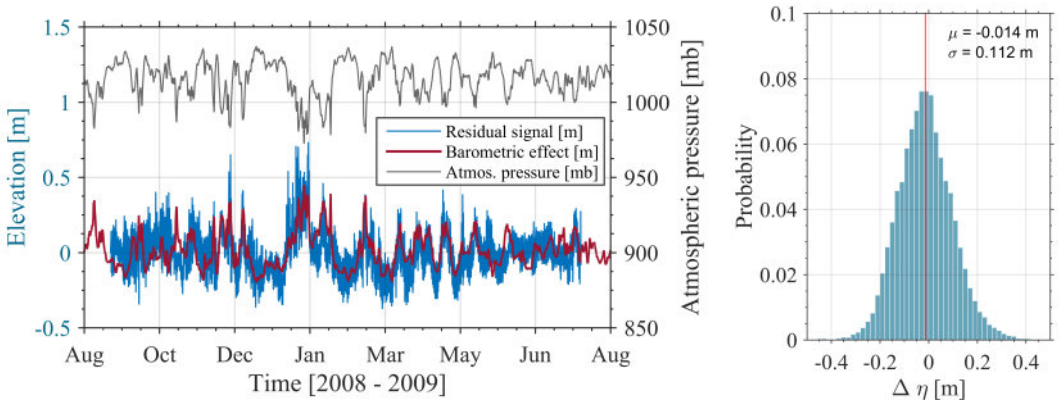


(a) (b)

Figure 3.6: a) Residual tidal elevation signal [measured - reconstructed] in blue, atmospheric pressure data in grey and the inverse barometric effect in red. b) represents the over ($> 0$) and under-prediction ($< 0$) of the tidal elevation after the inclusion of the inverse barometric effect

## 3.3 Topography and bathymetry data collection

The topography dataset at Porthtowan is one of the few long-term datasets in the world conducted in a macro-tidal environment. Porthtowan is situated in the lee of the WaveHub wave energy test facility. The inter-tidal data collection started in order to assess the long-term impact of renewable wave energy fields on near shore sediment dynamics after the initiation of the WaveHub project in 2008 (Poate et al. 2009). The initial monitoring scheme at Porthtowan started in 2008 and finished in 2010 but was re-initiated around 2012 for this work and still continues [2016]. The inter-tidal surveys are carried out on a regular basis. Every month the survey is conducted during the highest spring tide in order to cover as large as possible an inter-tidal area. Bathymetry measurements at Porthtowan were specifically carried out to ground-truth the video-based depth estimations. In total two bathymetries have been measured on 9 April 2014 and 19 September 2014.

### Typical surveying domain

Figure 3.7 shows the typical domains for the inter-tidal beach surveys [blue] and the bathymetry measurements [red]. The topography and bathymetry domain have an overlap to account for vertical shifts. During the measurements, depending on the environmental conditions, these offshore (topography) and onshore (bathymetry) boundaries were pushed as far as possible. Therefore, the cross shore extent of the surveys differs from survey to survey. The alongshore

domain is kept constant.

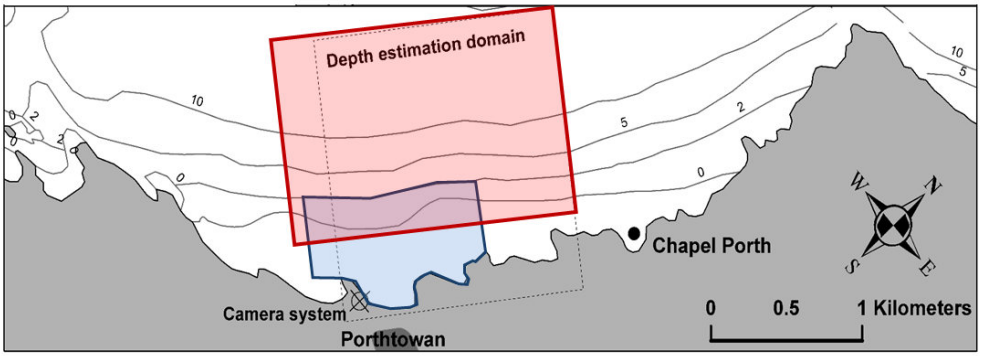


Figure 3.7: Typical survey domains for the topography [blue] and bathymetry [red] measurements

### Measuring technique

For the topography and the bathymetry measurements a real-time kinematic [RTK] Global Positioning System [GPS] was used. For the inter-tidal measurements, the GPS receiver was mounted on an all-terrain vehichle [ATV] (Haxel & Holman 2007). The ATV was driven following alongshore lines with a typical spacing of around 7 to 10 m. A point [XYZ - OSGB36] was stored in the GPS hand-held every second or every metre, depending which occurs first. The accuracy of this measurement is on the order of 5 cm.

The bathymetry measurements were collected in a similar fashion other than with the GPS-receiver mounted on a small boat or jet-ski. The XYZ points are still stored every metre or second and depth information was added. Depth-information was acquired using an echo sounder. The echo-sounder estimates a depth by using the principle of measuring the double way transit time of an acoustic signal reflected by the seabed. The vertical information of the GPS-receiver and the depth-information represent the bed-level elevation.

Both, topography and bathymetry were combined and the data is subsequently interpolated on a regular grid using a local regression (LOESs) model (Plant et al. 2008). Figure 3.8 shows a final result of the combined topographic and bathymetric data.

### Sub-domains

For the further reference and analysis, e.g. to determine RMS errors on a regional basis, three areas are considered in the survey domain following the definitions presented in Figure 2.1.

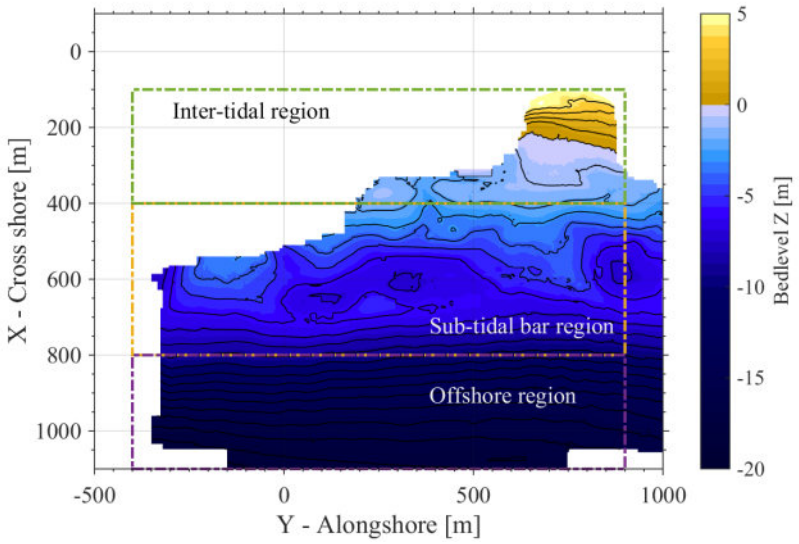


Figure 3.8: Measured bathymetry (10 April 2014) with the overlaying lines indicate the different regions for the further analysis; inter-tidal (green), sub-tidal bar region (yellow) and offshore region (purple).

The inter-tidal area (green lines in Figure 3.8) is the area where the quad bike surveys are carried out. In the sub-tidal zone, an area around the sub-tidal bars (yellow lines in Figure 3.8) is distinguished stretching from its boundary with the inter-tidal domain to well beyond the offshore extent of the bar. Seaward of the sub-tidal bar, from a depth of approximately 10 m, the offshore region is defined (purple lines in Figure 3.8).

## 3.4 Camera system at Porthtowan

The camera system at Porthtowan is positioned on the Southern cliff and the cameras are more or less orientated in North/North-West direction as shown in Figure 3.9a. The elevation of the camera system is around 44m. The camera systems operate with 4 cameras [a fifth one has only recently been installed]. Two wide angle cameras [camera 1 and 4] cover the total view but are mostly used for analysis closest to the cameras. Two zoomed cameras [cameras 2 and 3] complement the system and are required for an accurate analysis further away from the camera system and offshore. The footprints of the wide angle cameras are cropped to remove overlap with camera 2 and 3. This is a normal procedure for the Argus stations to avoid inaccuracies in the post-processing. The zoomed cameras have, in general, preference over the wide angle cameras because of their higher resolution hence more accurate analysis. Figure 3.9b shows the camera footprints in red and these lines represent the total footprint of cameras 2 and 3 and

the cropped domains of cameras 1 and 4. Figure 3.9 shows that the inter-tidal area is covered by all four cameras. The sub-tidal bar area is covered by cameras 2,3 and 4 although camera 4 has a limited offshore reach. The reach of camera 4 means that the sub-tidal bar is mostly visible through cameras 2 and 3. Only when the sub-tidal bar migrates onshore will camera four capture the sub-tidal bar. Nonetheless, as the bar migrates into the domain of camera 4, the sub-tidal bar will most probably only be captured partially and with limited accuracy considering the fact the outer domain of the cameras is generally the least accurate [due to larger footprint and distortion].

The camera system at Porthtowan collects a snapshot, timex and variance image every 30 minutes. Stack collections of user-defined pixels are collected hourly for 17 minutes and 4 seconds [2048 samples at 2Hz] 10 minutes after every whole hour. These stack collections are to be used for the video-based depth estimation technique.

### 3.4.1 Video-based depth estimation technique

In this section a video-based depth estimation technique [cBathy - (Holman et al. 2013)] is described in more detail compared to the introductory description in Section 2.2.4. This section presents the principle of operation of cBathy which existed at the start of the project. cBathy is based on the cross spectral correlation approach to estimate the 'time-lag' of a wave between pixel points. The main idea behind cBathy is that wave-modulated time varying pixel intensities can be used in combination with the linear dispersion relation for free surface waves to estimate a depth. The general concept is that the linear dispersion relation (2.7) can be rearranged so that a depth ($h$) can be found as a function of the wave frequency ($\sigma$) and wave number ($k$) (2.9).

In order to apply (2.9) to estimate local depths, corresponding pairs of wave frequency and wave number values have to be determined. In cBathy, these parameters are estimated hourly using collection of pixel intensities recorded at 2Hz. The time varying pixel intensities are decomposed by applying a Fast Fourier Transform from which the subsequent Fourier coefficients [$I$] are normalised by the absolute Fourier coefficients [$\tilde{I} = I/|I|$].

To calculate depth at a specific location, a subset of these normalised Fourier coefficients surrounding the point of interest $(x_m, y_m)$ are selected. Depending on the size of the sub-sampling domain (determined by smoothing scales $L_x$ and $L_y$), a subset contains typically $40-50$ sub-samples with pixel coordinates $x_p$ and $y_p$. The cross spectral density matrix (3.1) is computed

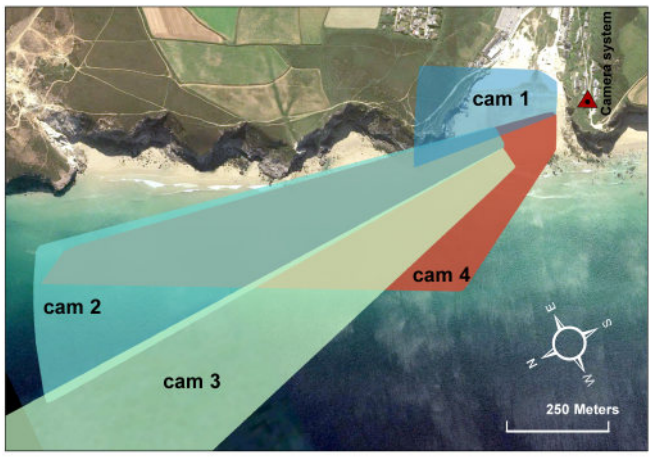


(a)

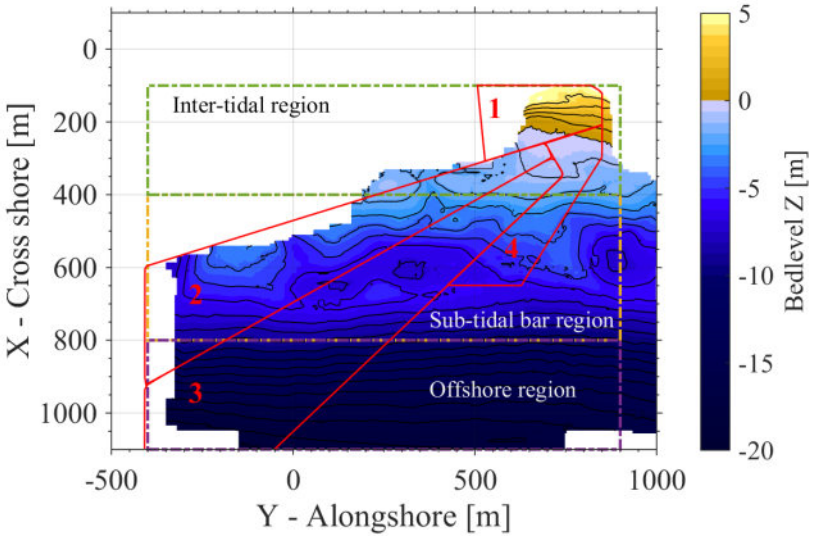


(b)

Figure 3.9: a) Camera footprint per camera for the video system at Porthtowan with 4 cameras overlaying satellite imagery and b) camera footprints over a surveyed bathymetry together with the earlier defined regions.

for all possible pixel pairs in this subset and averaged across each frequency.

$$C_{m,n}^{OBS}(f) = \left\langle \tilde{I}(x_m, y_m, f)\, \tilde{I}^*(x_n, y_n, f) \right\rangle = \gamma_{m,n,f} e^{i\phi_{m,n,f}} \tag{3.1}$$

where $\tilde{I}$ represents the subset of the normalised Fourier coefficients and $\tilde{I}^*$ is the complex conjugate, $\gamma$ represents the coherence and $\phi$ is the phase shift between pixel points. A selection (4 is the default) of the most coherent frequencies are identified [coherence is $\gamma_{m,n,f}$ in (3.1)] and these are then used through the remainder of the analysis. For each selected frequency the cross-spectral density matrix is kept while the rest is neglected. The cross-spectral density matrix essentially represents a noisy spatial (2D) wave pattern ($e^{i\phi_{m,n,f}}$) per selected frequency. Holman et al. (2013) included a complex empirical orthogonal function analysis in order to filter different physical components from the observed spatial pattern ($C_{m,n,f}^{OBS}$) per selected frequency. The inverse tangent of the dominant complex mode [1st complex eigenvector, $\upsilon_1(x_p, y_p, f)$] is assumed to represent a wave train pattern which contains a phase spatial pattern $\upsilon_1'(x_p, y_p)$ at the frequency of interest (Wallace & Dickinson 1972). This spatial pattern with known angular frequency can be represented by a wave phase as a function of the wave number $k$, wave angle $\alpha$ and phase shift $\Phi$, as expressed in the right-hand side of (3.2). A Hanning filter is applied to the observed spatial pattern in order to give more importance to the values closer to the point of interest. A non-linear Least Squares fitting procedure is then applied to identify optimal values of $k$, $\alpha$ and $\Phi$.

$$\underbrace{\upsilon_1'(x,y) = \tan^{-1}\left(\frac{Im(\upsilon_1(x,y))}{Re(\upsilon_1(x,y))}\right)}_{\text{Observed spatial phase pattern}} \cong \underbrace{k\cos(\alpha)x_p + k\sin(\alpha)y_p + \Phi}_{\text{Spatial wave phase for known frequency}} \tag{3.2}$$

The best-fit wave phase is determined for each selected frequency and results in a set of frequencies and corresponding wave numbers per point of interest where one wants to estimate a depth. This also means that multiple depth estimates are calculated "4 in the typical setup" at each point of interest. The set of depth estimates must be combined into a single depth, but simply averaging these depth estimates results in inaccuracies due to the non-linear character of the dispersion relation (2.8). Consequently, a single depth is found yielding the best-fit relation between the selected frequencies and corresponding wave numbers to the linear dispersion relation. For each hourly dataset (or sampling period), this process is repeated throughout the field of view until depths have been estimated for a predetermined grid of points of interest $(x_m, y_m)$.

Ultimately, the hourly estimated depths are combined through a Kalman filter to construct

daily or continuously evolving bathymetries. The Kalman filter accounts for decay in faith in the depth estimate over time. Faith here means reliance upon the precision of the depth estimate that decreases over time due to the knowledge that morphological change will occur to a certain extent related to (in this case) changes in the wave height [$H_{m0}$] and the accuracy of the depth estimate. When a new depth is estimated the filter updates the depth points with new estimates when the faith in the new estimate is considered greater than the faith in the previous estimate. The decay in faith is a function of three components, the natural variability in space over time depending on the wave height [$H_{m0}$], time and the error in depth estimation. The first is represented by the process variability function $Q$ (Holman et al. 2013). $Q$ is presented in (3.3), where a cross shore Gaussian distribution is constructed such that:

$$Q(x, H_{mo}) = C_Q H_{mo}^n \exp\left\{ -\left[ \frac{(x - x_0)}{\sigma_x} \right]^2 \right\} \tag{3.3}$$

in this relation, $C_Q$ represents a site specific constant, $\sigma_x$ is the cross shore standard deviation of the allowable area of change and $x_0$ the cross shore position where the highest level of morphological variability is allowed over time. This results in a matrix $P$ (3.4) representing the likelihood for change for all depth estimates.

$$P_t = P_{t-1} + Q\Delta t \tag{3.4}$$

The highest level of temporal variability in the depth estimates is allowed where the value for $Q$ and thus $P$ is maximum and so the decay in faith of the previous depth estimates is largest. This implies in practice that $x_0$ should be defined by the user as the cross-shore location where one expects the greatest morphological change, following (3.3), with the result that estimates in that region are updated most readily. $P$ is used to calculate the faith in the old estimate through

$$\text{Faith } [\%] = \left[ 1 - \frac{P_t}{P_t + h_{error}} \right] \times 100 \tag{3.5}$$

(3.5) shows that as the error is very small [close to zero], full confidence in the new estimates exists and faith in the old estimate vanishes completely. Since the belief in the new estimate is so strong, the old estimate is discarded and the "combined" depth is the new estimate. If the new estimate is less accurate and some faith remains in the old estimate [for example 50%], then the combined depth [old and new] contains 50% of the old and 50% of the new estimate. The decay in faith for the old estimate is plotted in Figure 3.10 per average depth estimation

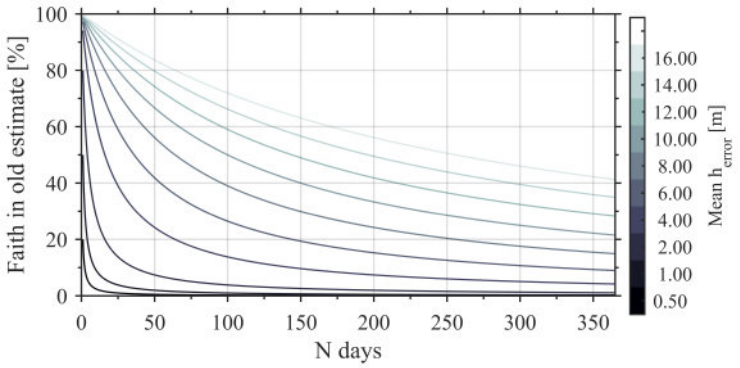


Figure 3.10: Temporal decay in faith of an estimate [prior] presented in percentage considering a **new** estimate with a certain depth estimation error [$h_{error}$]

error of the new estimate [lines].

To summarise, depths are estimated on a user defined grid using time-varying pixel intensities through the linear dispersion relation for free surface waves. Depth estimations are obtained per collection of pixel intensities, which is on an hourly basis for most *Argus* stations. The hourly depth estimations are combined through a Kalman filter based on the confidence in the particular estimate. The confidence in the prior estimate decays in time and confidence in the new estimate determines whether the prior or new estimate is used in the Kalman procedure for the next depth estimate.

### 3.4.2 cBathy settings at Porthtowan

cBathy requires model specific settings and boundary conditions such as domain settings, depth truncation, frequency domain and smoothing length scales. The camera system at Porthtowan is mounted on the Southern cliff and the cameras are looking alongshore in a Northerly direction, as shown in Figure 2. Considering the spatial domain for the pixel intensity collections, the strategy used is to create the largest possible spatial domain stretching as far offshore as the method will allow. Practical limits to the offshore boundary are imposed by the depth controlled wave dispersion and the pixel resolution of the cameras. A reasonable offshore boundary for the domain is typically determined using the footprint of the pixel and occurring wave periods. The combination of wave periods and pixel footprint determines, at the same time, the spatial resolution ($\Delta x$ and $\Delta y$) of the pixel collection ($x_p$ and $y_p$). The further offshore, the larger the camera footprint. At the most outer extent of the camera domain one pixel might cover an area of 100 m x 100 m and incident waves are barely visible. An offshore boundary is therefore introduced to reduce unnecessary data collection. The offshore boundary for the application of

cBathy at Porthtowan was chosen to be 1.2 km offshore with $\Delta x$ (cross shore) of 4 metres and $\Delta y$ (alongshore) of 10 metres.

Points in the domain where the depth will be estimated are introduced in the form of a (sub) grid $(x_m, y_m)$. The spacing between the gridded points for depth estimation is typically larger than the pixel intensity collection grid because for every depth estimate a set of sub-sampled pixel intensities around the depth estimation point is required. At Porthtowan the spacing for the depth estimation points is 10 metres in the cross shore direction and 25 metres in the alongshore direction.

Depth estimation values are filtered in cBathy by allowing depths within a reasonable site specific depth range. For this application of cBathy the depth truncation is set to a minimum depth of 0.25 metres and maximum depth of 20 metres. In addition to the depth truncation, a frequency range controls the depth estimations. Based on wave data a typical frequency range is determined. Considering the prevailing swell-dominated wave climate at Porthtowan, a range up to 18 seconds wave period is used. $\Delta f$ was chosen as $100s^{-1}$ to create enough resolution around the longer wave periods.

The dimensions of the pixel sub-sampling domain are determined by the smoothing length scales. Smoothing takes place such that the contribution of the pixels to the final depth estimate is weighted through a Hanning filter. More weight is assigned to the pixels close to a depth analysis point when the sub-sampling domain is smaller while more spreading of the weighted contribution occurs if the sub-sampling domain is larger. The sub-sampling domain around the depth analysis point for Porthtowan has a width of $\Delta x_m$ and a length of $\Delta y_m$ (10m and 25m respectively).

| Description | value(s) | units |
|---|---:|---:|
| Pixel collection spacing ($\Delta x_p$) | 4.0 | metres |
| Pixel collection spacing ($\Delta y_p$) | 10.0 | metres |
| Depth analysis spacing ($\Delta x_m$) | 10.0 | metres |
| Depth analysis spacing ($\Delta y_m$) | 25.0 | metres |
| Allowable depth range [$h_{min}$ to $h_{max}$] | 0.25 to 20.0 | metres |
| Frequency domain [$f_{min}$ to $f_{max}$] | 1/18 to 1/4 | 1/s |
| $\Delta f$ | 1/100 | 1/s |
| Smoothing scales (in depth analysis) | $\Delta x_m$, $\Delta y_m$ | |

Table 3.1: Overview of Porthtowan specific settings for cBathy

## 3.5 Momentary coastline

The momentary coastline is a concept developed in the 1990s in the Netherlands during a period of coastal zone management restructuring in The Netherlands (Hillen et al. 1991). The Dutch Ministry of Infrastructure and Public Works together with Water Boards observed the coastal volumes and morphological changes since 1963 through yearly cross shore profiles along the entire coast with spacing between the profiles between 200 m to 250 m. Although all this data was acquired [through different evolving techniques], no systematic analysis was applied to the dataset other than observing the change in profiles. Whether a decision had to be taken to strengthen the coastline remained an expert opinion based on an overall baseline. Hillen et al. (1991) introduced a systematic way of determining the *momentane kustlijn* or *instantaneous coastline* [commonly translated to *momentary coastline*] which would be compared to the 1990 *base* coastline to assess the coastal strength and if action has to be undertaken. Up until the 1990s the Dutch coast in general experienced a consistent long-term erosion threatening the economically valuable hinterland. However, locally the erosion rates were different between locations. An overall base coastline approach was therefore insufficient and a dynamic coastal zone management plan was introduced. The 1990 base profiles are the foundation profiles or benchmark to determine if action has to be undertaken. However since the 1990 profiles provide a snap shot of the coastal situation, the 1900 base coastline could be kept, changed or neglected [for some special coastal stretches expert opinion prevails] at the five-yearly coastal strength assessment (Hillen et al. 1991, TAW 2002) based on gained morphological insight from the past years. Year-long trends and predictions in the momentary coastline provide the morphological insight that forms the foundation of the decision to keep, change or neglect the base profile locally. The momentary coastline became the most important measure to decide if interventions [mostly coastal nourishments] are required.

The momentary coastline [MCL] quantifies sediment volumes present in the coastal zone between two vertical reference levels. In essence the MCL represents a coastline position based on the volume of sediments on the beach in a vertical reference frame. This implies that the MCL would not indicate any change if all the sediment moves between the vertical limits. Gain in the vertical frame means a seaward migration of the shoreline and vice versa. Figure 3.11 shows the principle of the MCL as in Hillen et al. (1991) and applied here.

The main differences between the MCL in this work [applied in Chapter 5 and 6] compared to Hillen et al. (1991) are the vertical limits. The MCL as firstly intended (Hillen et al. 1991) included a dune system and vertical limits based on tidal elevations. In Hillen et al. (1991) the upper limit is the dune foot and vertical range [here $H$] to the lower limit twice the vertical

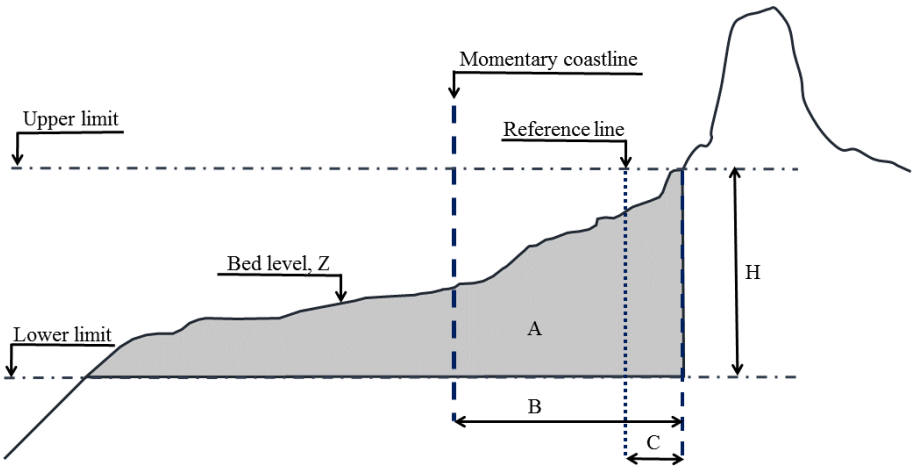


Figure 3.11: Momentary coastline principle in this work [modified from (TAW 2002)].

distance between the dune foot and the mean low water level. In this work, a slightly different approach is chosen due to the vertical limitations of the inter-tidal beach surveys. The upper vertical limit is the lowest maximum and the lower limit is the highest minimum over all the surveys. The reference line gives the opportunity to reference it to local or global coordinates. Here, the reference is set to zero. Calculation of the MCL is rather straightforward when all the limits and references are chosen. The area A, between the vertical limits and the bed level $Z$, is calculated by integrating the bed level elevation.

$$MCL = B = \frac{\int_{x_{low}}^{x_{high}} Z dx}{H} - C \tag{3.6}$$

In which $Z$ is the bed level and the reference levels are $x_{higherlimit}$ and $x_{lowerlimit}$. Distance $B$ is calculated by dividing $A$ by the vertical range $H$ $[x_{high} - x_{low}\ ]$ following (3.6). Then the actual referenced MCL is the calculated distance $B$ minus the reference location $C$. At Porthtowan the vertical reference levels are set to $x_{high}$ = 4 m and $x_{low}$ = -2 m. the upper boundary represents the typical maximum of the survey domain as presented in Section 3.3. $C$ is set to zero.

## 3.6 Disequilibrium modelling of the momentary coastline

Disequilibrium models are typical *behaviour-based* models (Hanson 1989, Dean 1991, Kramer 2005, Davidson et al. 2013) that are driven by the idea that disequilibrium results in change while keeping e.g. a cross shore profile shape constant. In behaviour-based models evolution of the beach is described by largely empirical formula, without attempting to solve underlying physics

in detail through for example the Navier-Stokes equations as in most *process-based* models. Behaviour based models are generally less computational expensive, more stable and therefore applied over longer time-scales [years to decades] than the process-based counter parts [days to months]. Here, a data-driven behaviour-based model is applied to the momentary coastline. The momentary coastline is measured intermittently with worst case intervals of a month. The modelled momentary coastline provides insight in the behaviour of the momentary coastline during the data gaps. The results are used throughout Chapters 5 and 6 for the storm impact and recovery analysis.

The modelling technique that is applied in this work is based on the disequilibrium principle of Wright et al. (1985) and uses measured data over a part of, or whole of the dataset, to calibrate shoreline response to a certain disequilibrium and wave power (Davidson et al. 2013). The calibrated settings of the model can subsequently be used to predict the temporal variability of the shore line (Davidson et al. 2013). The concept of Davidson et al. (2013) is not only applied to the temporal variability of the shoreline but also the temporal variability of bar three dimensionality (Stokes et al. 2015) and sediment grain size (Prodger et al. 2016). The variety of coastal parameters shows the potential of the disequilibrium concept.

The concept of this disequilibrium model [DST13] is rather straight forward: more disequilibrium stress = more shoreline change. The dimensionless fall velocity (2.2) incorporates the wave height, wave period and fall velocity. These parameters are time-varying, however the fall velocity [$w_s$] is kept constant [temporal variable $w_s$ is applied in Prodger et al. (2016)] in DST13. Figure 3.12a shows the wave dependent dimensionless fall velocity [grey line]. Wright et al. (1985) showed that the instantaneous dimensionless fall velocity gives by itself a poor representation of morphological change. Wright et al. (1985) proposed that antecedent waves are important and should be incorporated through a weighted mean [equilibrium $\Omega$] following (2.4), for which $D$ has been changed to $2\phi$ for the modelling following (3.7).

$$\bar{\bar{\Omega}}_{eq} = \left[\sum_{j=1}^{2\phi} 10^{-j/\Phi}\right]^{-1} \sum_{j=1}^{2\phi} \Omega_j 10^{-j/\Phi} \tag{3.7}$$

In (3.7) $j = 1$ is a day index where 1 refers to the day of evaluation and larger indicates earlier days, $\Omega_j$ represents the dimensionless fall velocity for the $j^{th}$ day and $\Phi$ in days represents the time for the weighting factor to decrease to 10%. The orange curve in Figure 3.12a represents this weighted equilibrium of the dimensionless fall velocity. Figure 3.12a shows that weighting the dimensionless fall velocity with prior data shows a delay in the minima and maxima of the instantaneous $\Omega$ data. The orange curve represents a proxy for temporal variable equilibrium in

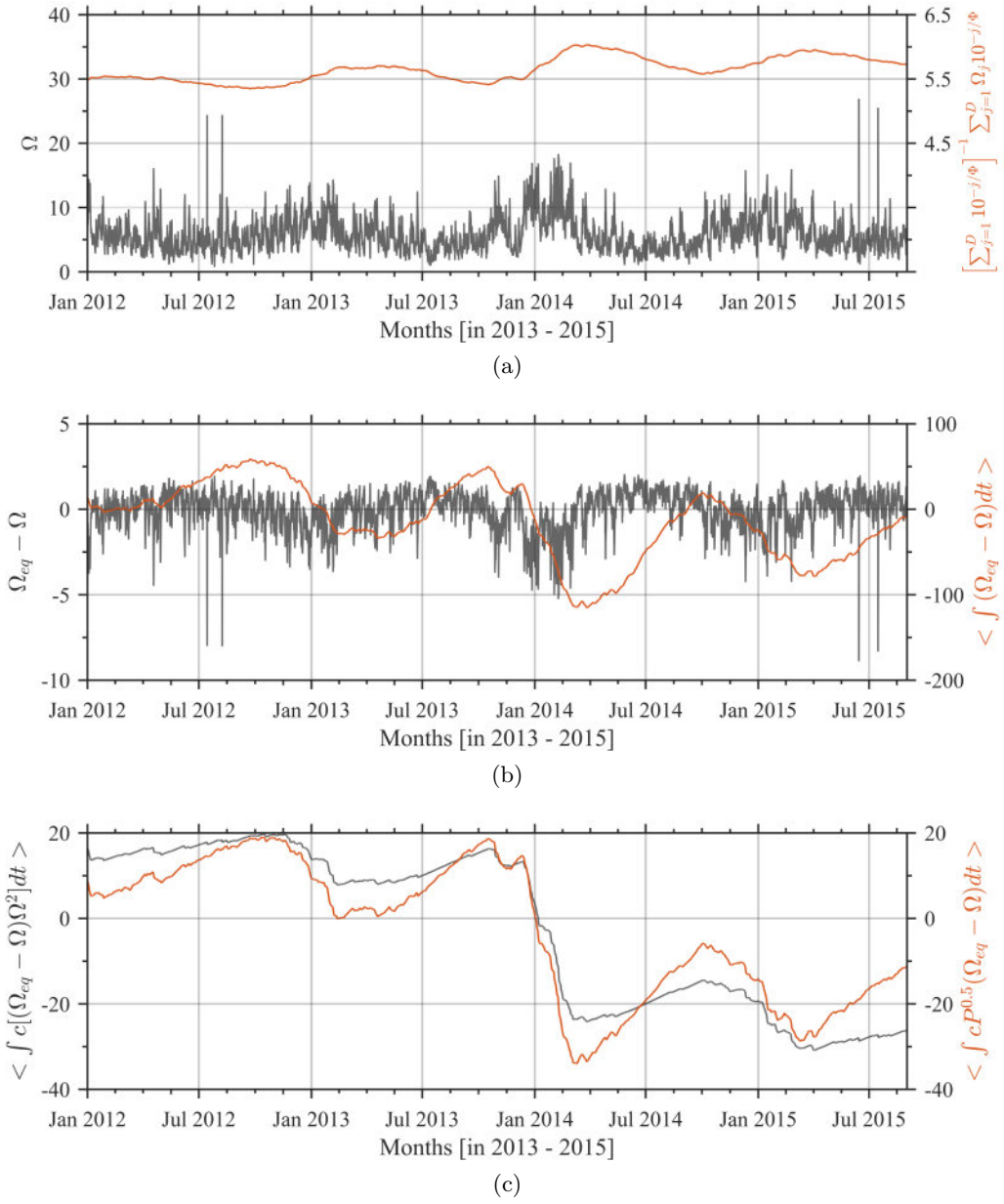


Figure 3.12: Example of disequilibrium modelling results using the wave data as presented in Section 3.2. a) instantaneous dimensionless fall velocity in grey and weighted dimensionless fall velocity in orange. b) disequilibrium in grey and the time integrated disequilibrium in orange [a proxy for DLT10 if $k = 0$]. c) final model results of DLT10 with $k = 2$ following Wright et al. (1985) in grey and DST13 in orange.

dimensionless fall velocity. In other words, if the instantaneous $\Omega$ is equal to the $\Omega_{eq}$ no change happens and vice versa. This (dis)equilibrium (Wright et al. 1985) is expressed in (3.8).

$$\Delta\Omega(t) = \Omega_{eq} - \Omega \tag{3.8}$$

where $\Omega_{eq}$ is the equilibrium dimensionless fall velocity calculated through (3.7) and $\Omega$ represents the instantaneous dimensionless fall velocity. Figure 3.12b shows an example of modelled disequilibrium [grey line]. Wright et al. (1985) couples this disequilibrium to a rate of change in beach state through a disequilibrium stress [$ds/dt \propto (\Omega_{eq} - \Omega)\Omega^2$]. An earlier version of the DST13 adopted this relation to model shoreline change (Davidson et al. 2010) [From here on this model is referred to as DLT10] as shown in (3.9).

$$\frac{\Delta x}{\Delta t} = b + c\left[\Delta\Omega\,(t)\,\Omega^k(t)\right] \tag{3.9}$$

wherein $b$ represents a shoreline trend, $c$ is the optimised response time for a given $k$, $\Delta\Omega$ represent disequilibrium [determining mainly the direction of change] and $\Omega$ is the dimensionless fall velocity. The power $k$, $b$ and $c$ (related to $k$) are free parameters that are optimised with a calibration dataset. Davidson et al. (2010) showed that the skill is relatively insensitive to $\Omega^k$ and could therefore be neglected, resulting in a shoreline change proportional to the orange curve in Figure 3.12b which represents the time-integrated disequilibrium. The time-integrated disequilibrium is a proxy for the instant beach state or shoreline position following Davidson et al. (2010). However, the contribution of antecedent wave conditions in DLT10 was diminished by taking an overall mean of the dimensionless fall velocity as $\Omega_{eq}$. One of the fundamental differences between DLT10 and DST13 is the inclusion of antecedent wave conditions following (3.7). Instead of a mean dimensionless fall velocity, a value for $\phi$ in (3.7) is estimated that yields the best correlation with the observations. This is achieved by iteratively changing the response variable $\phi$ from 1 days [representing short memory and rapid change] to 1000 days [representing long memory and seasonal change]. Also, DST13 redefined the disequilibrium stress term as such that the incident offshore wave power [$P$] plays a role by replacing $\Omega^k$ for $P^{0.5}$. The "forcing" disequilibrium stress term in DST13 that represents the rate of change of the shoreline is presented in (3.10).

$$\frac{\Delta x}{\Delta t} = b + c^{\pm}_{a,e} P^{0.5}(t)\Delta\Omega(t) \tag{3.10}$$

In this Equation $b$ represents the mean shoreline position, the constant $c^{\pm}$ is a scaling

factor that contains the a ratio between accretive (+) and erosive (-) conditions, $P$ is the time-varying incident wave power and $\Delta\Omega(t)$ represents disequilibrium normalised to units of standard deviation which in essence captures the direction of change. (3.9) and (3.10) have both the fitting constant $c$ and the sign of resulting curves of both models is a function of the disequilibrium. The fundamental difference between (3.9) and (3.10) is the time dependent amplifier. The temporal amplifier is $\Omega^k$ in (3.9) and $P^{0.5}$ in (3.10). These temporal amplifiers in essence control the magnitude of the rate of change, $c\Omega^k$ in DLT10 and $cP^{0.5}$ in DST13. As mentioned before, considering the insensitivity of DLT10 to $\Omega^k$, the results of DLT10 are in line with the orange curve in Figure 3.12b. Wright et al. (1985) couples the change to $k = 2$, in DLT10 which is represented by the grey line in Figure 3.12c. The orange curve in Figure 3.12c shows an example of DST13. Both time-integrations are de-trended [denoted by the square brackets <>] to account for a negative trend related to the over-contribution of erosional, generally steeper, waves. This while a negative trend over the complete time-series is not expected.

Figure 3.12c shows the fundamental but expected difference between DLT10 with $k = 2$ and DST13. The signs and direction of change are identical consistent with the fact that the direction is determined by the same values for $\Delta\Omega$. The constant $c$ is adapted for both approaches to follow the observations to the best extent. The rate of change differs due to the difference in temporal amplifier [respectively $\Omega^k$ and $P^{0.5}$]. DLT10 [with $k = 0$] and DST13 are both used in the storm by storm analysis in Chapter 6. To assess the wave-based shoreline response in between storms in terms of momentary coastline, only DST13 is used in Chapter 5 considering the increased skill in Davidson et al. (2013) and a higher found correlation between the measured MCL and DST13 [$R^2 = 0.58$ with $p < 0.01$] compared to DLT10 [$R^2 = 0.55$ with $p < 0.01$].

## 3.7 Sub-tidal bar extraction

A sub-tidal bar extraction is introduced in order to assess the three-dimensional behaviour and migration of the sub-tidal bar systems. The extraction of the sub-tidal bars discussed here is in many ways similar to Plant et al. (1999). A reference profile is determined to subtract from the data in order to detect sandbars. Many different approaches have been used in the past, among others a linear trend, the Dean profile, or mean cross shore profile. Plant et al. (1999) used the average profile obtained from years of data. Here, the mean cross shore profile from the video-based depth estimations over 1.5 years is used and it is filtered following Plant et al. (2008).

For every bathymetry at an arbitrary point in time the base-bathymetry is subtracted. The

result is a map where bar features are highlighted and where the positive areas represent sandbar areas, as shown in Figure 3.13. For every cross shore profile of the de-trended bathymetry the bar areas are identified and sub-sampled. To the sub-sampled bar areas, a $4^{th}$ order polynomial is fitted so that local maxima representing the cross shore bar position can be determined consistently without noise. The fourth order polynomial also has the advantage of detecting bar merging where two bars come together. The local maxima of the polynomial represent the bar position.

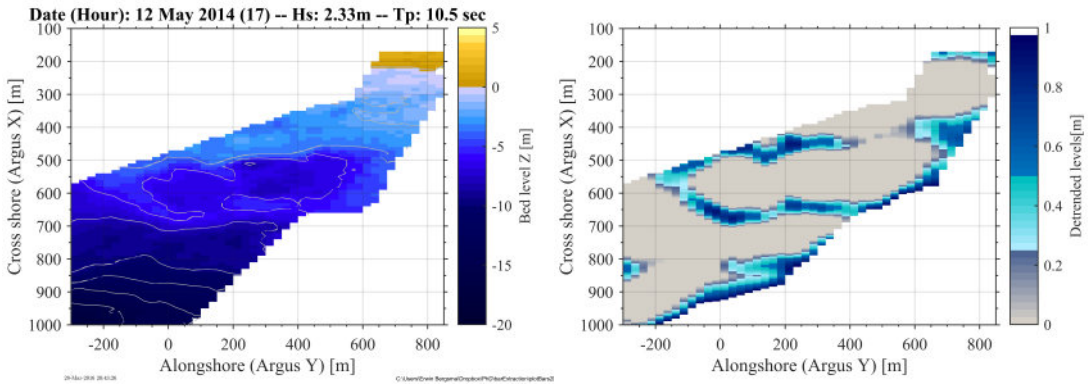


(a) (b)

Figure 3.13: Example of the bar-line identification after de-trending an arbitrary bathymetry. The left figure represent a bathymetry estimate and at the right the base profile is subtracted from the depth estimate.

### Grouping bar points

For every bathymetry a set of points where the system thinks the bar is located are identified. These bar identifiers are subsequently grouped in the alongshore direction. The grouping or alongshore bar detection is based on three criteria: 1) an allowable distance between a point and all the other points, 2) an allowable angle between a point and all the other points that satisfy 1) and 3) a group that satisfy 1) and 2) should have a minimum of 3 points. Let X and Y be two vectors so that the distance [r] and angle [$\theta$] between all points is found following (3.11) and (3.12). If there are points within the distance criterion (1) than firstly the closest of the points is assessed on the angle criterion. If both criteria are satisfied the points are automatically grouped, if not the second closest point is assessed so on and so forth.

$$X_{xx} = X - X^T \text{ and } Y_{yy} = Y - Y^T \tag{3.11}$$

$$r_{xx,yy} = \sqrt{X_{xx}^2 + Y_{yy}^2} \text{ and } \theta_{xx,yy} = \arctan\left(\frac{Y_{yy}}{X_{xx}}\right) \tag{3.12}$$

### 3.7.1 Application at Porthtowan

Hourly bathymetries give the opportunity to investigate the short term behaviour of the inter and sub-tidal bars. The method described in Section 3.7 is applied to Porthtowan in order to extract the sandbar locations for the all the hourly bathymetries. The mean bathymetry is derived from the total dataset. From the mean bathymetry the alongshore average represents the input for the filtering as described in Section 3.7 and the construction of the base-bathymetry. The alongshore mean profile is presented in the right side of Figure 3.14 as the dashed red line. The filtering technique (Plant et al. 2008) incorporates a variety of length scales to find an average profile with minimized errors. This technique is applied to the red dashed line using length scales of 300, 350, 400, 500, 600 m. The result of the filtering is presented by the blue line in the right-hand plot of Figure 3.14. The filtered profile shows that the modulations in the mean profile [red line] are filtered out. The filtered cross shore profile shows four slopes: 1) a slope of 0.0211 between 100 and 175 m, 2) a slope of 0.0157 between 175 and 700 m, 3) from 700 m to 850 m the slope is 0.0248 and 4) the offshore part of the domain from 850 onwards a slope of 0.0462. This filtered profile is subsequently used for the alongshore uniform base-bathymetry. The resulting base bathymetry is presented in the left-hand plot of Figure 3.14. This base-bathymetry is used in the further analysis to subtract from instant hourly bathymetry estimates to distil the bar positions.

Figure 3.15 shows an example of the bar-line extraction. Here, an arbitrary bathymetry estimate is used as an example and the bathymetry estimate is presented in Figure 3.15a. Subsequently the base-bathymetry [Figure 3.14] is subtracted from Figure 3.15a which results in Figure 3.15b.

Figure 3.15b shows that the bars are distilled quite clearly after this step. Nevertheless, identifying local maxima as bar positions will result in a noisy and inconsistent bar position estimation. A fourth order polynomial is fitted to every blue highlighted positive area in Figure 3.15b to overcome these inconsistencies following Section 3.7. Some of the blue areas in Figure 3.15b are on/around the outer edge of the cBathy domain. The bar estimation will not work there as the system cannot determine if these areas are bar areas with zero-crossing or that these areas represent other features. For the bar between $500 \text{ m} < X < 700$ m [cross shore] this means that one can expect a bar line extraction between $-150 \text{ m} < Y < 400$ m [alongshore]. For the grouping of the bar positions as described in Section 3.7 the allowable distance and angle

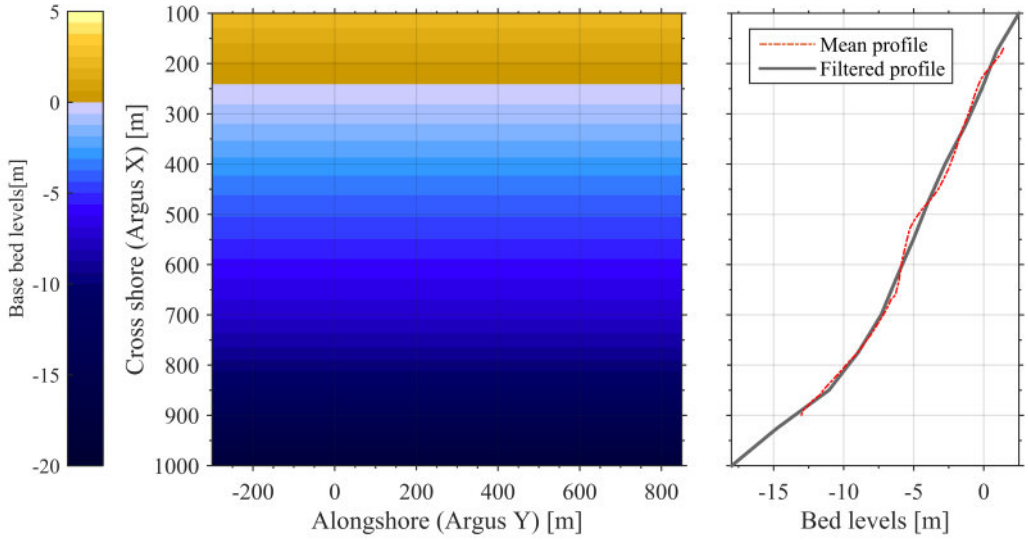


Figure 3.14: Base bathymetry on the left and cross shore profile on the right. The red line is the mean profile and the blue line is the base profile that is used to construct the base bathymetry.

should be quantified. Considering the resolution of the bathymetry estimates at Porthtowan the allowed distance is set to $3\Delta y$ which is equal to 75 m and the allowed angle is $\arctan(2\Delta y/4\Delta x)$ = 51 degrees. The results are shown in Figure 3.16. The white asterisks represent the local maxima of the $4^{th}$ order polynomials and the red-line represent the grouped bar lines.

Now the bar line can be extracted with this application, typical indicators are bar height, bar width, alongshore mean bar position of a given bar line section, alongshore standard deviation of the bar line and the skewness of the bar cross section.

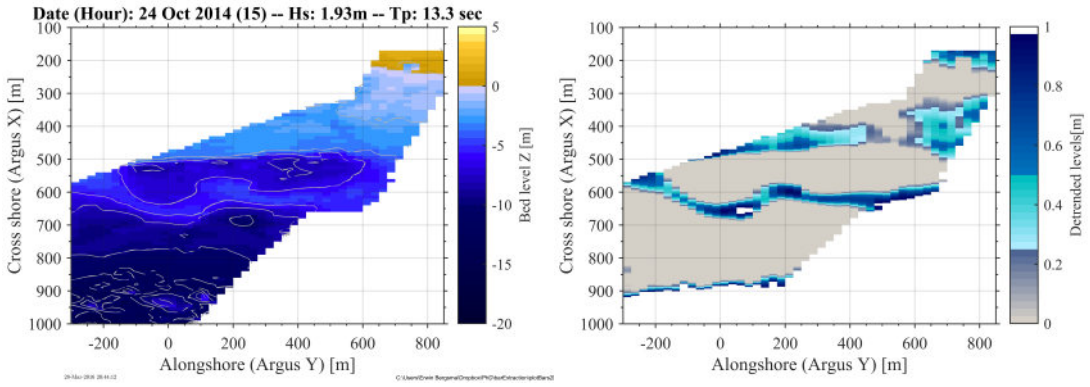


(a) (b)

Figure 3.15: Example of the bar-line identification after de-trending an arbitrary bathymetry. The left figure represent a bathymetry estimate and at the right the base profile is subtracted from the depth estimate.

## 3.8 Empirical Orthogonal Functions

The camera system at Porthtowan is typically set to collect data on an hourly basis. The high temporal resolution is a nice characteristic of the video-based depth estimation. However, it results in such large datasets that a type of filtering is required to capture morphological patterns and understand the story the data comprises. Empirical Orthogonal Functions (EOF) analysis [also known as Principle Component Analysis (PCA) (Pearson 1901)] is a technique purposely created for this filtering and capturing of (complex) patterns in (large) datasets. This EOF technique is, for example, applied in weather forecasting (Lorenz 1956). The main concept of EOFs is that the complexity of the data is decomposed into more comprehensive mutually orthogonal patterns [Eigen Vector or Principle Components (PCs)] that represent a percentage of the total variability in the data. The first PC represents the largest percentage of the total variability. The second PC constitutes a smaller part of the total variability. The decreasing trend of the represented percentage of the total variability per PC continues, the third PC represents an even smaller part of the total variability, and so forth. EOFs are generally used for two purposes: 1) to investigate a single Principle Component [PC] with certain encapsulated process and 2) as a filtering technique where the PCs that constitute a relatively small part of the variability are neglected in the reconstruction. In the sections below, the concept of (complex) Empirical Orthogonal functions and combining the Principle Components in order to reconstruct the data will be discussed in more detail.

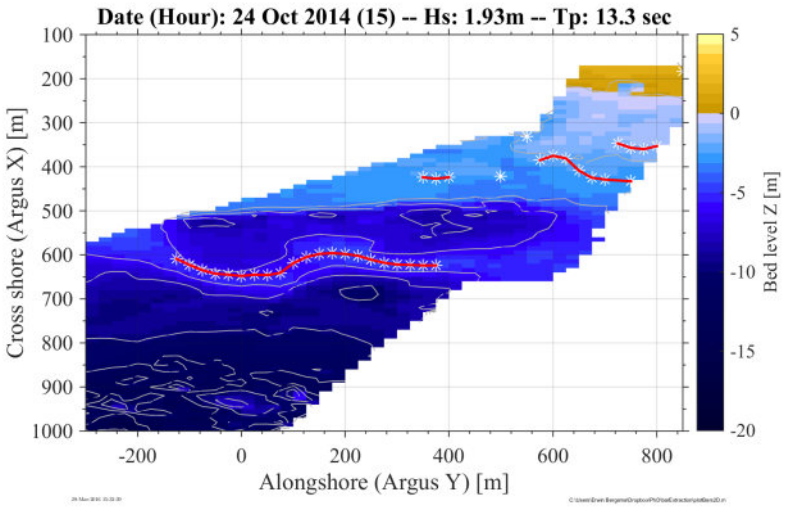


Figure 3.16: Estimated bar positions [white asterisks] and the bar lines in red for the same example as in Figure 3.15

### 3.8.1 Ordinary and Complex Empirical Orthogonal Functions

The process of the ordinary (Wallace & Dickinson 1972) and complex (Horel 1984) Empirical Orthogonal Functions (EOF) is in many ways similar. Here, the EOF procedure is explained and the differences between the ordinary and complex EOFs are highlighted. The input for the EOF analysis starts with the assumption that data points are non-overlapping and independent. Data points can possibly be correlated to each other. The resulting eigenvectors are linearly uncorrelated. Here, the 3D depth estimates are varying in time, resulting in a 4D matrix $(x,y,z,t)$. For the EOF procedure here, only the time varying depths corresponding to a certain $x$ and $y$ are used. The exact x, y and timing is not relevant for the EOF analysis, solely to post process the results. This results in a 2D matrix where the depth $Z$ varies as a function of $x,y,t$ as show in the EOF input matrix A presented in (3.13).

$$A\left(z_{x,y,t}\right) = \begin{bmatrix} z_{x_1,y_1,t_1} & z_{x_2,y_1,t_1} & \cdots & z_{x_i,y_1,t_1} & z_{x_1,y_2,t_1} & \cdots & z_{x_i,y_{j-1},t_1} & z_{x_i,y_j,t_1} \\ z_{x_1,y_1,t_2} & z_{x_2,y_1,t_2} & \cdots & z_{x_i,y_1,t_2} & z_{x_1,y_2,t_2} & \cdots & z_{x_i,y_{j-1},t_2} & z_{x_i,y_j,t_2} \\ \vdots & \vdots & \ddots & \vdots & \vdots & \ddots & \vdots & \vdots \\ z_{x_1,y_1,t_k} & z_{x_2,y_1,t_k} & \cdots & z_{x_i,y_1,t_k} & z_{x_1,y_2,t_k} & \cdots & z_{x_i,y_{j-1},t_k} & z_{x_i,y_j,t_k} \end{bmatrix} \tag{3.13}$$

If the input data is non-complex it has to be modified for the complex EOF analysis. Essentially, the non-complex dataset has to be transformed to a complex representation of itself. This

transformation can be achieved through a Hilbert transformation function. The Hilbert transform essentially takes the original data signal and adds a 90 degree phase shifted copy as a complex part [for example with $u(x) = \sin(x) \rightarrow H(u(x)) = \sin(x) + i\sin(x+\pi/2) \Leftrightarrow \sin(x) + i\cos(x)$] to the original data set, shown in (3.14).

$$H(A(z_{x,y,t})) = A(z_{x,y,t}) + i\tilde{A}(z_{x,y,t}) \tag{3.14}$$

(3.14) shows the Hilbert transform ($H$) of dataset $A(z_{x,y,t})$. $\tilde{A}(z_{x,y,t})$ is the 90 degrees phase shifted part of the dataset. In summary, the ordinary EOFs have the original data and the complex EOFs have the Hilbert transformed version of the dataset as input for the EOF procedure A second data preparation step is to subtract the temporal mean per single data point so that we end up with solely the temporal deviation around the mean for every single data point. All the mean values in space together form the spatial pattern of a temporal mean, around which the principle patterns vary. Subsequently the eigenvalues ($\lambda$) and eigenvectors ($\vec{v}$) are found through linear algebra procedures for the de-trended dataset, demonstrated with an example below where $A$ is the input matrix, $\vec{v}$ is the eigenvector and $\lambda$ the set of eigenvalues.

$$A\vec{v} = \lambda\vec{v} \Leftrightarrow (A - \lambda I)\vec{v} = 0 \tag{3.15}$$

$$A = \begin{bmatrix} -1 & 3 \\ -2 & 4 \end{bmatrix} \rightarrow (A - \lambda I) = \begin{bmatrix} -1-\lambda & 3 \\ -2 & 4-\lambda \end{bmatrix} \tag{3.16}$$

$$p(\lambda) = \det(A - \lambda I) \Leftrightarrow \det \begin{bmatrix} -1-\lambda & 3 \\ -2 & 4-\lambda \end{bmatrix} \tag{3.17}$$

This results in $\lambda_1 = 2$ and $\lambda_2 = -5$, now the eigenvectors are easily found taking the right

hand side of (3.15) using $\lambda_1 = 2$.

$$\vec{v} = \begin{bmatrix} \vec{v}_1 \\ \vec{v}_2 \\ \vdots \\ \vec{v}_n \end{bmatrix} \rightarrow \begin{bmatrix} -1-2 & 3 \\ -2 & 4-2 \end{bmatrix} \begin{bmatrix} \vec{v}_1 \\ \vec{v}_2 \end{bmatrix} = \begin{bmatrix} 0 \\ 0 \end{bmatrix} \tag{3.18}$$

$$-3\vec{v}_1 + 3\vec{v}_2 = 0$$

$$-2\vec{v}_1 + 2\vec{v}_2 = 0$$

This leads to an eigenvector $\vec{v}_1 = \begin{bmatrix} 1 \\ 1 \end{bmatrix}$, the same process can be conducted for $\lambda_2$.

(3.15) to (3.18), show the procedure of finding eigenvectors and eigenvalues. Finding the eigenvalues and eigenvectors for such a small matrix ($A$) is straightforward and can be performed manually relatively quickly. For larger, more complex, matrices, with multiple dimensions, an optimised standard MatLAB function can calculate the eigenvalues and eigenvectors numerically. The eigenvalues found are normalised to represent the percentage of captured variance per eigenvalue. Normalisation for the ordinary EOFs is rather straightforward. The individual values are normalised by dividing by the sum of all the components, as shown in (3.19).

$$\hat{\lambda}_{k,ord} = \frac{diag\left(\lambda_{k,ord}\right)}{trace\left(\lambda_{ord}\right)} \tag{3.19}$$

In the case of the complex dataset results, eigenvectors and eigenvalues come in a complex format. The eigenvalues are therefore normalised through complex normalisation. First, the eigenvalues are separated in the real and imaginary component. The resulting individual components are then divided by the mean of the absolute eigenvalues, as shown in (3.20) and (3.21).

$$\tilde{\lambda}_{k,cplx} = \frac{\Re\left(\lambda_{k,cplx}\right)}{\left|\overline{\lambda_{cplx}}\right|} + i * \frac{\Im\left(\lambda_{k,cplx}\right)}{\left|\overline{\lambda_{cplx}}\right|} \tag{3.20}$$

$$\hat{\lambda}_{k,cplx} = \frac{diag\left(\tilde{\lambda}_{k,cplx}\right)}{trace\left(\tilde{\lambda}_{cplx}\right)} \tag{3.21}$$

$\hat{\lambda}$ represents the captured percentage of total variance found in the dataset. Now, one can filter, for example, the data by a certain variance threshold. Also, a number of eigenfunctions can be determined based on statistical confidence (Monte Carlo analysis is shown in section 6.2.1). The sum of eigenvalues corresponding to the determined number of eigenfunctions gives the total amount of variance described by the subset.

### Data reconstruction using EOFs

In this work, EOF analyses are applied to three dimensional depth estimates with input matrix shown in (3.13). The eigenvectors (here, $E_n$) returned by the Eigenfunction analysis contain values for $z$ for that particular mode. These $z$ values are corresponding to a certain position in space and time. Translation of the ordinary eigenvector to a spatial pattern is straightforward as the positions correspond directly to the x,y of the input. The time signal is captured in the temporal variation of the eigenvalue. Multiplication of the eigenvector and temporal eigenvalue reconstructs an EOF mode and its variation in time. The complex EOF (cEOF) analysis requires a bit more modification of the eigenvalues and vectors.

**Reconstruction with complex EOFs** The major advantage of the complex EOF analysis is the ability to capture moving patterns in a single eigenvector, a progressive wave for example. To describe moving patterns, an amplitude (pattern) and a corresponding phase are required. The complex eigenvectors contain this spatial amplitude and phase information. The spatial amplitude is calculated by taking the norm of the real and imaginary part of the vector, as shown in (3.22). The phase results from the arctan between the imaginary and real part of the eigenvector, presented in (3.23).

$$\xi_i(x,y) = \sqrt{E_\mathrm{n} E_\mathrm{n}^T} \Leftrightarrow \sqrt{\Re\left(\mathrm{E_n}\right)^2 + \Im\left(\mathrm{E_n}\right)^2} \tag{3.22}$$

$$\theta_i(x,y) = \arctan\left(\frac{\Im\left(\mathrm{E_n}\right)}{\Re\left(\mathrm{E_n}\right)}\right) \tag{3.23}$$

A sense of the temporal variation is obtained by computing the dimensional Eigenfunctions $A_n$ per $n^{th}$ mode, shown in (3.24). In (3.24) $H\left(A\left(z_{x,y,t}\right)\right)$ represents the de-trended Hilbert transformed input matrix and $E_\mathrm{n}$ is the corresponding eigenvector for the $n^{th}$ mode.

$$A_n = H\left(A\left(z_{x,y,t}\right)\right) E_\mathrm{n} \tag{3.24}$$

A temporal amplitude and phase are derived from the Eigen function $A_n$ in a similar fashion as for the spatial equivalent, presented in (3.25) and (3.26)

$$\eta_i(t) = \sqrt{A_{\mathrm{n}} A_{\mathrm{n}}^T} \Leftrightarrow \sqrt{\Re(\mathrm{A_n})^2 + \Im(\mathrm{A_n})^2} \tag{3.25}$$

$$\psi_i(t) = \arctan\left(\frac{\Im(\mathrm{A_n})}{\Re(\mathrm{A_n})}\right) \tag{3.26}$$

The spatial and temporal amplitudes and phases combined construct a time varying spatial pattern around the temporal mean. Therefore, to reconstruct the input matrix, and thus pattern, the de-trended mean matrix [here, $\overline{Z}(x,y)$] has to be added. (3.27) shows the full reconstruction. The spatial and temporal amplitudes are multiplied and the phases are subtracted.

$$Z(x,y,t) = \overline{Z}(x,y) + \sum_{i=1}^{n} \eta_i(t)\xi_i(x,y)\cos(\theta_i(x,y) - \psi_i(t)) \tag{3.27}$$

## 3.9 Application of the methods

Obtained field data such as the wave, tidal and bed level information are used throughout the work and the data analysis is applied in more specific Chapters. The video-based depth estimates [introduced in Section 3.4] are applied to a macro-tidal environment. The performance of the video-based depth estimation technique in a high energetic macro-tidal environment was unknown. The application and performance assessment of the video-based depth estimations is described in Chapter 4. The application of the video based depth estimations in Chapter 4 requires the occurring wave conditions and tidal elevation as principle input [elaborated below and further explained in Chapter 4].

The storm impact is described based on the observations from the inter-tidal beach surveys and video-based depth estimations in Chapter 5. The coastal strength during the storms and recovery is presented in the form of the measured and modelled momentary coastline. The measured momentary coastline is introduced in Section 3.5 and the modelling of the momentary coastline is shown in Section 3.6. Chapter 5 discusses the long-term perspective of the 2013-2014 winter season. The obtained depth estimations are used to highlight the bar behaviour over the 2013-2014 winter season and subsequent recovery in Chapter 5. The discussion elaborates on the mean cross shore bar position and three-dimensionality. The sub-tidal bar structure is extracted from the video-based depth estimations which is described in Section 3.7.

Empirical Orthogonal Functions [EOF] are used to filter the video-based depth estimates into principle modes of morphological change for a storm by storm analysis in Chapter 6. The EOF-procedure is introduced in Section 3.8 and shows a background, validation of the technique for extracting the principle modes and filtering application. In the last paragraphs of this Chapter the application of the EOF procedure to the video-based depth estimation dataset obtained at Porthtowan is presented.

# Chapter 4

# Video-based depth estimation in a Macro-Tidal environment

*This chapter is based on Bergsma et al. (2014) and Bergsma et al. (2016)*

## 4.1 Introduction

In this chapter video-based depth estimation as described in Section 3.4.1 is applied to the video camera system at Porthtowan. Porthtowan is the first site with a macro-tidal regime in combination with a highly energetic wave climate where this depth estimation technique is applied. The aim of this Chapter is to analyse the use of multiple cameras in a cBathy domain, assess whether the large tidal range has an effect on the accuracy and present solutions where required.

### 4.1.1 Environmental conditions

Here, depth estimates are assessed on their accuracy compared to a measured bathymetry survey. In particular one representative bathymetry measurement is used throughout the Chapter: the bathymetry obtained on 10 April 2014. Sub-tidal bathymetry surveys at the North coast of Cornwall mostly happen during neap tides considering the high tide around mid-day and associated surveying time-frame. The accuracy analysis is extended to the next spring tide [17 April 2014] in order to assess the effect of a macro-tidal regime. Here, the assumption is made that limited morphological change took place between the neap tidal measurement and the next

spring tide. This seems valid considering the limited maximum wave height of approximately 2 m that occurred during this period [2 m is in the calmer segments of incident wave height at Porthtowan]. The environmental conditions during the survey and for the next spring tide are presented in Table 4.1.

| Dates | $TR_{max}$ [m] | Hs [m] | Tp [sec] | Dir [°] |
|---|---|---|---|---|
| **10 April 2014** | 2.78 | 1.16 | 10.51 | 278.4 |
| 17 April 2014 | 6.03 | 0.52 | 10.38 | 278.9 |

Table 4.1: Tide range and day-average wave conditions during **surveys** and estimates

Table 4.1 shows that the tidal range [TR] during the bathymetry measurement is around 2.8 m and increases significantly to approximately 6 m during the next spring tide. and that the wave height is halved from the 10th of April to the 17th. The wave period and wave direction are relatively unchanged between the two dates. Holman et al. (2013) showed that the wave height has a strong effect on the accuracy of the cBathy estimates. The accuracy of the depth estimates during mild wave conditions is typically distinguishably better compared to depth estimates during more energetic wave conditions. Without knowing the impact of the larger tidal elevation one would therefore expect that the estimate during the 17th of April would be the more accurate of the two.

## 4.2 Using multiple cameras in a cBathy domain

As mentioned in Section 2.2.2, on camera boundaries, issues occur. cBathy requires a time series of pixel intensities and uses a subset of pixels containing pixels from multiple cameras on the camera boundary. As a result, cBathy estimates are particularly inaccurate on the camera boundaries due to two main issues: 1) the combination of pixels from different cameras on the camera boundary in a pixel subset and 2) every slight movement in cameras creates a gap between the different cameras on the camera boundaries. Here we present two corresponding solutions, namely a camera boundary solution to overcome 1) and an adaptive pixel intensity collection scheme to resolve for camera movements.

### 4.2.1 Camera boundary issue

Stack collection dataset are a set of time varying pixel intensities on (mostly) a regular grid in the real world. The Argus collection scheme initiation routines are set in such a way that there is no overlap between the cameras. There is, however, a hard boundary between pixels from different cameras. Slight timing and pixel intensity differences between cameras exists and these can play a crucial role in the cBathy analysis. The timing difference between cameras can cause a 'lag' between the observed phase per camera over the analysis tile. However, with the current video-system set-up no clear differences (meaning $\geq 1$ second) in time is found. Pixel intensities are normalised in the preparation phase of cBathy in order to eliminate the effect of a general difference in pixel intensities between multiple cameras. The normalisation does not affect the further analysis since the cBathy routines are only interested in the phase information. Nevertheless, discrepancies in depth estimation are commonly observed at Porthtowan, as indicated in Figure 4.1, which shows Kalman filtered results over one single day with the red line indicating the camera boundary between cameras 2 and 3. On the camera boundary between cameras 2 and 3, the estimated depth is clearly deeper in a fashion which is highly unlikely to be an accurate representative of reality.

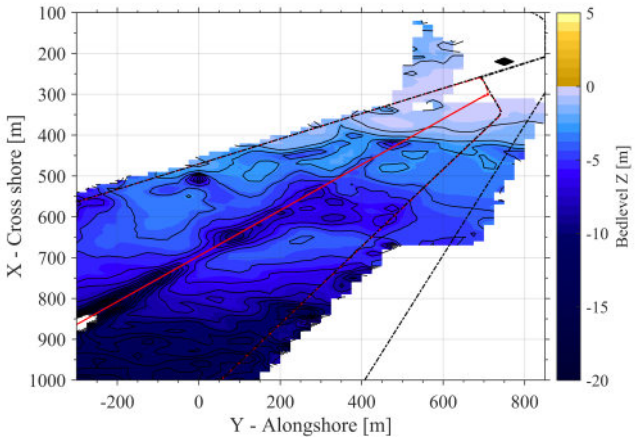


Figure 4.1: Estimated depths on an arbitrary day with the camera boundaries(lines)

The magnitude of the bias on the camera boundaries varies under different conditions. Although the bias varies in magnitude, the depth is consistently overestimated on the camera boundaries as shown in Figure 4.2a,b which shows the final, single estimate (4.2a) and the Kalman-filtered(4.2b), depth estimation. For individual estimates (the whole domain at a single point in time) this camera boundary effect can be rather large O(1m). However, the combination of numerous estimates in the Kalman filter process tends to smooth the effect. This can be

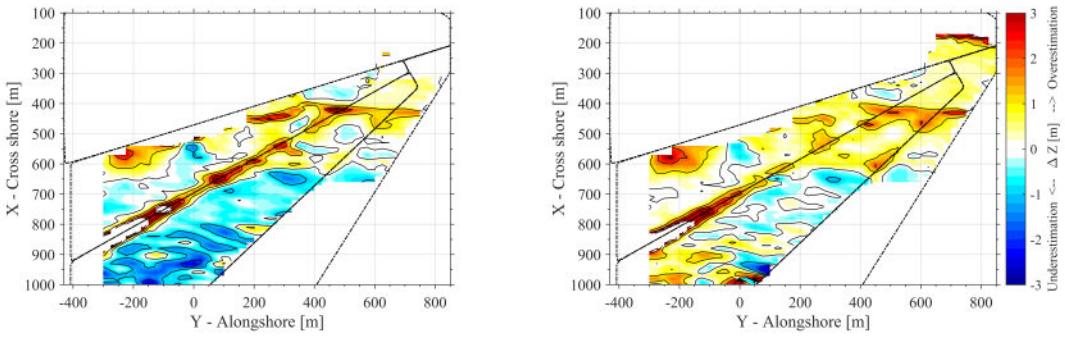


(a) (b)

Figure 4.2: Difference between the survey (10 April 2014) and estimates (9 april 2014). (a) represents the difference between the survey and a single estimate (18:00) and (b) is the difference between the survey and the daily Kalman filtered result. The black lines represent the camera boundaries.

observed in Figure 4.2b, in which most of the domain experiences an underestimation but over most of the camera boundaries an overestimation is visible. As the distance from the camera system increases, the impact of the camera boundary issue increases.

Higher inaccuracies around the camera boundaries are identified when cBathy is compared to the surveys (e.g. see Figure 4.2a,b). Such inter-camera differences are found at most of the sites where cBathy is applied [Duck (USA), Egmond aan Zee and the ZandMotor (Netherlands)]. A common work-around is to increase the spatial smoothing by enlarging the sub-sampling domain (Sembiring, pers com). Another approach seeks to derive perfect camera-geometries by adjusting individual camera geometry parameters in order to stitch the camera views perfectly together (Stanley, pers com). However, such approaches may not provide sufficiently accurate resolution or be practical, and so there is not yet a consensus about how to effectively overcome inaccuracies on the camera boundaries.

It is likely that even small errors in camera geometry solutions could lead to a significant difference between the estimated and real-world position of pixels. Such differences would result in a mismatch between the estimated phases across the camera boundary. Where the sub-sampling domain solely contains pixels from a single camera, depth is estimated independently from this phase shift, meaning that only wave number $k$ and wave angle $\alpha$ are used from (3.2). However, on the camera boundary, where the sub-sampling domain contains pixels from multiple cameras, the fitting procedure of a single wave phase is unable to incorporate a sudden apparent shift in the phase over the sub-samples. Nevertheless, the fitting procedure will seek to find the best fitting solution which in most cases means that the wave angle is increased. When the wave

angle is larger, the estimated wavelength is larger and so the resulting wave number $k$ is smaller than it should be. Using this underestimated wave number in the linear dispersion relation then leads to an overestimation of the depth.

A new and effective solution to overcome this issue is presented here. If the sub-sampling domain contains pixels from multiple cameras the processing system automatically splits the depth estimation procedure into separate but parallel processes in which only pixels from single cameras are used. In this way any potential difference in phase is removed (3.2) as intended and only the wave number and wave angle are used. However, with this method, two wave numbers and two wave angles are found for the sub-sampling domain while only one depth estimate is desired. To counter this, the two separate depth estimates are combined through a weighted average based on the location of their centre of mass relative to the required location of the depth estimate. An accuracy measure is not incorporated in the weighting as the normal quality control within the cBathy routines determines whether a depth estimate is reliable or not. Figure 4.3 illustrates the significant improvement that is achieved when the camera boundary solution is applied. Figure 4.3a represents the bathymetry estimation without the camera solution. A clear overestimation of the depth on the camera boundaries is found between cameras 2 and 3. Figure 4.3b shows a depth estimation with the camera boundary solution implemented. Improved depth estimations on the camera boundaries are the result, and the camera boundary issue is no longer apparent.

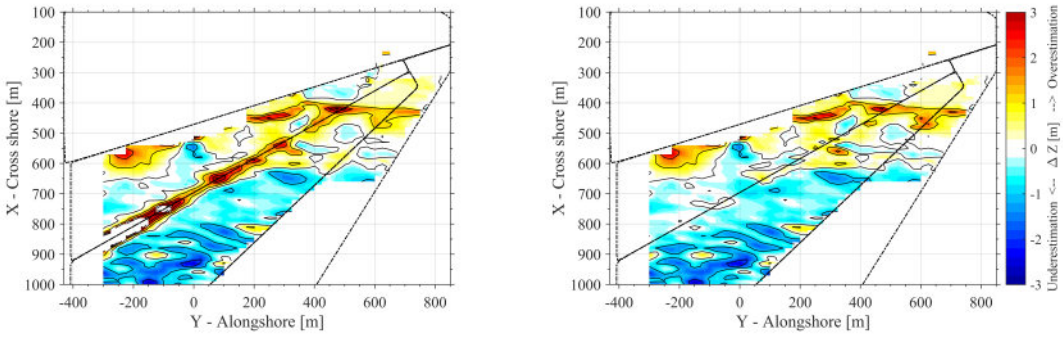


(a) (b)

Figure 4.3: Difference between the survey (10 April 2014) and estimates (9 April 2014). (a) represents the difference between the survey and a single estimate (18:00) without the solution and (b) shows the difference between the survey and the same single estimate (18:00) with the camera boundary solution. The black lines represent the camera boundaries.

### 4.2.2 Camera movement and adaptive collection scheme

Cameras move. Rotation/change in orientation of the camera, albeit small, happens regularly when the cameras are out in the open and exposed to the elements. Minor rotations O(0.1 deg) have an effect on the exact pixel locations over a long distance in the far edge of the camera domain. In addition, if the cameras move away from each other a gap between the cameras appears. As a result, the depth estimation is less accurate and there is a higher likelihood of patchy depth estimation.

A gap between the camera does not have to exist since the full camera footprints have an overlap, shown in Figure 4.4a. Here, an adaptive collection scheme is presented to overcome the gap issue in case of camera movement. This modified collection scheme collects pixels from all cameras over the whole footprint of the camera but still on a pre-defined regular grid. Figure 4.4a,b show the overlap of the cameras. The renewed collection scheme can account for small changes [O(1 deg)] in camera orientation since an overlap between cameras is allowed. As mentioned above, the depth estimation cannot cope easily with pixel intensities from multiple cameras at similar geographical locations. The spatial distribution of the wave phases becomes noisy despite the pixel normalisation. A solution is found by re-initiating a camera boundary between two cameras of equal importance. Also, a user-defined hierarchy is introduced as an input parameter to discard a certain camera if there is a large area of overlap, not necessarily on camera boundaries, for example cameras 4 and 2 in Figure 4.4a.

#### Traditional pixel collection

Pixel intensity time-series are collected without overlap of pixel positions between the cameras as mentioned in the section 4.2.1. Geographical pixel locations and selection of pixels are determined when data collection is initially scheduled. The pixel locations and selection is based on a fixed reference level [mostly Z = 0]. Pixels that are closest to the requested location on a pre-defined regular grid are selected. If there is overlap between two or more cameras there is a hierarchy in camera importance and thus which pixel from which camera is selected. Since in the traditional collection scheme there is no overlap between the cameras every slight change in orientation of the cameras creates a gap between the camera footprints.

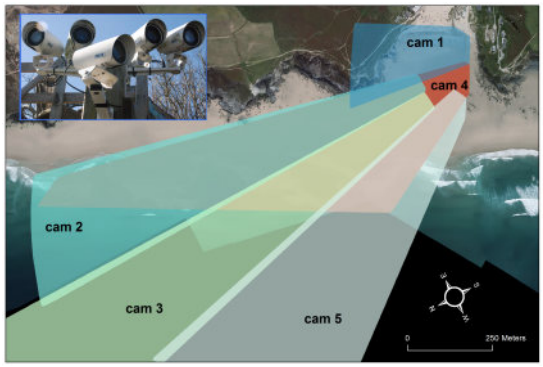


(a)

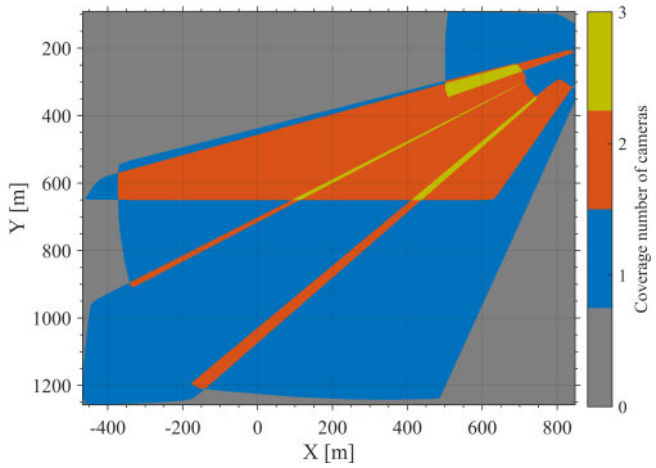


(b)

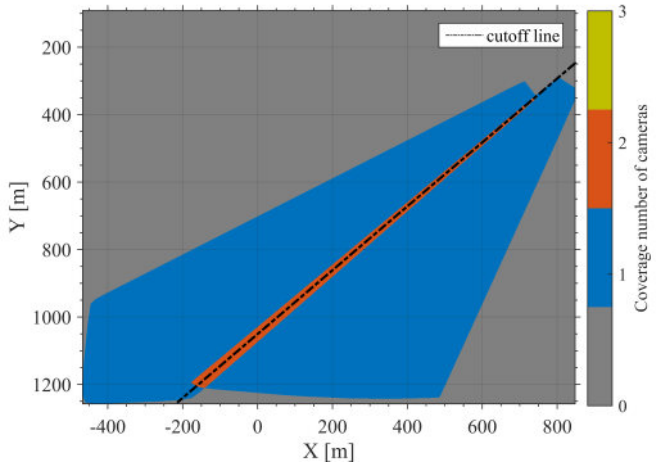


(c)

Figure 4.4: Adjustment of the camera footprint after modified data collection scheme. a) overview of the camera footprint, b) Coverage number of cameras over the whole domain c) re-initiation of a camera boundary between to equally important cameras

### Adaptive collection scheme

Considering that pixel intensities over the whole footprint are collected (so with overlap between cameras), incorporation of the rotation and recalculation of the actual positions should be done on a collection by collection basis. The camera overlap should be removed after the pixel positions are recalculated to include the rotation of the camera. If a rotation occurred, geometries have to be recalculated in order to know the new position of the pixels. For this recalculation of geometries one needs to know Ground Control Points (GCPs) in the field so that pixels can be related to real-world coordinates. Going to the field to collect new GCPs would be labour intensive and expensive. A tool was developed in the past so that fixed known Ground Control Points in the image were used to recalculate the geometry (autoGeom). The process of recalculating the geometries could be done automatically if a template for the specific camera is known. However, this automatic geometry correction tool is only applicable if you have fixed and easily identifiable points in the camera's field of view. Most of the cameras at Porthtowan have cliffs in the image that are fixed and could potentially be used as fixed GCP points. The cliffs seem to be a perfect template but difficulties have been found to get accurate reference points on the cliffs. This can be explained by the fact that the surface of the cliffs is rough, lighting differs substantially from time to time, and an exact point is hard to pick and hard to measure. Alternatively, if pixel data is collected over the whole camera, periodical new Ground-Control-Points should be collected every inter-tidal beach survey so that the geometry can be assessed and if required [as the accuracy diminished too much] recalculated.

### Pixel selection overlapping collection

The camera footprints are readjusted and joined together when the pixel locations are updated based on the latest geometry. Some parts of the pixel intensity dataset are discarded in this process. The main idea here is that the footprint resolution of the camera determines which camera to use. This is shown here though a practical example at Porthtowan but the principle is applicable at any video camera system. Figure 4.4b shows the camera coverage per camera over the whole domain. Some parts have coverage of 2 or 3 cameras but most of the domain is covered by just one video camera. The introduced hierarchy is based on the type of lens per camera. Camera 1 and 4 have wide-angle lenses while camera 2, 3, 5 have smaller angle lenses. In general, higher resolution (the smaller the lens angles the higher the resolution) results in better, more accurate, depth estimation. Cameras 2, 3 and 5 have equal importance but are higher in hierarchy than camera 1 and 4. Also camera 1 and 4 are considered of equal importance. Therefore, where camera 4 coincides with cameras 2, 3 or 5, pixel intensity data of camera four

is discarded. Pixel intensity data from camera two has priority over pixel data from camera 1, therefore if the two coexist in the same domain pixels from camera 1 will be removed. After the elimination of overlap between the wide and smaller angle cameras, parts with double coverage only exist on the camera boundaries between cameras 2, 3 and 5 and cameras 1 and 4.

In the absence of a preference for a certain camera due to the comparable resolution of the cameras, re-initiation of the camera boundaries requires an alternative approach. Figure 4.4c shows two overlapping camera domains, in this case camera 3 and 5. The orange area in Figure 4.4c represents the part where the two cameras both give pixel intensity data. Over this orange stretch an artificial camera boundary is created by computing the linear regression of solely the orange part, represented by the black dashed "cut-off" line in Figure 4.4c. This line is added to the convex envelope of the camera footprint to crop the footprint itself.

## 4.3 Performance in a macro-tidal environment

### 4.3.1 cBathy in a macro-tidal environment

A bathymetry is estimated for all available hourly stack collections collected during daylight using the unmodified version of cBathy as presented in Holman et al. (2013). These hourly bathymetries (in the order of 12 per day around 10th of April) are combined into one bathymetry for the whole day through the Kalman filter. These filtered bathymetries are subsequently used for comparison with the bathymetric survey. Figure 4.5a shows the bathymetry estimates for the 10th of April (neap tide and survey day), and results for the 17th of April (spring tide) are presented in Figure 4.5b. The coast is in the upper part of the figures and offshore corresponds to the higher values along the X-axis (as Figure 3.8). Similar features at corresponding locations are observed in the bathymetric survey (Figure 3.8) and the estimate on the survey day (Figure 4.5a,b), for example the sub-tidal bar at approximately 700 m cross shore position in the survey can also be found in the depth estimate and the trough at the onshore side of the sub-tidal bar shows a similar shape. In contrast to this performance are the estimates during the next spring tide (17th of April). The shape of a bar in both estimates is recognisable but it seems that the bar shape is more smeared out in the cross shore direction over the complete alongshore domain for the spring tide estimate.

The difference between the bathymetry survey which was collected on 10 April 2014 and the cBathy depth estimates calculated for 10 April 2014 and 17 April 2014 are presented in Figures 4.5c and 4.5d respectively. The $17^{th}$ represents spring tide conditions. Although only a single

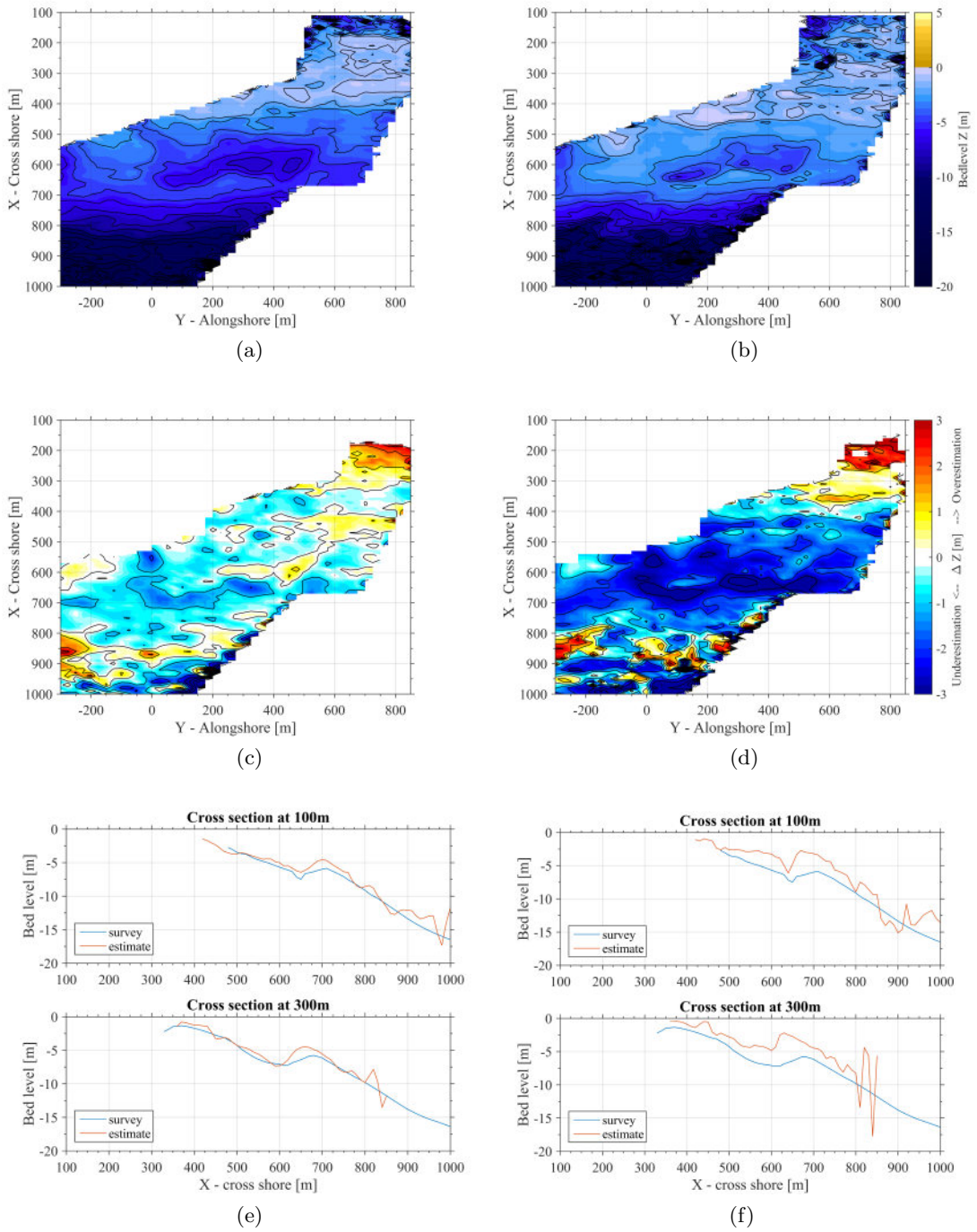


Figure 4.5: On the left side respectively the bathymetry estimate on the 10th of April 2014 (a), the difference to the survey (c) and two cross sections (e) (at 100m and 300m) are shown. On the right side respectively the bathymetry estimate (b), the difference to the survey (d) and two cross sections (f) (at 100m and 300m) on 17 April 2014 are presented.

realisation is presented here, a considerable difference in accuracy exists for the neap and spring tide depth estimation. Over most of the domain values of ±3 m are found during the spring tidal depth estimate while for the neap tidal depth estimate the difference is more in the order of ±1.5 m. Both difference plots show that cBathy underestimates the depth in most of the domain except for the shallowest parts of the domain. Holman et al. (2013) relates this overestimation of depth in shallow water to wave non-linearity due to breaking and hence poor correspondence with the linear dispersion relation in the surf zones. Tests including non-linear models have been carried out (Rutten 2014) but significant improvements in estimating the depth in the shallower waters have not yet been achieved. Wave-induced currents due to wave breaking are a recognised source of error in the surf zone since the linear dispersion relation without currents is applied. Furthermore, Tissier et al. (2015) showed that the short-wave celerity depends largely on infragravity modulations (infragravity wave height and induced velocity) in the surf zone. However, depth estimations are found not to be significantly more accurate when these infragravity modulations are accounted for. Closer to shore, when the waves break, the more bore-like wave motion shows increased propagation speeds of around $c_{bore} \propto 1.3\sqrt{gh}$ (Svendsen et al. 1979, Stive 1984). cBathy observes a rather coherent and relatively fast moving structure, this results in significant overestimation of the depth. Also, one can argue that the inter-tidal zone does not experience as much wet-time as the deeper areas. This means that the final estimates using the Kalman filter will be constructed with less depth estimates.

Two representative cross shore profiles, at respectively 100 m and 300 m alongshore, are presented for both dates in Figure 4.5e,f. The estimate during neap tide on the 10th of April (Figure 4.5e) shows a significant underestimation of the depth over the bar (at 700 m crossshore) in both cross sections (100 and 300 m). An underestimation of the depth is also observed over the sand bar at Duck, NC (Holman et al. 2013). However, the sandbar at Duck is smaller and less pronounced than the sand bar at Porthtowan. Similar ground truth tests have been carried out at Egmond aan Zee in the Netherlands (Sembiring, pers. comm.). The comparison between a survey and cBathy estimates at Egmond shows a similar pattern to those from Porthtowan - an underestimation of the depth over the sand bar followed by an overestimation of the depth at the bar trough. Figure 4.5f shows the cross section during the next spring tide. The cross sections for the spring tidal estimate show that most of the domain experiences a significant underestimation of the depth. However, features are in approximately the right places but with a significant vertical offset. Differences between the survey and estimates up to 4.5 m can be found.

### 4.3.2 Accuracy assessment

Figure 4.5 qualitatively shows that the depth estimation during spring tide is rather poor. Here, a more quantitative approach using basic statistics is elaborated. In Figure 4.6a,b estimates are plotted against the surveyed depth at identical locations. If a perfect agreement between the estimate and survey occurs the data point will be on the blue line (diagonal). Everything above the blue line means underestimation of the depth and values below the line of perfect agreement represent overestimation of the depth. The overestimation in the shallowest areas of the domain, found in Figure 4.5, can be seen in Figure 4.6a,b. Figure 4.6a,b shows for both estimates a rapid accuracy decay between 0 and -10 m depth as the data points move further away from the blue line. For estimates during neap tide (4.6a) most accurate depth estimations are achieved between 10 and 0 m water depth. The spring tidal estimates perform with a similar tendency but with an offset underestimation. In deeper waters the spreading of over and under estimation is considerably larger.

For datasets in general, $R^2$ values (a coefficient of determination) can be calculated and supply an indication of how well the dataset follows a statistical model (linear regression in this case). A higher $R^2$ value means better correspondence to the linear fit, less spreading around the linear fit. The $R^2$ values found here, presented in table 4.2, are respectively 0.85 for the neap tide estimate and 0.77 spring tide estimate over the whole domain. This means that the $R^2$ reduced by almost 10% between the neap and spring tidal depth estimates.

In an optimal estimate, the distribution of errors (Figure 4.6c,d) would be expected to display a narrow banded normal distribution [minimising the standard deviation ($\sigma$)] and a mean error around zero. A narrow banded normal distribution indicates that minimised random errors. For the neap tidal estimates, a nicely normal distributed error distribution is found, with a $\sigma$ of 0.85 m. The mean error (red line) is slightly towards an overall underestimation. Around 35.5% of the estimates is within $\pm$0.4 m of the surveyed depth. In contrast, the spring tide estimates do not show normally distributed errors. The distribution is strongly skewed towards underestimation and the mean error is not close to zero but is around 1.2 m underestimation. The standard deviation of the distribution is almost 1.5 m. Approximately 9.1% of the errors are within $\pm$0.4 m of the surveyed depth. From these plots one can confidently say that the spring tidal estimate is not performing well enough to be useful.

A Root-Mean-Square error was determined over the whole domain and per sub-domain (as indicated in Figure 3.8) for the neap and spring-tide estimates and presented in Table 4.2. Over the whole domain this analysis reveals an RMS-error that is almost doubled during the spring-tide (2.05 m) compared to the neap tide (1.06 m). Around the sub-tidal bar region, the most

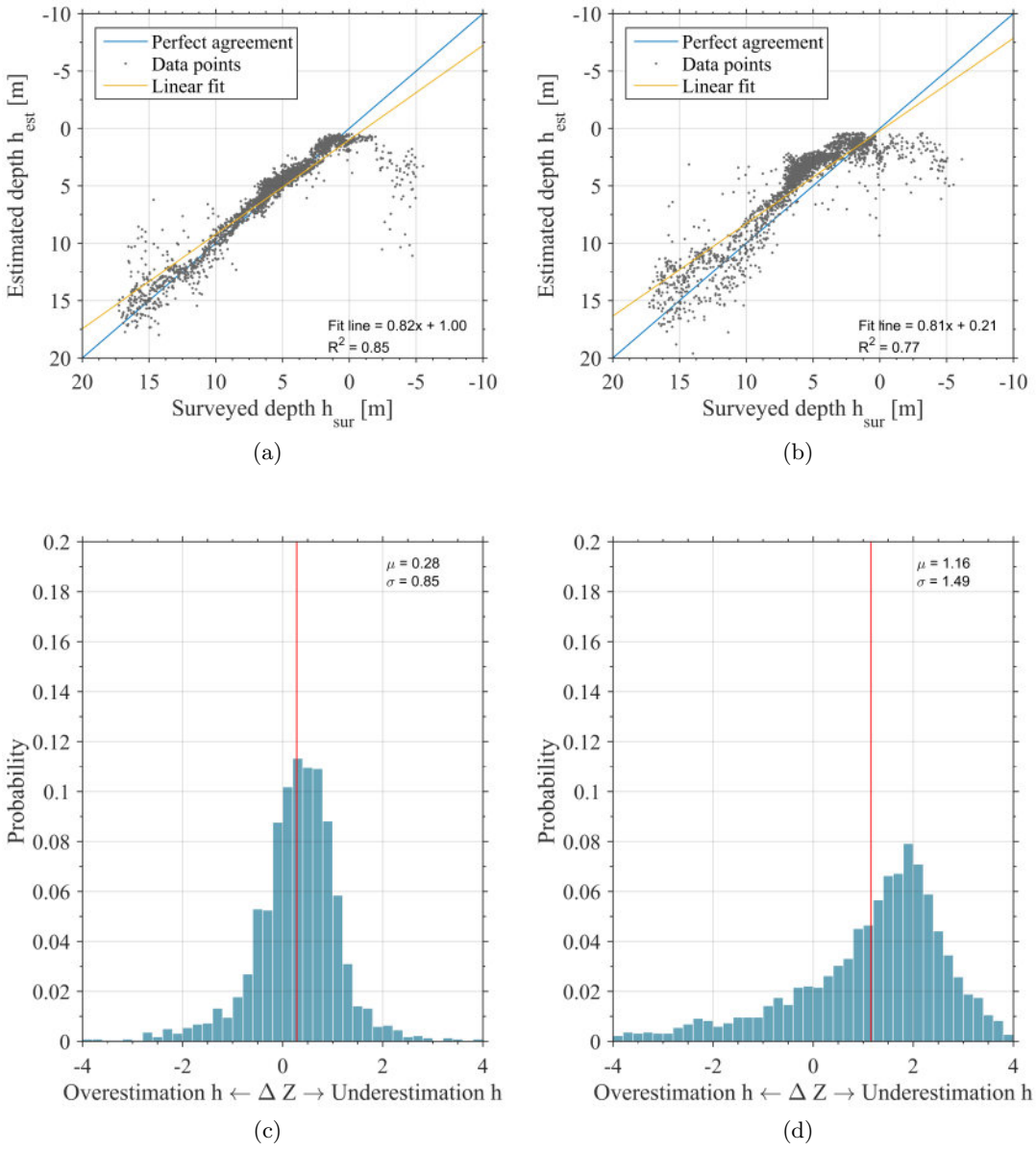


Figure 4.6: a) and b) represent the estimated depth plotted against the surveyed depth for respectively the estimates on the 10th of April 2014 and 17th of April 2014. c) and d) show the corresponding probability distribution for both estimate dates.

accurate estimates (RMS-error of 0.77 m) can be found. However, for the same region during spring tide the RMS error increases to 2.03 m. The dramatic increases in RMS-errors in all the domains suggests that the tide related accuracy is clearly a factor and directly relates to the accuracy of cBathy. Especially taking into account the expected higher accuracy concerning the smaller waves during the spring tide estimates [larger waves = larger bias (Holman et al. 2013)].

| | 10 April 2014 | 17 April 2014 |
|---|---|---|
| $RMSE_{All}$ [m] | 1.06 | 2.05 |
| $RMSE_{IT}$ [m] | 1.15 (350%) | 1.77 (623%) |
| $RMSE_{ST}$ [m] | 1.05 (14%) | 2.12 (36%) |
| $RMSE_{ST\ bar}$ [m] | 0.77 (14%) | 2.03 (39%) |
| $RMSE_{off}$ [m] | 1.84 (13%) | 2.43 (17%) |
| $r^2$ [$m^2$] | 0.84 | 0.77 |
| $\mu_{\Delta Z}$ [m] | 0.28 | 1.16 |
| $\sigma_{\Delta Z}$ [m] | 0.85 | 1.49 |
| $\lvert\Delta Z\rvert < 0.4$ m [%] | 35.54% | 9.16% |

Table 4.2: Accuracy values: Root Mean Square error (RMSE), $R^2$ and the mean error ($\mu$), standard deviation ($\sigma$) for $\Delta Z$ for the neap and spring tide case. The RMS error is divided in the whole domain [All], the inter-tidal area [IT], the sub-tidal area [ST], sub-tidal bar domain [ST bar] and the offshore domain [Off]. For the RMS error the error percentage of the local depth is presented between brackets.

An increase in RMS-error with tidal range is not only found during the test case above but it is observed consistently. Although many additional factors can play a role (for example, wave height and water on the camera lens), a systematic increase of the RMS-error over the whole domain with tidal range ($TR$) is found at Porthtowan as indicated in Figure 4.7.

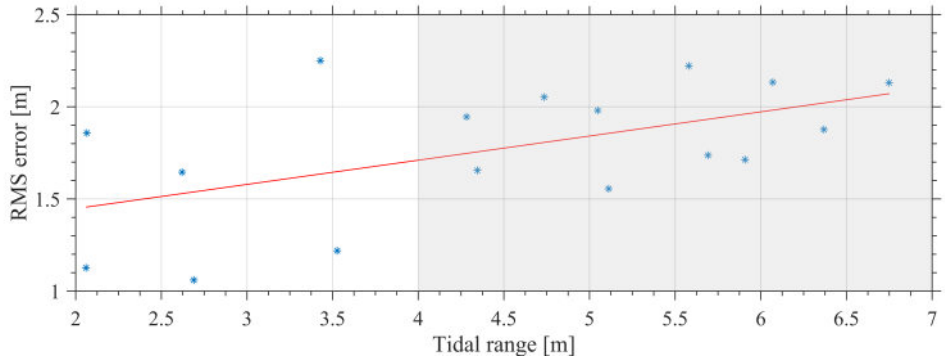


Figure 4.7: RMS error compared to wave height and tidal range. Red line is represents a linear regression with $r^2 = 0.295$ and is significant ($p = 0.024$) at the 95% confidence interval. Grey patch indicates the domain of the macro tidal range ($TR > 4$).

For the lower tidal ranges (2 m$< TR <$ 4 m) a large spread of the RMS-error is found. One

of the reasons for this is that wave heights up to 4 m were measured in the days before the survey. Larger waves show, in general, less accurate results with cBathy (Holman et al. 2013). For the larger tidal ranges ($TR > 4$ m) the wave climate was relatively calm which results in a smaller range in RMS-error. Taking the context into account a slight trend of an increasing bias with increasing tidal range is observed.

## 4.4 Floating pixel modification

A significant variation in performance of cBathy with the tidal range is a consequence of the limited inclusion of tidal elevation in the code which results in fixed geographical pixel locations. The only use of tidal elevation is to transform depth estimates to an absolute reference level. Geographical pixel locations are determined only once when data collection is initially scheduled. However, in contrast to the artificially fixed reference level, the true sea surface elevation and hence the set of geographical pixel locations, changes as the water level rises and lowers with the tide. A set of pixels moves towards the camera system, and at the same time the spatial footprint of the set contracts, during a rising tide, while during a falling tide the opposite occurs, with pixels moving further from the camera and relative expansion of the pixel set footprint. Figure 4.8a presents this process schematically, where the orange squares represent the pixel domain in the version of cBathy (Holman et al. 2013) and the blue and green squares represent the true pixel position in the real world for respectively low and high tide. At Porthtowan pixel displacements up to 130 m are found from mid to high tide during the largest spring tide, as indicated in Figure 4.8b. Incorrect pixel positions result in a shorter sensed wavelength than in reality at low tide which leads to an overestimation of the wave number [right-hand side of (3.2)] and thus an underestimation of the depth, and vice versa for high tide.

Figure 4.8b shows as well that pixels further away from the camera system move to greater extent. The larger pixel displacement in the outer extent of the domain is the result of greater ratio camera height and distance from the camera. The pixel shifting is not solely dependent on the tidal elevation but, rather, is a function of tidal elevation, vertical position of the camera system and distance to the camera. The maximum shift as a percentage of the distance between pixel and camera system can be found with the ratio $TR_{max}/z_{cam}$ where $TR_{max}$ is the maximum tidal range and $z_{cam}$ is the vertical position of the camera system. The instantaneous pixel shifting can be calculated using (4.1).

$$(dx(t), dy(t)) = \frac{\eta_{tide}(t)}{z_{cam}} \left(x_{ref} - x_{cam}, y_{ref} - y_{cam}\right) \tag{4.1}$$

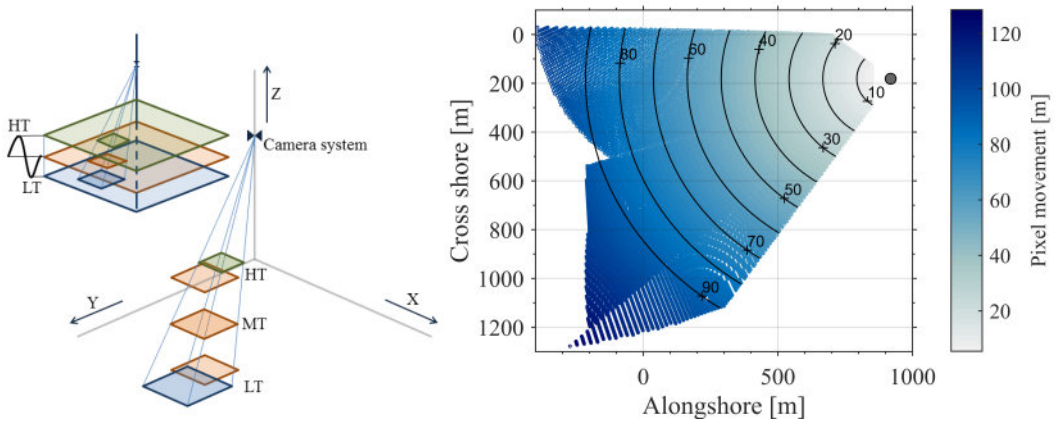


Figure 4.8: a) Schematic representation of the pixel movement and contraction/expansion of a patch of pixels. b) Horizontal pixel movement during largest spring tide at Porthtowan. Grey dot indicates the position of the camera system

where $dx$, $dy$ represent the shift in respectively $x$ and $y$ direction, $\eta_{tide}$ relates to the tidal elevation, $z_{cam}$ is the camera height and the subscripts ref and cam refer respectively to the reference and camera position for x and y. For Porthtowan, a ratio of 15.9% is found using $z_{cam}$ = 44 m and a $TR_{max}$ = 7 m. This means that with a camera range of around 1880 m in the far end of the domain the pixels move around 300 m back and forth between low and high spring tide. The horizontal shift of the pixel location is +/- half the total shift since the excursion that should be accounted for starts at the initial pixel location obtained using the vertical reference level, as presented in Figure 4.8b. Although shallow water inaccuracies are found and partially associated with the poor relation between the actual wave physics and the linear dispersion relation in the section above, an improvement in particularly the shallowest parts of the domain should be achieved with the inclusion of the correct pixel positions. The displacement of the pixel is largest during the extrema of the tidal range, i.e. at low and high tide. Notably, the shallowest parts of the near-shore zone only experience the high tide conditions.

To overcome this issue an additional inclusion of the tide in the code was implemented following (4.1). For every stack collection the pixel location is recalculated according to the tidal elevation.

## 4.5 Performance with modifications

Bathymetry estimates for neap (left) and spring (right) tide including the floating pixels and camera boundary solution are presented in Figure 4.9a-d. Unlike the estimates with the original version of cBathy (Figure 4.5), estimates with the modifications show corresponding bar features in both spring and neap tidal estimates. Features like a rip channel (X = 600 m, Y = 0 m) and the sub-tidal bar are better resolved compared to the original version which indicates a clear improvement in performance. Inaccurate depth estimates are still found in the very shallow parts of the domain but as mentioned before this is likely due to the invalidity of the linear dispersion relation for that area.

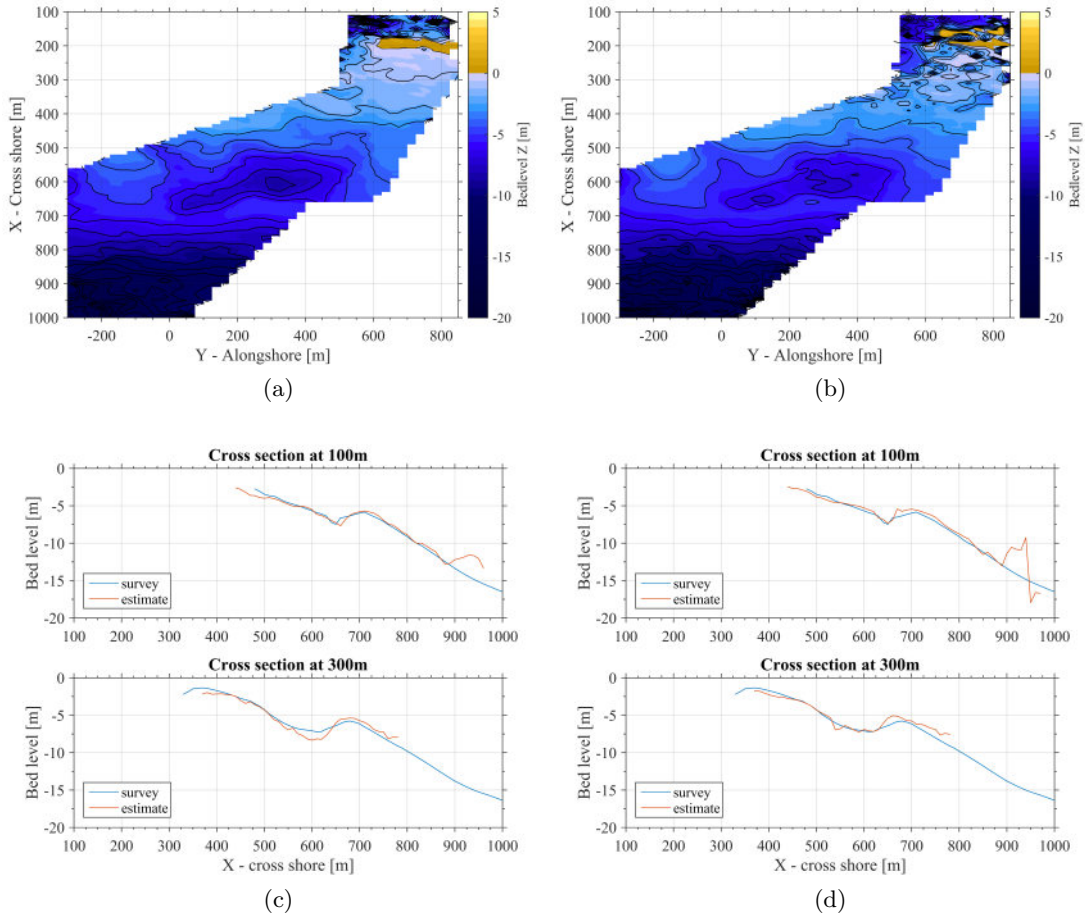


Figure 4.9: On the left panel respectively a renewed bathymetry estimate using the modifications on the 10th of April 2014 (a) and two cross sections (c) at X=100 meters and X=300 meters. On the right is the renewed bathymetry estimate (b) on 17 April 2014 and the corresponding cross sections (d) at X=100 and X=300

### 4.5.1 Improved accuracy

Implementation of the floating pixel solution should improve and remove the tidal dependency of the accuracy. Another modification, for camera boundaries, is explained and applied in section 4.2.1. Here, we will therefore discriminate between the effects of solely the floating pixels and a simultaneous application of the floating pixel and the camera boundary solution. Table 4.3 shows the old (orange column) and renewed results; grey column represents the values for the floating pixels and the blue column shows the results for the floating pixels and camera boundary solution together.

Considering the whole domain, a reduction of 8.5% with exclusively the floating pixel solution is found. If the floating pixel and camera boundary solution (section 4.2.1) are applied simultaneously the RMS error is reduced up to 19%. For the next spring tide, a larger reduction is found with solely the floating pixel (49%). The combination of the floating pixels and the camera boundary solution results in almost 53% reduction of RMS error. The improvement in accuracy was greatest for the sub-tidal bar area shifting from 2.03 m RMS error to 0.49 m. The RMS error as a percentage of the depth reduced in the sub-tidal bar region from 39% to 9%.

The overall RMS error is comparable (between 0.86 and 1.05 m) for all the new configurations. For the sub-tidal region, a significant improvement is reached, the RMS error decreased from 2 m to 50 cm with the modifications. The difference between neap and spring tide depth estimates in the sub-tidal bar domain for the original version is 260%. When both the new camera boundary and floating pixel solutions are implemented simultaneously, the best performance occurs around the sub-tidal bar region (RMS-error of around 50 cm), around 9-10% of the local water depth.

Figures 4.10a, b shows the depth estimates against the depth measurements as above in Figures 4.6a, b for the estimates with the floating pixels and camera boundary solution. Progress is especially visible for the spring tidal estimated in Figure 4.10b if compared to Figure 4.6b. Depth estimates between 10 and 2 m water depth are significantly closer on the line of perfect agreement (blue line). Depth estimation in the inter-tidal zone remains an issue. More depth points are closer to the line of perfect agreement but overestimation of the depths seems more striking (+5 m overestimation). The expected reduced overestimation for the shallowest parts of the domain did not occur and actually deteriorated. No clear explanation has been found to date. Overestimation in the shallowest part of the domain ($< -2$ water depth) is also observed for the neap tide estimates but did not however increase noticeably compared to the unmodified application of cBathy. At the offshore side (depths $> 10$ m) the depth estimates continue to be largely over and underestimated. However, an improvement here is reached for both neap

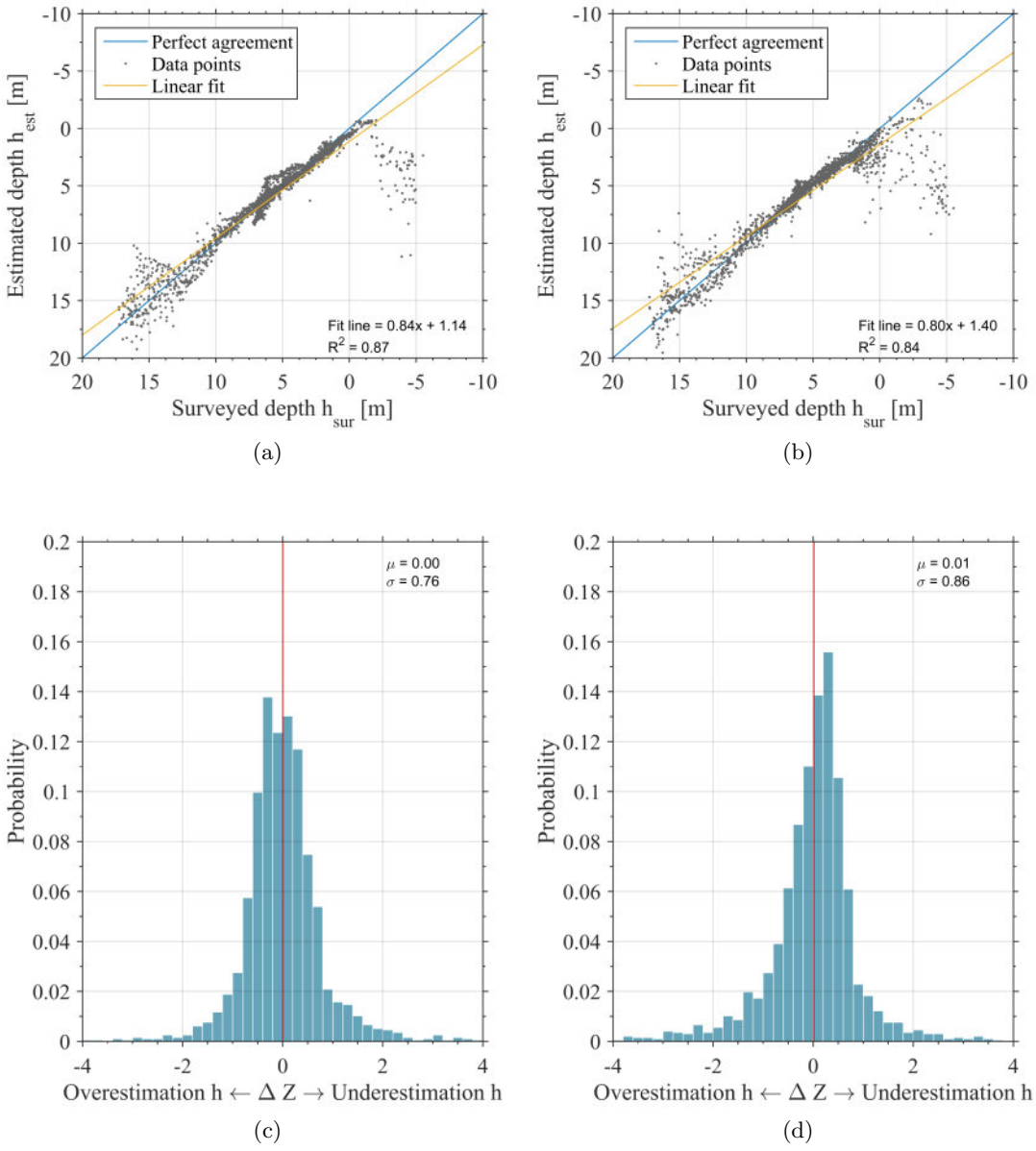


Figure 4.10: a) and b) represent the estimated depth plotted against the surveyed depth for respectively the estimates on the 10th of April 2014 and 17th of April 2014. c) and d) show the corresponding probability distribution for both estimate dates.

| | 10 April 2014 | 17 April 2014 | 10 April 2014 | 17 April 2014 | 10 April 2014 | 17 April 2014 |
|---|---|---|---|---|---|---|
| $RMSE_{All}$ [m] | 1.06 | 2.05 | 0.97 | 1.05 | 0.86 | 0.97 |
| $RMSE_{IT}$ [m] | 1.15 (350%) | 1.77 (623%) | 0.98 (160%) | 1.63 (610%) | 0.99 (160%) | 1.51 (600%) |
| $RMSE_{ST}$ [m] | 1.05 (14%) | 2.12 (36%) | 0.97 (13%) | 0.90 (11%) | 0.83 (10%) | 0.84 (10%) |
| $RMSE_{ST\ bar}$ [m] | 0.77 (14%) | 2.03 (39%) | 0.73 (14%) | 0.59 (10%) | 0.55 (9%) | 0.49 (9%) |
| $RMSE_{Off}$ [m] | 1.84 (13%) | 2.43 (17%) | 1.70 (12%) | 1.74 (12%) | 1.59 (11%) | 1.70 (12%) |
| $R^2$ [$m^2$] | 0.84 | 0.77 | 0.87 | 0.86 | 0.87 | 0.84 |
| $\mu_{\Delta Z}$ [m] | 0.28 | 1.16 | -0.10 | -0.15 | 0.00 | 0.01 |
| $\sigma_{\Delta Z}$ [m] | 0.85 | 1.49 | 0.86 | 0.91 | 0.76 | 0.86 |
| $\lvert\Delta Z\rvert < 0.4$ m [%] | 35.54% | 9.16% | 49.19% | 47.24% | 50.86% | 49.14% |

Table 4.3: Accuracy values: Root Mean Square error (RMSE), $R^2$ and the mean error ($\mu$), standard deviation ($\sigma$) for $\Delta Z$ for the original (orange), floating pixel (gray) and floating pixel with camera boundary solution (blue). The RMS error is divided in the whole domain [All], the inter-tidal area [IT], the sub-tidal area [ST], sub-tidal bar domain [ST bar] and the offshore domain [Off]. For the RMS error the error percentage of the local depth is presented between brackets.

and spring tide. In particular, the number of times that depths are overestimated seems to be decreased while the underestimation is of similar order. For neap and spring tidal estimates one can see the $R^2$ to be of similar order. This means that the difference in predictability between the neap and spring tidal estimates has been narrowed.

Figure 4.10c,d show the error distribution for the floating pixel and camera boundary solution applied simultaneously. A significant improvement of the error distribution is shown for the spring tidal estimates (Figure 4.10d). The strongly skewed error distribution in Figure 4.6d has been improved to the "desired" normal distribution. The standard deviation $\sigma$ is reduced from 1.49 m to 0.86 m. The mean error ($\mu_{\Delta Z}$) is now close to zero for neap and spring tide estimates, as shown in Table 4.3. Interestingly, the overestimation on the camera boundaries becomes noticeable in $\mu_{\Delta Z}$ considering that $\mu_{\Delta Z}$ is negative if only the floating pixel solution is incorporated.

Percentages of estimates within 40 cm of the measured depth [approximate accuracy in the surf zone] are presented in Table 4.3. If the floating pixel solution is applied significant progress is found in these percentages and most certainly the percentages became of similar order, diminishing the tide related effect. For solely the floating pixel modification, the percentage for the neap tidal estimates increased to 49% and for spring tide 47% of the estimates are found within 40 cm of the measured depth. Concurrent application of the camera boundary and floating pixel solution leads to over half the neap tidal depth estimates within the 40 cm of the measured depth. The spring tide estimates reach just over 49% of the estimates within 40 cm of the measured depths.

## 4.6 The effect of the Kalman filter

One of the major additions in Holman et al. (2013) compared to earlier versions is the assimilation of data through a Kalman like filter. Kalman filters are well-known for combining multiple types of input data to find an accurate and updated value more accurate that any of the input datasets. In Holman et al. (2013), the Kalman filter does not combine different types of data but it joins depth estimates for the same locations in time based on an accuracy measure. The accuracy measure in Holman et al. (2013) comes from the fitting as presented in (3.2). A perfect fit between the observed wave pattern and the modelled wave pattern means high accuracy and a Kalman gain close to 1. A poor fit between the observed and modelled wave pattern means less faith in an accurate depth estimate and a lower value for the Kalman gain. The Kalman filter compares the Kalman gain values to the value of the existing estimate to determine if

the new estimate has more faith in accuracy than the existing estimate, as explained in section 3.4.1.

In the section above, a set of daily estimates are joined through the Kalman filter in order to isolate the effects of estimating depths with different tidal ranges. Every daily estimate is a result of approximately 12 estimates over the day. A typical strength of Kalman filters is that the filtered result is more accurate when more data is supplied to the Kalman filter. This suggests that more truthful combined depth estimates will be achieved if the Kalman filter is supplied with all the depth estimations since the start of our data collection (16 October 2013). The results for the neap and spring tidal estimates, in the form of $r^2$ and $\Delta Z$, are shown in Table 4.4. Figure 4.11 shows the results for the spring tidal estimates. Daily Kalman filtered results are depicted in Figure 4.11a,c and long-term Kalman filtered results are shown in Figure 4.11b,d.

| | 10/04/14 | 17/04/14 | 10/04/14 | 17/04/14 |
|---|---|---|---|---|
| $RMSE_{All}$ [m] | 0.86 | 0.97 | 0.63 | 0.61 |
| $RMSE_{IT}$ [m] | 0.99 | 1.51 | 0.76 | 0.81 |
| $RMSE_{ST}$ [m] | 0.83 | 0.84 | 0.61 | 0.56 |
| $RMSE_{ST\ bar}$ [m] | 0.55 | 0.49 | 0.51 | 0.42 |
| $RMSE_{Off}$ [m] | 1.59 | 1.70 | 0.97 | 0.98 |
| $r^2$ [$m^2$] | 0.87 | 0.84 | 0.98 | 0.98 |
| $\mu_{\Delta Z}$ [m] | 0.00 | 0.01 | -0.02 | 0.03 |
| $\sigma_{\Delta Z}$ [m] | 0.76 | 0.86 | 0.63 | 0.61 |
| $\lvert\Delta Z\rvert < 0.4$ m [%] | 50.86% | 49.14% | 59.00% | 56.72% |

Table 4.4: Root mean square errors for all zones and accuracy values: $R^2$ and the mean ($\mu$), standard deviation ($\sigma$) for $\Delta Z$ for daily Kalman filtered depth estimates using the floating pixel and camera boundary solution (blue) and long-term (months) Kalman filtered depth estimates using the floating pixel and camera boundary solution (white).

The results are significantly improved using the Kalman filter over a longer time scale (months). To reiterate, an $R^2$ of 1 shows perfect predictability with the used statistical model (linear regression in this case). Here, $R^2$ values of 0.98 are found for neap and spring tide estimates. Furthermore, the line of perfect agreement has a slope of 1. The slope of the linear fit found for the long-term Kalman filtered results is 0.95. Before, a slope of 0.80 was found for the daily Kalman filtered results. This improvement in slope of the linear fit indicates that with the long-term Kalman filtered results an enhancement in depth estimation over the whole domain is achieved. In addition it means that with a long-term Kalman filter smaller overestimations in the shallowest parts and smaller underestimations in the deepest parts of the domain are achieved.

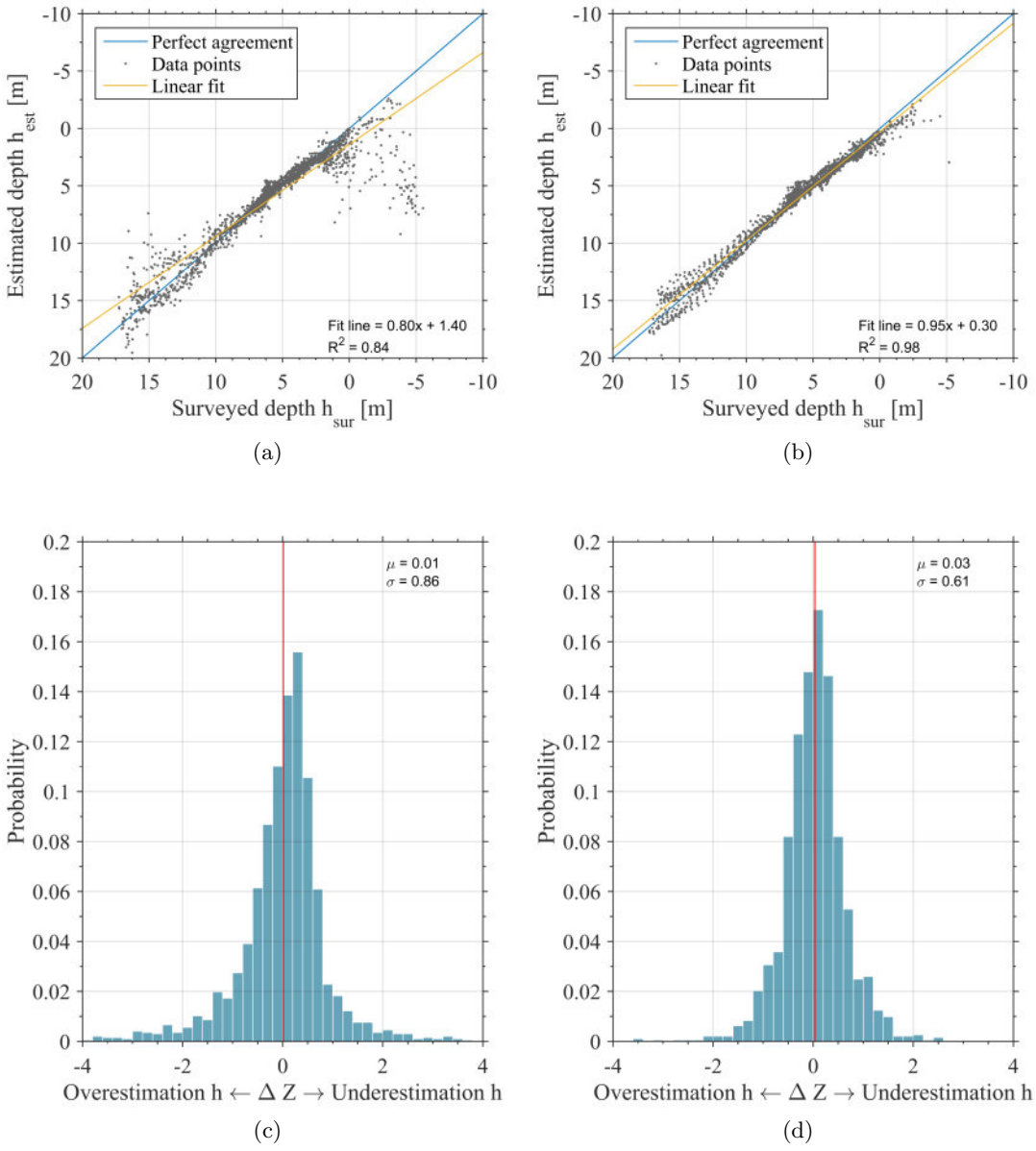


Figure 4.11: a) and b) represent the estimated depth plotted against the surveyed depth for respectively the estimates using a daily Kalman Filter and a long-term Kalman Filter. c) and d) show the corresponding probability distribution for both applications.

The distributions of errors are presented for the spring tidal estimates in Figure 4.11c,d. The distribution of errors continued to be nicely normal distributed for the short and longer-term Kalman filter. Between Figure 4.11c and Figure 4.11d it is apparent that the distribution of errors became slightly narrower. The mean error ($\overline{Z}$) didn't move much in absolute value from 0.01 to 0.03 m. Almost 60% of the neap tidal estimates are within 40 cm of the measured depth and for the spring tidal estimates this value reached over 56%.

### Final derived bathymetry

The modifications lead to a significantly improved depth estimation in situations where the camera is mounted relatively low compared to the tidal range. Figure 4.12 shows data of the final derived bathymetry with the modifications and Kalman filter in comparison to measurements.

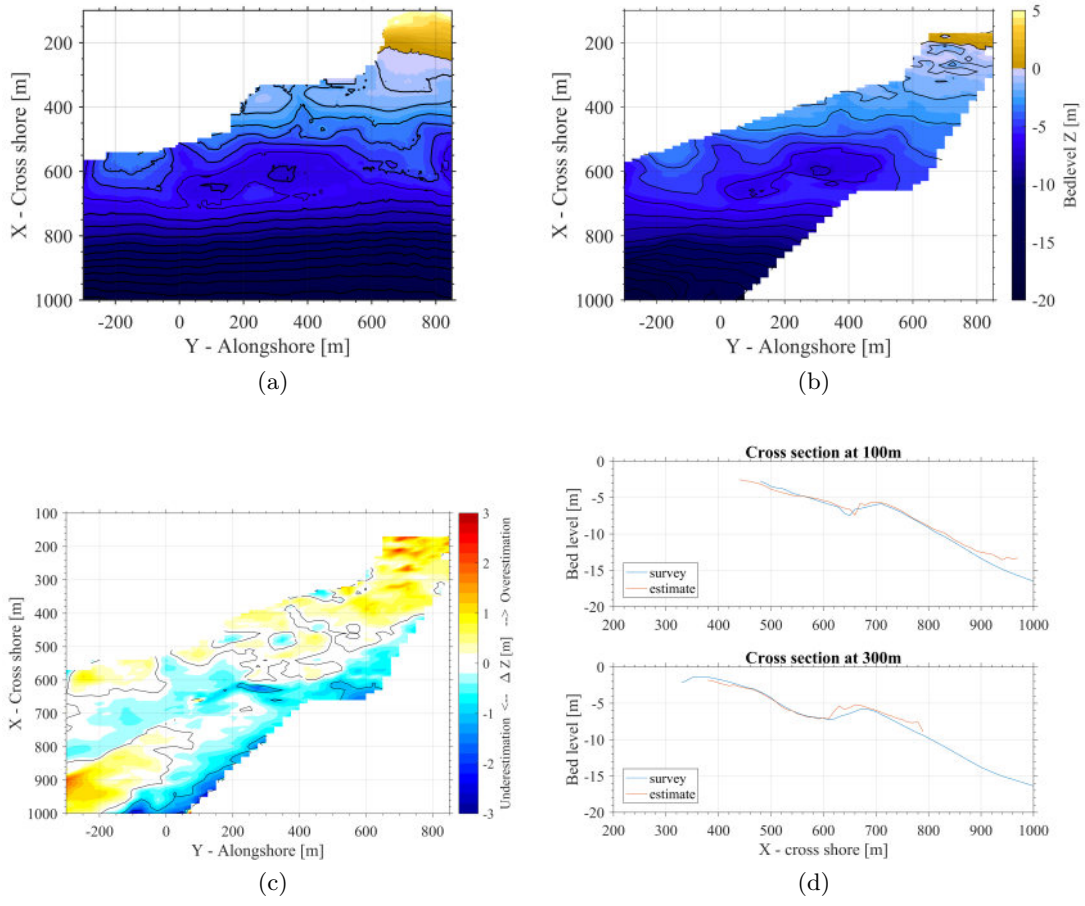


Figure 4.12: The untimate comparision between the measured bathymetry in a) and estimated bathymetry in b) under the largest tidal range conditions at Porthtowan. c) represents the difference over the domain and d) shows cross shore profiles at Y = 100 m and Y = 300 m.

Comparing 4.12a with 4.12b, one can see that sub-tidal bar features (between 400 and 800 m cross shore) qualitatively well represented. Best depth estimates are obtained in the sub-tidal bar domain as shown in Figure 4.12c considering the lightest blue and yellow colours. In the inter-tidal domain overestimation of the depth main occurs most likely due to the validity of the linear dispersion relation. The offshore domain shows large over and under estimations and seems to be related to the camera; overestimations predominantly at the Northern side of the cameras' field of view and under estimations at the Southern side of the cameras' field of view (see Figure 3.9b for camera footprints). Seemingly, small geometrical errors in combination with the large footprint over these relative large distances from the camera makes the depth estimation sensitive.

## 4.7 Discussion

The results, in particular Figure 4.9 and Table 4.3, show a significant improvement using the two modifications compared to the estimates without the modifications. However, the data shown only comprises a single survey campaign and it remains a question whether the accuracy of the depth estimates is consistently ameliorated. Figure 4.13 shows that an improvement in estimating depth is found when the modifications are applied to other arbitrary depth estimations around the time of the survey (Figure 3.8).

Figures 4.13a and 4.13b show the RMS error over the whole domain against tidal range and wave height for the exact same points in time. Figure 4.13c shows the reduction in percentage of the RMS error between cBathy (Holman et al. 2013) (4.13a) and cBathy with both corrections (4.13b). Depths estimated with the original cBathy code at a tidal range larger than 4.5 m seem to coincide with RMS errors larger than 1.5 m. With the inclusion of the floating pixels and the camera boundary solution the same estimates have a RMS error lower than 1.5 m. Figure 4.13c shows that the largest improvement is achieved for the largest tidal ranges (as expected) during relatively calm wave conditions. At maximum, a reduction of 60% in RMS error over the whole domain is reached. The largest reductions in RMS error are found with limited wave heights ($< 1$ m).

The depth estimates shown in Figure 4.13 are representative for the day consisting of a set of daily Kalman-filtered depth estimates (using approximately 12 hourly depth estimates). Depending on the number of light hours per day, a certain amount of hourly depth estimates (maximum 16 hours during the longest day) are combined together for a daily estimate. As mentioned in section 4.6, with more data the Kalman filter achieves significantly more accurate

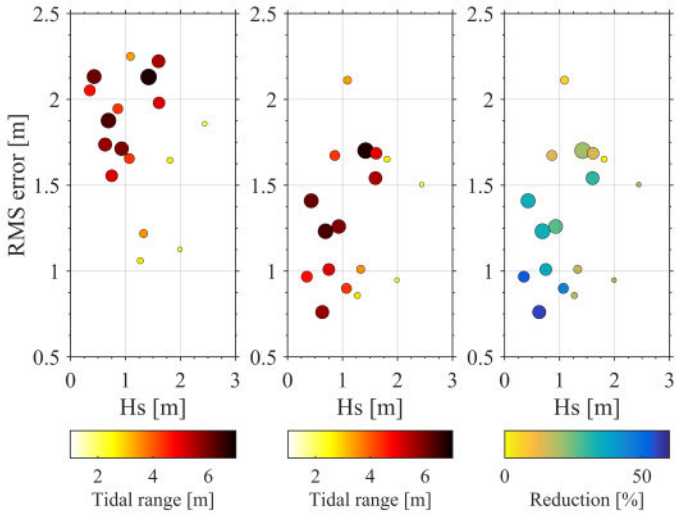


Figure 4.13: RMS error for modified cBathy over the whole domain against wave height and tidal range. a) represent the RMS error for cBathy without all modifications, b) shows the RMS error with the modifications and c) shows the reduction in percentage of the RMS error between the a) and b).

depth estimates. Furthermore, if the Kalman filtering starts with a measured bathymetry it starts from an accurate starting point.

### 4.7.1 Potential effects at other sites

The reduction in bias of the depth estimation related to the floating pixel solution is site specific. (4.1) suggests that tide-related inaccuracies in the cBathy depth estimates are not exclusively occurring at sites with a large tidal range. The vertical angle (ratio between tidal range and vertical camera position) is the key-factor and can potentially cause tide related inaccuracies in micro/meso tidal environments when the camera system is mounted relatively low. Figure 4.14 shows the pixel displacement (presented on logarithmic scale) in relation to tidal range and the ratio between the distance from the camera ($d$) and the camera height ($h$) for a range of sites. The greyed area in Figure 4.14 shows the pixel displacement for all the pixels considered at Porthtowan. The pixels farthest away from the camera experience almost $10^{2.5} = 316$ m displacement.

Pixel displacement information for some other sites where video camera systems are sited but with smaller tidal ranges is also presented in Figure 4.14. The chosen (most 'famous') Argus sites are Duck NC (USA), Palm Beach (Australia) and Egmond aan Zee (The Netherlands) and

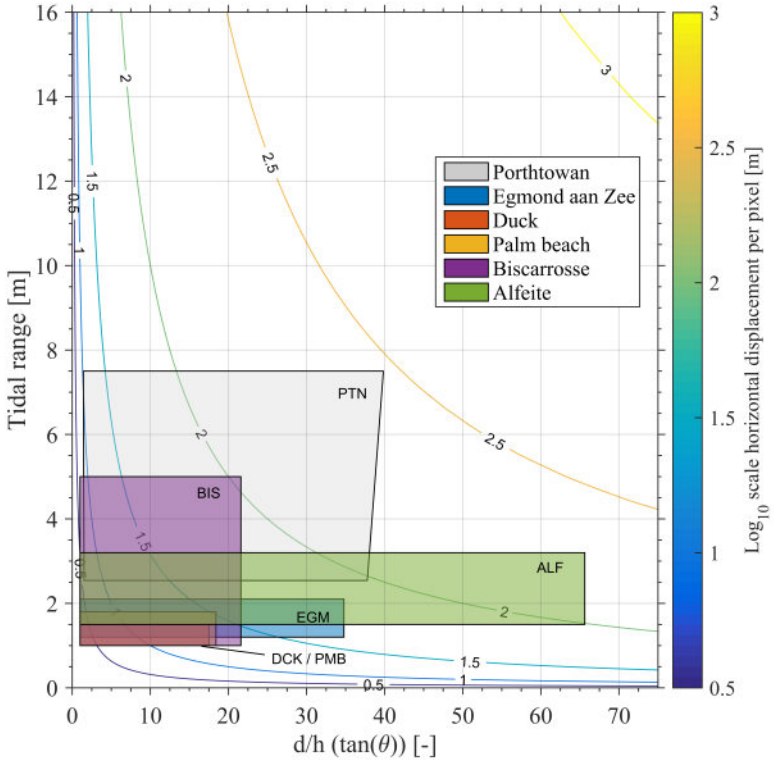


Figure 4.14: Horizontal pixel displacement (log scale) as function of the tidal range and ratio d/h (d = distance from the camera and h = camera height)

non-Argus sites are Biscarrosse (France) (Almar et al. 2008, Sénéchal et al. 2009) and Alfeite (Portugal) (Silva et al. 2009). Although the tidal range at all the sites is significantly lower compared to Porthtowan, the total pixel displacement between low and high tide due to the tidal elevation is up to 80 m in the outer edge of the domain at Egmond aan Zee. If this is not taken into account this displacement would mean that pixels are used to estimate a depth that are not around the point of interest but 40 m further away from the camera (if the vertical reference level is mid-tide).

Figure 4.14 also shows the non-Argus sites Biscarrosse in France and Alfeite in Portugal. The video camera system in Biscarrosse is situated in a meso-macro tidal environment. The camera height and maximum reach demonstrated in Almar et al. (2008), Sénéchal et al. (2009) are respectively 27 m and on the order of 580 m. A maximum pixel movement with the characteristic of the camera system at Biscarrosse is over 100 m. The camera system at Alfeite (Silva et al. 2009), is situated in a meso-tidal environment, maximum spring tidal range up 3.7 m. The range is around 525 m and the camera height in Silva et al. (2009) was set to 8 m. Although the tidal

range is not extreme, large pixel movements (more than 200 m) can be found here due to the low camera position.

### 4.7.2 Relation between wave height and accuracy

Tide related inaccuracies are diminished using the floating pixel solution but a dependency on the wave height is still observed, as in Figure 4.13. With larger wave heights the depth estimates become generally less accurate, this has been observed in Holman et al. (2013). If cBathy is applied under different wave conditions (also during storms) a feeling for the accuracy is required to quantify the faith in the estimates for further analysis. However, one of the issues is that bathymetries can only be accurately measured in the case of low wave height conditions. Errors and accuracy values found for the low wave heights have to be extrapolated to values corresponding with larger wave heights. Here, the accuracy values are placed in perspective relative to the corresponding measured wave height. Linear regressions found for the lower wave heights are extrapolated initially and presented in Figure 4.15.

Figure 4.15a is a similar plot Figure 6 shown in Holman et al. (2013) and shows the RMS error versus significant wave height. Here, the tendency of larger errors with larger wave heights is also found. The RMS error is quite scattered ($r^2$ is 0.31) around the trend line (blue line). Following linear extrapolation, the RMS error rises 0.13 m for every metre increase in significant wave height. The mean error over the whole cBathy domain at Porthtowan ($\mu_Z$ in Figure 4.15b) represents the mean bias and can be (set aside zero) negative (overestimation of depth) or positive (underestimation of depth). The data during the small to moderate wave conditions shows an inclining trend (16 cm shift per 1 m increase in wave height) of overestimation of the depth when the wave height increases. As shown for the RMS error also here the scatter is large around the linear fit ($R^2$ of 0.35).

A measure for the standard deviation is required in order to estimate the width of the distribution under the assumption that the errors are actually normally distributed around a mean. Figure 4.15c shows the inclination in standard deviation as the wave height goes up. For every metre increase in wave height the standard deviation increases by 10 cm. The final accuracy measure demonstrated in Figure 4.15d is the percentage of depth estimates within 40 cm accuracy. Figure 4.15d shows the decline in percentage in correspondence with a gain in significant wave height. The percentage of estimates within 40 cm accuracy decays approximately 8% per every metre increase in significant wave height.

The low but significant $R^2$ values for all the tendencies demonstrated in Figure 4.15 indicate

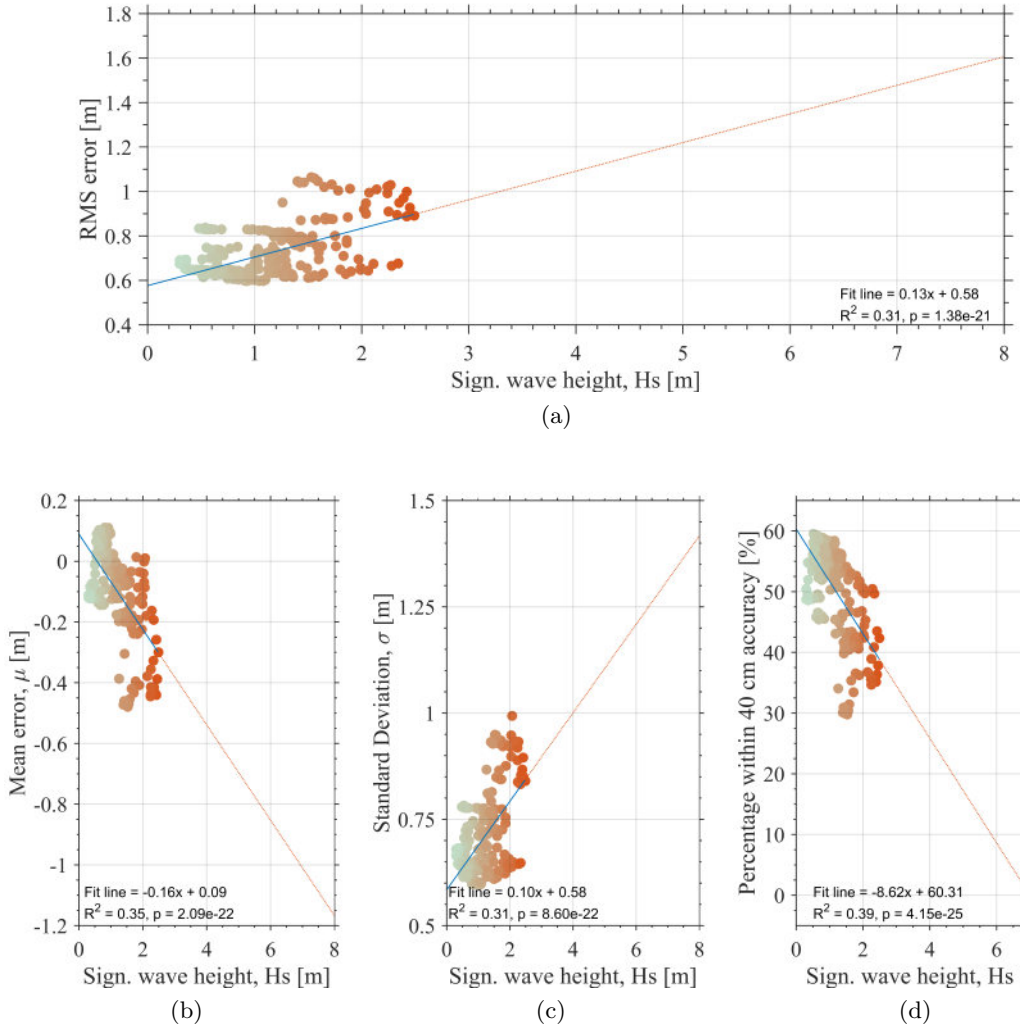


Figure 4.15: Accuracy values versus wave height; trends and extrapolation. a) RMS error, b) the mean error ($\mu$), c) the standard deviation ($\sigma$) and d) $|\Delta Z| < 0.4$ m for mulitple depth estimates.

that the fitting using a linear model doesn't fit the data greatly, however a trend is certainly observed. All the presented accuracy indicators tell a similar story: when the wave height rises, the accuracy of the depth estimations declines. Considering the linear trends displayed in Figure 4.15, limited accuracy will be observed if the depth estimations would be in extreme storm conditions.

### 4.7.3 Offshore extent of cBathy

A frequently asked question is if cBathy can estimate depths until the depth of closure. The offshore extent of the depth estimations is mostly dictated by the camera resolution; as the pixel footprint becomes large the accuracy of the estimations reduces. Nonetheless, in theory a depth inversion technique based on linear wave theory should work better with less non-linear wave interactions the further offshore. The waves have to be depth-limited [intermediate to shallow water] for the linear dispersion relation to be valid for depth inversion.

$$\frac{L_o}{20} < h_{int} < \frac{L_o}{2} \tag{4.2}$$

$$h_{sh} < \frac{L_o}{20} \tag{4.3}$$

wherein both equations $L$ represents the offshore wave length, (4.2) indicates the depth criterion for intermediate water depth [$h_{int}$] and (4.3) represents the criterion for shallow water [$h_{sh}$]. The shortest measured wave period between 2007 and 2015 is 4.2 seconds which relates to a deep-water wavelength of approximately 25 metres. Following (4.2) this means that the intermediate water depth for this wave starts at 12.5 m. The mean measured wave period between 2007 and 2015 is 11 seconds which is means that the offshore wave length is around 200 m. The intermediate water depth for the average wave period at Porthtowan is 100 m. 100 m depth is well beyond the depth of closure and more in the order of the boundary of the continental shelf. From this we can conclude that the linear dispersion relation is not a limiting factor for the offshore extent and that if the cameras have enough resolution to distinguish the incident waves there should be no reason why depth inversion would not work. This reasoning is purely conceptual and subject to some rigorous assumptions. In order to know the seaward extent of cBathy, it should to be investigated. Waves with larger periods than the mentioned mean are common at Porthtowan and the South West of England.

**Does cBathy estimates depth until the depth of closure?** Hypothetically the linear dispersion relation is valid until much greater depth than the near-shore zone and littoral cells as defined in Chapter 2. The limiting factor mentioned above is, in particular, the restrictions of the cameras. Nonetheless, the question remains if cBathy was able to estimate depths until or beyond the depth of closure. The depth of closure is typically calculated with year-mean values for significant wave height and the associated standard deviation, following Hallmeier (1981) as presented in (4.4).

$$h_c \approx 2\bar{H}_s + 11\sigma_{H_s} \tag{4.4}$$

In which $h_c$ is the depth of closure, $\bar{H}_s$ the annual mean significant wave height and $\sigma_{H_s}$ represents the year-long standard deviation. Figure 4.16 shows the average depth of closure per year from 2008 until 2015.

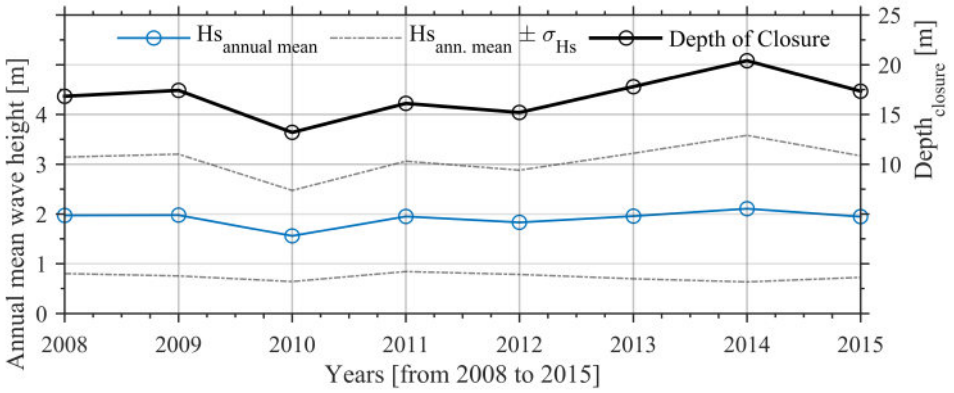


Figure 4.16: Annual mean wave height [$\bar{H}_s$] and corresponding depth of closure from 2008 to 2015.

The average depth of closure at Porthtowan over the time-frame from 2008 to 2015 is 16.8 m. cBathy depth estimates at Porthtowan are obtained between October 2013 and February 2015. The typical maximum depth for the obtained depth estimates is approximately 16 to 17 m, as shown in Figure 4.11b. The accuracy in the form of absolute error tends to increase significantly from approximately 12 m water depth to deeper waters. From Figure 4.16 one can see that if the year is relatively energetic the year-averaged depth of closure can be over 20 m water depth. However, if the year experiences relatively calm wave conditions the year-averaged depth of closure is around 13 m. Nonetheless, considering this, one can only conclude that the camera system at Porthtowan is not able to estimate the depths until the depth of closure with the current camera system set-up.

## 4.8 Conclusions

Video-based bathymetry estimations are obtained at Porthtowan using an inverse method following linear dispersion relation of free surface elevations. Two identified sources of inaccuracy are 1) a camera boundary issue and 2) a tide dependent inaccuracy. For the first source, a camera boundary is introduced in this Chapter that overcomes the consistent overestimation of the depth on the camera boundaries. For the second source, the formerly fixed positions of the pixels in the real-world have been changed to floating pixel positions depending on the instant tidal elevation and the camera height. Floating pixels are not only important in macro-tidal environments, since the magnitude of this effect depends on the tidal range and camera height. The floating pixel modification applied to the unmodified cBathy version as presented in Holman et al. (2013) lead to significant improvements over the whole domain at Porthtowan. Depending on multiple environmental variables, up to a 60% reduction in RMS-error over the whole domain (Figure 4.13) and 75% reduction in RMS error in the sub-tidal bar domain has been demonstrated (Table 4.3) here. The video camera system at Porthtowan, with the inclusion of the modifications, is then shown to be capable of estimating the sub-tidal depths with a bias of around 10% of the local depth for daily estimates. Furthermore, the depth estimates improve considerably when a long series of depth estimates is combined through the Kalman filter. Up to 30% decrease in standard deviation is found, as shown in Table 4.4.

# Chapter 5

# Observations of storm impact and recovery winter 2013-2014

## 5.1 Introduction

Chapter 1 gives a concise introduction to the 2013-2014 winter season in the perspective of western Europe and the United Kingdom. The storms that hit the South-West of England during the winter of 2013/2014 were extreme and unprecedented (Masselink et al. 2015). Severe coastal erosion / coast line retreat was observed across Europe from Portugal to Ireland. Metoffice (2014) shows that the South-West of England was particularly hit due to the storm trajectory over the Atlantic Ocean. The eye of the storms hit the South-West due to a more Southern track than considered normal (Metoffice 2014) resulting in larger impact. The winter of 2013-2014 contained multiple exceptional large storm events at a high frequency. In this chapter the storm impact of winter 2013-2014 at Porthtowan is assessed by utilising inter-tidal beach surveys and video-based depth estimates for the near shore area that has not been captured often during storms. First, the normal beach state dynamics based on available long-term wave data is presented. This is followed by a detailed description of the storm impact by using inter-tidal beach surveys before and after storm events or clusters of storm events over different time-frames [discussed below]. The coastal strength or representation of available sediment volume on the beach is presented in the form of the momentary coastline. Subsequent to the storm impact is the following recovery over the remainder of 2014. The discussion brings the impact and recovery results together in an overview over the period from October 2013 to December 2014. In the discussion, the impact of the 2013-2014 winter is placed in a multi-year perspective to

reflect on the relative extremeness of the 2013-2014 winter season. The last part of the Chapter discusses the impact of the stormy winter of 2013-2014 on the sub-tidal bars and their "recovery" behaviour during the remainder of 2014.

## 5.2 Overall storm impact and recovery October 2013 to December 2014

The impact of the extreme conditions during the 2013-2014 winter is assessed using the momentary coastline [as described in Section 3.5]. The momentary coastline is measured for the inter-tidal beach surveys and modelled using a disequilibrium model [as described in Section 3.6] using incident wave conditions. Figure 5.1 shows the wave power over the period and the measured [black curve] and modelled [orange curve] momentary coastline for the inter-tidal beach over the mentioned period. In October 2013 the momentary coastline was approximately 253 m. Over the winter season that followed, the minimum value [218 m] for the momentary coastline indicating maximum erosion was reached around mid-February 2014. A total retreat of 35 m corresponds to an average erosion of -207 $m^3/m$ or a -1.4 $m^3/m$ per day erosion rate. Near to full recovery of the inter-tidal beach is achieved over the remainder of 2014 as represented by the measured momentary coastline. Over the 9 months after the storm the measured momentary coastline was restored to 253 m. Between February and September 2014 roughly 58% of the beach volume between the vertical reference was recovered. The average recovery rate over this period is approximately 0.6 $m^3/m$ per day. Over October, November and the beginning of December the other 42% of the recovery of the inter-tidal happened on a much larger average recovery rate of 1.1 $m^3/m$ per day.

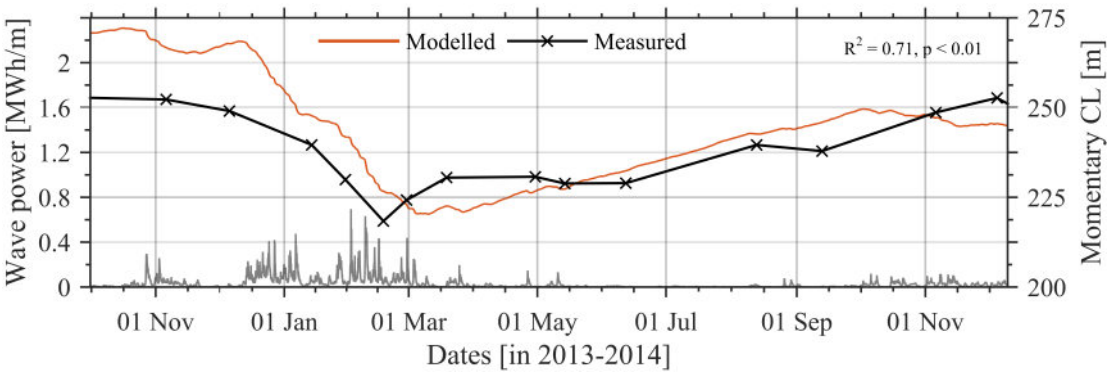


Figure 5.1: Measured [black line] and modelled [orange line] momentary coastline with underlying wave power from October 2013 to December 2014.

In general, the correlation between the measured and modelled momentary coastline is expressed in the form of $R^2$. The $R^2$ value is 0.71 over the period starting end-2013 until end-2014 and the correlation is statistically significant with a p-value $<< 0.01$. The modelled disequilibrium principle based momentary coastline shows a more instantaneous value for the momentary coastline, as the inter-tidal beach surveys are intermittent. Nonetheless, there are some fundamental differences between the measured and modelled momentary coastline concerning erosion/accretion in time. The model over-predicts the erosion rates compared to the measured rates over the winter-season between November 2013 and mid-February 2014. The instantaneous and antecedent wave conditions indicate a longer period of erosion. As the measured momentary coastline gains value [from mid-February] the modelled momentary coastline is still showing erosion [until March 2014]. The modelled accretion over a period from March to October 2013 shows a similar average accretional rate compared to the measured momentary coastline over the same period. However, also here the model shows a different switching point in time from accretion to erosion. The model shows that the relationship between instantaneous compared to the antecedent waves became erosive around early October 2014. The measured momentary coastline continued to show accretion until early December 2014.

## 5.3 Sectioned storm impact winter season 2013-2014

In this section results from the inter-tidal beach surveys and video-based depth estimations are shown and analysed over the course of 2013-2014 winter season. The impact is assessed over two consecutive dates of the inter-tidal beach surveys or a set of 2 if the interval between the surveys is less than 2 weeks. The interval between inter-tidal beach surveys is normally a month but during the 2013-2014 winter season extra surveys were conducted to assess storm groups [typically a survey after two big storm events]. During the 2013-2014 winter, inter-tidal beach surveys at Porthtowan were carried out on:

- 7 October 2013
- 6 November 2013
- 6 December 2013
- 14 January 2014
- 30 January 2014
- 17 February 2014
- 28 February 2013
- 19 March 2014

In addition to the surveys, incident wave conditions determined the sectioned presentation of the results. For example, if the wave conditions are moderate over a time-frame of three surveys, there wouldn't be a specific reason to assess the storm impact over this period. In order to determine time-frames wave conditions should be determined first.

### 5.3.1 Wave conditions and storm identification

Figure 5.2 shows the wave conditions at the South West coast of England from the Sevenstones Lightship during the stormy period in winter 2013/2014 from October 2013 to March 2014. The grey line represents the wave height and the orange line corresponds to daily tidal range. The red dashed line represents the line of 1% exceedance and the green dashed line 5% of exceedance. The 1% exceedance value of significant wave height of 5.9 metres.

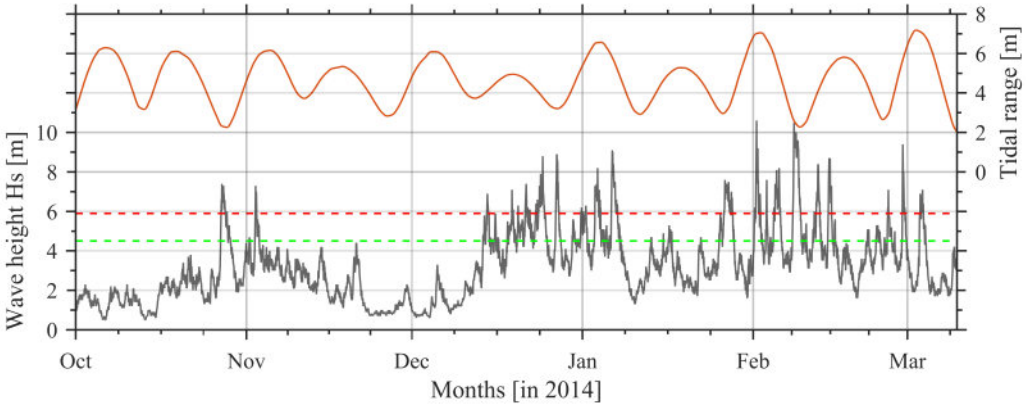


Figure 5.2: Wave conditions during the winter 2013-2014. Wave height and period, red and green line represent respectively the 1% and 5% exceedance threshold.

Here, storms are identified using a peak-over-threshold approach as carried out in a similar fashion in Masselink et al. (2015). A storm corresponds to a wave height that exceeds the 1% line and the duration corresponds to the up and down-ward crossing of the 1% exceedance line. During the end of December to beginning of January and the first half of February waves were particularly energetic. Significant wave heights exceeding the 1 percent exceedance were regularly measured. In early November, wave conditions first exceeded the storm threshold. What followed were several months of energetic wave conditions, occurring in some cases simultaneously with spring high tide with tidal ranges over 7 m. Also the sequences of storms were extraordinary in the first two weeks of February, the wave buoy recorded six major storms, all with a wave height $> 7.5$ metres, 9 metres $H_s$ on average, and duration between 10 to 38 hours. The absolute maximum significant wave height was measured on the 1st of February 2014, 10.6 metres.

**Storm naming** The generally assigned names are used to identify the storms throughout the sections below. Here the following storms are considered: The November storms (27 October 2013 - 3 November 2013), the Christmas storms (23 December 2013 - 28 December 2013), Hercules (6 January 2014), Brigid (1 February 2014), Petra (5 February 2014) and Ruth (8

February 2014).

### 5.3.2 Time-frame selection

Considering the inter-tidal beach survey dates and the identified storms, time-frames are selected to describe the morphological impact of 2013-2014 winter. The first time-frame covers the very first storms [November storms] of the 2013-2014 winter season from 7 October 2013 [last beach survey that didn't experience storms] to 6 December 2013. The second time-frame captures the first period of *extreme* storminess, in storm frequency and intensity over December 2013 and January 2014 [6 December 2013 to 30 January 2014]. The third time-frame covers the second period of extreme storminess from end of January to mid-February 2014 [30 January to 17 February 2014]. After this time-frame there was a period of relative calmness. The relative calm period and the last extreme storms are covered in the last time-frame of the 2013-2014 winter season from mid-February to mid-March 2014 [17 February to 19 March 2014].

#### Presentation of the results

For each period two representative beach surveys are compared to one-another to identify accretion and erosion over the survey domain. A difference map of the two surveys is presented to show areas of erosion in blue and accretion in yellow/red. In addition to the inter-tidal maps, the momentary coast line is presented per period to assess the coastal strength of the beach. The presented momentary coastline [following Section 3.5] is measured from the inter-tidal beach surveys and modelled using the disequilibrium principle explained in Section 3.6. The measured and modelled momentary coastline give an overview of what morphological change occurred and what should have happened based on incident wave conditions. The yellow line in the presented inter-tidal beach survey plots represents the lower boundary of the momentary coastline and the black dashed line represents the measured momentary coastline.

In addition to the inter-tidal data, corresponding video-based depth estimations are presented to indicate the impact on the sub-tidal area. The video-based depth estimations show great accuracy reliance on the wave conditions [Section 4.7.2]. Higher waves result in less accurate estimates. During storm conditions the depth estimates are relatively poor. Therefore, bathymetry estimates are selected here that correspond with the lowest wave height during the few days around the presented inter-tidal data.

### 5.3.3 October to December 2013

The first time-frame considered covers the November storms [from October to early December 2013]. Figure 5.3 shows the associated inter-tidal beach levels, difference plot and momentary coastline.

This period starts with the pre-storm season inter-tidal beach map of October 2013 as shown in Figure 5.3a. The inter-tidal beach levels presented in Figure 5.3b represent the inter-tidal area in December 2013. The inter-tidal beach shows few morphological features; it is mostly planar. In the December 2013 survey a clear rip-channel [around X= 350 Y = 650 Argus coordinates] appears. This rip channel is a common feature observed at Porthtowan. Between the two surveys significant erosion of around 0.5 m is observed around the rocky outcrop in the difference plot [Figure 5.3c]. The blue colour [erosion] seems to dominate the difference plot suggesting that the domain lost sediment. The sum of the values in the difference plot indicate that 11500 $m^3$ sediment has eroded from the inter-tidal domain. The erosion should show up as a clear reduction in momentary coastline represented in Figure 5.3d.

The momentary coastline in October 2013 was situated at approximately 253 m cross shore. For the December 2013 survey the momentary coastline reduced to 249 m. This indicates an average sediment loss -22 $m^3/m$ for the inter-tidal domain. The average erosion rate over this period is -0.3 $m^3/m$ per day. The disequilibrium model over-estimates the amount of sand between the pre-set vertical levels. Following the modelled momentary coastline, it seems that after the erosion during the November storms slight accretion is predicted. The sub-tidal domain suffers changes in the sub-tidal bar configuration over this period. In October, evidence of a transverse bar system is shown in Figure 5.3e, while Figure 5.3f indicates a more welded crescentic structure. The deeper, eyes, around 600 m cross shore seem to have shifted Southwards [to higher Y values]. A bar formation around 650-700 m cross shore is also more pronounced than compared to the situation in October 2013.

### 5.3.4 December 2013 to end-January 2014

From mid-December to end of January the first longer sequence of storms hit the coast at an unprecedented frequency (Masselink et al. 2015). Considering this almost continuous battering of the coast, significant erosion would be expected. Figure 5.4 starts in a) with the survey from 6 December 2013, the same as in Figure 5.3b. Figure 5.4b represents the result of the inter-tidal beach survey on 30 January 2014. Immediately from these two plots it is clear that the survey area has reduced significantly. The lower limit of the momentary coastline, represented by the

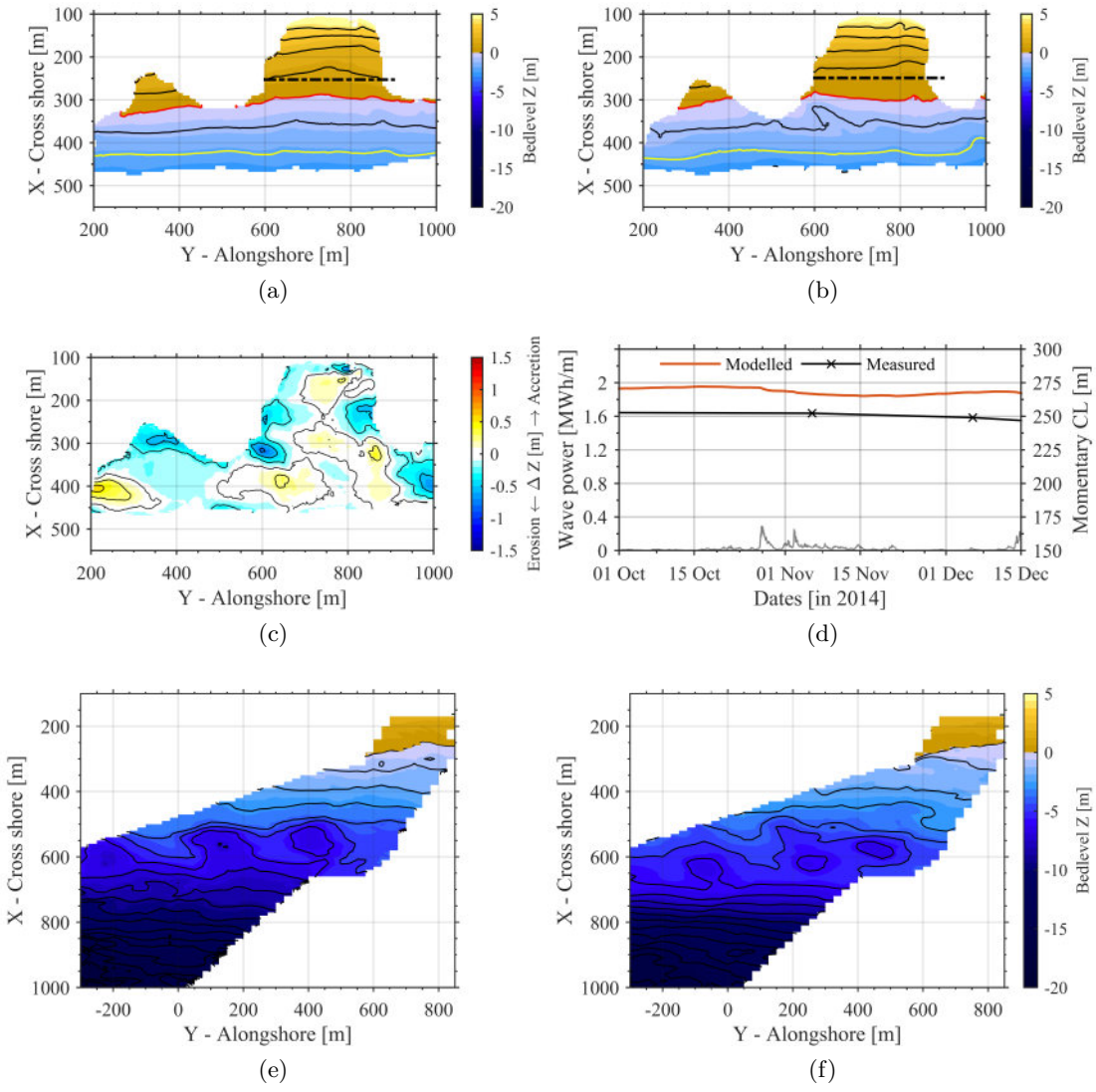


Figure 5.3: Inter-tidal beach survey 7 October 2013 (a) and 6 December 2013 (b). The red is mean sea level, the yellow line represents the lower boundary for the momentary coastline and the black dashed line is the calculated cross shore position of the momentary coastline. c) the difference between the two surveys dates and d) measured and modelled momentary coastline. e) and f) represent the most accurate depth estimation within a few days of the inter-tidal beach surveys

yellow line, moved approximately 50 m shoreward. Since the vertical range of the surveys are approximately similar this indicates that the severe erosion occurred over this period.

The difference plot between the two surveys is presented in Figure 5.4c. The difference plot shows and confirms the severe erosion. Some areas in the survey domain experienced erosion of over a meter. The momentary coastline is presented in Figure 5.4d. The momentary coastline decreased from 249 m in December 2013 to 229 m in January 2014. This resulted in an average erosion of -115 $m^3$/m over this period. This means that the beach experienced an average erosion rate of -2.1 $m^3$/m per day. The measured momentary coastline does not provide insight into when this erosion actually happened but the modelled momentary coastline gives a good indication. The modelled momentary coastline shows a very similar decay in momentary coastline. The model indicates that most of the erosion over this period occurred between 14 December 2013 and 10 January 2014.

The sub-tidal domain is shown in Figure 5.4e,f. As previously discussed, around 6 December 2013 the sub-tidal domain shows three dimensional sub-tidal bar features and structure in Figure 5.4e. The depth estimate for end-January 2014 presented in Figure 5.4f shows that not much of this three dimensional structure remained present over this period. The depth estimate in Figure 5.4f shows evidence of mega-rips that can catalyse erosion of the beach. The most prominent mega-rip can be found around 50 m in the alongshore direction and 500 to 600 m cross shore. This particular mega-rip has an estimated width of around 100 m. The sub-tidal bar has straightened and is positioned between 700 and 750 cross shore.

### 5.3.5 End-January to mid-February 2014

After January 2014 the 2013-2014 winter season was already considered extreme. Nonetheless, the extreme waves recorded in February 2014 were significantly more powerful than in January 2014, as shown by a comparison between Figure 5.4d and Figure 5.5d. In January, the maximum recorded wave power was around 0.65 MWh/m, while in February the extremes exceeded 0.8 MWh/m. The larger wave power would be expected to cause even more erosion over this period following the relationship between storm wave power and volume change (Birkemeier et al. 1999). Figure 5.5a shows the bed levels of the inter-tidal beach survey on 30 January 2014 and the bed levels of 17 February 2014 are presented in Figure 5.5b. The survey domain reduced over this period so that only the large embayment at Porthtowan could be surveyed.

The difference between the two surveys is presented in Figure 5.5c. Erosion that is visible here occurred especially between 300 and 400 m in cross shore direction. The higher part of

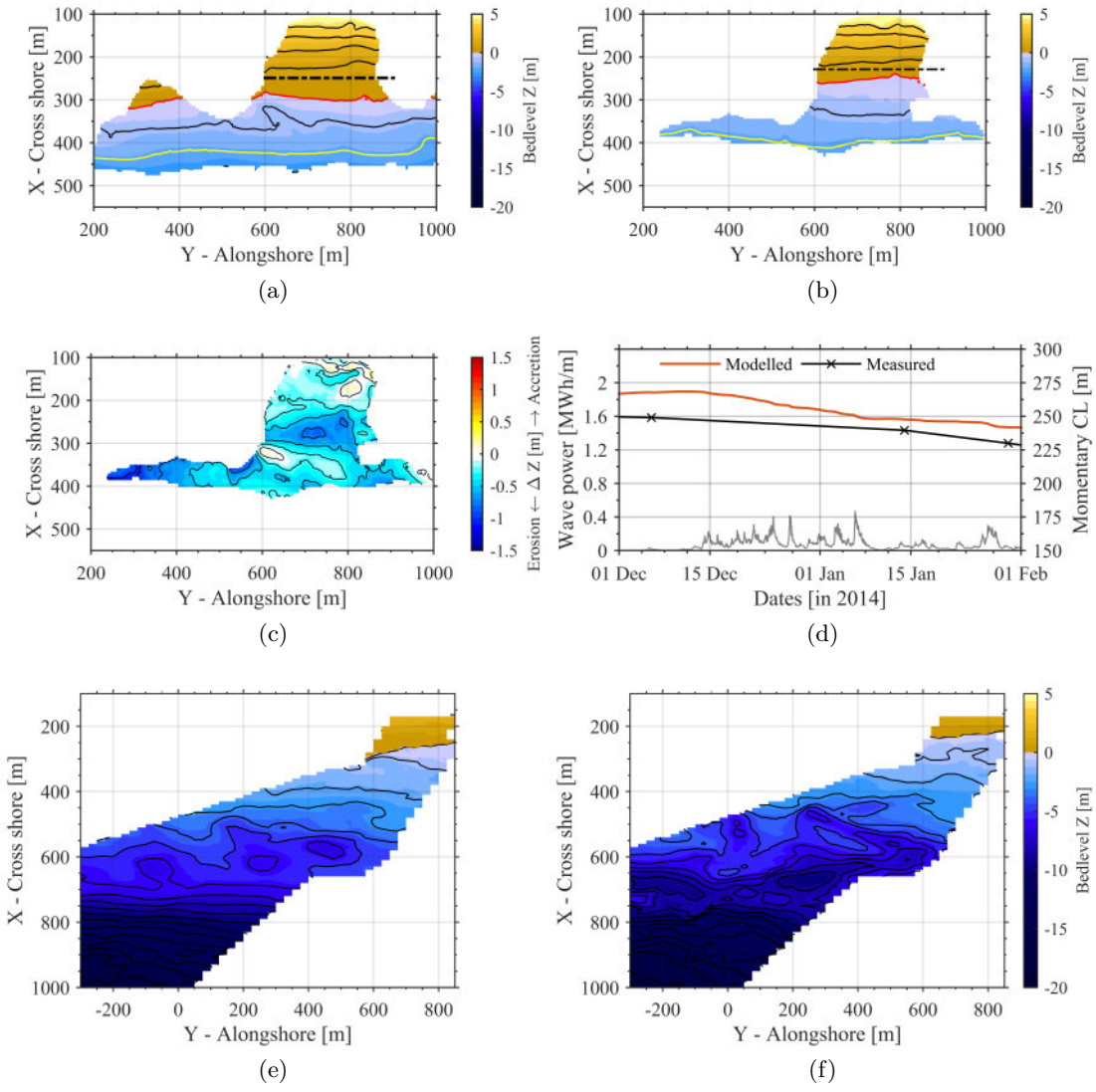


Figure 5.4: Inter-tidal beach survey 6 December 2013 (a) and 30 January 2014 (b). The red is mean sea level, the yellow line represents the lower boundary for the momentary coastline and the black dashed line is the calculated cross shore position of the momentary coastline. c) the difference between the two surveys dates and d) measured and modelled momentary coastline. e) and f) represent the most accurate depth estimation within a few days of the inter-tidal beach surveys

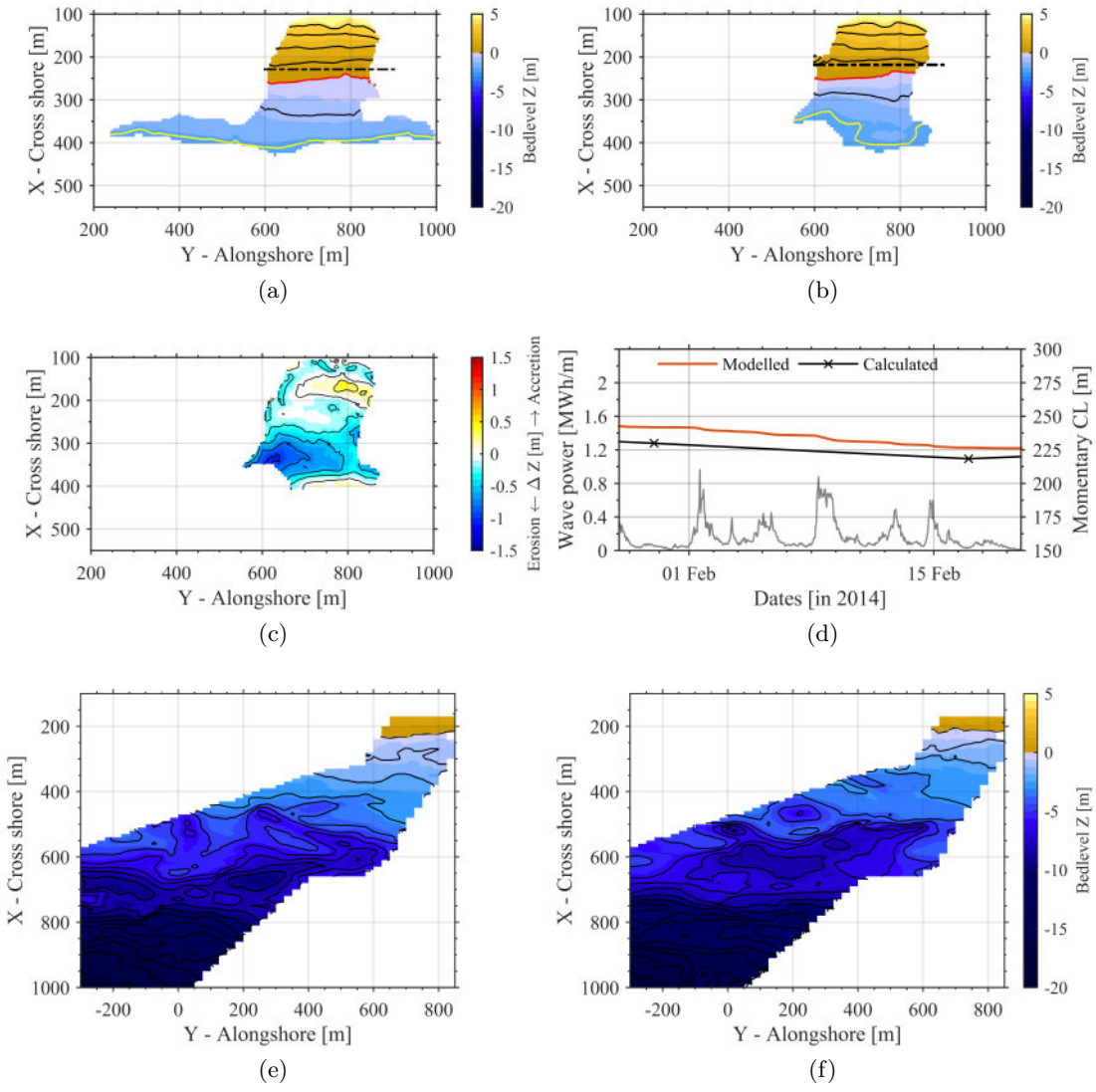


Figure 5.5: Inter-tidal beach survey 30 January 2014 (a) and 17 February 2014 (b). The red is mean sea level, the yellow line represents the lower boundary for the momentary coastline and the black dashed line is the calculated cross shore position of the momentary coastline. c) the difference between the two surveys dates and d) measured and modelled momentary coastline. e) and f) represent the most accurate depth estimation within a few days of the inter-tidal beach surveys

the inter-tidal zone did not experience a significant change in contrast to the previous period [December 2013 - January 2014]. This is rather interesting because the storms of 1 and 5 February 2014 [Brigid and Petra] had peak intensity at spring tides with a tidal range around 7 m. A possible explanation for this is that the waves were so large and powerful that wave breaking occurred further offshore and surf zone width was large and saturated. Nonetheless, once again erosion of up to 1.5 m is observed over this period of time.

The measured momentary coastline is presented as the black line in Figure 5.5d. The measured momentary shoreline shows further retreat. The momentary coastline was around 229 m end-January and over these three weeks it moved to 218 m. The total average erosion is -69 $m^3/m$ over the whole domain. Considering the time frame this leads to an erosion rate of -3.84 $m^3/m$ per day. The video-based depth estimates are presented in Figure 5.5e and f for respectively the January and February survey. The sub-tidal area shows a more pronounced and linear sub-tidal bar around X = 700 [cross shore]. Evidence for the persistence of the earlier identified mega-rip is present [around X = 500-600 m and Y = 0-100 m in Argus coordinates]. The rip-channel seems to be deeper and the orientation of the rip rotated toward the South. Next to the earlier identified mega-rip is the evidence for a secondary mega-rip around the Argus coordinates Y = 150-250 m and X = 400-500 m.

### 5.3.6 mid-February to mid-March

The most erosive months for Cornwall are generally September to February. Nonetheless, the last storm of the 2013-2014 winter season happened in early March. Early-march is considered the end of the period for the storm assessment. To assess the impact, the first inter-tidal beach survey after the end of the storm assessment is used. Considering that end-February / begin-March a storm with wave heights up to 9 m hit the coast one could expect erosion. However, initial recovery is firstly observed between the mid-February and end-February surveys and continues to the inter-tidal beach survey of 19 March 2014. Figure 5.6a shows the bed levels obtained on 17 February 2014, the most erosive state the surveys covered. Figure 5.6b shows the surveyed inter-tidal beach levels on 19 March 2014. Figure 5.6b indicates that the upper beach is rotated a few degrees clockwise considering the red-line and a rip-channel is present along the Northern rocky outcrop [X = 225-350 m and Y = 650 m in Argus coordinates]. Also, evidence of the presence of a low tide level rip-channel can be found in Figure 5.6b. Around X = 375 m and Y = 400 m a depression in bed levels indicates a rip channel at this position.

Overall the survey domain increased significantly between mid-February and mid-March indicating that the beach experienced accretion. The difference plot shows that substantial

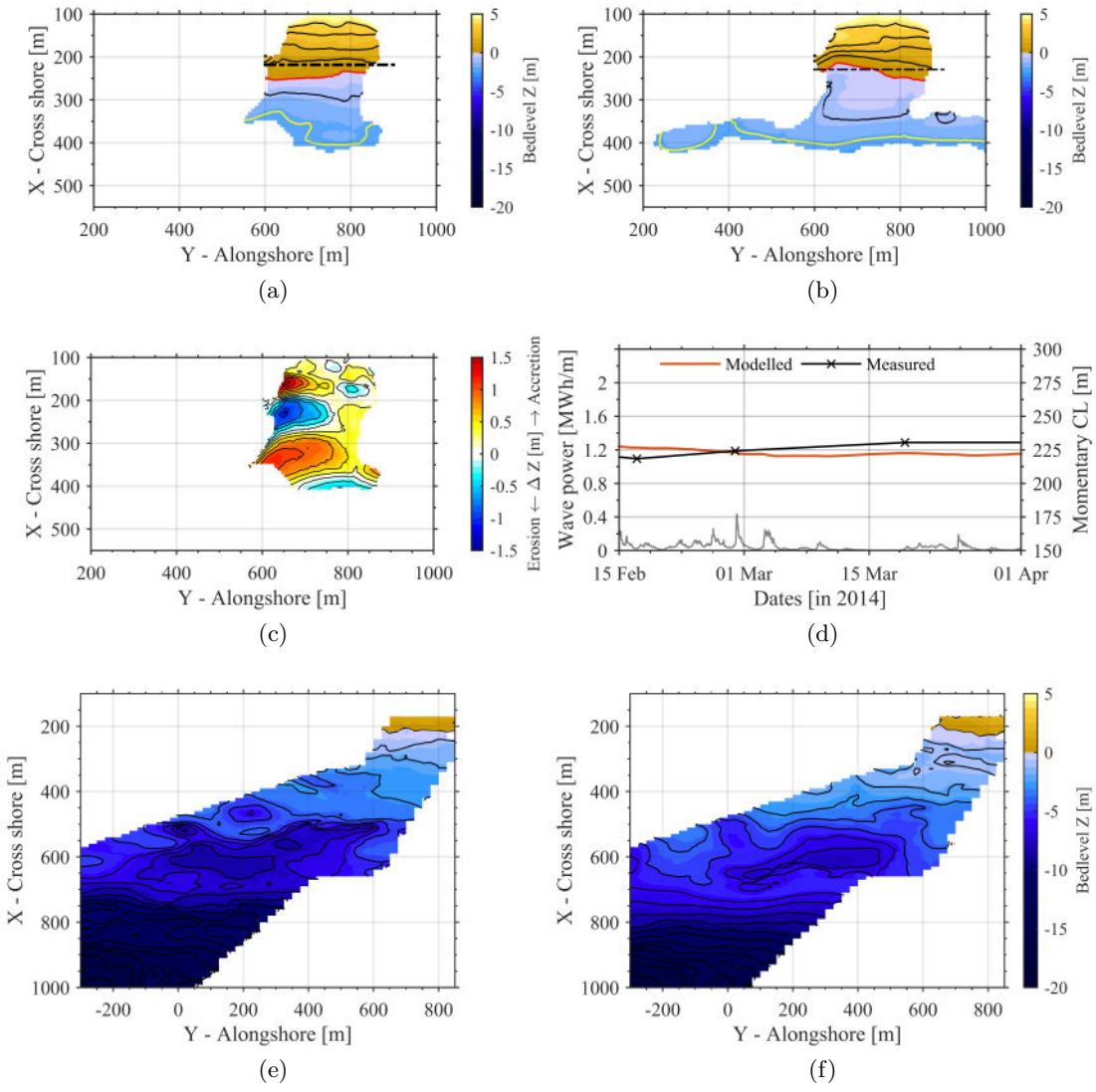


Figure 5.6: Inter-tidal beach survey 17 February 2014 (a) and 19 March 2014 (b). The red is mean sea level, the yellow line represents the lower boundary for the momentary coastline and the black dashed line is the calculated cross shore position of the momentary coastline. c) the difference between the two surveys dates and d) measured and modelled momentary coastline. e) and f) represent the most accurate depth estimation within a few days of the inter-tidal beach surveys

accretion occurred around X = 350 m [cross shore] and at the most shore-ward section of the domain over almost the whole width of the embayment. Deposits at the Southern rocky outcrops are indicative of the beach rotation. Erosion is observed between X = 200 and 300 m and along the rocky outcrop on the Northern side of the embayment. The measured momentary coastline shows an overall accretion between the vertical reference levels in Figure 5.6d. Between mid-February and end-February the momentary coastline increased from 218 m to 224 m. This increase in momentary coastline indicates an average accretion of 35 $m^3$/m. The rate of inter-tidal beach accretion is around +3.2 $m^3$/m per day. Secondly, over the period from end-February to mid-March a further increase in momentary coastline value is observed from 224 m to 230 m. Over this second period the inter-tidal beach gains on average around 38 $m^3$/m. This results in an average rate of accretion of approximately +2.0 $m^3$/m per day. The modelled momentary coastline line based on the disequilibrium principle shows a fundamentally different trend of erosion over this period. The model shows erosion during the storms while the momentary coastline derived from the inter-tidal beach surveys shows initial recovery. The instantaneous and antecedent wave conditions indicate erosion during the storms. However, the increase in momentary coastline values suggests that the relatively calmness [compared to the extreme in early-February] of these storms can lead to accretion of the inter-tidal domain.

The video-based depth estimates within a few days of both inter-tidal beach surveys are presented in Figure 5.6e,f. The sub-tidal domain shows similar patterns between both estimates. The estimate representative of March 2014 shows more organisation. The mega-rip identified in the two previous discussed time-frames [around X = 500 - 600 m and Y = 0-100 m in Argus coordinates] is still present. The sub-tidal bar contained a similar shape but is more pronounced in March compared to mid-February. An interesting coupling between Figure 5.6b and Figure 5.6f can be made if one looks at the low-tide rip-channel identified above in Figure 5.6b. The same rip-channel [around X = 350-400 m and Y = 350-400 m in Argus coordinates] shows up in the depth estimate in Figure 5.6f. This shows the intrinsic added value of the video cameras.

### 5.3.7 Observation of storm deposits

Minimum bed levels in the inter-tidal domain are observed around mid-February 2014. Over a metre erosion is measured at some parts of the inter-tidal domain between October 2013 and mid-February 2014. Figures 5.7a and b show the measured inter-tidal beach surveys. The size of the measurable inter-tidal domain has reduced significantly. The difference plot between these two surveys is presented in Figure 5.7e. The difference plot confirms the significant erosion over this time as the vast majority of the inter-tidal domain shows erosion of up to and over a metre.

From these three plots it is clear that the inter-tidal domain lost sediment but where did it end up?

This is a illustrative example where the video-based depth estimates can provide the answer. Figure 5.7c and d show the video-based depth estimates within a few days of the corresponding inter-tidal beach surveys. The difference plot of the two video-based depth estimates is presented in Figure 5.7f. The video-based depth estimates and derived difference plot show some significantly large erosion at particular parts of the domain. Transverse bars are eroded and diminished over this period of time. At these locations erosion up to 3 m is estimated. At the same time, the deeper parts of the eye-structure [∞] in October 2013 did not necessarily fill in but stayed at similar depths or became even deeper. In the February 2014 estimate in Figure 5.7d evidence of a mega-rip channel is present around X = 400 m to 500 m and Y = 200 [in Argus coordinates]. Some sediment deposits are estimated seawards of this mega-rip channel as shown in Figure 5.7d around X = 500 m to 550 m and Y = 200 m to 250 m. This deposit is also present in the difference plot in Figure 5.7f. As discussed above, the three dimensional structure of the sub-tidal bar domain present in October 2013 has been reorganised. The three-dimensionality is largely diminished and a more linear sub-tidal bar appears in February 2014. In the vicinity of the cross shore bar location [Y = 625 m to 750 m in Argus coordinates] accretion is estimated over the whole width of the camera domain. Seawards of the resulting sub-tidal bar, erosion occurred. It is inconclusive, but this effect might be a consequence of transport towards the sub-tidal bar as the waves break over the bar. In the most offshore 200 m of the camera domain the depth estimations show significant accretion in Figure 5.7f. With some imagination a second bar can be identified at a cross shore position of approximately 850 m to 900 m.

If we take the alongshore average of the difference plot, a negative balance [sediment loss from the video-camera domain] is found of approximately -353 $m^3/m$. This means that although the video-cameras can give an idea where the sediment moves, it still does not capture the storm related closure depth and thus a complete picture of the storm morphodynamics. Nonetheless, Figure 5.7f shows the inter- and sub-tidal dynamics and the accumulation of sediment around a sub-tidal bar.

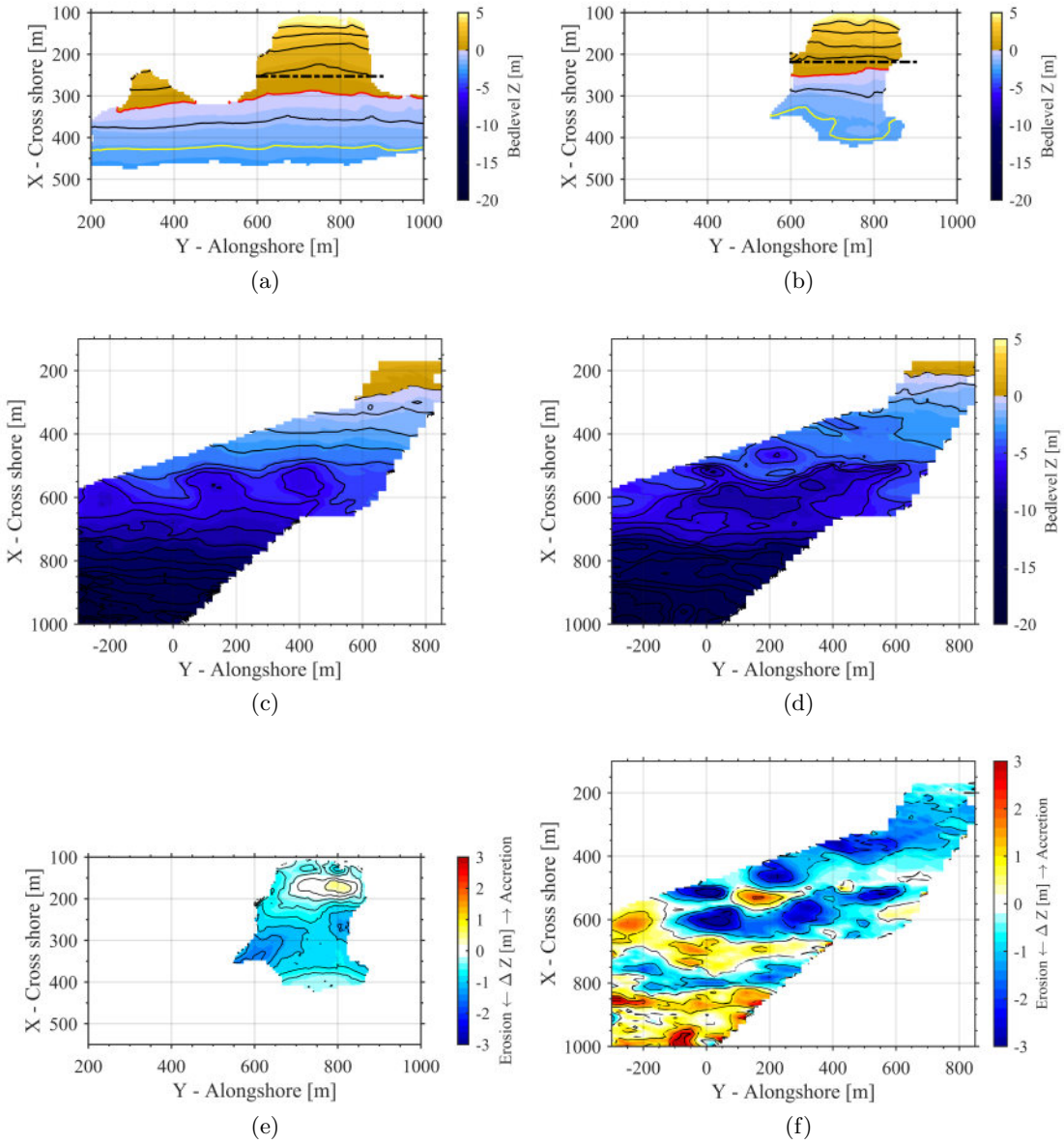


Figure 5.7: Inter-tidal beach survey 7 October 2013 (a) and 17 February 2014 (b). The red is mean sea level, the yellow line represents the lower boundary for the momentary coastline and the black dashed line is the calculated cross shore position of the momentary coastline. c) and d) represent the most accurate depth estimation within a few days of the inter-tidal beach survey. e) and f) are the difference plots for respectively the inter-tidal beach surveys [e)] and video-based depth estimations [f)].

## 5.4 Recovery over the remainder of 2014

### 5.4.1 Recovery wave conditions

Mid-February was the last inter-tidal beach survey that shows overall erosion during the stormy 2013-2014 winter season. Recovery of the storm impact is likely to happen under calmer wave conditions. The summer wave-conditions are perfect candidates to recover as much of the beach volume as possible to be prepared for the next winter. Figure 5.8 shows the wave height and tidal range from end-February to the remainder of 2014. After the March storms the wave height did not exceed the storm threshold [1% exceedance] until mid-December 2014.

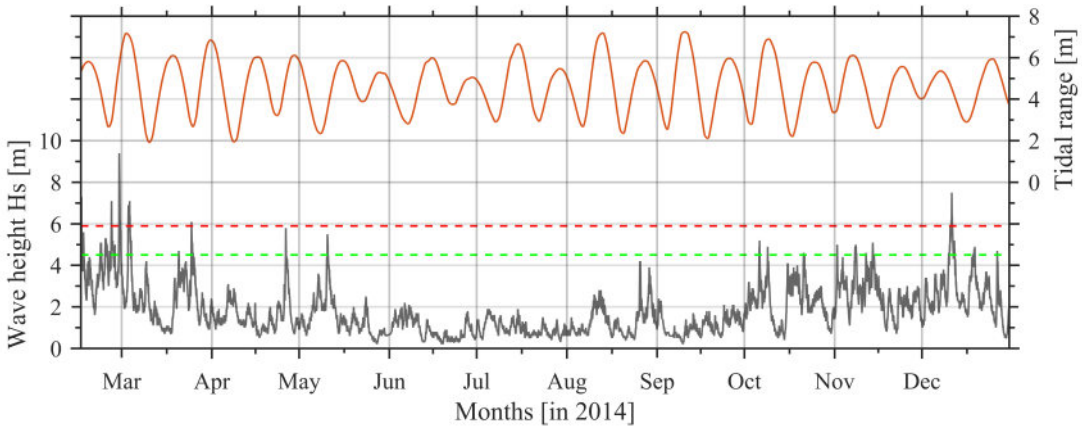


Figure 5.8: Wave conditions [grey] and tidal range [orange] during the recovery period. The red dashed line represents the 1% exceedance and the green dashed line is the line of 5% exceendance

For the recovery analysis the remainder is separated into three sub-sections for individual analysis: 1) March and May 2014, as the wave height steel exceeded the 5% of exceedance during this period 2) May to September 2014 covers the summer period of relative calm wave conditions and September to mid-December 2014 since the wave conditions are picking up again. Here, the final day of the recovery is defined as the first day on which the wave height exceeds the 1% exceedance threshold for the first time [before that particular point in time, recovery was still observed].

### 5.4.2 March to May 2014

The first period after the stormy 2013-2014 winter season from March to May still experiences some fairly energetic waves with wave heights up towards the 1% exceedance [and storm]

threshold. The bed levels from the inter-tidal beach surveys on 19 March and 14 May 2014 are presented in respectively Figure 5.9a and b. From March to May the survey domain has increased slightly. The beach-face rotated anti-clockwise diminishing the earlier observed rotation of the upper beach.

The rip-channel next to the Northern rocky outcrops in the inter-tidal beach survey of mid-March has disappeared in the May 2014 survey. The rip-channel that was present around X = 350 and Y = 400 [in Argus coordinates] in the March survey seems to have migrated towards the South and merged with the former rip-channel next to the Northern rocky outcrop. The larger rip channel is positioned around X = 300 to 450 m and Y = 450 to 600 m [in Argus coordinates] and increased in size compared to previously found rip-channels. A large feeder channel seems to run across the embayment around 350 m cross shore. The difference plot in Figure 5.9c shows a blue band of erosion diagonally over the survey domain between X = 300 to 400 m and Y = 400 to 800 m highlighting the deepening of the previously exiting rip-channel and feeder alongshore. In the very top of the domain some unexpected accretion occurred. This is due to landscaping the very top and entrance of Porthtowan beach after the storm season as a flood avoidance measure.

Figure 5.9d shows the momentary coastline. The momentary coastline is rather stable between March 2014 and end-April 2014. Over this period the momentary coastline advances a metre from 230 m to 231 m. Between the end of April and mid-May a decrease of the momentary coastline is observed from 231 m to 229 m. This indicates that the inter-tidal area lost around -11 $m^3/m$ which results in -0.8 $m^3/m$ per day. The measured and modelled momentary coastline do not differ significantly. The model shows that inter-tidal beach recovered sightly between the March and May surveys.

Corresponding video-based depth estimates within a few days of the inter-tidal beach surveys are presented in Figure 5.9e,f. The position and shape of the sub-tidal bar around X = 700 is fairly similar. The bar might have become slightly wider. The mega-rip [around X = 500 to 600 and Y = 0 to 100 m in Argus coordinates in Figure 5.9e] that was observed in all the video-based depth estimations since January 2014 disappeared in the estimate of May 2014 in Figure 5.9f. The enlarged rip-channel observed in the inter-tidal beach survey shows up in the video-based depth estimation at the same position and with the same orientation [around X = 300 to 450 m and Y = 450 to 600 m in Argus coordinates]. Also the feeder of the rip-channel is nicely represented in the video-based depth estimate in Figure 5.9f.

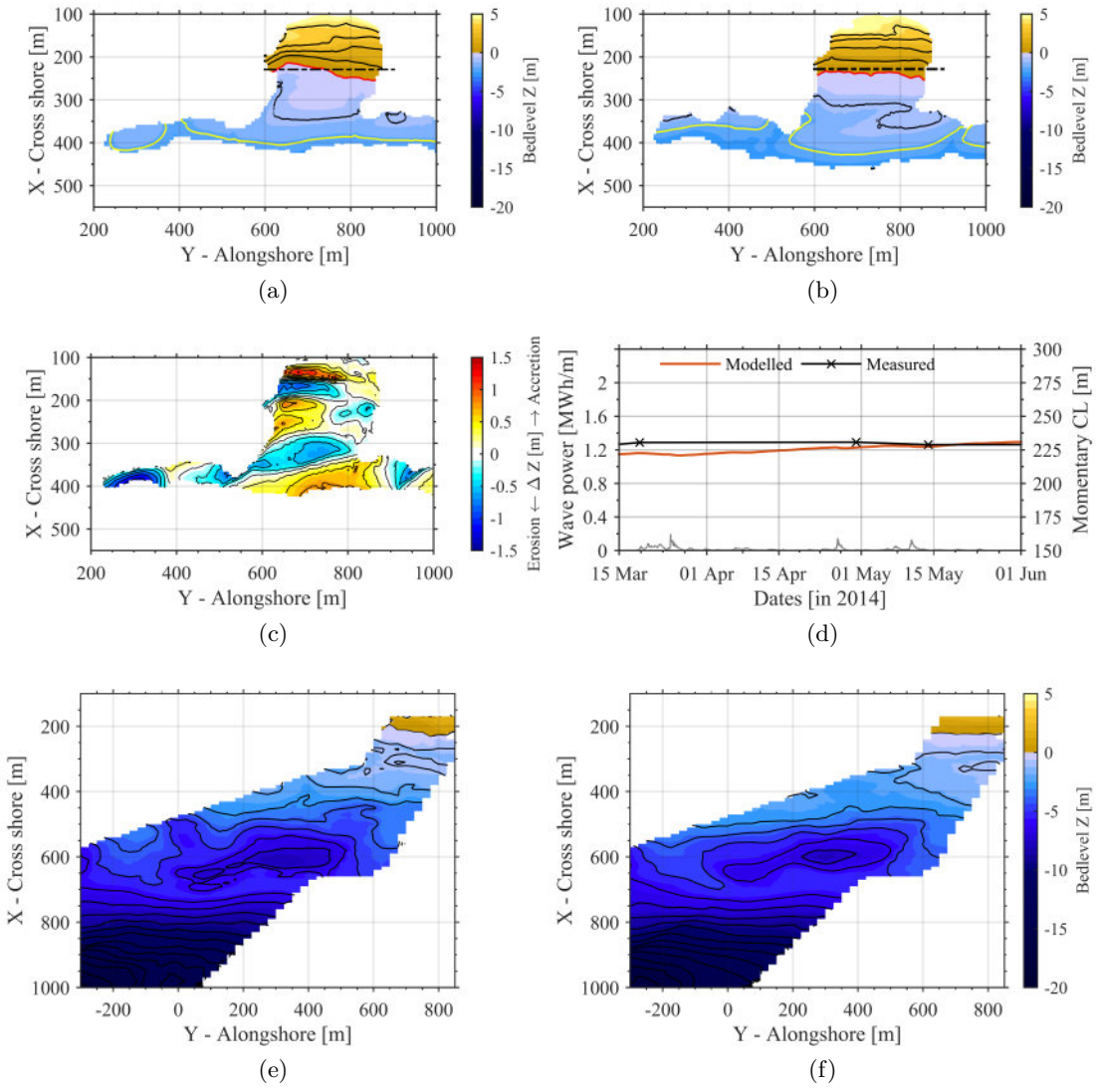


Figure 5.9: Inter-tidal beach survey 19 March 2014 (a) and 14 May 2014 (b). The red is mean sea level, the yellow line represents the lower boundary for the momentary coastline and the black dashed line is the calculated cross shore position of the momentary coastline. c) the difference between the two surveys dates and d) measured and modelled momentary coastline. e) and f) represent the most accurate depth estimation within a few days of the inter-tidal beach surveys

### 5.4.3 May to September 2014

The summer months are traditionally known as the period where the recovery from the winter occurs. It is a period of general accretion of the beach due to the substantially calmer wave conditions. Figure 5.10a shows the measured bed levels of the inter-tidal on 14 May 2014 and Figure 5.10b the bed levels on 13 September 2014. These inter-tidal beach surveys should be seen as respectively the pre- and post-summer survey.

The enlarged rip-channel with the feeder across the inter-tidal beach domain [in Figure 5.10a around X = 300 to 450 m, Y = 450 to 600 m] is less pronounced and has partially been filled in over this period. Along the Northern rocky outcrop a rip-channel is present, considering Figure 5.10b [X = 250 to 350 and Y = 600 m in Argus coordinates]. Also the upper beach has rotated counter clockwise [following the red line Figure 5.10b] over this period. A similar effect has been observed before during the inter-tidal beach survey of 19 March 2014 [Figure 5.9a]. It seems that when the rip-channel along the Northern rocky outcrop is present sediment is taken from the North side. As a consequence, the upper beach rotates anti-clockwise. Such a mechanism is often assigned to oblique incoming waves that result in a rotational embayment current (Loureiro et al. 2012).

The difference between the two surveys is presented in Figure 5.10c. The difference plot shows the partial infilling of the large rip-channel and feeder [X = 300 to 350 m and Y = 600 to 850 m in Argus coordinates]. The erosion that leads to the rotation of the upper beach shows up nicely between X = 200 to 300 m and Y = 600 to 700 m. From the difference plot it seems that the inter-tidal domain predominantly experienced accretion. Considering the momentary coastline in Figure 5.10d this is confirmed. An increase in momentary coastline indicates overall accretion over the period from May to September 2014. However, the momentary coastline also suggests that slight erosion occurred between August and September 2014. The momentary coastline increased from 229 m to 240 m from May to August 2014. This relates to a total average accretion of 64 $m^3/m$ over this period and a daily average accretion rate of 0.9 $m^3/m$ per day. After August, the momentary coastline reduces from 240 m to 238 m. This retreat in momentary coastline corresponds to a total average loss of -10 $m^3/m$ and an erosion rate of -0.3 $m^3/m$ per day. The modelled momentary coastline based on the disequilibrium principle does not pick-up the slight retreat of the momentary coastline but shows an overall accretion over this period. The measured and modelled momentary coastline show a rather good agreement concerning the accretional period between May and August. The erosion between August and September is underestimated in the model.

The video-based depth estimates within a few days of the presented inter-tidal beach surveys

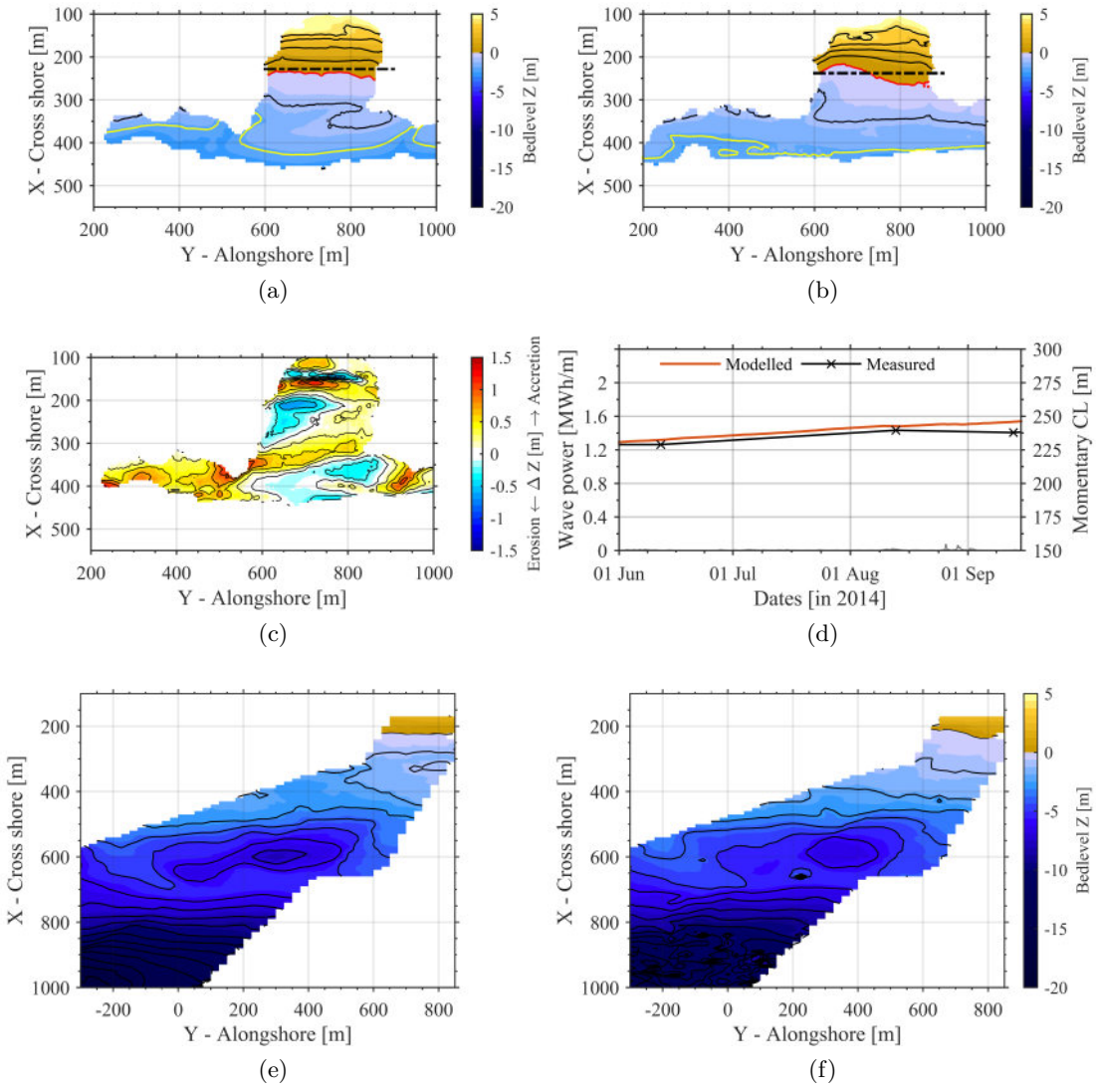


Figure 5.10: Inter-tidal beach survey 14 May 2014 (a) and 13 September 2014 (b). The red is mean sea level, the yellow line represents the lower boundary for the momentary coastline and the black dashed line is the calculated cross shore position of the momentary coastline. c) the difference between the two surveys dates and d) measured and modelled momentary coastline. e) and f) represent the most accurate depth estimation within a few days of the inter-tidal beach surveys

are presented in Figure 5.10e and f. From the bathymetry estimates one can also see that the large rip-channel has mostly diminished and the rip-channel along the Northern rocky outcrop is more pronounced. The upper beach rotation is also represented well in Figure 5.10f. The sub-tidal bar seems to have moved approximately 30 m shore-wards. The alongshore ∞ shape between X = 500 to 700 m and Y = 0 to 600 m in Argus coordinates] is persistently present since March 2014 after reorganisation of the sub-tidal features/structures [firstly observed in Figure 5.6f]. The offshore wiggle [at X = 0 to 100 m and Y = 50 m] of the sub-tidal bar seems to relate to the mega-rip channel that was present in March 2014. This feature stays very much stable but migrating shoreward over summer. In March the position is approximately at 725 m, in May approximately 700 m and in September a similar structure is found at 675 m.

### 5.4.4 September to early-December 2014

The wave climate became increasingly powerful after the September 2014 inter-tidal beach survey, as shown in Figure 5.8. During the beginning of October, the wave height passes the 5% exceedance threshold [4.5 m] several times. Nonetheless, the first storm is after the considered period. In general September until February are the more energetic, erosive, months in the South-West of England. Considering this, one might expect erosion associated with the increasingly energetic wave conditions over this period. Figure 5.11a and b present the measured inter-tidal beach levels on respectively 13 September 2014 and 5 December 2014. Intriguingly, more brown/yellow is present in Figure 5.11b than in Figure 5.11a. More brown/yellow indicates that the inter-tidal beach has accumulated sediment over this period. The previously observed rotation [following the red line in Figure 5.11a] has diminished as the beach rotated counter-clockwise between September and early-December. The second smaller embayment to the North has experienced accretion and could be surveyed for the first time since the winter.

The difference between the two inter-tidal beach surveys is shown in Figure 5.11c. Accretion is measured between X = 200 to 300 m over the whole embayment width. In some parts the accretion is over 1 m. The very upper part of the beach shows erosion. Seaward of the second smaller embayment between Y = 200 and 450 m [in Argus coordinates] significant accretion occurred. From the inter-tidal beach surveys and the difference plot it can be concluded that the inter-tidal beach experienced overall accretion between September and early-December 2014. The measured momentary coastline as presented in Figure 5.11d confirms the accretional trend considering the increase in the value for the momentary coastline. Between September and early-December 2014 the momentary coastline increased from 238 m to 253 m. This increase in momentary coastline relates to a total average accretion of 89 $m^3/m$ and an accretional rate

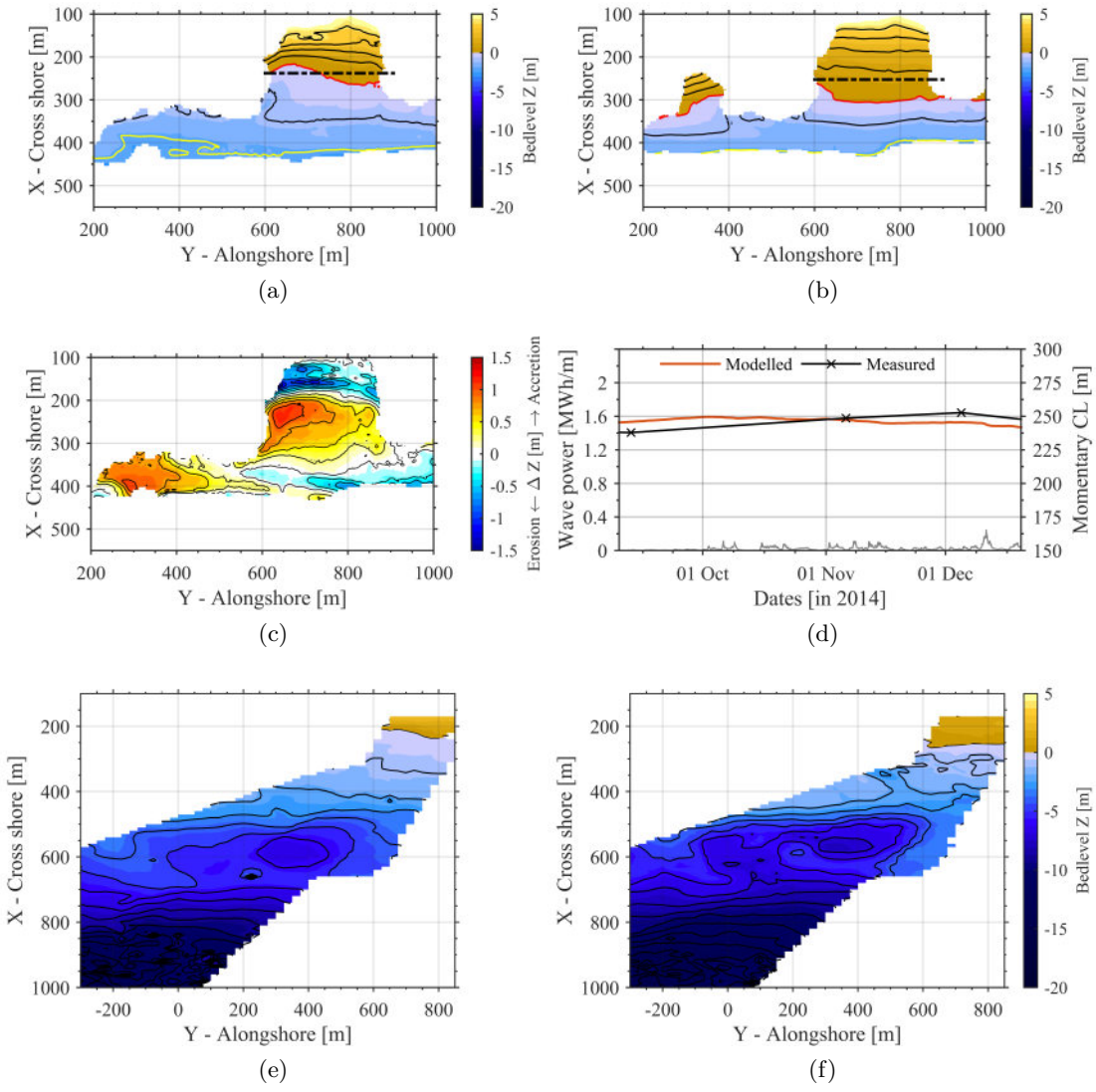


Figure 5.11: Inter-tidal beach survey 13 September 2014 (a) and 5 December 2014 (b). The red is mean sea level, the yellow line represents the lower boundary for the momentary coastline and the black dashed line is the calculated cross shore position of the momentary coastline. c) the difference between the two surveys dates and d) measured and modelled momentary coastline. e) and f) represent the most accurate depth estimation within a few days of the inter-tidal beach surveys

of 1.1 $m^3$/m per day for the inter-tidal beach. The accretional rate between September and November is slightly larger 1.25 $m^3$/m per day associated with a total average accretion of 64 $m^3$/m and an increase in momentary coastline from 238 m to 249 m. From November to December [as the waves are slightly more powerful compared to September to November] the momentary coastline changed from 249 to 253 which relates to a total average accretion of 24 $m^3$/m. This means that from November to early-December 2014 the accretional rate of 0.84 $m^3$/m per day is reduced relative to the earlier period. The modelled momentary coastline indicates a fundamentally different trend of erosion from October to early-December 2014. This shows that the wave conditions are powerful enough compared to the antecedent wave conditions to cause erosion. However, since the measured momentary coastline show an increase it might mean that these more powerful waves are relatively calm but powerful enough to bring sediment back on shore.

The video-based depth estimations corresponding to the inter-tidal beach surveys are presented in Figure 5.11e and f. Also in the video-based depth estimates it shows that the inter-tidal beach gained volume considering the increase area of brown/yellow colours. A mega-rip channel shows up in Figure 5.11f around X = 300 m to 400 m and Y = 500 m. Intriguingly, this mega-rip is present while the inter-tidal beach levels show accretion [mega-rips are most commonly linked to be erosional catalysts]. The sub-tidal bar moved further onshore to approximately 625 to 650 m in the cross shore direction and some parts start to weld with inter-tidal area [around Y = 200 m]. The sub-tidal bar shows more curvature which indicates more three dimensionality. This means that as the sub-tidal bar moves shoreward, increased three dimensionality happens, even under more powerful autumn wave conditions.

### Pre-storm season difference between October 2013 and December 2014

The inter-tidal beach shows full recovery over the summer and autumn. Recovery of the inter-tidal beach occurred until December 2014 and this is considered the maximum strength before the next winter-storm season started. Figure 5.12a,b shows the measured inter-tidal topographies on 7 October 2013 and 5 December 2014. The momentary coastline values are identical for both inter-tidal beach surveys as indicated in Section 5.4.4. In Figure 5.12a and b the red and yellow line are at very similar cross shore positions confirming a similar beach volume in both surveys. The difference between the two inter-tidal beach surveys is presented in Figure 5.12e. Intriguingly, erosion along most of the rocky outcrop, North and South, is measured. In the middle of the embayment and the upper beach part of the secondary smaller embayment up North [between Y = 300 m and 400 m in Argus coordinates] the beach contains more sediment

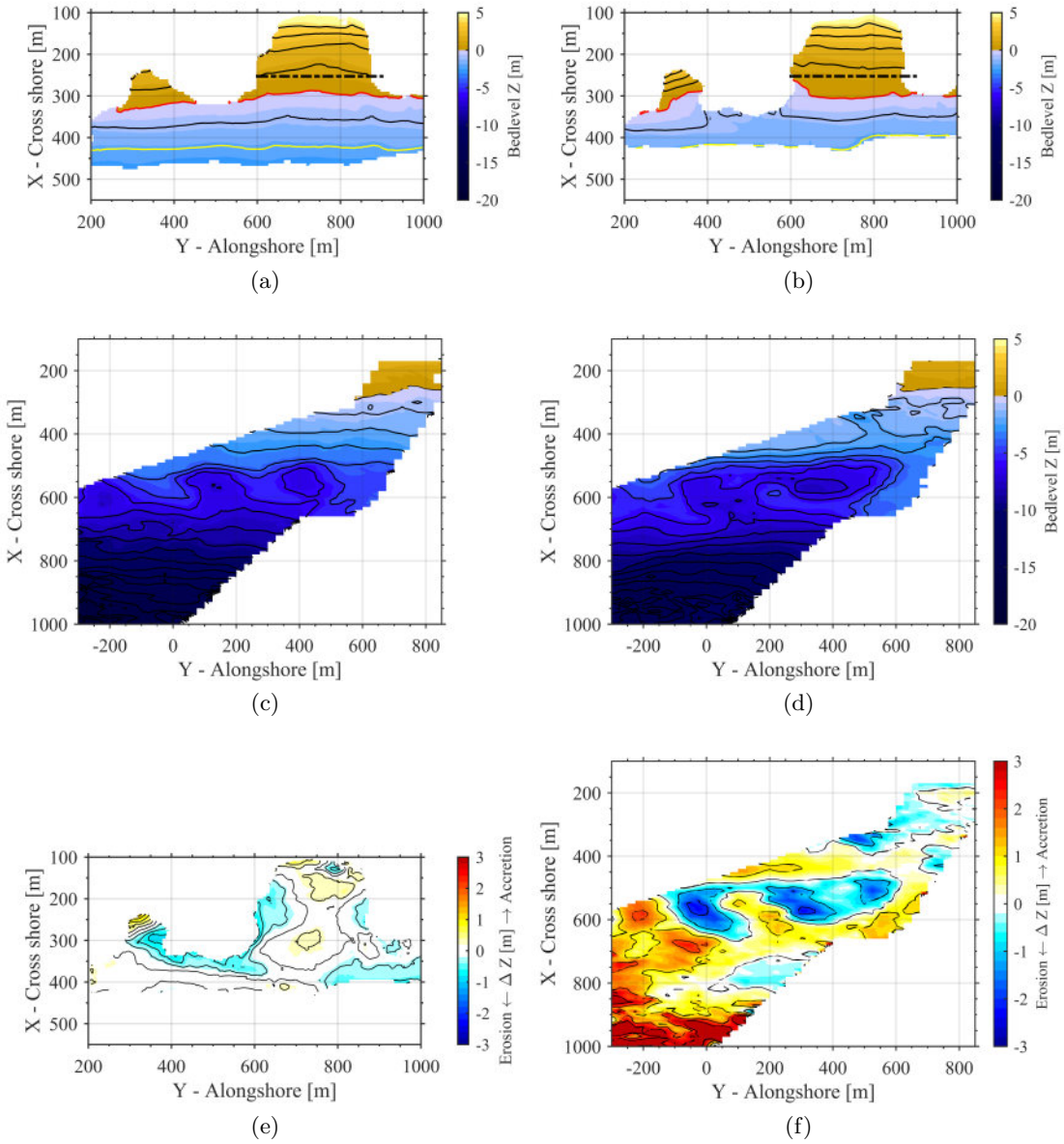


Figure 5.12: Inter-tidal beach survey 7 October 2013 (a) and 5 December 2014 (b). The red is mean sea level, the yellow line represents the lower boundary for the momentary coastline and the black dashed line is the calculated cross shore position of the momentary coastline. c) and d) represent the most accurate depth estimation within a few days of the inter-tidal beach survey. e) and f) are the difference plots for respectively the inter-tidal beach surveys [e)] and video-based depth estimations [f)].

in December 2014 compared to October 2013.

The video-based depth estimates are presented in Figure 5.12c and d within a few days of the inter-tidal beach surveys. The difference plot associated with these two video-based depth estimates are presented in Figure 5.12f. The main difference between the two video-based depth estimates between X = 150 m and 500 m is the evidence of a large rip-channel around X = 350 m to 450 m and Y = 450 m to 550 m [in Argus coordinates]. The transverse bars in Figure 5.12c are not present in Figure 5.12d and the significant erosion that shows up in the difference plot in Figure 5.12f between X = 500 m and 650 m contributes mainly to the change in sub-tidal bar structure. The beach is considered more resilient in the case there is more sediment volume in the near shore domain. Considering the inter and sub-tidal domain the difference in available volumes between October 2013 and December 2014 gives a representative indicator. The difference in volume in the video-camera domain is estimated on an average of 4.8 $m^3/m$. This suggests that the near shore zone contains more sediment volume in December 2014 compared to October 2013 and can therefore be considered as slightly healthier situation.

## 5.5 Inter- and sub-tidal interaction

From Chapter 4 it became clear that the area where cBathy results are most accurate are in the sub-tidal bar region. Here, we take the two components that we trust most; the inter-tidal beach surveys and sub-tidal bar region cBathy estimates to assess the interaction between the two zones. Figure 5.13 shows these two datasets in cumulative volumetric change per meter shoreline where the baseline topography and bathymetry is early November 2013.

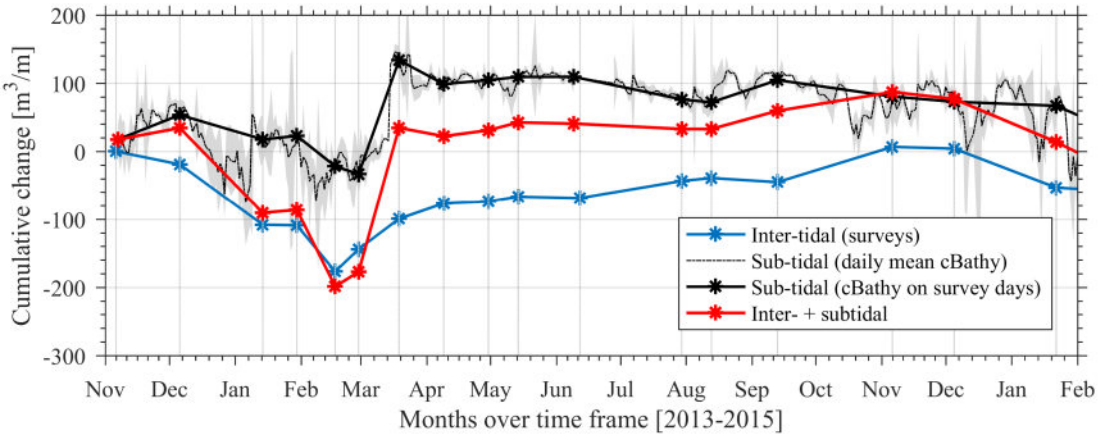


Figure 5.13: Cumulative volumetric change per meter shoreline from November 2013 to February 2015

In Figure 5.13, the blue line represents the inter-tidal surveys, the black line daily mean cBathy estimates and the red line shows the two combined. The volumetric change of the inter-tidal follows an identical path as described in section 5.2. The sub-tidal data covers the sub-tidal bar region only and covers the storm bar as observed in section 5.7. The storm conditions in November 2013 had the effect of eroding the inter-tidal area, at the same time an increase in volume for the sub-tidal domain is observed. This suggests that the eroded material from the beach ends up in the sub-tidal domain. Over the severe storms the two zones show similar erosional behaviour. From the daily derived cBathy estimates one can see that the sub-tidal zone shows rapid recovery just after the largest storms. After the storm peak in February, both, the inter-tidal and sub-tidal domain, show initial recovery while the wave conditions calm down. Hereafter, in March 2014, Figure 5.13 shows that sub-tidal area contains more sediment compared to the start in November 2013. Also, the inter-tidal zone recovered 40% of the initial erosion. From March to November 2014 the two zones shows inverse patterns suggesting that sediment is interchanged between the two zones; accretion in the inter-tidal zone leads to erosion of the sub-tidal domain and vice-versa. Only as the waves pick-up during the subsequent winter of 2014-2015, the zones show in phase behaviour although the volume in the sub-tidal domain reduces significantly less than the inter-tidal domain.

The two lines combined provides a picture of the overall behaviour of the nearshore zone and sediment lost from the system (red-line in Figure 5.13). From the starting point, the two zones seem to gain sediment over the storms in November 2013. A significant loss of sediment is observed during the most severe storms; the main contributor to the large overall erosion is the erosion of the inter-tidal zone. After the storms (March 2014) the amount of sediment in the overall domain is near equal the situation of November 2013 before the storms. The sediment is not on the beach yet, but seemingly stored in the sub-tidal domain. The inverse behaviour of the inter-tidal and sub-tidal domain results is a near constant value of the red-line from March to mid-August 2014. As wave conditions pick up in September 2014 the inter-tidal beach shows temporary stagnation of the recovery while the sub-tidal zone gains more sediment which leads to more sediment in the overall domain. From November, onward, waves are picking up resulting in an overall erosion of the domain. From Figure 5.13 it becomes apparent that during calmer conditions the inter-tidal and sub-tidal domain behave inversely; exchanging sediment as a cross shore closed system. During the more energetic conditions sediment from the beach ends-up further offshore which is indicated by the in-phase behaviour of the zones.

## 5.6 Sub-tidal bar behaviour at Porthtowan [2013-2015]

In Section 3.7.1 a bar detection technique is applied to the raw video-based depth estimates [not the filtered EOF data]. The temporal results are presented here in the form of mean bar position and three-dimensionality of the sub-tidal bar system.

**Mean bar position** Figure 5.14 presents the instantaneous wave power in blue, the grey curve is the unfiltered bar position and the black line represent the low-pass filtered mean sub-tidal bar position.

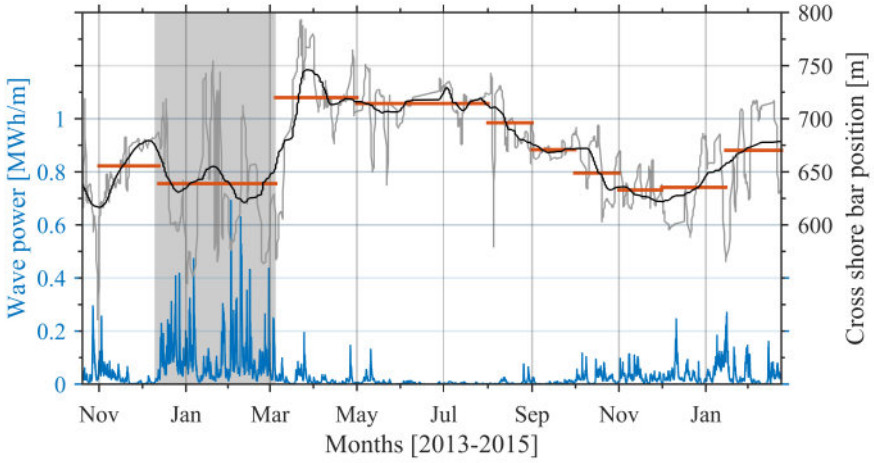


Figure 5.14: The blue line represents the wave power over time, the black line is the daily mean cross shore sub-tidal bar position over time with the grey patch indicating the standard deviation of the bars.The orange line represents a mean cross shore bar position over a period between surveys

The horizontal orange bars represent the mean derived from the unfiltered data over periods between surveys. The sub-tidal bar position is determined from any bar position that is in the sub-tidal bar region indicated by yellow/orange lines in Figure 3.8. The position of the bar is in Argus coordinates. An increase in position means on offshore displacement of the bar and vice versa for a reduction in cross shore value.

The sub-tidal bar position range is around 625 m and 725 m cross shore in Argus coordinates from October 2013 to December 2015 following the black curve in Figure 5.14. In October 2013, the starting point of the depth estimations, the average cross shore bar position is around 650 m. Over the storms the bar seems to be pushed [consistently] onshore. One might think that this represent the sediment removal from the inter-tidal domain into the sub-tidal domain during

highly energetic events. However, this seems to be more an artefact of the depth estimation during highly energetic conditions. The depth estimates become unstructured and considering the negative bias overestimate the depth largely. The fact of unstructured depth estimates leads to the detection of multiple bars though the bar detection routines. This period is indicated with the grey patch in Figure 5.14. Around March 2014 the sub-tidal bar moved relatively quickly seawards to approximately 725 m. If we look at the raw data, some period of reorganisation in the cBathy estimates takes place after the inaccurate storm estimates. This might explain the sudden shift to be more related to the depth estimation itself than a natural process. Over the summer months the bar stays relatively stable around 725 m cross shore. The waves seem not powerful enough to push the bar back onshore over the summer months. The sub-tidal bar migrates onshore as the waves start to become more powerful after August 2014. This seems counter intuitive since the consensus and 'textbook' example is that the breaker point is normally a reasonable indicator for the cross shore bar position. Considering this it means that with larger wave heights the bar should be more seawards. A possible explanation is that the bar is not experiencing waves that are powerful enough to activate sediment transport around the sub-tidal bar. The onshore migration of the sub-tidal bar continues until December 2014 as the first storms of the 2014-2015 winter hit Porthtowan. After December the storms push the sub-tidal bar in seaward direction.

**Three dimensionality** The standard deviation of the picked bar positions [varying around an alongshore mean] is an indicator of three dimensionality as in Plant et al. (2006) and Stokes et al. (2015). Here, the indicator for three dimensionality using video based depth estimations is extended with the number of detected bars. A three dimensional estimated bathymetry shows larger standard deviation in case of a single detected alongshore bar. Also alongshore intermittent bar sections relate to three dimensionality of the sub-tidal bar section as shown in Figure 5.15a. Figure 5.15b shows an example of where the bar is considered alongshore linear. Here, a proxy for three dimensionality of the sub-tidal bars is measured using the product of number of alongshore bars and the cross shore standard deviation of the detected bars in the sub-tidal area. Due to less accurate depth estimations during storm conditions cBathy estimates indicate sub-tidal bars all over the sub-tidal domain. This results in a high value for the proxy of three-dimensionality during storm conditions and should be considered a model artefact. Therefore, an additional criterion is introduced for the intermittent bar sections: the detected sections must be within a certain relative cross shore range to be included for the proxy as a group of bars. In this way structures are included while random bar detections are excluded.

The process of determining the "3D-ness" is carried out for the whole dataset from October

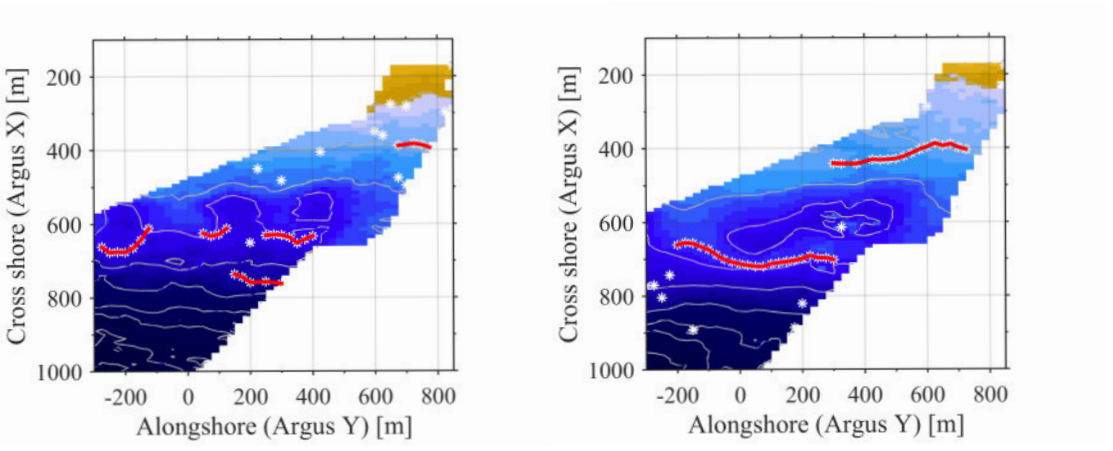


(a) (b)

Figure 5.15: a) A three dimensional example of the bar detection b) A linear example of the bar detection

2013 to February 2015. Figure 5.16 represents the wave power in blue and the normalised proxy for three dimensionality [$\sigma_{bar}$ x $N_{bar}$] in black. The black curve shows the standard deviation multiplied by the number of bars filtered over 7 days. The orange lines represent the mean over periods in between surveys derived from the unfiltered data.

In Figure 5.16, normalised, means that the time-series is divided by the maximum range over the total period between October 2013 to February 2015. This, in essence, means that the proxy for three-dimensionality is all relative to its maximum value and says very little about the absolute state. At the starting point of the time-series in October 2013 the sub-tidal area shows highly three dimensional features and the sub-tidal bar is in crescentic attached mode. In fact, the sub-tidal area did not experience such three-dimensionality over the rest of the period according to Figure 5.16. Figure 5.15a represents an example depth estimate representative for this period. As the wave power increases the proxy for three-dimensionality decreases quite rapidly. Over and after the storms the bar straightens and detaches until August, the bar mode is more between an alongshore bar and a crescentic bar. Figure 5.15b is an example from this period. The camera system experienced geometry issues with camera 2 from mid-August to end August. The effect on the depth estimation is indicated in Figure 5.17. The geometry issue led to inaccurate estimation of the bar three dimensionality. The geometry related inaccuracy covers relative long period and shows therefore as a peak in the black line in Figure 5.17.

From September to December the three dimensionality increases as the average bar position migrates shoreward [as has been observed in other cases (Stokes et al. 2015)]. However, the indicator for three-dimensionality does not reach the levels of October 2013 during the recovery

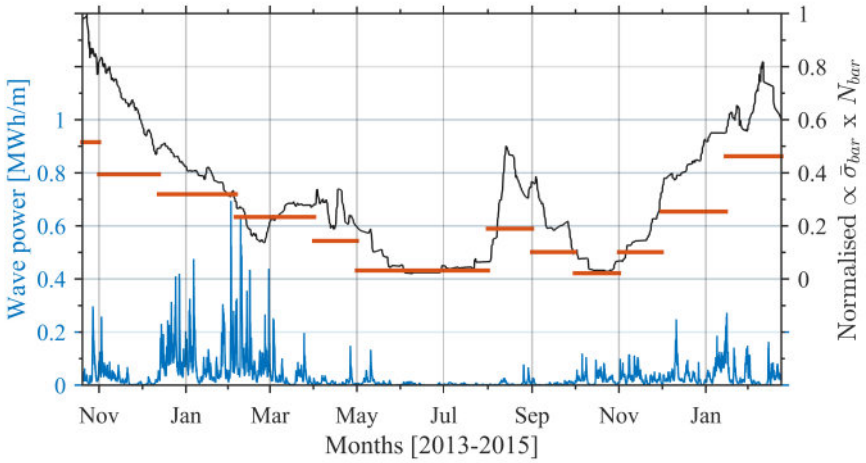


Figure 5.16: The blue line represents the wave power and the black line represents a continuous proxy for bar three dimensionality, the orange line is a mean over a period between surveys.

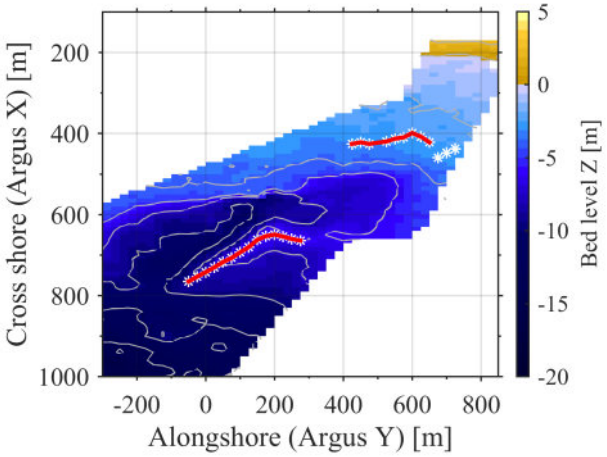


Figure 5.17: An example bathymetry estimate mid-August that indicates the geometry problem at this time and the artificial increase in three-dimensionality.

period after March 2014. Figure 5.16 shows that the three dimensionality was not introduced during the calm summer conditions. Only during moderate wave conditions does the bar become more three dimensional again and more crescentic features start to occur.

Figure 5.16 together with Figure 5.18 give more confidence to the observations of the sub-tidal bar detection. From October to December 2013, the orange line indicates three dimensional features; Figure 5.18a confirms this. After the storms, the sub-tidal bars became linear and stay relatively linear until October 2014 [confirmed by Figure 5.18b,c,d]. From November onwards, the bar becomes more three dimensional as shown in Figure 5.16 and Figure 5.18e,f. Following Figure 5.16, it shows that three-dimensionality was introduced as wave conditions got more energetic later in 2014. This is interesting since the shoreward migration of the sub-tidal bar starts a little earlier. As the bar moves shoreward, the three dimensionality seems to increase. Over that period, bar welding or cross shore bar attaching is observed in Figure 5.18e. Figure 5.18f compared to Figure 5.18e shows that the detected sub-tidal bar migrated seawards while increasing in three dimensionality.

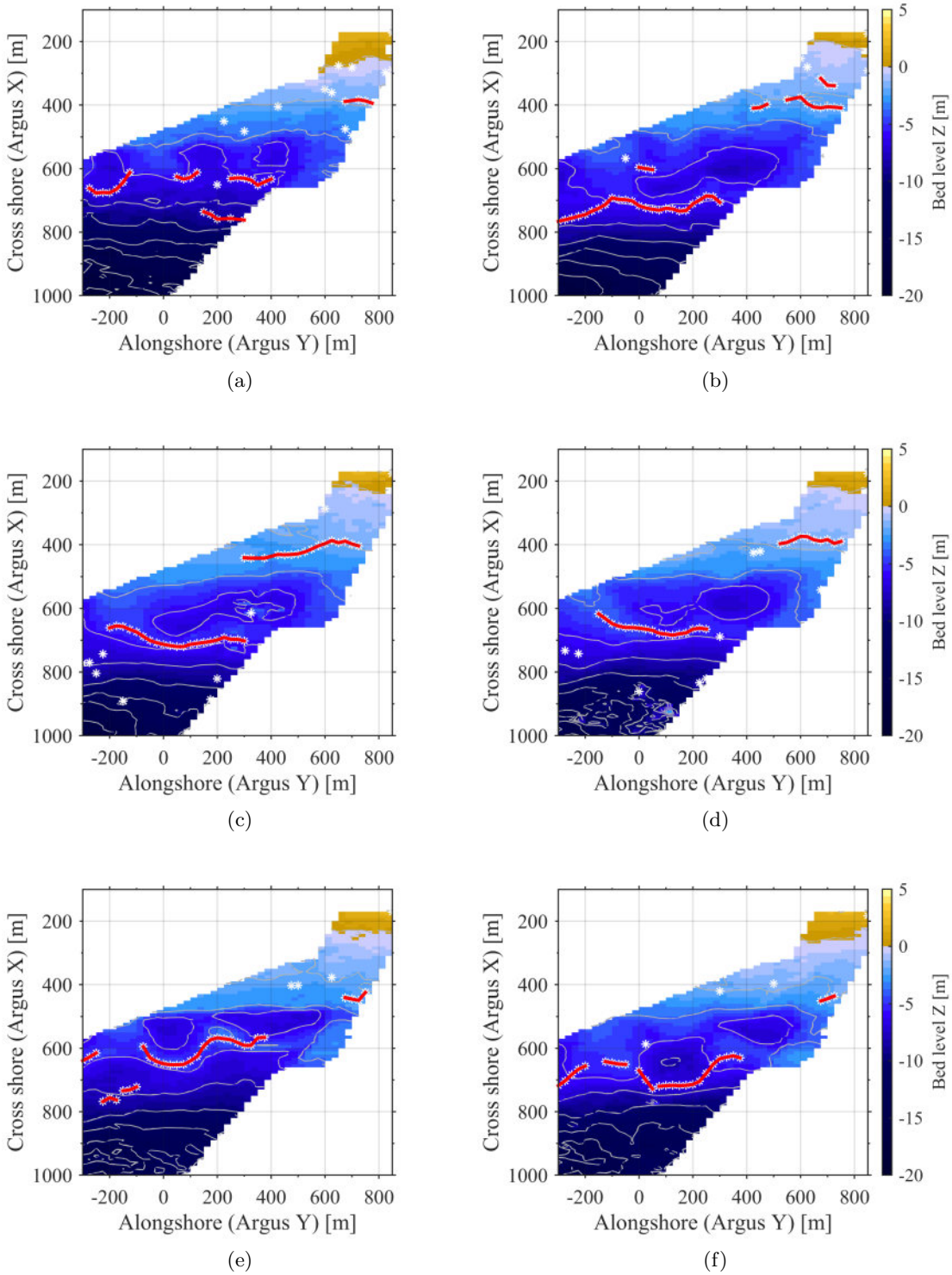


Figure 5.18: Representative example bar detections a) 20 October 2013, b) 25 April 2014, c) 31 May 2014, d) 5 September 2014, e) 27 November 2014 and f) 30 December 2014

## 5.7 Discussion

### 5.7.1 Long-term perspective of winter 2013-2014

The impact of the 2013-2014 winter season is described above and it has earlier been identified as huge and unprecedented (Masselink et al. 2015). In this section the 2013-2014 winter season and the subsequent recovery over the remainder are placed in a multiyear perspective. Figure 5.19 shows the momentary coastline derived from inter-tidal beach surveys and a modelled momentary coastline over a period from 2008 to mid-2015. The modelled momentary coastline is modelled using a disequilibrium model (Davidson et al. 2013) that is described in Section 3.6. The orange curve in Figure 5.19 [corresponding to the model] shows the interaction of instantaneous and antecedent wave conditions to determine the erosive/accretive nature of the wave conditions.

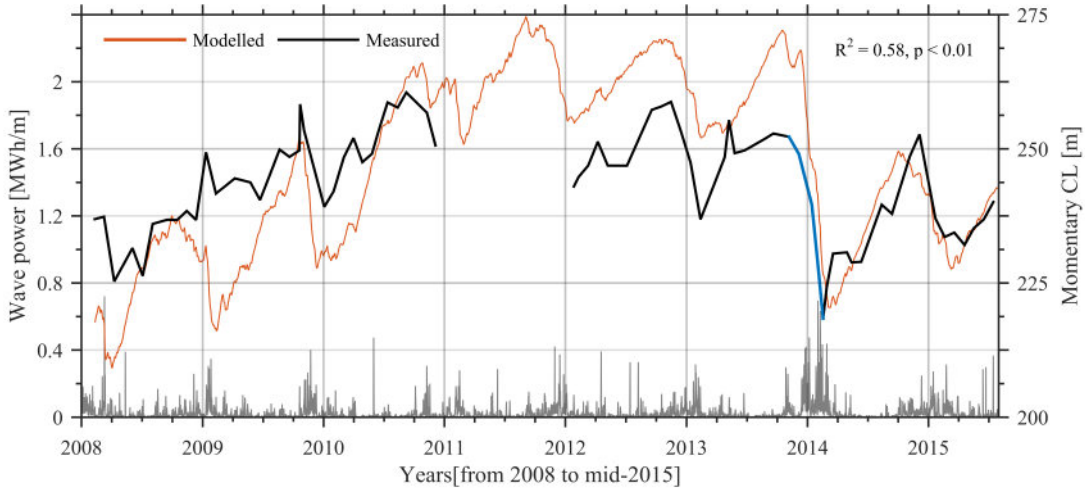


Figure 5.19: Measured [black curve] and modelled [orange curve] momentary coastline presented together with the wave power [grey curve] over a period from 2008 to mid-2015.

The measured and modelled momentary coastline curves are moderately correlated with an $R^2$ value of 0.58 and the correlation is statistically significant [$p < 0.01$]. From 2012 onwards the modelled and measured momentary coastline show a better correlation considering a $R^2$ of 0.81 and a p-value $< 0.01$. The modelled momentary curve gives a sense how extraordinary the wave conditions were at the time, while the momentary coastline shows the change in volume between two vertical reference levels. A first observation from Figure 5.19 is the seasonality in the signals. In both signals the signal decreases around the end of the year and the beginning of the following year, mostly during the winter months. In between, over the summer months,

the modelled and measured momentary coastline values increase, indicating accretion. Besides the seasonal trend, a multi-year accretional trend is found between 2008 and end-2010 in the momentary coastline data. This accretional trend continues in absence of momentary coastline data over 2011 in the time-integrated disequilibrium. Between 2012 and 2015 a slight decreasing multi-year trend is shown in Figure 5.19.

The blue part of the black line [measured momentary coastline] in Figure 5.19 represents the "seasonal" decay over the winter of 2013-2014. The momentary coastline shows a decrease from 253 m to 218 m [the lowest over the whole period from 2008 to mid-2015]. The modelled momentary coastline shows a significantly larger decay in momentary coastline of 51.5 m (from 272 m to 220.5 m). The average measured decay in momentary coastline over this period is 20.9 m excluding the 2013-2014 winter. The modelled momentary coastline shows an average decay over 2008-2013 of 20.1 m. Considering the average momentary coastline retreat it shows that the impact of the 2013-2014 winter season is respectively 67% more retreat in the measured momentary coastline and 156% more momentary coastline retreat following the disequilibrium model. This shows that the wave conditions were exceptional compared to the antecedent wave conditions [in this case the long-term average]. However, the impact that the inter-tidal beach suffered is significantly lower. Not only does the model start the winter of 2013-2014 with a substantially larger value for the momentary coastline the model does not account for sediment availability. During the mid-February surveys rockier outcrop was exposed and bed-rock at parts of the inter-tidal domain was found. This is a natural lower limit of the beach and should in fact be a lower boundary of the momentary coastline calculations.

Figure 5.19 shows the different recovery rate for the measured and modelled momentary coastline over the remainder of 2014. Compared to other years the recovery captured is probably one of the best. An intriguing aspect is that over 8 years of inter-tidal beach level data in Figure 5.19 some energetic wave conditions result in an increase in measured momentary coastline, while the instantaneous wave conditions are considered erosive compared to the antecedent wave conditions. This is most clear over the winter of 2008 to 2009 in Figure 5.19.

### 5.7.2 Alongshore wave power and three dimensionality

The sub-tidal (outer) bar transformed from a three dimensional to rather linear and the bar position migrated offshore over the course of the storms as previously observed e.g. (Lippmann & Holman 1990, van Enckevort et al. 2004, Almar et al. 2010, Price & Ruessink 2011). Almar et al. (2010) indicated that the behaviour of the outer bar is mainly controlled by the significant wave height while Price & Ruessink (2011) showed the incident wave angle drives straightening

of the bars. Numerical modelling exercises point in similar direction (Garnier et al. 2013) and evidence can be found at Porthtowan as well. Figure 5.20 shows the alongshore wave power at Porthtowan (see Figure D.1 for more information).

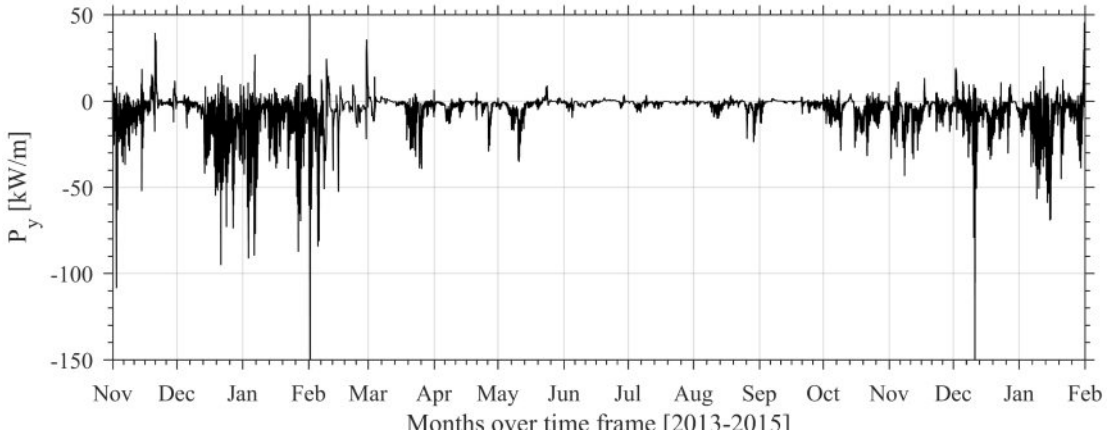


Figure 5.20: Alongshore wave power at Porthtowan

From Figure 5.20 we see that an increase in wave height during storms coincides with a significant increased alongshore wave power component, considering that the ocean swell waves come from the South. Intriguingly, as the storm deposits are activated and three dimensionality reoccurs late summer/fall 2014, the alongshore component is relatively small compared to the storm condition (half the storm condition).

## 5.8 Conclusions

In this chapter inter-tidal beach surveys and optical bathymetry estimations are used to assess the impact of the 2013-2014 winter divided in certain time sections at Porthtowan. The year-long momentary coastline indicates that the erosional impact of the 2013-2014 winter on the inter-tidal beach was between 67% to 156% larger compared to the average erosion over the period 2008-2015. The inter-tidal and cBathy data show a great loss in sediment over the storms. The sub-tidal depth estimates show that large rip-channels are present during the extreme storm conditions. Nonetheless, the total loss of sediment within the cBathy domain is limited. The recovery from this unprecedented energetic winter is captured over the remainder of 2014. Intriguingly, the inter-tidal area shows near full recovery from March to December 2014. Over the summer [March to September 2014] the inter-tidal beach shows around 58% recovery of the total 2013-2014 winter season loss. While the waves become more powerful [and presumably erosive compared to antecedent wave conditions] the beach recovers sediment

volume in the inter-tidal domain at a faster rate. This resulted in the remaining 42% recovery in just over 2 months in October, November and the first few days of December 2014.

**Storm impact observation with video-cameras**

The optical bathymetry estimates give a sought for insight in the sub-tidal storm configuration. However, the largest issue here is the accuracy dependency of the video-based depth estimations on wave conditions [in particular the wave height]. Nonetheless, bathymetry estimates were selected that were obtained during relative calm conditions within a few days of the inter-tidal beach surveys for comparison. Confidence in the estimated bathymetries is gained as signature features in the inter-tidal domain, such as rip-channels, show up in overlapping areas between the inter-tidal beach surveys and the estimated bathymetries. The configuration of the camera system at Porthtowan does most probably not allow to capture the complete storm morphodynamics as the data is not collected to storm depth of closure. A negative balance [sediment loss] of the domain has been observed. Nonetheless, substantial advantages of the video-based depth estimations such as, for example, capturing mega-rip systems and even beach rotation shows the capabilities and potential of the video-based depth estimations.

**Sub-tidal bar behaviour**

Sub-tidal bar detection has been applied to the raw video-based depth estimations. After the storms the cBathy bathymetries show that the sub-tidal bar becomes more linear and the cross shore mean of the sub-tidal bar moved offshore to around 725 m in Argus coordinates. This most probably happened over the winter storms but only shows up after March. The wave conditions are not powerful enough to move the bar onshore and introduce three dimensionality to the sub-tidal bar. As the bar migrates shoreward three dimensional features are slowly re-introduced. The shoreward migration should not be seen separately from the three dimensionality estimator. On the one hand the process is likely to be natural [bar merging / welding] and on the other hand with the three dimensionality and large standard deviation the determination of the mean seems also to be more shore wards. The bar detection estimates the bar reasonably well and can be used for a three dimensionality analysis. Nonetheless, the bar detection is sensitive to the quality of the cBathy estimate and requires some filtering.

# Chapter 6

# The application of EOFs to video-based bathymetries

## 6.1 Introduction

The video-based depth estimates show their added value of revealing the sub-tidal domain over storm periods in Chapter 5. The accuracy of the video-based depth estimates is however strongly restricted by the incident wave conditions. Chapter 4 and in particular Section 4.7.2 shows that as the wave height increases the accuracy diminishes. The bias is shown to be negative during more energetic waves. The estimates show erosion as an artefact of the depth estimation but more energetic waves are intrinsically linked to erosion as well. The artefact and real erosion should be filtered in a way to use the video-based depth estimations on a much higher time-scale [hourly]. This filtering is achieved in this Chapter by applying Empirical Orthogonal Functions to the video-based depth estimates in order to filter and obtain principle modes of morphological change. The principle modes of morphological change are subsequently used to investigate storm impact on a storm by storm basis.

In the next Section, the application of the EOFs to the video-based depth estimations and the resulting principle components are presented. The section that follows shows how the EOF modes are used to filter the video-based depth estimations and the volumetric data that will be used in the remainder of the Chapter to analyse the storm by storm impact. Volumes are derived from the EOF modes to be used in the storm by storm impact. The hourly volume changes are compared to wave power, tidal elevation, tidal range and storm duration to assess

the storm impact and subsequent recovery.

## 6.2 Application of EOFs at Porthtowan

In this Section the complex EOF-technique as described in Section 3.8 is applied to the hourly video depth estimates. The EOF results are analysed and explained step by step. First, the modal confidence in all the EOF modes is assessed in order to identify which modes are statistically significant and will be used in further analysis. The modal results of the statistically significant EOF modes are presented in the spatial domain. Subsequently the spatial results are presented including an artificial synthetic phase shift to imitate what the effect of a certain temporal phase shift involves. The alongshore average behaviour is explained in a similar fashion and the Section ends with an overview of which temporal phase conditions at what part of the cross shore domain shows an accretive or erosive behaviour.

### 6.2.1 Input dataset and modal confidence

The complex EOF procedure is applied to the video-based depth estimation dataset. This dataset is de-trended in time to represent the variation around a temporal mean bathymetry, as discussed in Section 3.8. Figure 6.1a shows the mean bathymetry as a result of de-trending the input matrix. After de-trending the input data a Hilbert transformation is applied to make the dataset complex, as described in detail in Section 3.8.1. The slope of the mean bathymetry shown in Figure 6.1a is 0.0168. This value for the beach slope is in line with the computed value using the topographic beach surveys, presented in Section 3.2. Intriguingly, the resulting bathymetry is not completely featureless. The bed-levels in Figure 6.1a indicate that the three-dimensional features between 500 and 700 m cross shore are persistent over a large part of the dataset. Potentially a part of the variability, captured in one of the EOF modes, will fill or straighten these features.

#### Modal confidence at Porthtowan

The EOF procedure is applied to the total depth estimates dataset obtained at Porthtowan in order to reduce the noise levels [using the EOFs as filter] and obtain statistically significant principle modes. The EOF analysis results in a large set of principle modes and the question remains of how many EOF modes to consider. A confidence interval supports determining which components to neglect by assigning a probability or reliance per EOF component. Through a

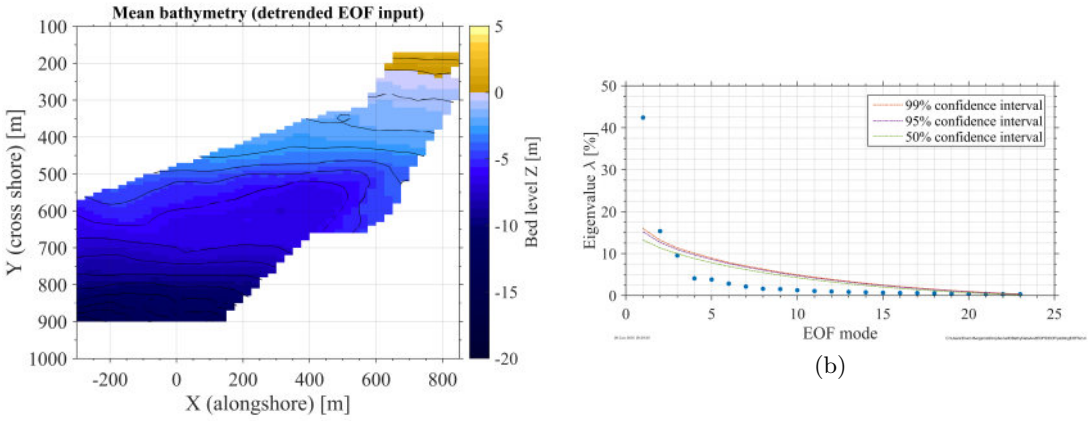


Figure 6.1: a) Mean bathymetry is subtracted from the input matrix $A$. All the variation found in the EOF modes varies around this mean bathymetry. b) Monte Carlo simulation analysis to assess the statistical relevance of the EOF modes for the Porthtowan depth estimates dataset. The blue dots represent the found eigenvalue per EOF mode, the lines indicate the 99%, 95% and 50% confidence interval.

Monte Carlo analysis confidence intervals depending on the number of degrees of freedom are obtained. These confidence intervals give threshold of the statistical relevance per EOF mode. For the EOF analysis this means that the confidence interval/threshold has a higher value of $\lambda$ for the first EOF mode than the second, so on and so forth. The obtained EOF-modes with a higher $\lambda$-value than the threshold-$\lambda$ are statistically significant.

The Monte Carlo simulation analysis [repetition of varying input of the method based on the degrees of freedom of the EOF input], is carried out for the EOF analysis on the Porthtowan dataset. Figure 6.1b shows the calculated 99%, 95% and 50% confidence interval through a Monte Carlo analysis. The blue dots in Figure 6.1b represent the actual eigenvalues [$\lambda$] per mode. Figure 6.1b indicates that the first two modes from the Porthtowan dataset are exceeding the 95-99% threshold and are therefore statistically reliable. The third mode is statistically relevant if the confidence interval is below 50%. Nonetheless, 50% confidence in a single mode is not robust enough and here the 95% confidence interval is considered the minimum. Following the 95% confidence interval Figure 6.1b shows that only the first two modes are statistically significant. In the remainder of this work only the first two modes are considered and these two modes together represent 57.75% of the total variance.

### 6.2.2 Spatial amplitude and phase patterns

The spatial amplitude and phase of the two statistically relevant and most dominant EOF modes are presented in Figure 6.2.

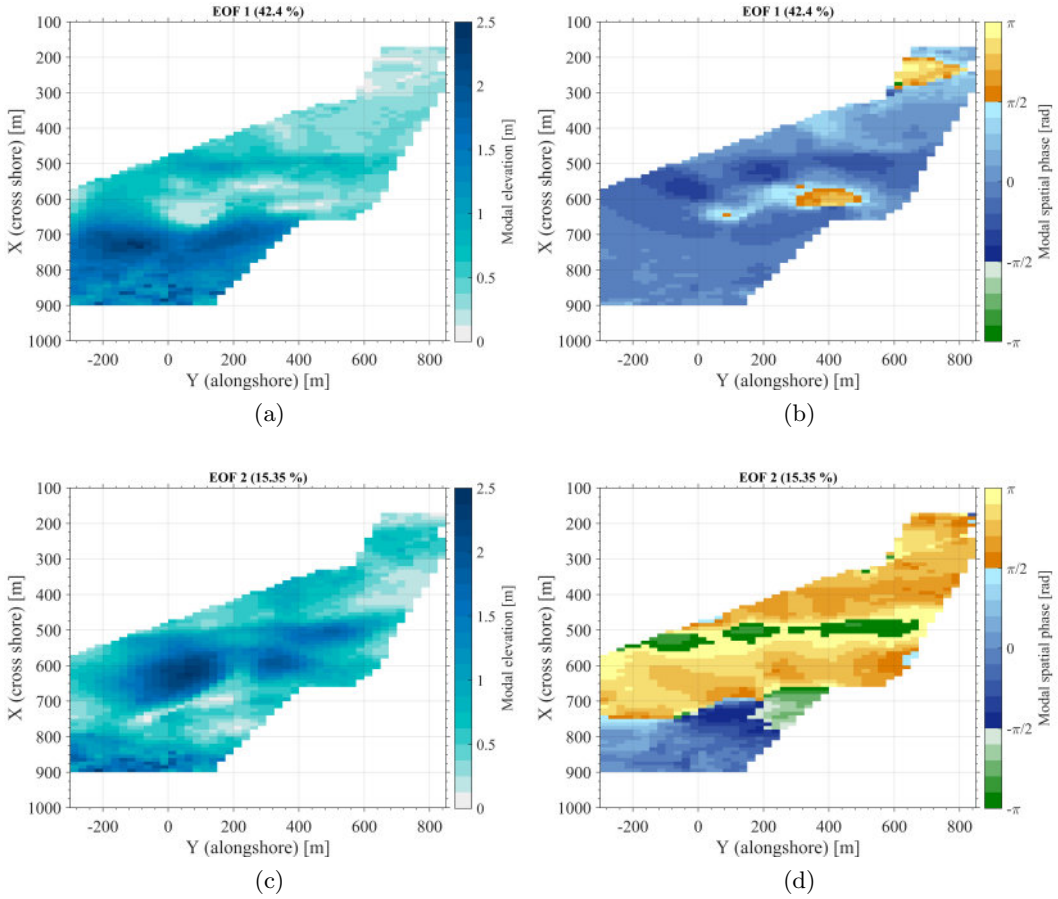


Figure 6.2: Two most dominant modes at Porthtowan. a) and c) represent the spatial amplitude and the b) and d) show the corresponding spatial phases.

Figure 6.2a,c represent the spatial amplitudes for respectively the first and second mode. Figure 6.2b,d show the corresponding spatial phases.

**Spatial amplitudes** $[\xi(x,y)]$ Large spatial amplitudes represent potential areas of large temporal variations, vice versa for small amplitudes. Considering this, Figure 6.2a reveals that large temporal excursions around the mean bathymetry are going to be found in the offshore region of the domain and smaller temporal excursions in the shallowest parts of the domain. The spatial amplitude also shows that the identified troughs in the mean bathymetry do not experience much change over time since the spatial amplitude is small. The spatial amplitudes

associated with the second mode are presented in Figure 6.2c and reveal that in the second principle mode the largest temporal excursions occur in the seaward side of the sub-tidal bar region. The inter-tidal and offshore domain have similar values for the amplitude with much lower excursions in general except for the most offshore part of the domain.

**Spatial phases** $[\theta(x,y)]$ The spatial phases are the base phases for the domain and in essence represent the relation between neighbouring depth points. The spatial phases indicate the state of the bathymetry compared to the other points. The corresponding spatial phases are presented in Figure 6.2b for the first mode and 6.2d for the second mode. The colour division indicates a positive (between $-\pi/2$ and $\pi/2$) and negative (between $\pi/2$ and $-\pi/2$) response to the amplitude [considering $\cos(\theta_n(x,y))$]. Here we refer respectively to positive or negative frame. Figure 6.2b shows that the spatial phase for the 1st mode is quite equally distributed and mostly in the positive frame (blue). Some parts are in the negative domain (orange/green) and those areas correspond with areas of limited spatial amplitudes. Figure 6.2d shows that most of the domain in the second mode is in the negative frame (orange/green), only the most offshore part is in the positive frame.

**Spatial amplitude and phase together** As described above, the spatial results of the complex EOF is a set of spatial amplitudes and spatial phases. The spatial phases determine the mutual relation between depth points and the amplitude is the magnifier. A near constant phase across the whole domain for the first EOF-mode in Figure 6.2b suggests that all the depth points behave in a similar fashion; as one becomes maximal [$\cos(0)$] the others do as well. The spatial amplitude reveals the behaviour of the first mode. The spatial distribution of the amplitudes of the first mode can be considered as the temporal excursion envelope. Considering this, one can see that first mode represents more or less a tail wave effect [$\prec$] in the cross shore direction, the further offshore the higher the maximum variation. The second mode is more challenging to visualise but considering the large amplitudes between 500 m and 700 m large excursion will be found there. Besides, the spatial phase in Figure 6.2d shows more variation and indicates a switch in sign around 750 m. The amplitudes are generally small around this cross shore point and increase further offshore. This means that a see-saw effect for the second mode can be expected with a nodal point around X = 750 m.

### 6.2.3 Spatial pattern variation due to phase shift

The spatial amplitude and phase only do not deliver a complete picture of the behaviour of the EOF modes. The reconstruction of the modes together also includes temporal components [amplitude $\eta_i(t)$ and phase $\psi_i(t)$] following Equation 3.27. The temporal amplitude should be seen as 'just' a time-varying multiplier: values greater than 1 amplify the spatial pattern and values lower than 1 reduce the spatial maps of Section 6.2.2. The temporal phase forces a phase shift which applies uniformly to the complete domain. In this Section the temporal phase shift is imitated with synthetic phase shifts between $-\pi$ and $\pi$ with steps of $\pi/4$ to investigate the behaviour that can be expected per mode. The temporal amplitude is neglected or set to 1 so that Equation 6.1 is followed to reconstruct synthetic cases presented in Figures 6.3, 6.4 and 6.5.

$$Z_{part}(x,y,t) = \xi_i(x,y)\cos(\theta_i(x,y) + \psi_i(t)) \tag{6.1}$$

All the three Figures [6.3, 6.4 and 6.5] show the first EOF mode in the left column and the second EOF mode in the right column. The phase shift starts with $+\pi$ in Figure 6.3a,b and ends with $-\pi$ in Figure 6.5e,f. The behaviour of EOF mode 1 with different $\psi_i(t)$ value indicates that the initial observation from just the amplitude map [a cross-shore tail wave effect with large variation in the offshore domain ($\prec$)] is not far off. The second EOF mode represents more a cross-shore see-saw behaviour [alternating increase/decrease onshore decrease/increase offshore] with the rotational point of the beach around X = 750 m. In the cross-shore domain around 500 to 750 m (shoreward/around the rotational node) the three dimensional features are diminished or pronounced depending on the added phase $\psi_i(t)$.

### 6.2.4 Alongshore average behaviour

To highlight and capture the behaviour with synthetic phase-shifts in one figure the impact of the phase shift is averaged over the alongshore direction. This alongshore average behaviour in combination with the obtained temporal amplitudes and phases is later used for the storm by storm impact analysis. In this section the cross shore domain is divided in zones that describe a similar behaviour of accretion/erosion. In this way, an overall understanding of the behaviour under certain temporal phases is achieved. However, this will only describe the cross shore behaviour. Figure 6.6 shows two main components; 1) alongshore average contribution to the bed level of the modes with varying phase shifts and 2) the minimum and maximum impact of the mode on the mean depth profile before multiplication with the temporal amplitude [$\eta_i(t)$].

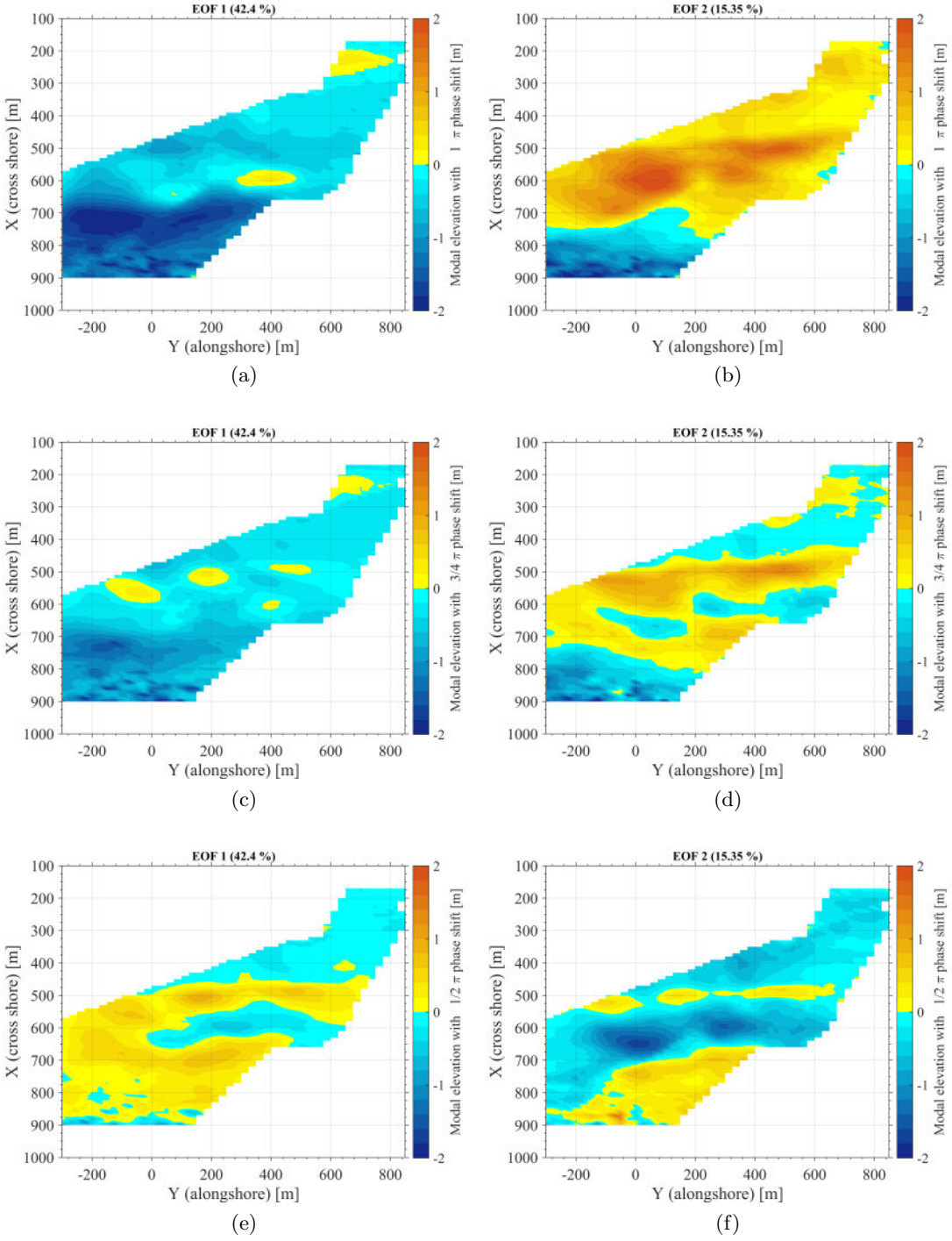


Figure 6.3: Spatial EOF modes with phase shift, a) 1st mode + $\pi$ shift, b) 2nd mode + $\pi$ shift, c) 1st mode + $\frac{3\pi}{4}$ shift, d) 2nd mode + $\frac{3\pi}{4}$ shift, e) 1st mode + $\frac{\pi}{2}$ shift, f) 2nd mode + $\frac{\pi}{2}$ shift

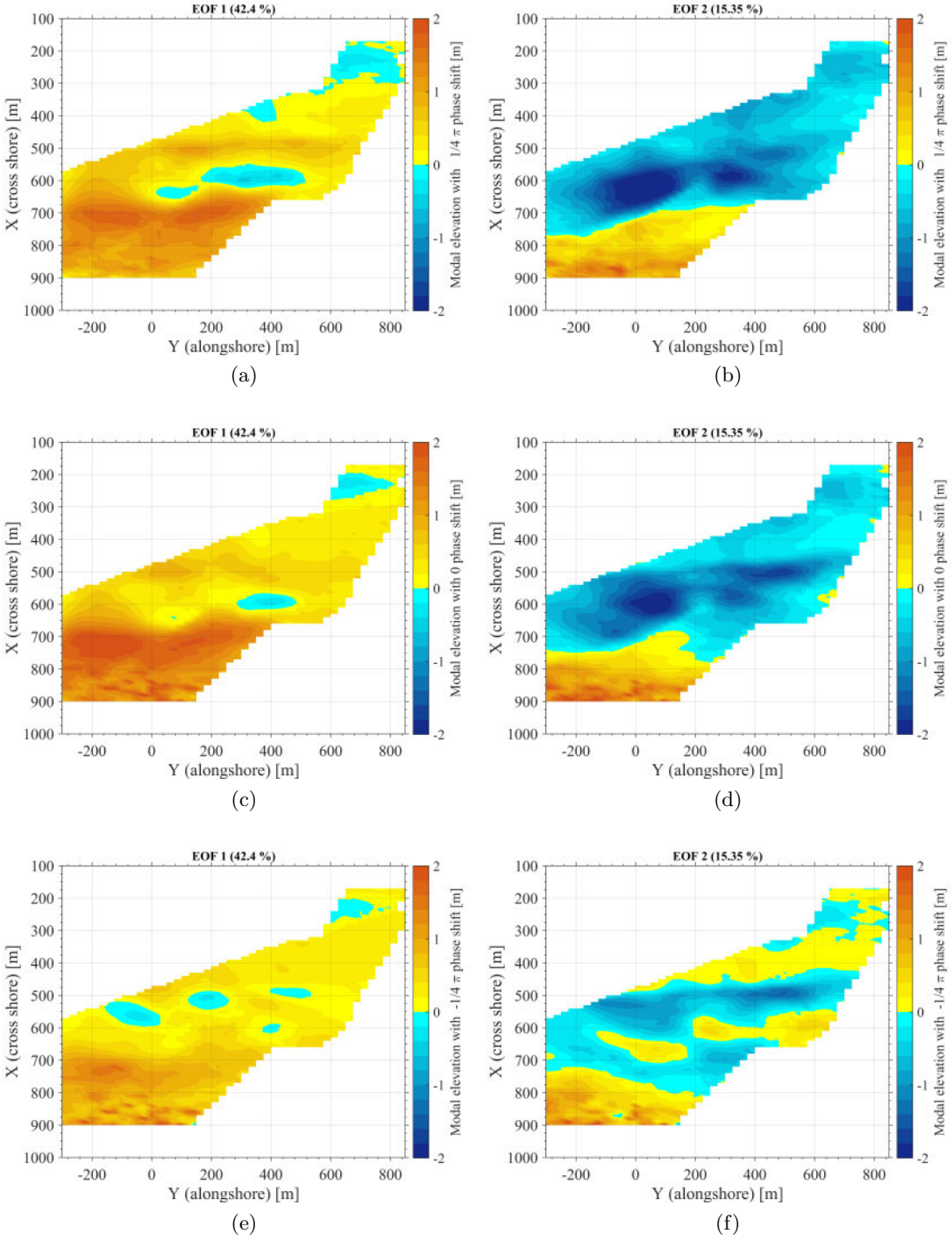


Figure 6.4: Spatial EOF modes with phase shift, a) 1st mode + $\frac{\pi}{4}$ shift, b) 2nd mode + $\frac{\pi}{4}$ shift, c) 1st mode + 0 shift, d) 2nd mode + 0 shift, e) 1st mode $-\frac{\pi}{4}$ shift, f) 2nd mode $-\frac{\pi}{4}$ shift

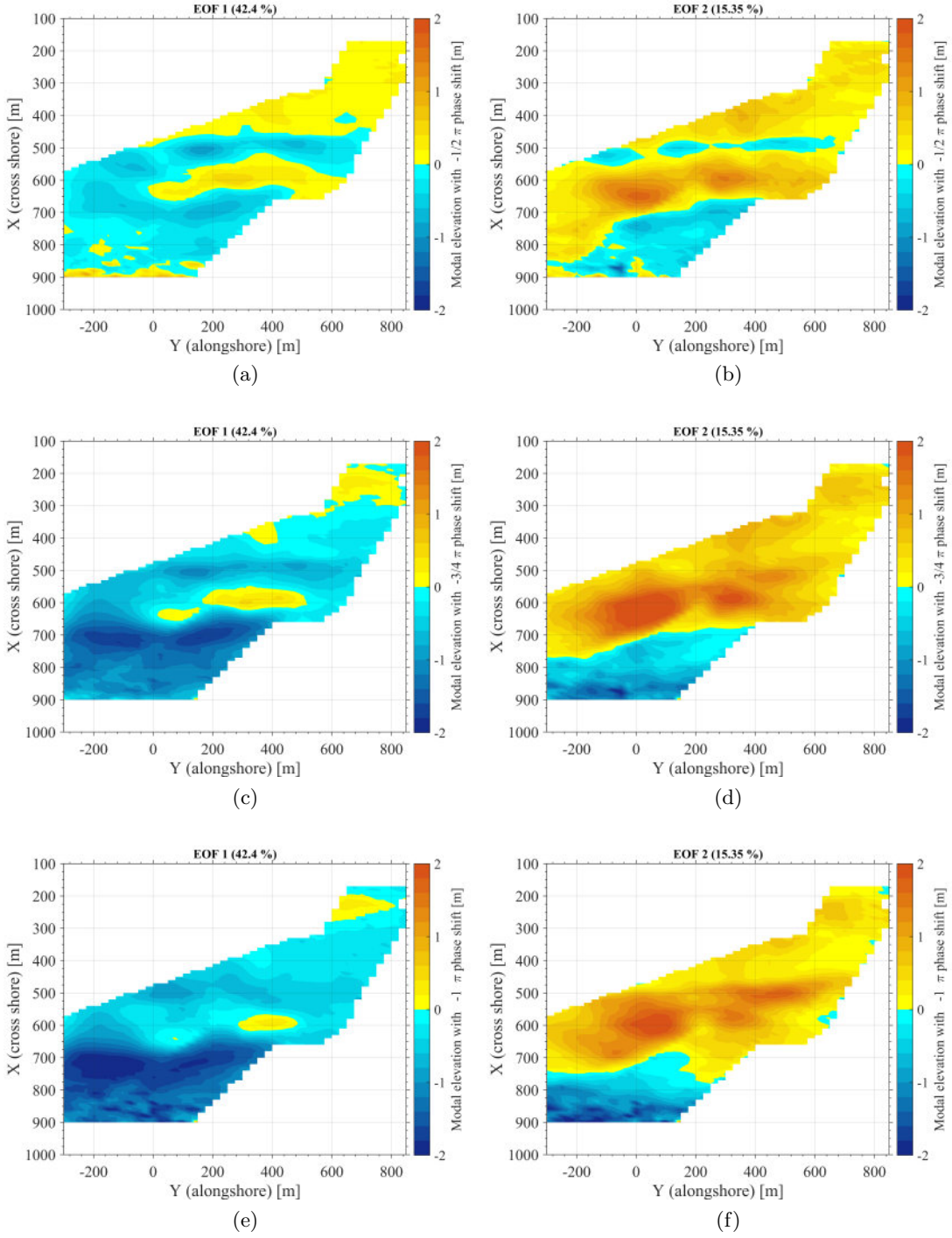


Figure 6.5: Spatial EOF modes with phase shift, a) 1st mode $-\frac{\pi}{2}$ shift, b) 2nd mode $-\frac{\pi}{2}$ shift, c) 1st mode $-\frac{3\pi}{4}$ shift, d) 2nd mode $-\frac{3\pi}{4}$ shift, e) 1st mode $-\pi$ shift, f) 2nd mode $-\pi$ shift

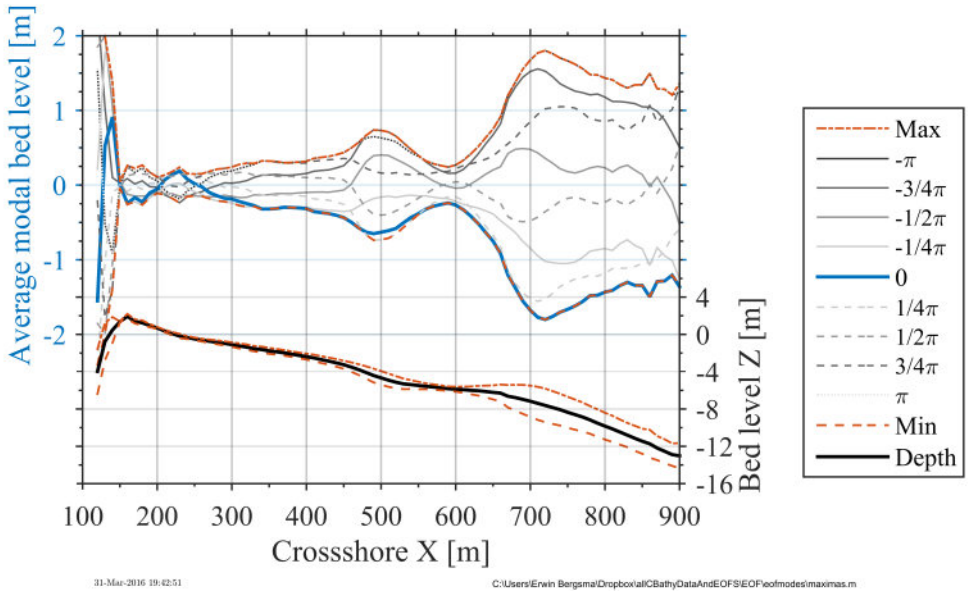


(a)

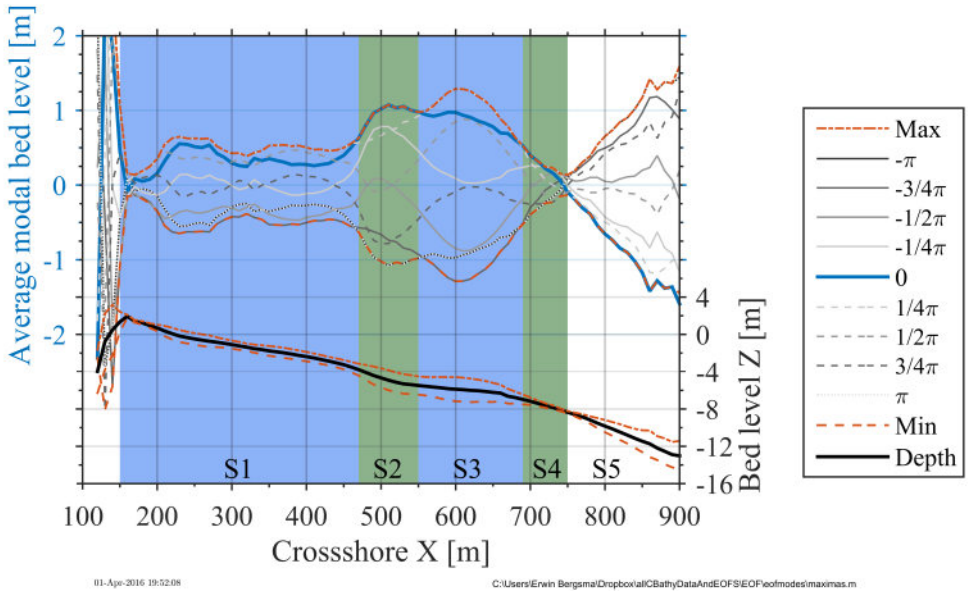


(b)

Figure 6.6: Alongshore average EOF mode profiles with different (artificial) temporal phase shifts. a) represents the first EOF mode and b) corresponds to the second EOF mode. The mean profile (black line) is plotted in the bottom of a) and b) with the minimum and maximum impact of the EOF modes before multiplication with the temporal amplitude.

Consider Figure 6.6a, the first mode of the depth estimates. Figure 6.6a shows that the largest bed level variability occurs in the offshore part of the cross shore domain [X $>$ 700 m] as suggested by the observed behaviour above. Also, around X = 500 m of the cross shore domain, on both sides approximately 50 m shows significant variation. Most of the cross shore domain follows a similar trend of accretion/erosion for a given pattern of change in phase shift. Only between 200 and 250 m in cross shore direction the behaviour is inverse to the rest of the domain. At the starting point [$\psi_1(t) = -\pi$], the cross shore profile of the first mode is accreted to its maximum. In this stage the cross shore profile follows the orange dashed-dotted line. As the phase shift moves from $-\pi$ towards 0 [blue line] the accretive stage changes into an erosive stage. At $\psi_1(t) = 0$ the first EOF mode is in its most erosive stage. As the phase shift changes from 0 to $\pi$ an inverse behaviour is observed. The contribution of the first mode is marginal when the phase shift is in the order of $\pm\pi/2$ [$|\psi_1(t)| = \pi/2$].

The second EOF mode is a little more complex due to the inhomogeneous response over the cross shore domain. Figure 6.6b shows the results for the second EOF mode. The cross shore domain is divided in 5 sections where a different phase shift results in minima and maxima. Section 1 [S1] starts at X = 150 m and continues until X = 470 m. From X = 470 m to X = 550 m is section 2 [S2]. Section 3 [S3] goes from X = 550 m to X = 690 m. The fourth section [S4] starts at X = 690 m and reaches until 750 m cross shore. Section 5 [S5] is resembles the offshore part of the domain for $X > 750$ m. The section can be grouped based on their behaviour: section 1 and 3 follow the same pattern as the phase shift changes and section 2 and 4 correspond to the same response to an advancing phase shift. The grouped sections correspond to a similar colour scheme [blue S1, 3 and green S2, 4] in Figure 6.6. Section 5 is the inverse of section 2 and 4. In the paragraph below, the response of the grouped sections 1, 3 and 2, 4 are explained.

For sectional-zone 1, 3 the second EOF mode is its most erosive state when the phase shift is around $-3\pi/4$. The most accretive stage is reached as the phase shift changes toward $\pi/4$. When the phase shifts changes advances towards $-3\pi/4$ the mode shows erosion and moves "forward" to the most erosive state. For section 2 and 4 the most erosive state of the $2^{nd}$ EOF mode corresponds to a $\psi_2(t) = \pm\pi$. The maximum accretive contribution of the second mode for the sections 2 and 4 is achieved when the phase shift develops towards 0. When the phase shift advances towards $\pm\pi$ the second EOF mode for sections 2 and 4 moves back to the most erosive state. The behaviour at section 5 is the inverse of sections 2 and 4. This simplification of the behaviour does not tell the actual contribution of the mode at a given phase shift. This should be seen as a indicative band of phase shift behaviour. The contribution of the modes is summarised in Table 6.1.

| Behaviour | EOF mode 1 | EOF mode 2 |
|---|---|---|
| **Accretive** | if $\frac{d\psi_1}{dt} > 0$ and $0 < \psi_1(t) < \pi$<br><br>if $\frac{d\psi_1}{dt} < 0$ and $-\pi < \psi_1(t) < 0$ | **S1 and S3**<br>if $\frac{d\psi_2}{dt} > 0$ and $-3\pi/4 < \psi_2(t) < \pi/4$<br><br>if $\frac{d\psi_2}{dt} < 0$ and $\pi/4 < \psi_2(t) < 5\pi/4$<br><br>**S2 and S4**<br>if $\frac{d\psi_2}{dt} > 0$ and $-\pi < \psi_2(t) < 0$<br><br>if $\frac{d\psi_2}{dt} < 0$ and $\pi < \psi_2(t) < 0$<br><br>**S5**<br>if $\frac{d\psi_2}{dt} > 0$ and $0 < \psi_2(t) < \pi$<br><br>if $\frac{d\psi_2}{dt} > 0$ and $0 < \psi_2(t) < -\pi$ |
| **Erosive** | if $\frac{d\psi_1}{dt} > 0$ and $-\pi < \psi_1(t) < 0$<br><br>if $\frac{d\psi_1}{dt} < 0$ and $0 < \psi_1(t) < \pi$ | **S1 and S3**<br>if $\frac{d\psi_2}{dt} > 0$ and $\pi/4 < \psi_2(t) < 5\pi/4$<br><br>if $\frac{d\psi_2}{dt} < 0$ and $-3\pi/4 < \psi_2(t) < \pi/4$<br><br>**S2 and S4**<br>if $\frac{d\psi_2}{dt} > 0$ and $\pi < \psi_2(t) < 0$<br><br>if $\frac{d\psi_2}{dt} < 0$ and $-\pi < \psi_2(t) < 0$<br><br>**S5**<br>if $\frac{d\psi_2}{dt} > 0$ and $0 < \psi_2(t) < -\pi$<br><br>if $\frac{d\psi_2}{dt} < 0$ and $0 < \psi_2(t) < \pi$ |

Table 6.1: Overview of the morphological behaviour per mode per change in phase shift $\psi$

## 6.3 Results

### 6.3.1 Temporal results and volume estimation

The Empirical Orthogonal Functions are applied to the video-based depth estimation dataset obtained at Porthtowan to eliminate/reduce noise and extract principle morphological modes following Section 3.7.1. Figure 6.7 shows the temporal amplitude and phase for the representative two modes [following the modal confidence analysis in Section 6.2.1]. From the phases [represented by the grey line in Figure 6.7] in combination with Table 6.1 insight in the temporal behaviour and the state of the mode is obtained. The temporal amplitudes [blue lines Figure 6.7] acts as an amplifier [$\eta > 1$] or leads to a reduction [$\eta < 1$]. The phase of the first mode [Figure 6.7a] shows an erosive state of the mode over the period October to early November followed by a period where the mode switches toward accretion towards the end of December. From December to early February the phase indicates erosion. In early January, the sign of the slope of the phase switches but the domain sign of the phase switches simultaneously. From mid-February until October, the first mode shows accretion. After October the first mode turns to an erosive state again. If the value of the phase for the first mode is between $-\pi/2$ and $\pi/2$ it means that the resulting alongshore profile is zero to negative as $\psi = 0$ is the most erosive state. Figure 6.7 shows that the phase of the first mode is mainly between $-\pi/2$ and $\pi/2$ during the winter months and outside this phase domain in the summer months. This means that the first modes alongshore average value shows erosion during the winter and accretion during the summer.

The second mode is more complex and the cross shore profiles are separated into five sections following Section 6.2.4 and Figure 6.6b. Figure 6.7b shows that the phase of the second mode indicates that the second mode is in an accretive state October to March. Between March and mid-May the second mode switches rapidly between erosive and accretive states. From mid-May to January 2015 the sections S1 to S4 are predominantly in an erosive state while the offshore domain is in an accretive state. In January this switches to an erosive state offshore and accretive state in sections S1 to S4. The temporal amplitude and phase combined per mode give the total instantaneous [hourly] alongshore average contribution. This can be plotted in time as a time-stack as shown in Figure 6.8.

Figure 6.8 shows the two representative modes (6.8a and c) and in the middle (6.8b) the time-integrated disequilibrium stress. Figure 6.8a shows the time stack of the first mode. From Figure 6.8a three well distinguishable periods are identified. From October 2013 to March 2014 the modal elevation is generally negative, from March 2014 to mid-October generally positive

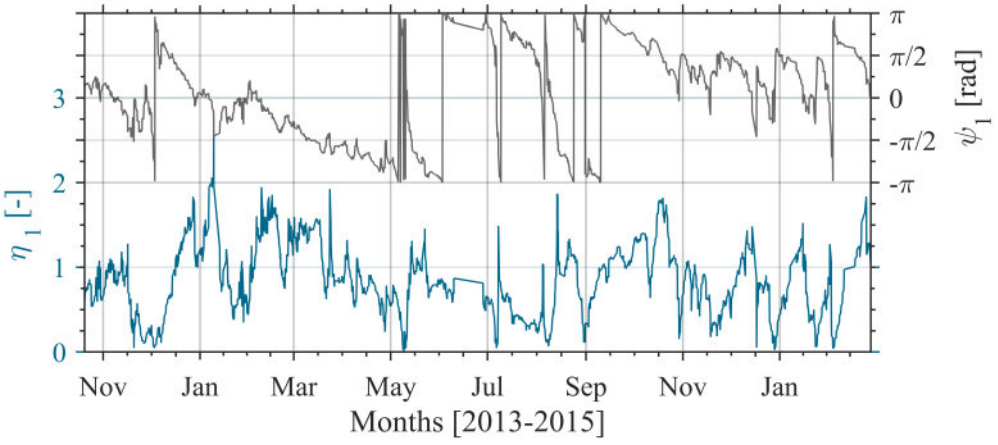


(a)

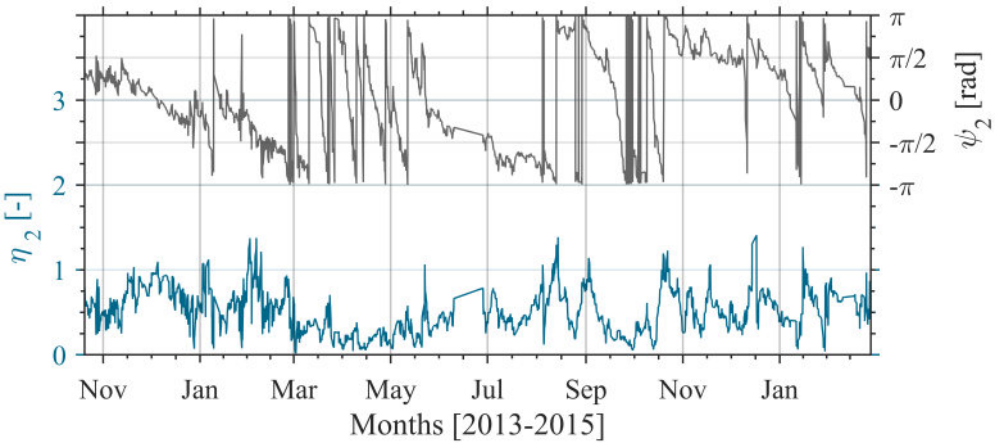


(b)

Figure 6.7: a) Represents the amplitude (blue) and phase (grey) of the first EOF mode. b) Represents the amplitude (blue) and phase (grey) of the second EOF mode.

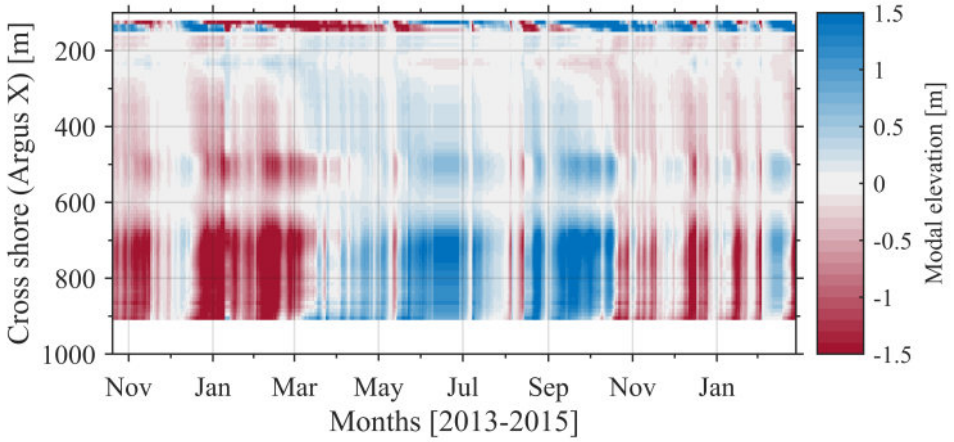


(a)

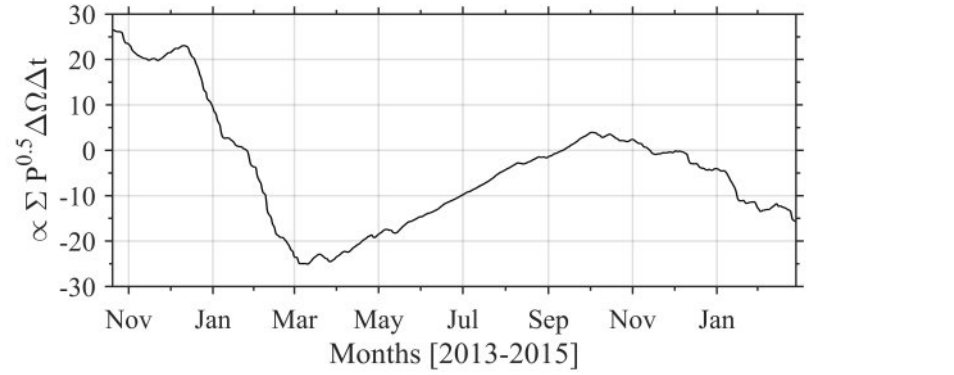


(b)

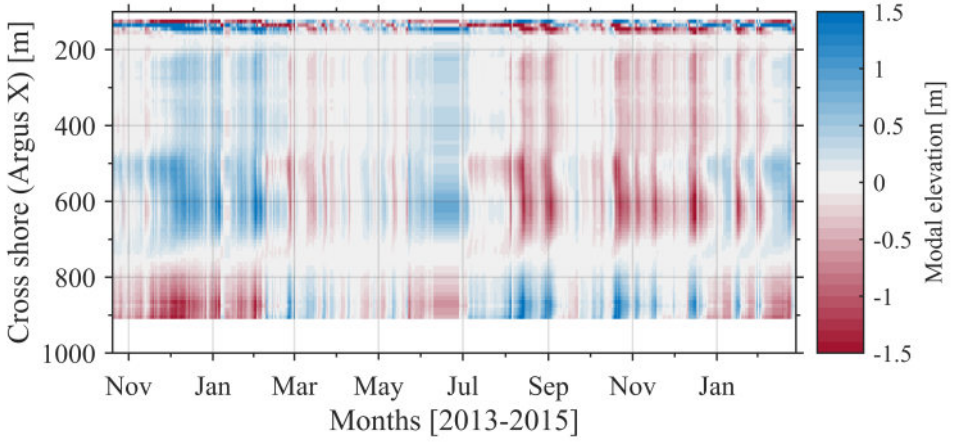


(c)

Figure 6.8: a) Time stack of the alongshore average profile [combination of spatial amplitude and phase and temporal amplitude and phase] corresponding to the first EOF mode [42.4% of the variance]. b) Modelled disequilibrium as described in Section 5.2 - c) Time stack of the alongshore average profile [combination of spatial amplitude and phase and temporal amplitude and phase] corresponding to the second EOF mode [15.35% of the variance]

and from mid-October to mid-January negative again. The second mode [Figure 6.8c] is merely positive for section S1 to S4 between October 2013 to February 2014, and between February and August the contribution of the second mode is marginal. From August 2014 to January 2015 section S1 to S4 are mostly negative and offshore positive. From January onwards, the mode switches to negative offshore and positive for section S1 to S4. The disequilibrium stress curve [Figure 6.8b] shows how closely related the disequilibrium stress and the modal elevations are for in particular for EOF mode 1. The time-integrated disequilibrium stress [black line] shows that the sign of the slopes corresponds to the dominant colour (+ = blue, − = red) in Figure 6.8a. The first EOF mode and the disequilibrium stress have a correlation coefficient of 0,62.

### EOF-results compared to beach surveys

The time-stacks, as shown above, can be summed in cross shore direction and shown cumulatively over time as presented in Figure 6.9; containingthe cumulative volumetric change of the first two modes (together representing 57.7 % of the variability) in comparison to the inter-tidal beach survey (yellow line).

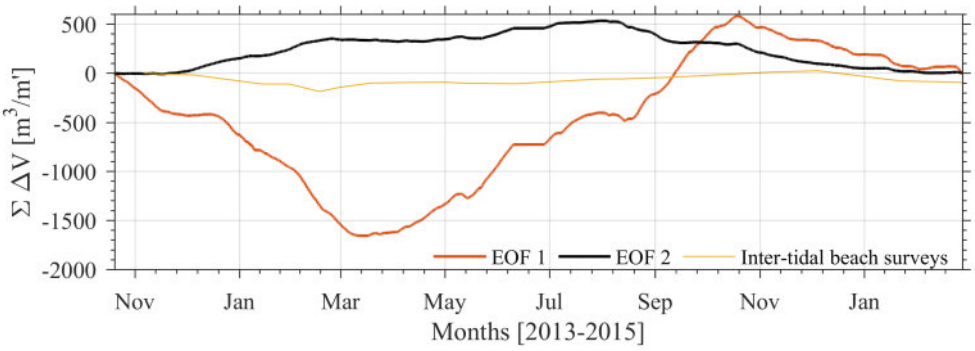


Figure 6.9: Cumulative volume per EOF-mode and for the inter-tidal beach survey.

The difference in absolute value can be explained by the fact that the EOF-modes represent a certain modal change, the sum of all 1500 components results in effectively the raw input. Also, the EOF results cover the total domain, inter- and sub-tidal regions. For comparison with other components that represent morphological change such as the momentary coastline and disequilibrium model (chapter 5) all values are normalised and presented in Figure 6.10.

Figure 6.10 shows the time-integrated disequilibrium stress [orange line], Momentary coastline [black line] and the instantaneous volume per m alongshore stretch from the first and second EOF mode is presented by the blue and purple lines. The normalised values for the first EOF mode show correspondence to the values for the momentary coastline and in particular the

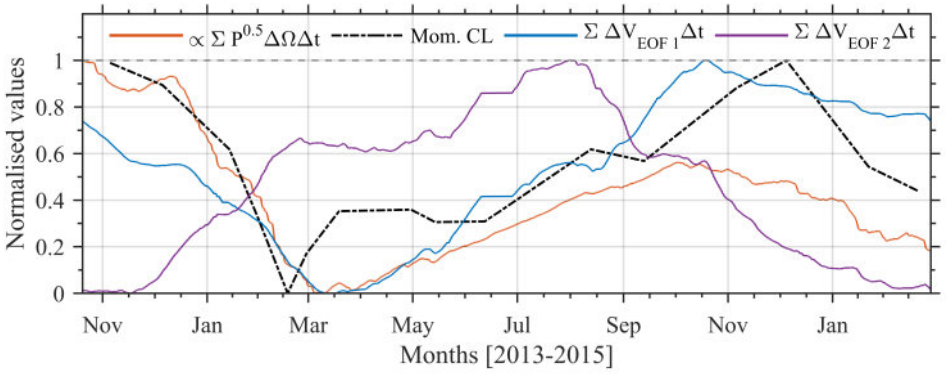


Figure 6.10: Orange line represents the normalised integrated disequilibrium based on wave data. Black line is the normalised momentary coastline of the inter-tidal beach surveys. The blue and purple line are the volume change for respectively the first and second EOF mode, integrated over time for the whole camera domain. All data are normalised over the time frame 2008 - 2015

time-integrated disequilibrium. The latter is interesting because the disequilibrium is merely a wave condition-driven parameter [after determination of $D$, $\Phi$ and a constant $\bar{w}_s$]. The first EOF mode represents erosion/accretion over the total cross section. Figure 6.10 confirms that the overall lowering of the beach and accretion is merely a direct function of the disequilibrium $\Delta\Omega$. The second EOF mode, representing cross shore beach rotation, does not show this direct relation to the disequilibrium. While the 2013-2014 winter storms hit, the second EOF mode shows an increase in volume. The volume stays more or less constant from end February to May after which the volume reaches its maximum around August. The volume decreases toward October to similar levels as at the end of the previous winter. As the waves pick up over the winter the total volume of EOF mode decreases towards its lower limit.

### 6.3.2 Hourly wave power versus morphology

Section 6.3.1 shows the volumetric changes derived from the EOF-results on an hourly basis. The volumetric change and associated shoreline changes are merely related to wave power in equilibrium models such as Hanson (1989), Dean (1991), Kramer (2005), Davidson et al. (2013) and the quantification of individual storm impact is mostly related to wave power (Birkemeier et al. 1999, Harley et al. 2009, Splinter et al. 2014). Here, the EOF-based volume changes are presented against the corresponding wave power. Offshore wave power is calculated following Equation 6.2, where $\rho$ is water density, $g$ gravitational acceleration, $H_s$ is the significant wave

height and $T_p$ relates to the peak wave period.

$$\sum P = \int_0^N \frac{\rho g^2}{64\pi} H_s^2 T_p \Delta t \tag{6.2}$$

Figure 6.11 shows hourly volumetric impact plotted against instantaneous wave power. The x-axis of Figure 6.11 is plotted on logarithmic scale. A direct relation between hourly wave power and volumetric change is less clear than one might expect but a log-relationship between the waver power and volumetric change is visible in Figure 6.11.

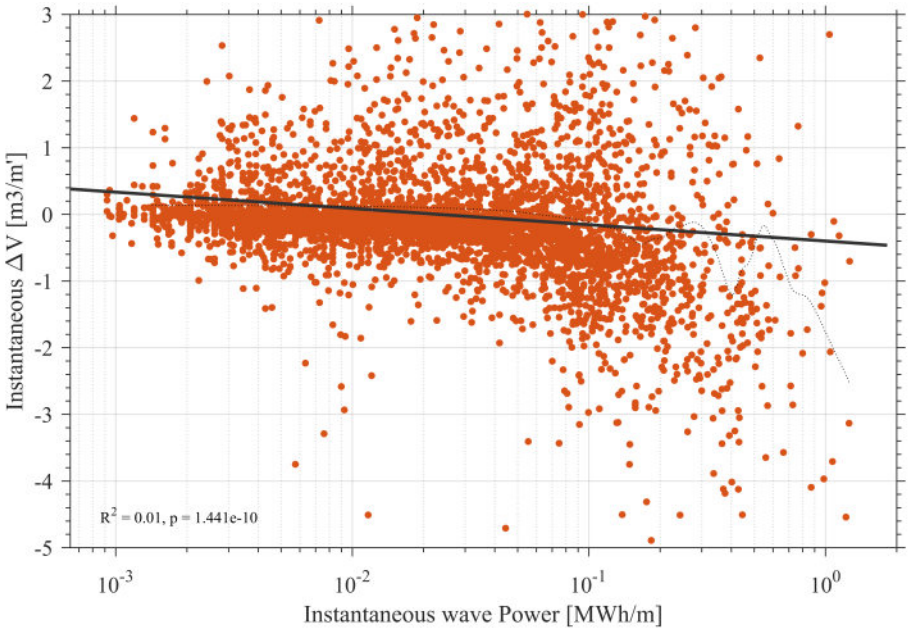


Figure 6.11: Instantaneous $\Delta V$ against instantaneous wave power [MWh/m]

A $R^2$ value of 0.41 confirms a weak correlation between the two quantities but is significant at the 99% confidence interval as the calculated p-value is $<< 0.01$. It is interesting that the relation between hourly volumetric change from the EOF modes and wave power seems to be logarithmic. Also, the smallest wave power relates to a relatively strong accretion. Assuming that wave power is the main contributor to sediment transport one should expect a volumetric change towards zero as there is very little [e.g. –hypothetically– 0] wave power. Intriguingly, this is not seen in Figure 6.11. The range of the scatter might be explained by the dis-equilibrium concept. Depending on the antecedent wave conditions a certain hourly average wave power has a certain effect. It would therefore be remarkable to find a perfect narrow error banded relation.

## 6.4 Discussion

### 6.4.1 Storm impact

In this section the storm impact [loss or gain in volume over the storm] is compared to various other indicators such as wave power, tidal elevation, tidal range and storm duration. For the impact assessment the EOF results are used to calculate volume gain or loss as presented in the previous Sections. The EOF results are filtered results and represent together 57.75% of the total variability observed with the video based depth-estimations. However, the combination of the two modes represent most of the cross shore loss / gain of sediment as shown in Figure **??**. The time-integrated volume $\Delta V$ presented below represents the total volume change over the alongshore average profile for the storm duration. The $\Delta V$ is calculated over a range from 100 m to 900 m in cross-shore direction. This means that the $\Delta V$ includes inter-tidal, sub-tidal and the offshore domain as defined in Section 3.3.

As the hourly wave power versus volumetric change shows quite a bit of scatter in Section 6.3.2 the accumulative wave power over a storm should better relate to the storm impact. Wave power is used as an indicator to storm impact Birkemeier et al. (1999), Harley et al. (2009), Splinter et al. (2014). For comparison to the storm impact, the instantaneous (per hour) power and accumulative deep water wave power is calculated over a single storm following Equation 6.2. Intuitively one would say that as the storm duration enlarges, the accumulative power over that same storm is increasing similarly. If this is true, the relation between the two should result in a $R^2$ close to 1 for a linear trend. In this work, the storm duration is the time between the upward and downward crossing of the 1% exceedance value for the significant wave height. Figure 6.12 represents the accumulative power over a storm plotted against the storm duration. Figure 6.12 shows, as expected, that the accumulative wave power over a storm is increasing as the storm duration increases.

The grey line in Figure 6.12 represents a linear fit to the data points. The data shows a $R^2$ value of 0.87 and a p-value of $<< 0.01$ which shows significance of the relationship. One can quite confidently say that the as the storm endures longer the total wave power that hits the coast is bigger (as expected). The storm duration and accumulative wave power over a storm should show a similar negative trend to the volume lost over the storm. Figure 6.13 shows $\Delta V$ per metre alongshore over storm against storm duration. Figure 6.13 indicates that the change in volume per metre in the alongshore direction is proportional to some extent to the storm duration. Compared to the linear fit [grey line] this moderate proportionality has a $R^2$ of 0.60 and is significant at the 99% confidence interval considering the p-value $<< 0.01$. Intuitively,

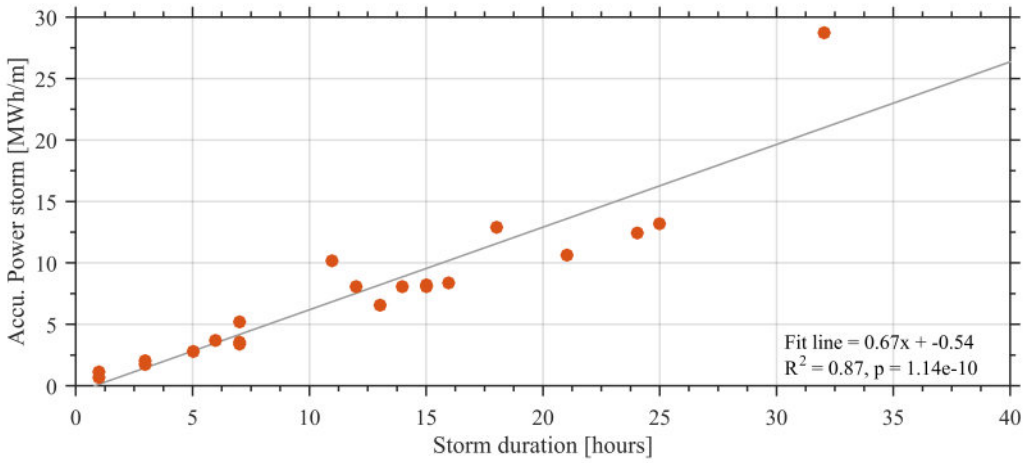


Figure 6.12: Accumulative wave power over a storm potted against storm duration in hours.

this makes sense as the storm endures for longer period the erosional impact is bigger.

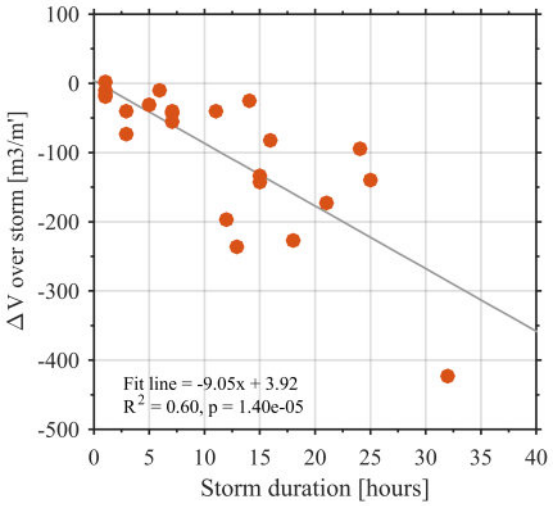


Figure 6.13: $\Delta V$ over a storm against the corresponding storm duration.

Figure 6.14 shows $\Delta V$ per metre alongshore plotted against the maximum wave power (a) during the storm and accumulative wave power (b) over a storm. Figure 6.14a indicates that the impact over a storm is weakly dependent on the maximum power that occurs during a storm considering the $R^2$ value of 0.31 for this linear fit [grey line]. Although the relationship is weak, it is still significant at the 99% confidence interval considering the p-value $< 0.01$. Compared to the maximum wave power, a significantly stronger trend is found concerning the accumulative wave power over a single storm and the corresponding change in volume. The R-squared value is

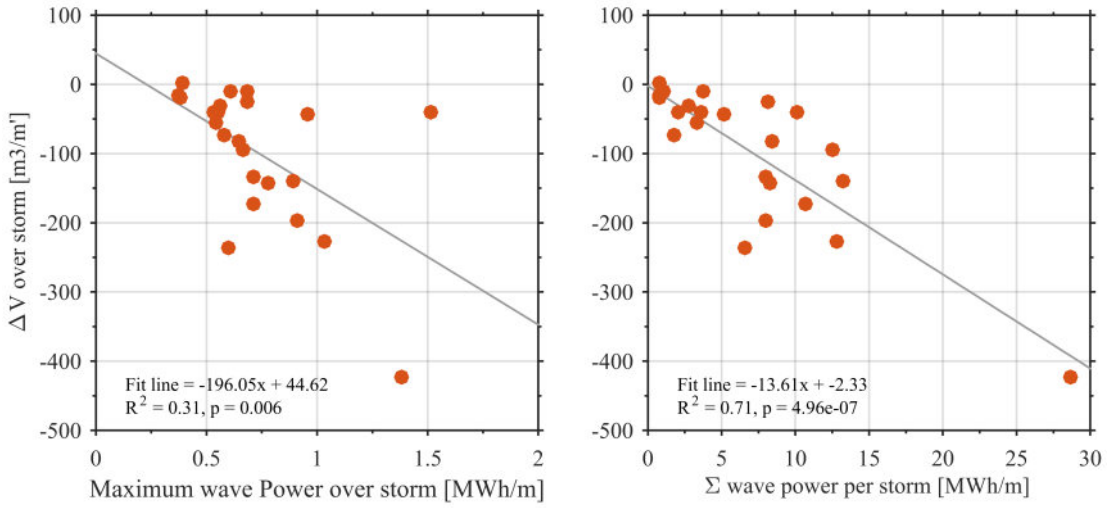


(a) (b)

Figure 6.14: a) $\Delta V$ over a storm against the corresponding maximum wave power during the storm. b) $\Delta V$ over a storm against the corresponding accumulative wave power.

0.71 and the relationship is more significant at the 99% confidence interval considering a p-value $<< 0.01$. The $R^2$ for the maximum wave power during the storm is considerably lower [$R^2 = 0.31$] compared to the accumulative wave power over a storm [$R^2 = 0.71$]. This means that the power of the storm is slightly more important than the storm duration. This is understandable, a short but very powerful storm can have the same potential impact as a longer less powerful storm as long as the accumulative power is in the same order.

Beach state and disequilibrium of the coastal system is another proxy for beach morphology. Figure 6.15 shows respectively the volumetric storm impact compared to the mean dimensionless fall velocity as a beach state indicator [$\Omega$] and disequilibrium [$\Delta\Omega$] over the individual storms. These two parameters show whether the mean beach state and disequilibrium over the storm have a direct relation to the storm impact. Figure 6.15a presents the mean beach state indicator. The linear relation between the volumetric change and beach state indicator is rather weak with a $R^2$ value of 0.30 but is considered significant with $p < 0.01$. The mean disequilibrium over the duration of the storm shows a similar weak relation [$R^2 = 0.32$ and $p < 0.01$]. A weak correlation between the mean beach state indicator and morphological change has been observed (Wright et al. 1985). A better measure for morphological change is found in $\Delta\Omega$. Intriguingly, Figure 6.15b suggests that the mean disequilibrium is not a great measure concerning storm impact or morphological change over storms.

Figure 6.16a shows the relation between the time-integrated disequilibrium over a storm and

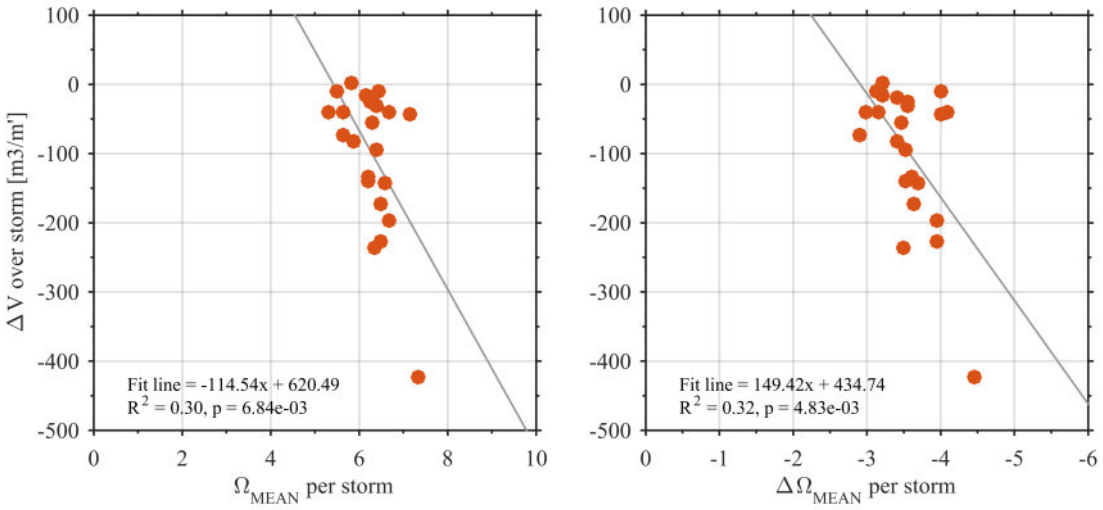


(a) (b)

Figure 6.15: a) $\Delta V$ over a storm against mean dimensionless fall velocity [$\Omega$] over the storms. b) $\Delta V$ over a storm against the corresponding disequilibrium $\Delta\Omega$.

the change of volume over the corresponding storm. Figure 6.16a indicates that compared to a mean value of $\Delta\Omega$ the time-integrated $\Delta\Omega$ has a substantial better correlation to the volumetric storm impact taking into account the $R^2$-value of 0.69 with a p-value $<< 0.01$. Considering the moderate relationship between the storm duration and volumetric impact [Figure 6.13] this confirms the importance of the incorporation of storm duration. An example of a shoreline change model based on this disequilibrium principle was proposed by Davidson et al. (2010). A proxy for shoreline change or volume change was found to related well to $c\Delta\Omega(t)\Omega^k(t)$. After some simplifications this was reduced to $c\Delta\Omega(t)$ wherein $\Delta\Omega$ used the mean fall velocity over the whole dataset [resulting in $c(\bar{\Omega} - \Omega(t))$]. However, this relatively "simple" model considering the simplifications does not take any antecedent wave conditions into account. An improved model based on disequilibrium stress [$cP^{0.5}(t)\Delta\Omega(t)$] was proposed a few years later (Davidson et al. 2013) taking these antecedent wave conditions into account with improved results. This raises the question if the volumetric storm impact presented in this work relates stronger to the disequilibrium stress than solely disequilibrium.

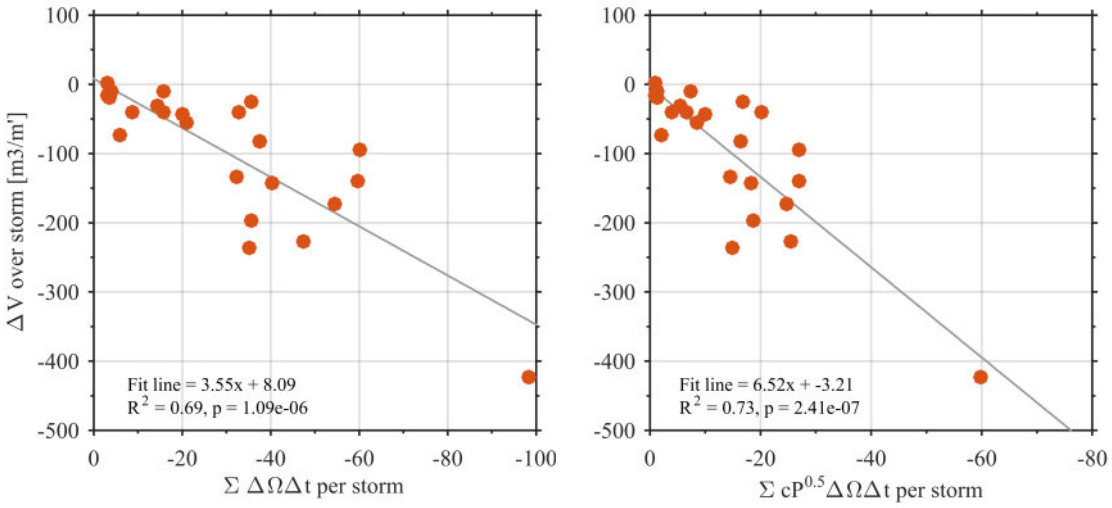


(a) (b)

Figure 6.16: a) $\Delta V$ over a storm the corresponding time-integrated disequilibrium during the storm. b) $\Delta V$ over a storm against the corresponding time-integrated disequilibrium stress over the storm.

Figure 6.16b shows the volumetric change presented against the time-integrated disequilibrium stress. The correlation between volumetric storm impact and time-integrated disequilibrium stress shows a $R^2$-value of 0.73 with a p-value $<< 0.01$. This relationship seems to be the strongest among all the examined morphological relationships so far. The strength of this correlation for time-integrated disequilibrium stress is slightly stronger compared to the time-integrated disequilibrium. The disequilibrium stress seems to be a slightly more suitable representation of morphological change [EOF-filtered volume change] and the volumetric storm impact.

### Tidal elevation and range

Amongst others Coco et al. (2014), Masselink et al. (2015) suggest that tidal elevation and range is important to determine the erosional impact a storm has. Here we test if the tidal elevation and range have a relation to the storm impact at Porthtowan. The tidal elevation and range is determined using the tidal model explained in Section 3.2. Figure 6.17a represents the volumetric impact plotted against the tidal elevation at the moment that the storm was most powerful. Figure 6.17b shows the mean tidal range over the storm duration. The colours in Figure 6.17 correspond to the accumulative wave power over a single storm.

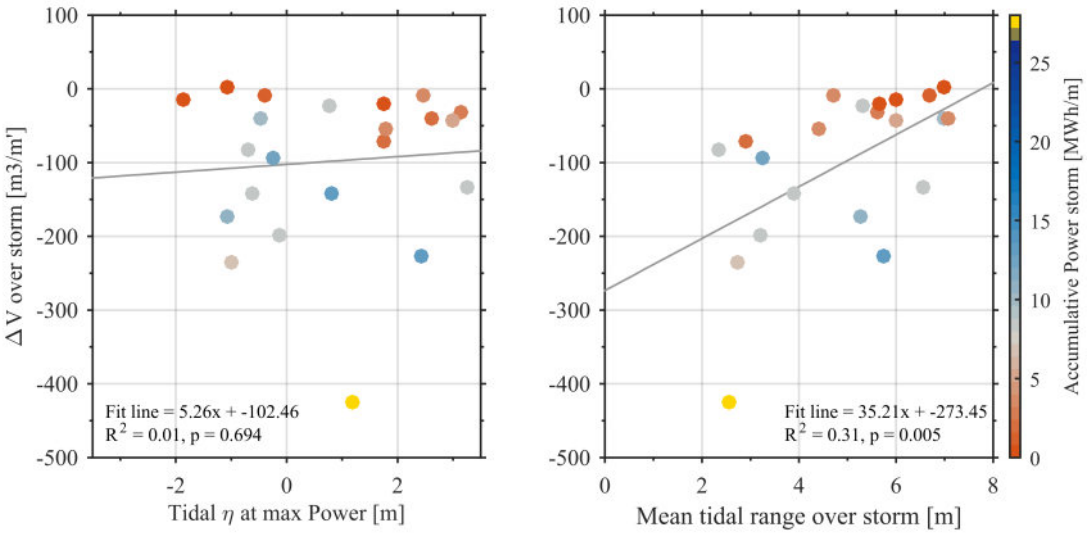


Figure 6.17: a) $\Delta V$ over a storm against the corresponding tidal elevation at maximum storm power. b) $\Delta V$ over a storm against the corresponding mean tidal range during the storm.

Interestingly Figure 6.17a shows little relation between the tidal elevation at the moment of maximum storm power and the volume change. The $R^2$ value is 0.01 and at the same time the trend is insignificant at the 99% confidence interval considering the p-value of 0.694. The tidal range during the storm shows an interesting trend in Figure 6.17b. As the tidal range over the storm increases the volumetric impact of the storm decreases. Although the relation is not particularly strong [$R^2 = 0.31$ but significant at the 99% confidence interval considering $p << 0.01$], it shows that a more stationary active zone [the region where the waves have an effect] induces a larger impact. This is the opposite that has been observed (Masselink et al. 2015). Nonetheless, the EOF results give the opportunity to assess the storm impact on a storm by storm basis while Masselink et al. (2015) uses data collected between an agglomerate of storms. Also, and potentially more important, the domain here comprises part of the inter- and sub-tidal domain while in most other work merely data covering the inter-tidal beach is used. Sediment that is eroded in the inter-tidal zone might end-up in the sub-tidal zone but still in the EOF domain resulting in little change in volume. In addition, Porthtowan has fixed rocky boundaries. In the case of a dune system, the impact of the tide can be significantly larger considering the greater likelihood of eroding part of the dunes.

### Storm Clustering

Storm groups or clusters might have a greater impact on the erosion than individual storms as earlier identified [e.g. (Southgate 1995, Birkemeier et al. 1999)]. If a storm is part of a group or should be considered as an individual storm depends on the recovery taking place between the storms. Morton et al. (1995) defines the recovery period as the time it takes to fully recover from a single storm before the next storm occurs. If the beach is not fully recovery from the storm, the storm and subsequent storm are grouped. This recovery period is hard to determine exactly as beach surveys are mostly carried out with larger time intervals and they are intermittent. This results in a variety of recovery time-scales to cluster storms from 2 weeks (Birkemeier et al. 1999) to 6 months (Splinter et al. 2014). Most of these studies focus on the inter-tidal area, while in this study the whole cBathy range [to 900 cross shore] is taken into account to calculate the volume differences. Figure 6.18 shows the individual storm impacts (a) and instantaneous $\Delta V$ in between the storms (b) over the winter of 2013-2014.

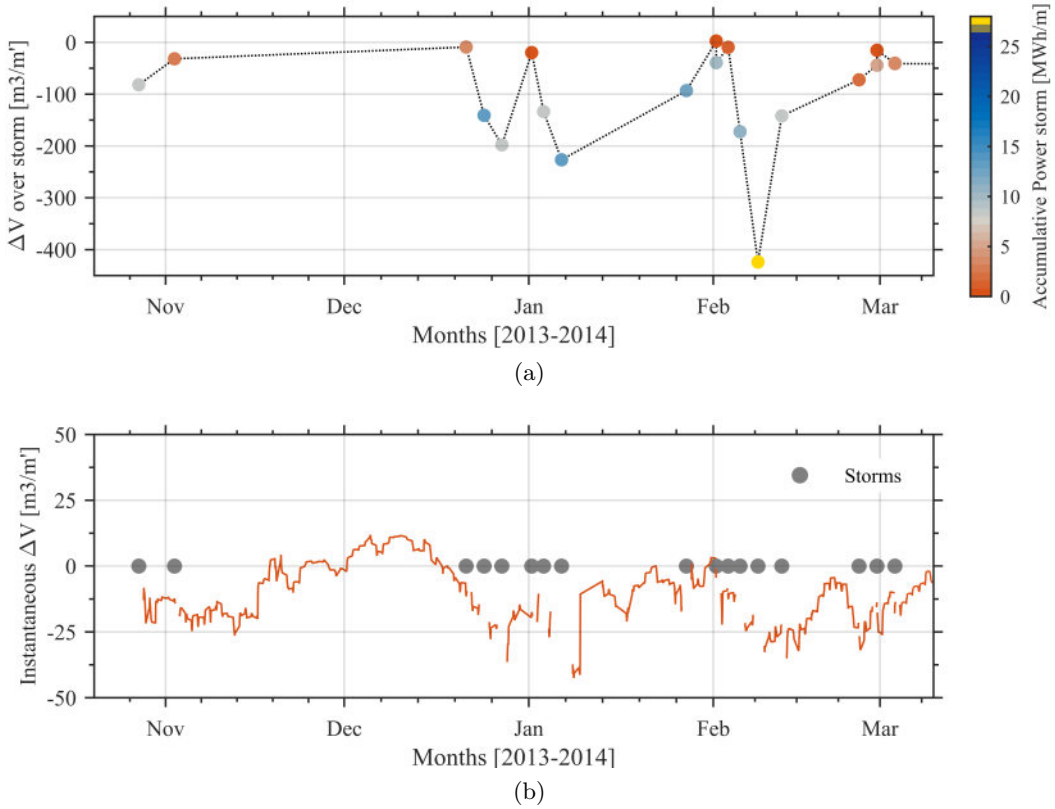


Figure 6.18: Storm impact (a) and instant $\Delta V$ (b) in time over the period covering winter 2013-2014

The colour scheme in Figure 6.18a represents the accumulative wave power over the storm considering the highest correlation between storm impact and accumulative wave power over the

storms. From Figure 6.18a one can see that the storm with the largest impact and accumulative wave power occurred in the beginning of February 2014. The storms occurring within days of the earlier storm are most probably part of the same low pressure system (Harley et al. 2009). These near consecutive storms are most probably a storm cluster. Nonetheless, here we are more interested in the longer periods between storms such as beginning of November to mid-December 2013 and mid-January to End-January 2014. The recovery over these periods is investigated using the hourly volume changes derived from EOF modes. The orange curve in Figure 6.18b shows these more instantaneous volume changes over this period and the grey dots indicate the timing of the storms.

The first period from the beginning of November to mid-December covers around 1.5 months and it is the longest period between storms observed during the 2013-2014 winter. Considering the recovery time scales suggested in earlier works (Birkemeier et al. 1999, Ferreira 2005, Splinter et al. 2014) this period might be the best candidate to show full recovery. Considering the instantaneous volume changes from Figure 6.18b over the period from early-November to mid-December one can see that from early November to end-November predominantly erosion of the cBathy domain occurs. Only from December to just before the next storm [End-December] beach volumes increase. However, the video-based depth estimation domain is far from fully recovered. The November, December and January storms are considered a storm cluster concerning the definition following Morton et al. (1995). For the rest of the winter storms the instantaneous volume change shows only negative [erosion] values. Immediate recovery between storms seems not to occur for the cBathy domain. The whole winter from November 2013 to March 2014 should be seen as a storm group, similar to the 6 months period Splinter et al. (2014) defined for the Gold Coast [Australia] in 1967.

### 6.4.2 Recovery over the remainder of 2014

The energetic 2013-2014 winter period ended around March as Figure 6.18a shows. The recovery of the inter-tidal area is described in detail in Section 5.4. Here, the (complex) EOF based results are added to link the interaction between the inter- and sub-tidal domain. The EOF results cover the inter- and sub-tidal domain while the momentary coastline only represents the inter-tidal part of the beach. Figure 6.19 shows the wave power, EOF derived volumes, momentary coastline and time-integrated disequilibrium starting from February 2014 until the end of February 2015. The values for the EOF derived volumes, momentary coastline and time-integrated disequilibrium are normalised over the whole impact period from October 2013 to end February 2015. In October 2013 the value for the EOF volume was 0.6 [as in Figure 6.10],

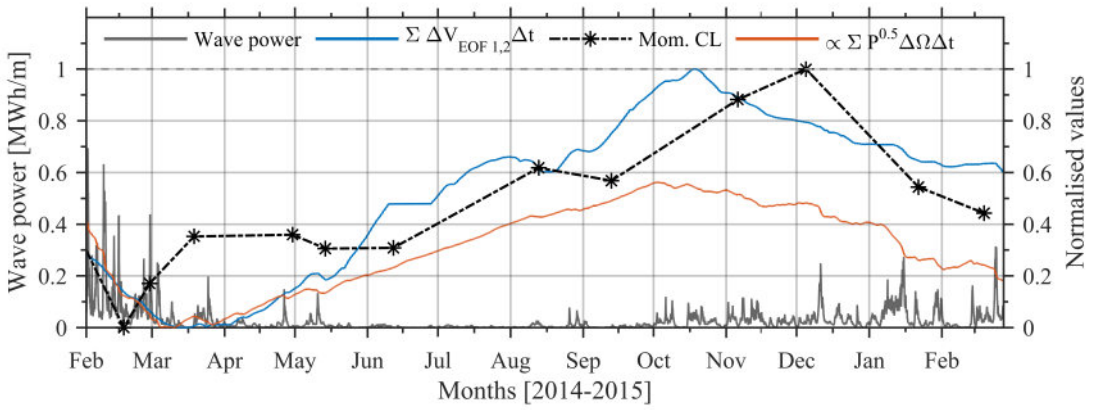


Figure 6.19: Recovery [March to November/December 2014] and subsequent erosion [December 2014 - February 2015] for the inter- and sub-tidal beach. Grey solid line is the wave power [corresponding to the left y-axis], the blue line represents the EOF derived volume, the black dashed line is the measured momentary coastline with the astrisks indicating the survey date and the orange line represents the modelled time-integrated disequilibrium.

momentary coastline $\approx 1$ and time-integrated disequilibrium $\approx 1$. Full recovery is achieved when the same value is reached after the storms.

Figure 6.19 indicates in particular that the coastal system at Porthtowan has shown the ability to recovery within a year from the severe impact the 2013-2014 winter had. At the same time the data indicates that although the wave power increases, the inter-tidal beach still shows recovery. Not only calm conditions [mid-June to mid-August] recover the inter-tidal beach levels but also the more energetic conditions have an accretive effect, even when the time-integrated disequilibrium suggests that erosion should occur. The EOF domain, that contains parts of the inter- and sub-tidal domain, follows more the time-integrated disequilibrium concerning the timing of erosional or accretional trends. The absolute values differ, for example the EOF volumes [blue line in Figure 6.19] suggest up to 100% recovery around mid-October while the time-integrated disequilibrium [orange line Figure 6.19] indicates a maximum recovery of 0.6 (60% recovery).

The time-integrated disequilibrium [orange line in Figure 6.19] essentially shows that the incident wave conditions are erosive compared to the equilibrium time scale of $\Delta\Omega$ from October 2014 and the EOF result [blue line in Figure 6.19] follows a similar trend. In this section we will focus on the interaction between the momentary coastline of the inter-tidal beach [black dashed line in Figure 6.19] and EOF result of inter- and sub-tidal beach together [blue line in Figure 6.19]. Interestingly, the momentary coastline of the inter-tidal beach [measured with RTK-

GPS] shows that the inter-tidal beach keeps gaining volume after October 2014 until December 2014. This accretion of the inter-tidal beach occurs while the incident waves are erosive and the overall camera domain loses sediment volume. Separating the inter- and sub-tidal domain from the EOF results and considering that the inter-tidal area gains sediment volume, the sub-tidal domain must lose sediment. The sub-tidal domain, does not lose sediment towards the inter-tidal domain [because than the EOF result should stay constant] but sediment is transported out of the EOF domain.

In an attempt to get grip on this observation we should look back at the sub-tidal behaviour in the sense of mean cross shore bar position and three dimensionality described in Section 5.6. The recovery of the inter-tidal beach and cross shore position/three dimensionality after the 2013-2014 winter, from mid-March 2014 onwards, show very similar patterns. Around mid-July 2014 the outer bar starts to migrate shoreward, gains three dimensionality and at the same time the momentary shows an increase in volume in the inter-tidal beach. The sub-tidal bar starts to migrate seaward and straightens up from December 2014 as the incident wave conditions become significantly more energetic. Simultaneously, the momentary coastline shows a decrease which indicates erosion of the inter-tidal beach. Over the course of this process, the EOF derived volume over the camera domain shows a steady increase in volume from mid-March to mid-October 2014. Hereafter, the volume decreases until February 2015 [end of depth estimations]. The onshore migration of the outer bar as the wave conditions become more energetic highlights the *activation* of the outer bar. The outer bar starts to have an effect on wave breaking and thus energy dissipation. The increased dissipation of the wave energy over the bar possibly results in onshore directed sediment transport in the lee of the bar. The EOF derived volumes suggest that storm deposits in the outer bar are partially transported shoreward while the other part is transported out of the camera domain. However, the EOF derived volumes are *only* derived from the first EOF mode. The first mode, presented in Section 6.2.3, represents the overall decreasing/increasing beach levels related [near linear] to incident wave conditions. A migrating structure such as the outer bar is not captured by the first mode. Considering the dominance of the first mode [42.4 % of the variance] the beach recovery might have been subject to overall increasing beach levels within the total depth estimation domain and as measured in the inter-tidal area. Later, as the wave conditions picked up, the beach experienced an overall lowering [so loss of sediment from the depth estimation domain] but a redistribution of sediment from the outer bar to the inter-tidal shallowest part of the domain.

## 6.5 Conclusions

In this Chapter the video-based depth estimations are filtered and principle modes are derived through an EOF analysis. These principle modes are used to derive a proxy for hourly morphological/volumetric change. The hourly morphological/volumetric change is presented against offshore wave power. The volumetric change found at Porthtowan seems to be to a greater extent proportional to the logarithm of the instantaneous wave power [$R^2 = 0.41$] compared to $P^{0.5}$ [$R^2 = 0.35$]. The lower the wave power the more accretive the response seems to be and as the wave power increases the response becomes more erosional. In addition to this general comparison, volume change over individual storms is derived from the proxy for hourly morphological/volumetric change. This storm by storm separation is used in assessment of the individual storms and their relationship to wave power, tidal elevation, tidal range, dimensionless fall velocity and disequilibrium. From this analysis, two groups can be separated in relation to the volumetric change over the individual storms; weak and reasonably well correlated. The former group contains maximum [instantaneous] wave power during a storm, mean dimensionless fall velocity over the storms, mean disequilibrium over the storms and mean tidal range during the storm. The latter group [reasonably well correlated] consists of accumulative wave power over a storm, time-integrated disequilibrium over a storm and time-integrated disequilibrium stress. A clear distinction is observed for the correlation between volumetric change and single values [mean or maximum] that poorly describe storm impact and the correlation between volumetric change and time-integrated values that describe the storm impact reasonably well.

#### Tidal range and storm impact

For the 2013-2014 winter the volumetric storm impact is compared to the mean tidal range over a storm and the tidal elevation during maximum wave power over the duration of the individual storms. The volumetric impact compared to the tidal range shows an interesting correlation where the volumetric loss reduces as the tidal range over the storm decreases. No relationship is found between the volumetric change and the tidal elevation at maximum strength of the storm. One remark has to be placed here and that is that Porthtowan is a closed system defined by local geology. There are no substantial dunes to erode large volumes of sediment from. In the case where dunes are present there is an obvious danger that high tide has higher probability to erode the dune foot or part of the dune.

### Storm Grouping/clustering

The hourly volumetric change and volumetric storm impact are used to assess sequencing of storms. Storm sequencing of multiple storms is described in the literature in the case of partial recovery in between two consecutive storms [large variation of this period is found from 2 weeks to 6 months]. The impact of the storms was significantly larger than the recovery and the recovery periods are relatively short periods in time during the 2013-2014 winter season. From the data one can be quite confidently state that the 2013-2014 winter season formed a total cluster of storms. We have to keep in mind that the 2013-2014 winter contained the most extreme storms ever measured at this location. The recovery period [full recovery] from this extreme winter was approximately 9 months. If *just* the impact of the last extreme storm in February as the decreased value for the inter-tidal momentary coastline is considered then the recovery period is in the order of 1 month.

### Recovery

The EOF derived volumes are used to further investigate the recovery from March to December 2014. Both the near-shore zone [EOF result over the video domain including the sub-tidal region] and just the inter-tidal area [momentary coastline] show full recovery over the remainder of 2014. The near-shore zone recovered on a quicker rate than the inter-tidal beach and the near-shore zone reached recovery around mid-October 2014 while the inter-tidal beach continues to recover until Early-December 2014. The difference in behaviour is assigned to the seaward migration of the outer bar which is not included in the first mode of the EOF.

# Chapter 7

# Discussion and conclusions

## 7.1 Synthesis

A large part of this work is the improvement of the video-based depth estimation technique so that cBathy is applicable to a larger range of environments and different video-camera systems with low incident angle to the beach. Depths are obtained over an period from October 2013 to February 2015 and provide insight in sub-daily morphological changes, especially in the sub-tidal bar region. Considering the direct link between beach state and coastal vulnerability (Vousdoukas 2011, Splinter et al. 2014, Coco et al. 2014), it is seemingly important to continuously monitor the near-shore zone. From the monitoring (inter-tidal beach surveys and the hourly obtained depth estimations), we learned that the erosional impact of the 2013-2014 winter was large (-200 $m^3/m$) but initial recovery of the inter-tidal beach rapid ($\approx$40% recovered within 2 months after the last storm) as observed by others e.g. (Splinter et al. 2011) but more importantly, the sub-tidal zone contained more sediment than before the storms. Similar observations can be derived from the bathymetry surveys with an echo-sounder at the nearby and well-studied beach of Perranporth (Scott et al. 2016). After the winter-season the inter- and sub-tidal zone at Porthtowan showed an inverse behaviour of sediment exchange between the zones. However, recovery on the inter-tidal beach catalysed during more energetic conditions after September 2014. By the beginning of November 2014, the inter-tidal beach volume at Pothtowan was at the same level as November 2013, before the storms. The recovery at Porthtowan is relatively quick compared to Perranporth. Perranporth beach recovered only around 50% of the eroded sediment over the period from February 2014 to November 2014 (Scott et al. 2016) despite the fact that both sites experienced a similar amount of volume loss

over the 2013-2014 winter season (approximately 200 $m^3/m$) and have similar environmental forcing. The main difference between Perranporth and Porthtowan is the geological constrains at Porthtowan that embay the very top part of the beach. As mentioned, intriguingly, the data shows that after the initial recovery, accretion of the inter-tidal beach stagnates under calm swell conditions contradicting previous observations (Plant et al. 2006, Gallagher et al. 1998). This is also observed at Perranporth (Scott et al. 2016), there the (de-)activation of the storm bar is suggestedd as a limiting control for inter-tidal recovery. In this perspective the extremely stormy season with such a large dis-equilibrium compared to antecedent conditions pushed the system far from its normal equilibrium conditions. The findings at Porthtowan and Perranporth suggest that beach recovery may not occur for all calm conditions but instead necessitates relative calm conditions of sufficient strength (compared to the extreme of the previous winter season) to mobilize sediment removed in the previous stormy conditions. In this sense storm-relative dis-equilibrium (to the extreme dis-equilibrium of that winter season) indicates if recovery occurs. This is well illustrated in Figure 5.1, the dis-equilibrium model (with $D >>$) shows that the waves are supposed to be erosive while the beach shows accretion.

The sub-tidal (outer) bar transformed from a three dimensional to rather linear and the bar position migrated offshore over the course of the storms. Linearization of the outer bar coincides with a strongly increased alongshore component of wave power (Price & Ruessink 2011, Garnier et al. 2013). During storm conditions the alongshore wave power component is twice as large compared to the recovery conditions as mentioned above (fall 2014). Increasing Three dimensionality during the fall 2014 coincides with recovery. Scott et al. (2016) also find increase three dimensionality as the wave conditions increase and the beach recovers at Perranporth. They suggest that three dimensionality is a vital ingredient and that the sub-tidal zone acts as a corridor for sediment which leads to recovery of the inter-tidal zone. The data obtained here shows however, that interaction between the inter- and sub-tidal zone (and slight recovery of the inter-tidal zone) occurs during calmer conditions and when the sub-tidal bar is linear. Nonetheless, the increased waves and coinciding three-dimensionality of the sub-tidal zone indicate the activation of the sub-tidal storm deposits and more rapid recovery of the inter-tidal beach, a slight reduction of the sub-tidal zone volume and an overall increase in volume. The latter suggest that as three dimensionality is re-introduced the corridor effect does occur.

## 7.2 Reflection on the research questions

The overall aim of this thesis was to enhance the capabilities to acquire high spatial and temporal bathymetry information and to examine the utility of using such data for examining issues of relevance to coastal geomorphology such as the assessment of the storm impact of individual storms and a winter season concerning morphology and sub-tidal bar behaviour. The objectives tackled over a number of Chapters as indicated below:

1. **Obtain high spatial and temporal video-based bathymetry information at the macro-tidal study site.** In Chapter 4 a state of the art video-based depth estimation tool is applied for the very first time in a macro-tidal environment at Porthtowan. Camera boundary issues and tide related inaccuracies are identified and tackled which led to significant improvements [up to 60% reduction in RMS error].

2. **Assess storm impact [2013-2014 winter season] and quantify the relationships between the volumetric impact over individual storms and environmental parameters such as wave power, tidal elevation and tidal range at the macro-tidal study site.** The storm impact at Porthtowan is assessed using inter-tidal beach surveys and the video-based depth estimations in Chapter 5. Per storm period determined by the interval of inter-tidal beach surveys the volumetric impact is described. The novelty here is the application of the video-based depth estimation to capture sub-tidal bathymetry changes pre- and post-storm. The video-based depth estimates are filtered into principle modes in Chapter 6. The novelty here is that the principle modes are utilised for a storm by storm volumetric impact assessment. A direct relation between the volumetric storm impact and the wave power, storm duration and tidal parameters could be assessed in this way.

3. **Assess the [long-term] storm impact and recovery of the 2013-2014 winter season in terms of coastal strength and sub-tidal bar dynamics.** The long-term [year to years] impact of the 2013-2014 winter season has been investigated in Chapter 5 in two manners: 1) long-term dynamics of the momentary coastline and 2) long-term sub-tidal bar behaviour. For the latter, bar characteristics such as position and standard deviation are used to quantify the temporal variability of the mean bar position and three dimensionality of the bar.

### 7.2.1 Hourly video-based bathymetric data collection

This works shows that the video-based depth estimation technique (Holman et al. 2013) itself is transferable to other video camera sites. However, the accuracy strongly depends on the camera

height and tidal elevation, as addressed in this work. The availability of hourly bathymetries [during daylight] opens a new possibility of more accurate near shore monitoring and research leading to better understanding of the near shore zone, for example the interaction between inter- and sub-tidal zone or inner and outer bars.

**What are the restrictions of video-based depth estimations in a multi camera domain?**

At Porthtowan a camera system with multiple cameras is deployed. Section 2.2.2 shows that video-based depth estimation (Holman et al. 2013) within the camera footprint without camera overlap between cameras the depth estimation performs normally. However, on the camera boundaries depths are consistently overestimated. The overestimation is related to incorrect pixel positions and differences in inaccurate pixel positions between two or more cameras. These abnormalities are due to the accuracy differences between geometries and differences in camera distortions. However, with the proposed camera boundary solution, the depth estimation over a multiple camera domain experiences very limited inaccuracies on the camera boundaries. Multiple cameras can also move independently from each other which creates gaps between the camera footprints. The novel adaptive stack collection scheme, proposed in Section 4.2.2, and separate treatment of cameras on camera boundaries overcomes this issue.

**How accurate are video-based depth estimations (Holman et al. 2013) in macro-tidal environments?**

The performance of cBathy (Holman et al. 2013) in a macro-tidal environment such as at Porthtowan is actually poor considering the RMS errors of $> 2$ m. However, it has little to do with the macro-tidal range, the same poor performance will be found in micro-tidal environments if the camera system is placed relatively low. The performance is merely a function of the ratio between camera height and tidal elevation. This implies that if the camera system is placed relatively high in a macro-tidal environment the inaccuracies due to the tidal regime can be reduced, although not completely diminished.

The impact of the tidal elevation can thus not be avoided completely; inaccurate depth estimations will be obtained due to the principle of fixed pixel positions in Holman et al. (2013). The fixed pixel positions mean that the pixels do not have the correct position due to the tidal elevation of the free surface. A set of pixels is spread or contracted more than the reality as the pixels move closer or away from the camera system depending on the tidal elevation. The novel floating pixel solution based on the tidal elevation overcomes this issue.

The floating pixel and the camera boundary solution show that cBathy can be accurate [RMS-error] to the order of tens of centimetres in the sub-tidal bar domain of the macro-tidal environment at Porthtowan. Over the whole camera domain, including the inter-tidal area, the accuracy is a little less, but the RMS-error for the test-case stays below 1 meter.

**What is the effect of bathymetry assimilation through a Kalman Filter?**

Data assimilation through a Kalman filter results in an aggregation of the most confident estimates over time. The Kalman filter assimilates data by comparing the confidence levels for a collection of estimates to the confidence in the prior value. The confidence of the prior estimate decays over time. A Kalman filter usually works better the more data it is fed. Therefore, what we expect is a more accurate Kalman filtered depth estimation as the time frame enlarges.

The daily estimate of the test case in Section 4.5 shows a $R^2$ value of 0.84 for the macro-tidal range test. After the Kalman filter application the $R^2$ increases to 0.98. A measure of the succes is that the percentage of estimates within 40 centimetres of the measured depth increases. For the macro-tidal case 49% of the estimates are within 40 centimetres of the measured depth. After the Kalman filter this percentage increased to 57% of the estimates within 40 centimetres of the measured depth, a more than 10% increase. The effect of the Kalman filter is that the resulting bathymetry estimates are significantly more accurate.

### 7.2.2 Storm impact and recovery

This thesis covers in particular the 2013-2014 winter storms, the impact and recovery. The storm conditions during the 2013-2014 winter were unprecedented and affected not only the United Kingdom but large parts of the west-coast of Europe, reaching to Portugal (Castelle et al. 2015, Scott et al. 2015, Masselink et al. 2015, 2016). The relation between individual storm impact and environmental forcing such as the combination between wave power and tidal elevation is largely unknown. One of the reasons for this is that existing datasets are often intermittent and surveys are merely carried out before and after a cluster of storms (Coco et al. 2014). Until recently the more continuous datasets that exist are video-camera system based dataset that obtain quantitative information of the inter-tidal beach by tracking the shoreline. The video-based bathymetries can now provide information about a much larger area. This gives the opportunity to assess whether sediment is lost from the sub-tidal domain or whether sediment is temporarily stored slightly deeper and is likely to be brought back onshore [Sections 5.6 and 5.7.1].

Gaining more knowledge about individual storm impact and subsequent recovery [after the storms and the subsequent months] is important for short and long-term coastal zone management. In the case of a severe storm, the near shore coastal zone can be assessed to see if it contains enough residual strength to protect the coastal communities adequately. On the long-term [month], coastal zone managers have to be able to understand if the sediment is lost from the coastal system, if the inter-tidal beach will recover before the next winter season and *thus* if mitigating measures are required.

**What is the impact of the 2013-2014 winter season and does the beach recover in remainder of 2014?**

**Storm impact** The erosional impact of the 2013-2014 winter at Porthtowan was significant considering over a metre of sediment was eroded in some places. The erosion is expressed in this work in terms of the retreat of the momentary coastline. Also, from the long-term perspective of the momentary coastline dynamics, the coastline retreat was unusually large, approximately 167 % of the average retreat of the momentary coastline retreat over individual winter seasons over a period from 2008 to 2015.

**Recovery** The storm impact of the 2013-2014 winter season was enormous and unprecedented and the winter storms eroded the beach and deposited sediments seaward. In Chapter 6 the different responses between the inter-tidal beach, the modelled momentary coastline and the sub-tidal domain are discussed. Analysis of the first EOF mode shows that the recovery is directly related to the disequilibrium of incident wave conditions compared to precedent wave conditions and the incident wave power. During the calm conditions of the summer, the inter-tidal beach and sub-tidal domain respond in a similar fashion, linearly to the disequilibrium stress and in this case accretive wave conditions. The outer bar stays stable and is perhaps just a corridor for sediment to enter from the seaward side to the inter-tidal beach domain. During more energetic wave conditions after this summer calmness, the sub-tidal bar configuration becomes more important. Wave conditions are now erosive in terms of disequilibrium and energetic enough to activate the outer bar. Now, a secondary process of the interaction between the active outer bar and inter-tidal domain - non-directly related to the erosive incident waves - becomes important. The bar migrates shoreward and sediment is deposited in the inter-tidal domain [resulting in greater resilience of the beach].

Coastal zone managers mostly focus on inter-tidal beach parameters such as beach width, beach volume [of the dry part] and [momentary] coastline position. These beach parameters

tell part of the real resilience of the near shore zone. The interaction between the sub-tidal part and the inter-tidal beach is effectively neglected while the obtained video-based depth estimations suggest that the direct interaction between sub-tidal and inter-tidal beach determine the recovery of the inter-tidal beach and thus modify the traditional definition of resilience. In addition, mitigating coastal zone management measures to restore coastal resilience might not be required to recover the beach completely right after the storm season since the beach is capable of self-reorganisation. Nonetheless, the recovery depends greatly on the actual storm impact of a winter season, the depth at which storm deposits are deposited and the timing and extent of storm conditions in the following storm season. For example, if a major storm had happened in October 2014, the beach most probably would not have recovered as observed. Great caution is required in adopting the theory that inter-tidal zones recover independently. Nonetheless, behavioural understanding of the sub-tidal area and interaction with the inter-tidal zone will supply insight for coastal zone managers to act on mitigating measures more accurately depending on identifying where storm deposits are deposited, likeliness for shoreward transportation of the storm deposits and act accordingly to stimulate full recovery of the near shore zone.

**How does the volumetric change over individual storms relate to the corresponding storm duration, wave power, disequilibrium. tidal elevation and tidal range?**

**Storm duration** The EOF modes allow for a storm by storm analysis and comparison to environmental parameters such as the storm duration. The storm duration is determined here by the moment of upward [start] and downward [end] crossing of the 1% exceedance threshold by the instant significant wave height. The storm duration relates to the impact as one might expect: as a storm endures the impact increases. The relationship is found in Section 6.4.1 is significant but not particularly strong considering a $R^2$ value of 0.6 for the correlation between the two. Nonetheless, the volumetric change [erosion] increases as the storms endure.

**Wave power** The wave power in relation to the volumetric change over individual storms is assessed in Section 6.4.1 in two manners: 1) the accumulative wave power over the individual storms and 2) the maximum strength in wave power over the individual storms. The first, accumulative wave power, shows a similar trend as the storm duration. This is also according to the expectation; as the storms endure the accumulative wave power is larger and the volumetric impact more severe. The relation between the negative volumetric change [erosion] and the accumulative wave power over the individual storms shows a stronger relation than the storm

duration considering the $R^2$ value of 0.71. The relation between the volumetric change and accumulative wave power is quite intuitive; more accumulative wave power results in more erosion during the storms.

Both accumulative wave power and storm duration make sense and are intuitively understandable. The relation between the maximum wave power during the storm and the total volumetric impact however is harder to comprehend. The relation between the maximum storm power and volumetric impact has been investigated in Section 6.4.1. The resulting $R^2$ value of 0.31 for the correlation [just significant] between the two is rather weak. This means that the maximum wave power is not that important compared to the accumulative power over the individual storms. The volumetric change is more related to the accumulative wave power than the instantaneous maximum during the storm.

**Disequilibrium** The main principle behind the disequilibrium concept is that morphological change occurs when the instantaneous dimensionless fall velocity is in disequilibrium with an equilibrium dimensionless fall velocity based on antecedent wave conditions. Recent advances in disequilibrium models such as Davidson et al. (2010, 2013) use this principle in a disequilibrium stress term which represents the change in cross shore shoreline position. Considering this, disequilibrium over a storm must be large since significant erosion [negative morphological change] is observed. In Section 6.4.1 the volumetric impact is presented against the mean dimensionless fall velocity, mean disequilibrium, time-integrated disequilibrium stress. Mean parameters [such as mean dimensionless fall velocity and mean disequilibrium] over individual storms show little correlation with volumetric storm impact. The extremes during the storm are basically flattened out. Time-integrated values for disequilibrium stress [$\Delta\Omega(t)$] and time-integrated wave power that both incorporate the extremes during the storm show better correlation with the volumetric impact over a storm. If the two factors, wave power and disequilibrium stress, are combined, a good correlation is found with volumetric storm impact. A way to indicate storm impact is though time-integrated wave power over a storm, as mentioned in Section 6.3.2. Here, we have shown that the correlation between the time-integrated wave power is reasonable but can be improved by adding a disequilibrium stress term.

**Tidal elevation and range** The tidal elevation and tidal range are suspects for affecting the impact of individual storms (Coco et al. 2014, Masselink et al. 2015). In Section 6.4.1 the volumetric impact is presented against the tidal range and tidal elevation at the time of maximum storm strength. Intuitively, it can be reasoned that tidal elevation at maximum storm strength is most likely important for the total volumetric impact of the individual storms.

However, the data at Porthtowan indicates that there is no relation between the two; the $R^2$ value is 0.01 and the p-value [0.694] indicates that the relation is insignificant.

The tidal range over the individual storms shows a relationship but a relation that one wouldn't expect. As the tidal range over the storm increases the volumetric impact over the storm decreases. The relationship is not particular strong with a $R^2$ of 0.31 but is significant [p-value = 0.005]. This is interesting because in for example Masselink et al. (2015) the opposite is proposed. However, in that study there is no storm by storm morphological data available.

We have to bear in mind that the relationship of the tidal range and elevation to the storm impact is very much a function of what domain one looks at. The varying tidal levels can have a direct impact on the erosion of the upper part of the beach in the inter-tidal area but if one considers a much larger domain this volume of sediment might still be available to the coastal zone. In the situation at Porthtowan, no substantial dunes are available to be eroded a large amount of sediment during storms. This means that if there is no direct possibility to erode the upper beach such as dune scraping and the considered domain has an extent far enough offshore [as in this test case 1000 m cross shore], the tidal elevation at maximum power or range in relation to the storm impact seems not to be important.

**Is the inter-tidal beach erosion due to the 2013-2014 winter unusual over year-long time scales?**

Section 5.7.1 describes the seasonal cycles over a 7 year period [2008 - 2015]. From 2008 to 2012 the inter-tidal beach gained sediment over the year time-scale. After 2012, erosion is observed over the year-long time scale. The 2013-2014 winter has a large influence on this negative trend. On average, the momentary coastline resets around 32.5 % over a winter season. The winter of 2013-2014 however, shows a reset of 80 %. The impact of the stormy winter of 2013-2014 is more than twice the average impact measured over 7 years. That makes the inter-tidal beach erosion over the 2013-2014 winter extreme and unusual in the view of the data collected over the last 7 years.

**How does the cross shore migration and three dimensionality of the bar relate to occurring storms and subsequent recovery?**

The video-based bathymetries obtained can also provide input for the understanding of sub-tidal bar behaviour besides risk awareness and reduction. In this work, a technique is presented for the extraction of bar characteristics from video-based depth estimations. The technique is

applied to the raw depth estimates over a period from 2013 to 2015. The extraction of the bar characteristics allows to investigation of the short-term temporal variability of the sub-tidal bar position, standard deviations and three dimensionality over long time scale [years].

The alongshore average cross shore position of the sub-tidal bar is one of the parameters that are extracted from the sub-tidal bar detection. In this thesis, the total alongshore average is used. However, the spatial scale for the averaging can be adjusted considering that the bar extraction tool determines the cross shore position for every alongshore data point. The alongshore average sub-tidal bar position is shifted approximately 100 m seaward over the stormy season of winter 2013-2014 and stays most seaward until September 2014. The shoreward migration is initiated when the wave power picks up after September 2014. A seaward migration of the alongshore average sub-tidal bar position is observed as the storm season picks up again around January 2015. The sub-tidal bar data shows that the bar shifted seaward over the latter storms of the season and might have become relatively inactive/stable after the last storm in March 2014. This can mean one of two things: 1) the waves were not energetic enough to restore the cross shore bar position shoreward or 2) the sediment input from offshore was in equilibrium with the sediment output to the inter-tidal area and did not cause significant change on the alongshore average bar position. In this case at Porthtowan, the data over 2013-2015 shows that more energetic wave conditions are required to push the alongshore average cross shore sub-tidal bar position shoreward.

The final question of this thesis covers the three dimensionality of the sub-tidal bars. The three dimensionality is determined using the standard deviation and number of bars detected in the predetermined sub-tidal bar domain [Section 3.8]. The sub-tidal bar domain is in a three dimensional state [crescentic attached bars] before the 2013-2014 winter storms. Over the storms the bar extraction shows more three-dimensionality, however this increase in three dimensionality is a result of depth estimation inaccuracies introduced by the poor weather conditions. Over May to November 2014 the sub-tidal bar stays relatively linear. After November 2014, three-dimensionality increases simultaneously with a further shoreward migration of the sub-tidal bar.

The storms had a straightening effect on the sub-tidal bar and the mostly linear/slight crescentic sub-tidal bar configuration stabilizes over the summer months. Only the more energetic wave conditions introduce more three dimensionality of the sub-tidal bar domain. This mechanism is observed to be still active while incident wave conditions are erosive. During these erosive, more powerful, wave conditions, the outer bar configuration becomes active and migrates shoreward. This implies that these wave conditions that represent relative calmness for

the storm deposits [still winter conditions], transport these storm deposits shoreward following breaking point theory. After wave energy dissipation over the bar, net shoreward sediment transport deposits sediment in the inter-tidal domain. This re-organisation shows that sediment that might have been thought to be lost from the system due to the lack of recovery during summer, can make it back into shallower water during more energetic conditions after the summer.

## 7.3 Suggestions for Future Research

**Video-based depth estimations**

- **Further and broader application of video-based depth estimations.** The depth estimation technique, cBathy, is only available at a limited number of sites. More insight, understanding and improvements can be achieved by applying this technique at other sites to cover a larger range of wave environments and tidal regimes. In order to speed up this process the cBathy depth estimation tools should be available to other coastal monitoring systems than Argus.
- **Improve understanding of the process variability.** The decay function is currently a cross shore Gaussian distribution [as shown in Section 3.4.1] that is alongshore uniform. Only one part of the cross shore domain experiences more decay in faith; the magnitude of decay is related to the instantaneous wave height and a user defined constant $C_0$. Currently the cross shore position of the Gaussian maximum and $C_0$ are user defined and seems to be based on best practice. An investigation should address the behaviour of this process error/variability and a guideline for the $C_0$ or a $C_0$ based on environmental parameters should be derived.
- **Improve the camera boundary solution.** The current implementation of the camera boundary solution is relatively simple and straightforward. The wave number - and so the depth - is found by fitting the phase-ramp of a known sinusoidal to the observed phase-ramp. The beauty of fitting a known sinusoidal is that it gives a direct error estimate of the observed and fitted phase-ramp and thus a sense of quality. This quality measure can be used in the camera boundary solution to weight the better estimate heavier compared to the least good estimate and include this in the weighting based on the centre of mass. In this way distortion differences between cameras [least distortion will give better result] are incorporated.
- **Install higher resolution cameras to estimate depths further offshore.** Depths in the offshore domain are not particularly well estimated; it is together with the inter-tidal

zone the worst zone for the depth estimations. There are a couple of issues in the far end of the domain. Firstly, if the orientation/geometry is slightly wrong it has a much larger effect than that it will have close by due to relative angles. Secondly, the footprint of the pixels becomes larger further offshore. The consequence is that waves become unrecognisable for the cameras [the same as it works with our eyes]. Higher resolution cameras allow for capturing wave signals further off shore and therefore the domain of cBathy can be further extended.

- **Introduce a higher sampling rate.** Most coastal camera systems still collect data on this 2Hz sampling rate. As stated before, the Kalman filter is stronger if it is fed with more data. Now, the camera system collects a 17-minute dataset every hour which feeds into the Kalman filter. If sampled at 4 Hz, the sampling time can be halved and 2 datasets could be collected over the same time. In addition, multiple pixel time stacks [with the same characteristics as the current time-stacks] could be derived from higher sampled data by shifting the stack collection a certain number of time steps, leading to numerous time stacks over the same period.

### Storm impact and recovery

- **Longer-term application of video-based depth estimations [years].** The video-based depth estimations presented in this work cover mostly one stormy winter. The work here, shows that the video-based depth estimations can be used for a storm by storm analysis. An application over longer time scale gives the possibility to assess whether patterns and found relationships between the volumetric change and environmental conditions reoccur over time. In addition, the EOF analysis becomes stronger in recognising different, more distinctive, principle modes around a smoother mean bathymetry. For example, in this case the mean bathymetry contains the stable outer bar.

- **Improve sediment tracking.** The video camera domain at Porthtowan is not optimal for a full analysis/assessment of cross shore and alongshore sediment transports. A 180-degree coverage of a beach gives a better view on the total erosion and where the sediment ends up. Better camera resolution and coverage enables better tracking of features in the sediment/beach morphology. Where the sediment deposits and what instantaneous recovery rates are would be questions that are answerable with a better camera resolution and coverage.

- **Investigate the coupling of inner and outer bars.** The extraction of sub-tidal bar parameters allows for a long-term high detail analysis on the bar behaviour and inter-bar and

bar-beach interactions as in Castelle et al. (2010b). This works shows the interaction and importance of the outer bar in the recovery of the inter-tidal beach as wave conditions became more energetic. A simple 1D model, such as UNIBEST, could provide insight in the progressing sediment transport rates over the bars. In addition, the video-based bathymetry estimations can function as the bathymetry boundary conditions in more complex 3D numerical models. The current camera set-up did not allow for an alongshore length-scale of the crescentic bar to be established but with a more 180-degree view of the beach this should be possible. The depth estimations with this high temporal and spatial scale should be explored to determine the extent to which they capture temporal information about the bar behaviour.

## 7.4 Conclusions

### 7.4.1 Video-based bathymetry estimation

- Video-based bathymetry estimations are obtained at Porthtowan using an inverse method following linear dispersion relation of free surface elevations. A first identified source of inaccuracy is the consistent overestimation on the camera boundaries due to a sudden shift in phase ramp on the camera boundaries. The camera boundary solution is applied to the unmodified cBathy version as presented in Holman et al. (2013) to overcome a sudden phase shift on the camera boundaries.
- A second identified source of inaccuracy is the tide dependent inaccuracy. Here, the formerly fixed positions of the pixels in the real-world have been changed to floating pixel positions depending on the instant tidal elevation and the camera height. Floating pixels are not only important in macro-tidal environments, since the magnitude of this effect depends on the tidal range and camera height. The floating pixel modification applied to the unmodified cBathy version as presented in Holman et al. (2013) leads to significant improvements over the whole domain at Porthtowan. Depending on multiple environmental variables, up to a 60% reduction in RMS-error over the whole domain (Figure 4.13) and 75% reduction in RMS error in the sub-tidal bar domain has been demonstrated (Table 4.3) here.
- The video camera system at Porthtowan, with the inclusion of the modifications, is shown to be capable of estimating the sub-tidal depths with a bias of around 10% of the local depth for daily estimates in the order of 10s of centimetres in the surf zone. Furthermore, the depth estimates improve considerably when a long series of depth estimates is

combined through the Kalman filter. Up to 30% decrease in standard deviation is found, shown in Table 4.4.

### 7.4.2 Storm impact and recovery

- 2013-2014 winter season had an exceptional erosional impact. The momentary coastline showed 167% momentary coastline retreat compared to the average storm winter impact from 2008 to 2015. Full recovery of Porthtowan beach is observed. From March to September 2014 around 58% of the loss was recovered and from October to Early-December 2014 the remaining 42 % was recovered.
- From the video-based depth estimates relationships between volumetric impact and wave power, tidal elevation and range, storm integrated dis-equilibrium and storm duration are assessed.
- The assessment shows that accumulative wave power over a storm, dis-equilibrium over a storm and storm duration are reasonable indicators for the storm impact.
- A weak correlation is found between the maximum [instantaneous] wave power during a storm and the impact versus the mean tidal range.
- The volumetric impact compared to the tidal range shows an interesting correlation where the volumetric loss reduces as the tidal range over the storm decreases.
- No relationship is found between the volumetric change and the tidal elevation at maximum strength of the storm.
- The volumetric storm by storm impact and recovery shows that limited recovery occurred between the storms during the 2013-2014 winter season. This means that between November 2013 and March 2015 the storms are clustered.
- Sub-tidal bar extraction/detection has been applied to the raw video-based depth estimations. The sub-tidal bar detection/extraction technique is applied to obtain sub-tidal bar information from the video-based depth estimations. After the storms, the cBathy bathymetries show that the sub-tidal bar becomes more linear and the cross shore mean of the sub-tidal bar moved offshore. From March to August 2014 the sub-tidal bar at Porthtowan remains at a stable cross shore position of around 725 m offshore and in a linear bar form. As the wave conditions pick up from August onwards, the bar migrates shoreward and simultaneously three dimensional features are slowly re-introduced.

# Appendix A

# Sinusoidal Least Square fitting

Flattened sections of the tidal data will be fitted [1] to a least squares sinusoidal wave.

$$\hat{y} \approx A sin(\sigma t + \theta) + \varepsilon \tag{A.1}$$

In which $A$ = amplitude, $\sigma$ = angular frequency, $\theta$ = phase correction and $\varepsilon$ = vertical shift.

In this case the angular frequency is kept constant on 28,984 degree per hour, representing a M2 tide. Equation A.1 can be decomposed following trigonometry rules [2]. By doing so, the equation becomes a linear system ($X\beta = y$) which can be solved by using Linear Algebra rules for Least-Squares analysis:

$$\hat{y} \approx \underbrace{sin(\sigma t)}_{x_1}\underbrace{Acos(\theta)}_{\beta_1} + \underbrace{cos(\sigma t)}_{x_2}\underbrace{Asin(\theta)}_{\beta_2} + \underbrace{\varepsilon}_{\beta_0} \tag{A.2}$$

This linear system can be written in matrix form representing every single observation point

[1] This means that the data is approximated with a formula, the system of equations is not the exact solution.

[2] $sin(x+y) = sin(x)cos(y) + cos(x)sin(y)$

(1,...,n):

$$\begin{bmatrix} 1 & x_{1,1} & x_{2,1} \\ 1 & x_{1,2} & x_{2,2} \\ \vdots & \vdots & \vdots \\ 1 & x_{1,n} & x_{2,n} \end{bmatrix} \times \begin{bmatrix} \beta_0 \\ \beta_1 \\ \beta_2 \end{bmatrix} = \begin{bmatrix} \hat{y}_1 \\ \hat{y}_2 \\ \vdots \\ \hat{y}_n \end{bmatrix} \tag{A.3}$$

For a Least-Square solution one has to obtain the normal equations $X^T X\beta = X^T y$ which allows solving $\beta$.

Once solved $\beta$, the amplitude, phase correction and vertical shift can be determined as follows.

$$\begin{aligned} \varepsilon &= \beta_0 \\ A &= \sqrt{\beta_1^2 + \beta_2^2} \\ \theta &= arctan\left(\frac{\beta_1}{\beta_2}\right) \end{aligned} \tag{A.4}$$

# Appendix B

# Tidal prediction routine

For cBathy a tidal elevation is required. This is provided to the cBathy routines via the following code:

```
function [Z] = pPorthTide(epochtime,atm)
%%%%%%%%%%%%%%%%%%%%%%%%%%%%%%%%%%%%%%%%%%%%%%%%%%%%%%%%%%%%%%%%%%%%%%%%%%%%%%%%
%   Created by Erwin Bergsma -- April 2013                                      %
%   erwin.bergsma@plymouth.ac.uk                                                %
%                                                                               %
%   Plymouth University, Marine Building | PL4 8AA | Plymouth | UK              %
%                                                                               %
%   Retrieving Tidal information at Perranporth                                 %
%                                                                               %
%   Input:  Epochtime - cBathy time of interest (normally start of stack)       %
%           Switch atmospheric pressure correction on (atm=1) or off            %
%                                                                               %
%   Output: Tidal elevation (predicted + atmospheric pressure correction)       %
%%%%%%%%%%%%%%%%%%%%%%%%%%%%%%%%%%%%%%%%%%%%%%%%%%%%%%%%%%%%%%%%%%%%%%%%%%%%%%%%
%% Predict tidal elevation with r-t tide ---------------------------------%
loc = fileparts(which('pTowanTide'));
file = dir([loc filesep '*PTN*.mat']);
data.input      =   load([loc filesep file.name]); clear loc file;
%% Retrieve atmospheric pressure data from the Coastal Observatory -------%
if atm == 1;
    web             =   ['http://www.channelcoast.org/data_management/'...
```

```
                    real_time_data/charts/'?chart=76&tab=met&start='...
                    mat2str(epochtime-(2*24*60*60)) '&end=' ...
                mat2str(epochtime+(2*24*60*60)) '&disp_option=1&datum=chart'];
        data.at         =   getTableFromWeb_mod(web,5); clear web;
        data.atm        =   datenum(data.at(2:end,1),'dd-mm-yyyy HH:MM');
        data.atm(:,2)   =   str2double(data.at(2:end,2));
        data.atm        =   flipud(data.atm);
    %% Predict tidal elevation with r-t tide ------------------------------%
    data.rt(:,1)    =   data.atm(:,1);
    data.rt(:,2)    =   r_t_predict(data.rt(:,1),data.input.PTN.name,...
        data.input.PTN.freq,data.input.PTN.tidestruc,...
        data.input.PTN.MSL,'latitude',data.input.PTN.lat,'synthesis',1);
    for ii = 1 : size(data.rt,1);
        data.rt(ii,1)   =   matlab2Epoch(data.rt(ii,1));
        data.atm(ii,1)  =   matlab2Epoch(data.atm(ii,1));
    end; clear ii mtime;
    %% Atmospheric pressure correction ------------------------------------%
    temp            =   data.rt(:,2)+((data.atm(:,2)-1000)*-0.01);
    diff            =   abs(data.atm(:,1)-epochtime);
    [~,r]           =   min(diff); clear diff;
    int.x           =   [data.rt(r-1,1) data.rt(r,1) data.rt(r+1,1)];
    int.y           =   [temp(r-1) temp(r) temp(r+1)];
    Z.zt            =   interp1(int.x,int.y,epochtime); %clear int r temp;
else
    temp.time       =   epochtime-(600):600:epochtime+(600);
    data.rt(:,1)    =   epoch2Matlab(temp.time)'; clear temp;
    data.rt(:,2)    =   r_t_predict(data.rt(:,1),data.input.PTN.name,...
        data.input.PTN.freq,data.input.PTN.tidestruc,...
        data.input.PTN.MSL,'latitude',data.input.PTN.lat,'synthesis',1);
    Z.zt            =   data.rt(2,2);
end
end%EOF
```

# Appendix C

# Validation of the reconstruction procedure

In order to assess if the procedure is correct a published application (Horel 1984, Ruessink et al. 2000) is used for guidance. Since this is a test for the complex EOF analysis, a propagating wave is used as input. A sinusoidal movement is combined with a low frequency more steady motion, shown in (C.1).

$$A(y,t) = C_1 \sin\left(2\pi\left[\frac{y-1}{50} - \frac{t-1}{60}\right]\right) + 15\sin\left(2\pi\left[\frac{t-1}{300}\right]\right) \tag{C.1}$$

The four components [$\xi_i(x,y)$, $\theta_i(x,y)$, $\eta_i(t)$ and $\psi_i(t)$] are extracted for the first two EOFs and presented in Figure C.1. The presentation of the components in Figure C.1 is identical to Ruessink et al. (2000) for comparison. Similar, almost identical, patterns are observed. The results for cEOF1 are identical but the second EOF show a different form for all the components. The second cEOF shows a spatial amplitude of 1 here compared to -1 in the publication, the spatial phase is 0 here and $\pm\pi$ in the publication. The temporal amplitude shows a varying signal with a constant phase while here the amplitude is constant and the phase varies. Nevertheless, the results in Figure C.1 are not incorrect. The difference can be explained by the fact that the EOF components are mutually orthogonal, so the final result is identical. The reconstruction result is identical if one combines the four components (3.27), as highlighted in Figure C.2.

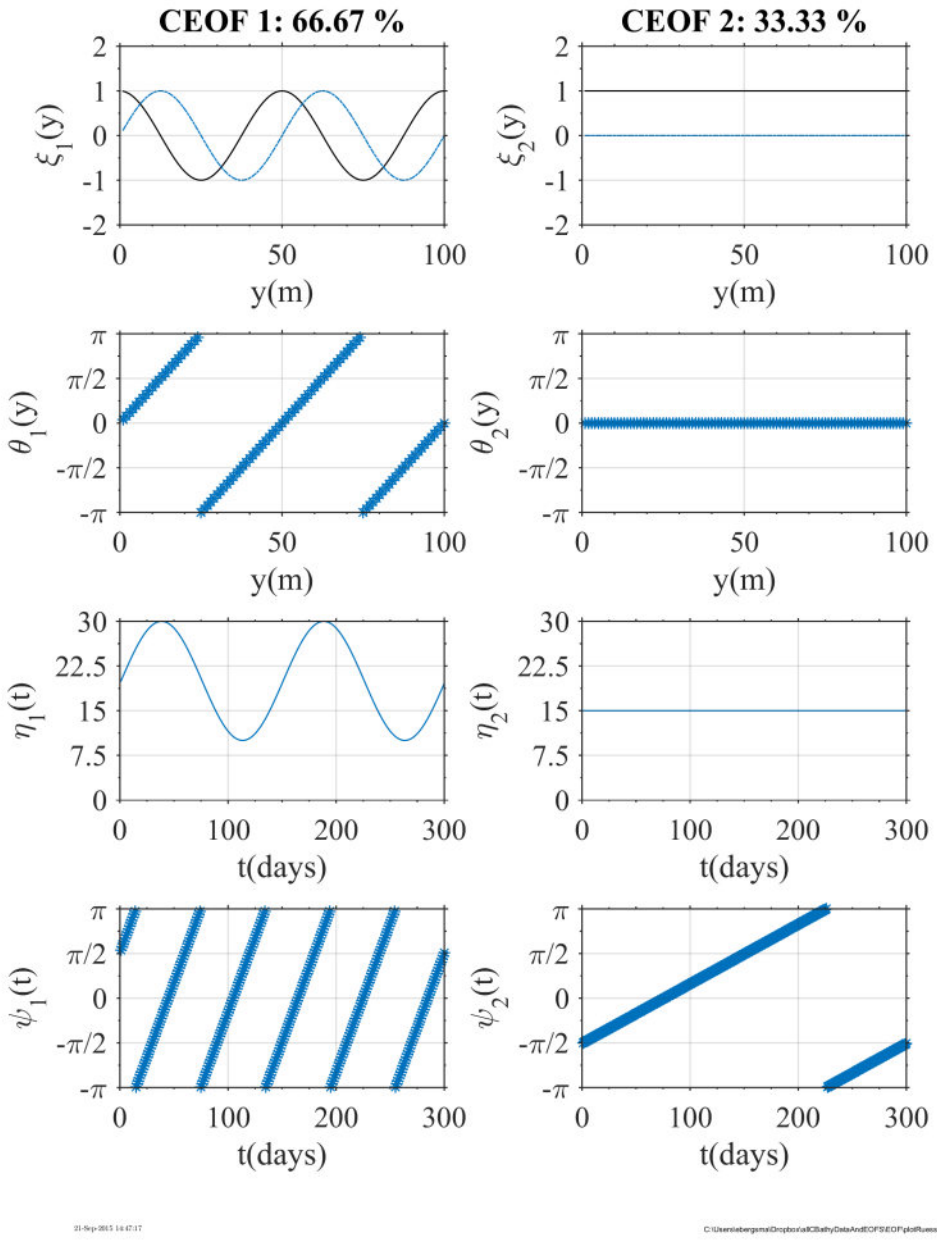


Figure C.1: Resulting four components of a complex EOF analysis using Horel (1984), Ruessink et al. (2000). In the top two plots, the black line is the real part and the blue line represents the imaginary part of the solution. The four bottom plots are the temporal multipliers.

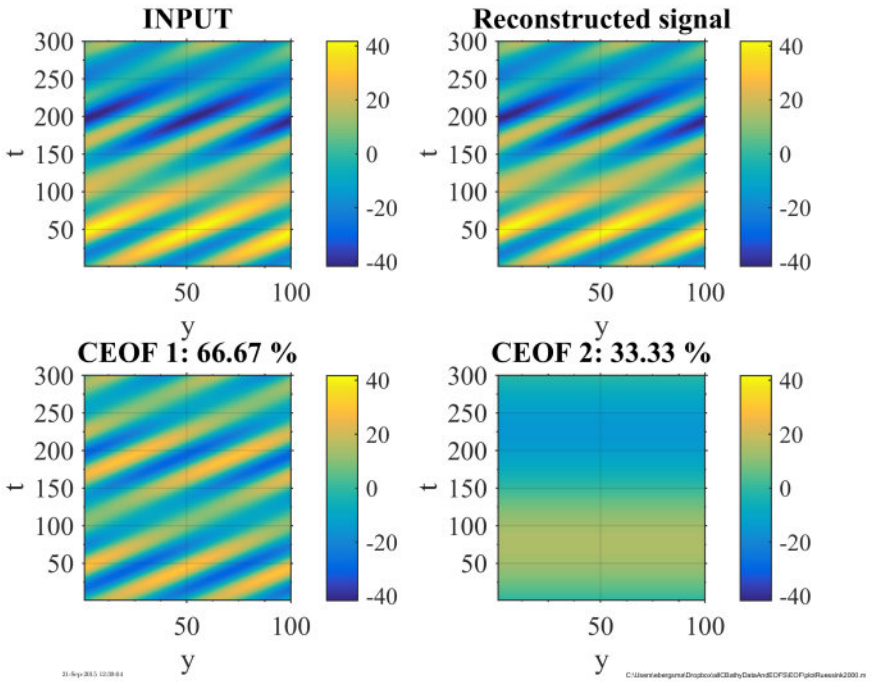


Figure C.2: Reconstruction test combining the four components of a complex EOF analysis using Horel (1984), Ruessink et al. (2000).

### C.0.1 Progressive wave test

In the previous section the difference between ordinary and complex EOF analyses is briefly highlighted. In contradiction to the ordinary EOF, complex EOF can capture moving structures in patterns in a single EOF mode. The ordinary EOF cannot do this and to illustrate this behaviour a test is shown using ordinary and complex EOFs with a progressive wave pattern following (C.2).

$$A(y,t) = 1.5\cos\left(2\pi\left[\frac{y-1}{400} + \frac{t-1}{250}\right]\right) \tag{C.2}$$

Figure C.3a shows the input, modes and reconstruction using the ordinary EOFs and Figure C.3b represents the input, modes and reconstruction of the complex EOF analysis. Figure C.3a shows that the ordinary EOF analysis requires two standing waves modes to solve the progressive wave. This is no surprise as a progressive wave can analytically be described with two standing waves. The complex analysis presented in Figure C.3b indicates that a single mode is capturing 100% of the variance and thus the complete progressive wave.

The example in Figure C.3 is simplified and clear but in real datasets this difference and

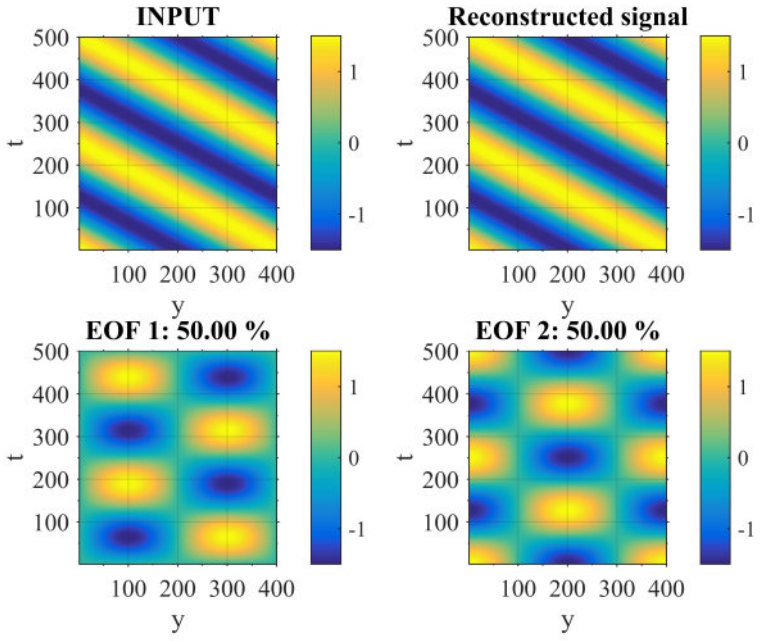


(a)

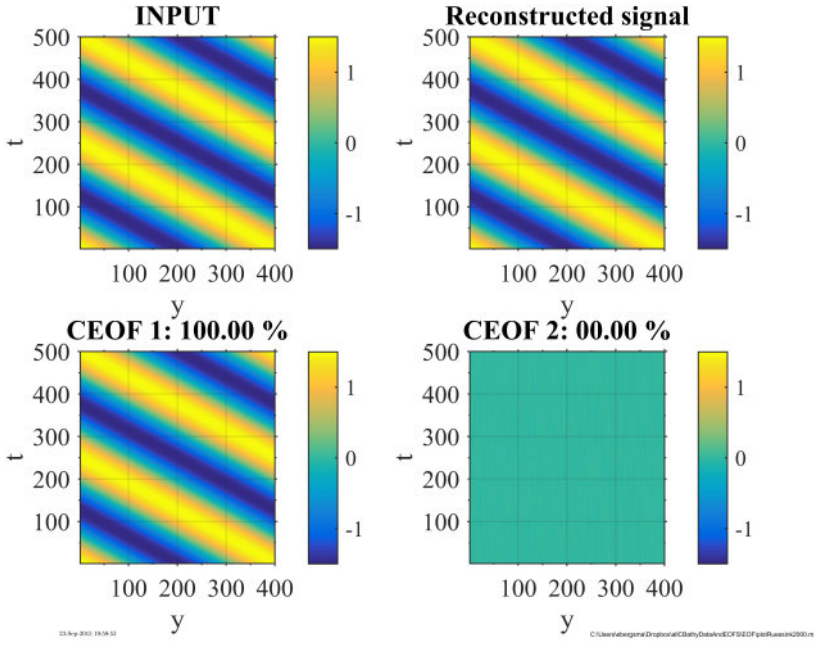


(b)

Figure C.3: Progressive wave test with a) an ordinary EOF analysis and b) a complex EOF analysis. For both the input, two EOF components and reconstruction is shown.

mixing of modes is less identifiable. If there is a moving feature in the dataset, the complex EOF will capture and describe it (with the phases), but the ordinary EOF might create equally important vectors without knowing if they are a progressive wave or separate patterns.

### C.0.2 Filtering with EOFS

Two main applications of the EOFs are identified in the introduction of section 3.8. The second application is the use of an EOF analysis to filter datasets for example based on a target variance coverage or model confidence. White noise is added to the progressive wave example in (C.2) to assess whether the original input of the progressive wave can be distilled through a complex EOF analysis.

Figure C.4 shows the input of the EOF analysis in the top left corner. The input reveals the progressive wave pattern but the extremes seem to be smeared out slightly by the noise. The total variance is no longer captured in a single EOF mode as in Figure C.3b due to the added white noise. Nevertheless, the progressive wave pattern is identified as the most dominant feature (91.01%). The reconstruction presented at the top right includes only the first EOF mode to illustrate the filtering.

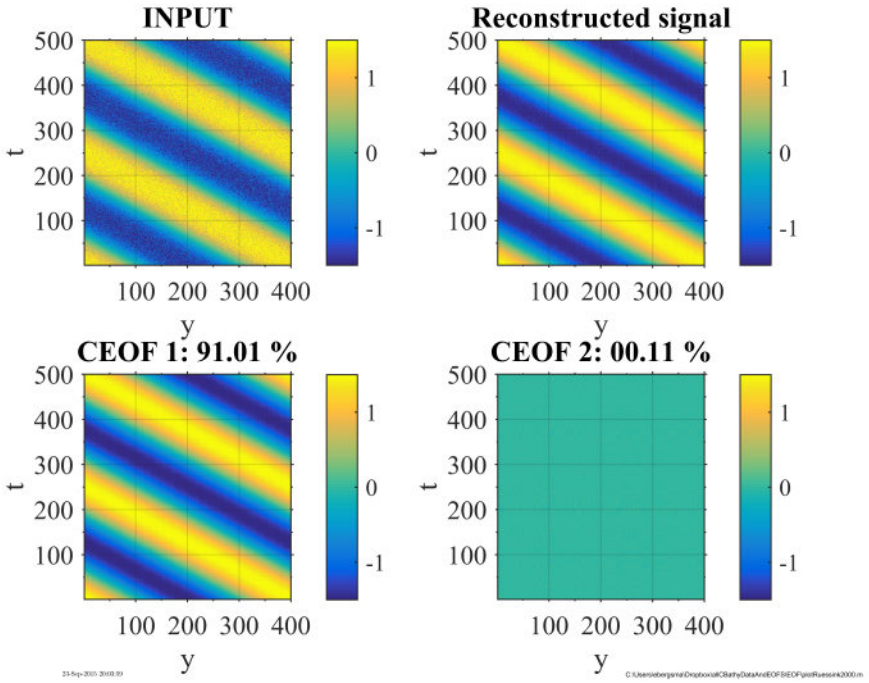


Figure C.4: Progressive wave test including noise using a complex EOF analysis. Two EOF components and reconstruction are shown.

Figures C.5 and C.6 show each of the four components on the complex EOF analysis. Figure C.5 shows the four components for the first two EOF modes in the case of the progressive wave example without the added noise. The second complex EOF mode is irrelevant here as it presents zero variance. In Figure C.6 the first two modes are presented for the progressive wave example with added noise. Here one can see that the found components for the first EOF mode are very similar to the components in the first mode of Figure C.5. The EOF analysis is capable in distilling the components correctly. However, it has to be mentioned that for $\xi_1(x,y)$ and $\eta_1(t)$ slight noise can be found in the signal of the first mode presented in Figure C.6.

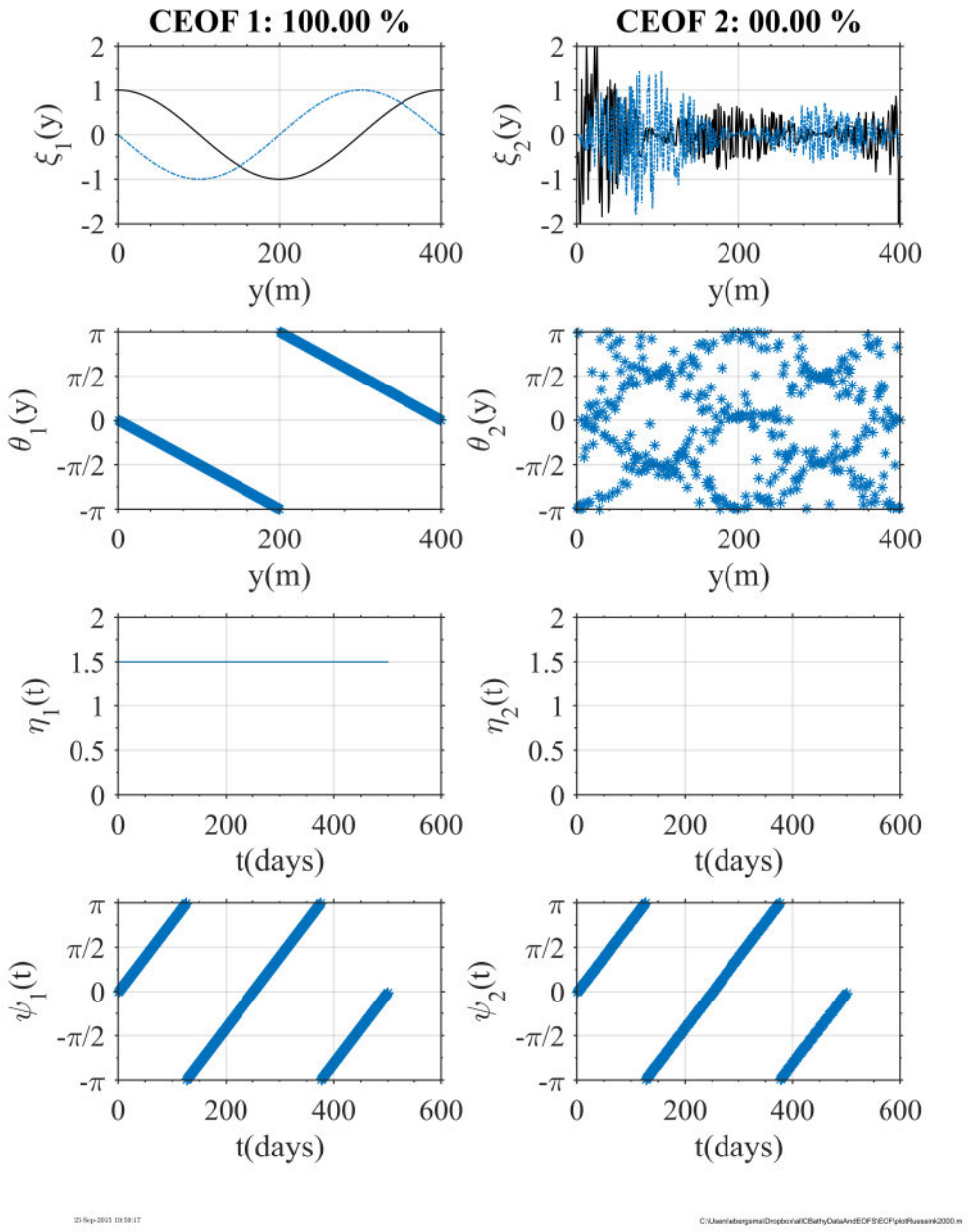


Figure C.5: Black line is real part and blue line is imaginary part. 2 Components case without noise; shows that the first EOF gets 100% of the input

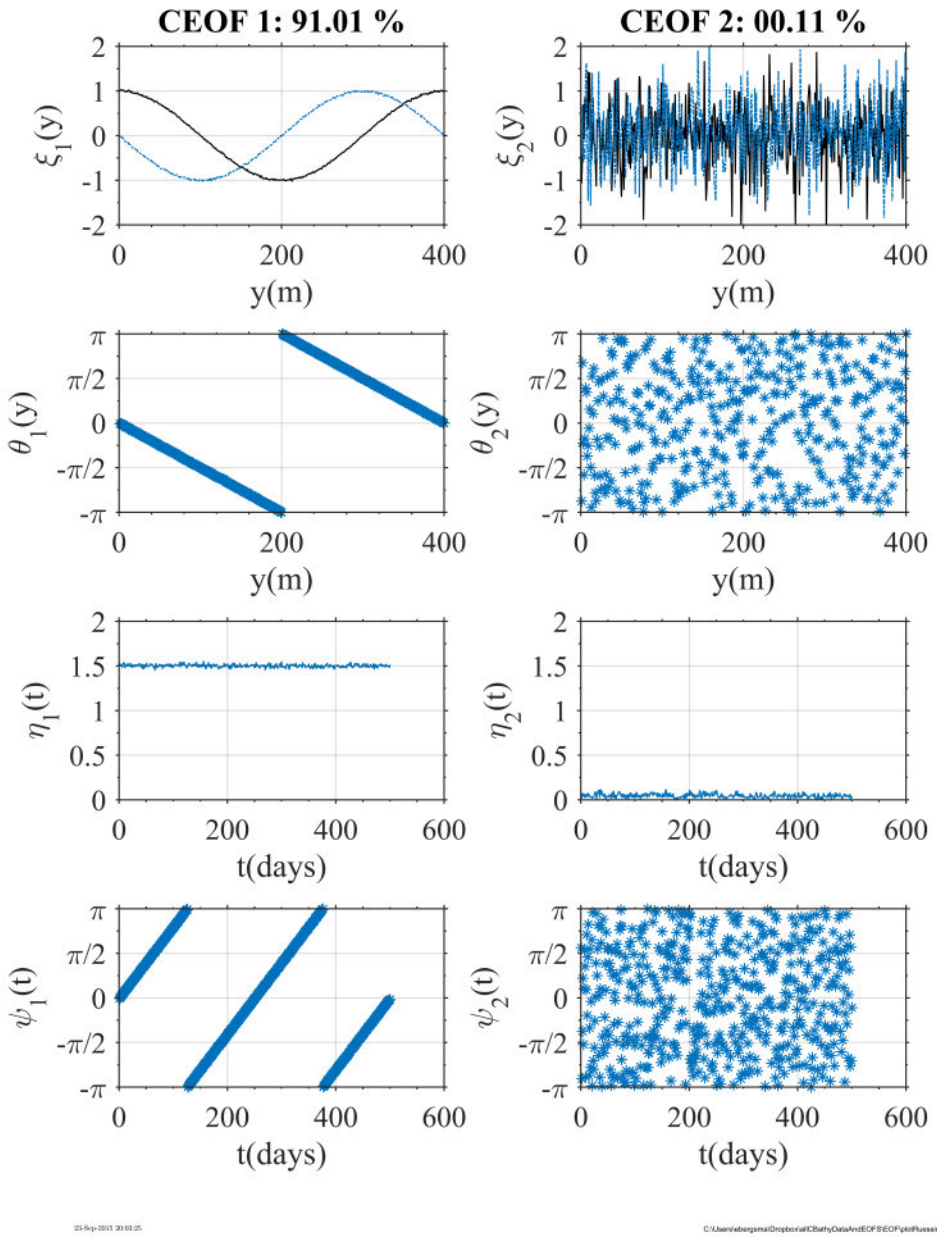


Figure C.6: Black line is real part and Blue line is imaginary part. If we introduce Gaussian White noise to the data we see that the EOF system is capable of extracting the input component without noise. EOFs could be used to as a filtering technique

# Appendix D

# Alongshore wave power

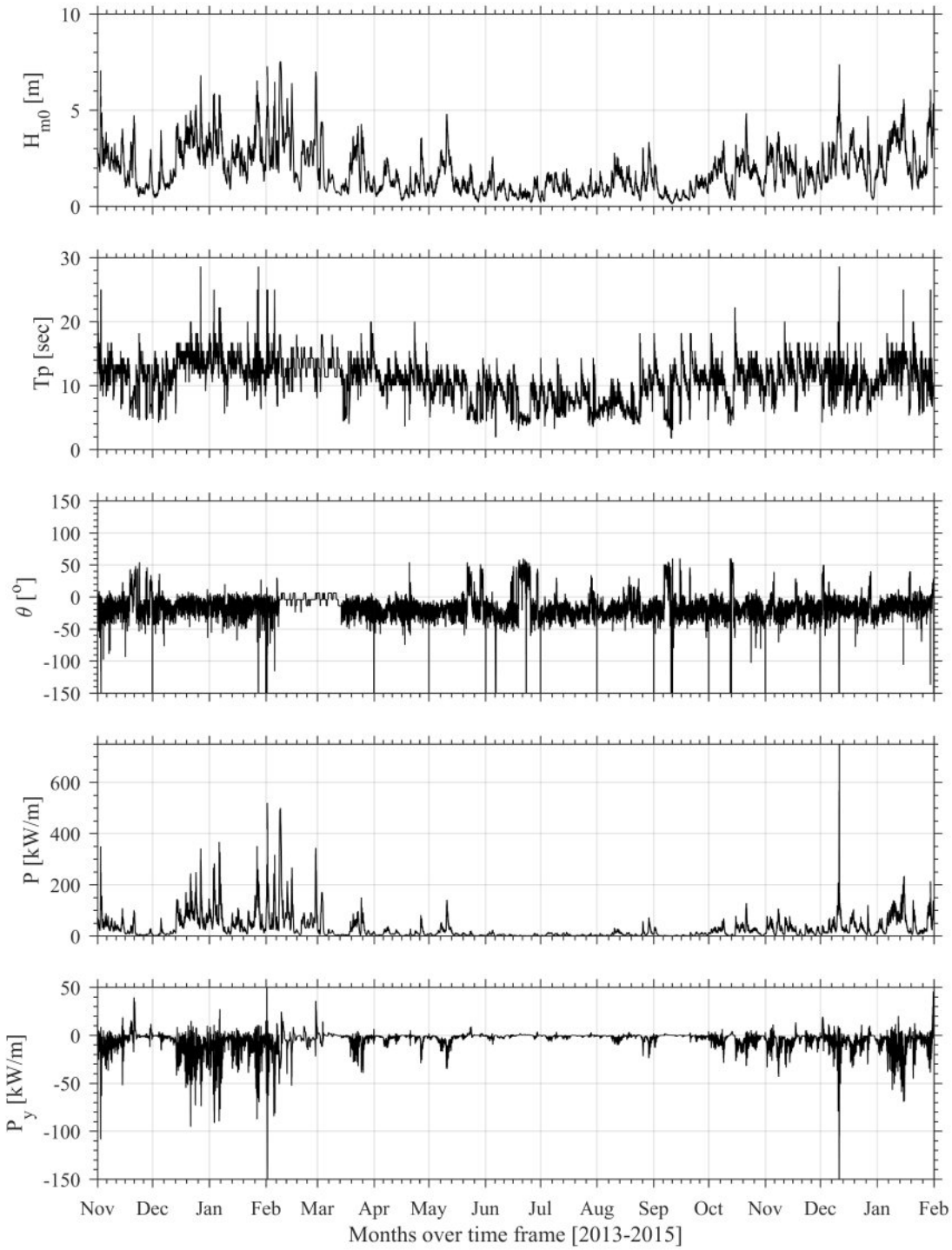


Figure D.1: Wave height ($H_s$), period ($T_p$), direction relative to shore normal ($\theta$), wave power (P) and alongshore wave power ($P_y$) at Porthtowan

# Bibliography


Aarninkhof, S. G. & Ruessink, B. G. (2004), 'Video observations and model predictions of depth-induced wave dissipation', *IEEE Transactions on geoscience and remote sensing* **42**, pp. 2612–2622.

Aarninkhof, S. G., Ruessink, B. G. & Roelvink, J. A. (2005), 'Nearshore subtidal bathymetry from time-exposure video images', *Journal of Geophysical Research* **110**, pp. 1–13.

Aarninkhof, S. G., Turner, I. L., Dronkers, T. D., Caljouw, M. & Nipius, L. (2003), 'A video-based technique for mapping intertidal beach bathymetry', *Coastal Engineering* **49**(4), pp. 275–289.

Almar, R., Bonneton, P., Senechal, N. & Roelvink, D. (2008), Wave celerity from video imaging: A new method, *in* 'Proceedings of the 31st International Conference Coastal Engineering', pp. 1–14.

Almar, R., Castelle, B., Ruessink, B., Sénechal, N., Bonneton, P. & Marieu, V. (2010), 'Two- and three-dimensional double-sandbar stystem behaviour under intense wave forcing and a meso-macro tidal range', *Continental Shelf Research* **30**, 781–792.

Almeida, L., Vousdoukas, M., Ferreira, O., Rodrigues, B. & Matias, A. (2012), 'Thresholds for storm impacts on an exposed sandy coastal area in southern portugal', *Geomorphology* **143**, pp. 3–12.

Arceneaux, K. & Stein, R. M. (2006), 'Who is held responsible when disaster strikes? the attribution of responsibility for a natural disaster in an urban election', *Journal of Urban Affairs* **28**, pp. 43–53.

Battjes, J. & Janssen, J. (1978), Energy loss aand set-up due to breaking of random waves, *in* 'Proceedings of 16th Conference on Coastal Engineering, Hamburg, Germany'.

Bell, P. S. (1999), 'Shallow water bathymetry derived from an analysis of x-band marine radar images of waves', *Coastal Engineering* **37**, pp. 513–527.

Bergsma, E. W. J., Conley, D. C., Davidson, M. A. & O'Hare, T. J. (2016), 'Video-based nearshore bathymetry estimation in macro-tidal environments', *Marine Geology* **374**, pp. 31–41.

Bergsma, E. W. J., Conley, D. C., Davidson, M. A., O'Hare, T. J. & Holman, R. A. (2014), An assesment of video-based bathymetry estimation in a macro-tidal environment, *in* P. J. Lynett, ed., 'Coastal Engineering, Proc. 34th Conference on Coastal Engineering', Vol. 34, Seoul.

Birkemeier, W. A., Baron, C. F., Leffier, M. W., Miller, H. C., Strider, J. B. & Hathawa, K. K. (1989), Superduck nearshore processes experiment: Data summary,miscellaneous report, Technical report, US Army Corps of Engineers.

Birkemeier, W., Nicholls, R. J. & Lee, G.-h. (1999), Storms, storm group and nearshore morphodynamic change, *in* 'Coastal Sediments '99', p. pp. 1109 1122.

Booij, N. (1981), Gravity waves on water with non-uniform depth and current, Technical report, Delft University of Technology.

Bos, C. (2006), Wave characteristics derived from video, Master's thesis, Delft University of Technology.

Bowen, A. J. & Inman, D. L. (1971), 'Edge waves and crescentic bars', *Journal of Geophysical Research* **76**, pp. 8662–8671.

Buscombe, D. & Scott, T. (2008), Coastal geomorphology of north cornwall: St ives to trevose head. internal report for wave hub impacts on seabed and shoreline processes, Technical report, University of Plymouth.

Callaghan, D., Nielsen, P., Short, A. & Ranasinghe, R. (2008), 'Statistical simulation of wave climate and extreme beach erosion', *Coastal Engineering* **55**, pp. 375–390.

Calvete, D., Dodd, N., Falqués, A. & van Leeuwen, M. (2005), 'Morphological development of rip channel systems: Normal and near normal wave incidence', *Journal of Geophysical Research* **110**, C10006.

Carter, T. G., Philip, L., Liu, F. & Chiang, C. M. (1973), 'Mass transport by waves and offshore sand bedforms', *Journal of the Waterways Harbors and Coastal Engineering Division* **99, issue 2**, pp. 165–184.

Castelle, B., Marieu, V., Bujana, S., Splinter, K. D., Robinet, A., Sénechal, N. & Ferreira, S. (2015), 'Impact of the winter 2013-2014 series of severe western europe storms on a double-barred sandy coast: Beach and dune erosion and megacusp embayments', *Geomorphology* **238**, pp. 135–148.

Castelle, B., Ruessink, B., Bonneton, P., Marieu, V., Bruneau, N. & Price, T. (2010a), 'Coupling mechanisms in double sandbar systems. part 1: Patterns and physical explanation', *Earth surface processes and landforms* **35**, pp. 476–486.

Castelle, B., Ruessink, B., Bonneton, P., Marieu, V., Bruneau, N. & Price, T. (2010b), 'Coupling mechanisms in double sandbar systems. part 2: Impact on alongshore variability of innerbar rip channels', *Earth surface processes and landforms* **35**, p.p. 771–781.

Catálan, P. A. & Haller, M. C. (2008), 'Remote sensing of breaking wave phase speeds with application to non-linear depth inversions', *Coastal Engineering* **55**, pp. 93–111.

Chen, Y. & Guza, R. T. (1998), 'Resonant scattering of edge waves by longshore periodic topography', *Journal of Fluid Mechanics* **387**, pp. 255–269.

Coco, G. & Murray, A. B. (2007), 'Patterns in the sand: From forcing templates to self-organization', *Geomorphology* **91**, pp. 271–290.

Coco, G., Sénechal, N., Rejas, A., Bryan, K., Capo, S., Parisot, J., Brown, J. & MacMahan, J. (2014), 'Beach response to a sequence of extreme storms', *Geomorphology* **204**, pp. 493–501.

Coleman, C. & Lundahl, A. (1948), 'Symposium of military photographic interpretation, under water depth determination by aerial photography', *Photogrammetric Engineering* .

Davidson, M. A., Splinter, K. D. & Turner, I. L. (2013), 'A simple equilibrium model for predicting shoreline change', *Coastal Engineering* **73**, pp. 191–202.

Davidson, M., Lewis, R. & Turner, I. (2010), 'Forecasting seasonal to multi-year shoreline change', *Coastal Engineering* **57**, pp. 620–629.

Davidson, M., van Koningsveld, M., de Kruif, A., Rawson, J., Holman, R., Lamberti, A., Medina, R., Kroon, A. & Aarninkhof, S. (2007), 'The coastview project: Developing video-derived coastal state indicators in support of coastal zone management', *Coastal Engineering* **54**, pp. 463–475.

Davies, J. L. (1980), *Geographical Variation in Coastal Development (2nd. Edition)*, Longman, New York.

Dean, R. (1973), Heuristic models of sand transport in the surf zone, *in* 'Proceeding of Conference on Engineering Dynamics in the Surf Zone'.

Dean, R. G. (1991), 'Equilibrium beach profiles: Characteristics and applications', *Journal of Coastal Research* **7**, pp. 53–84.

Dissanayake, P., Brown, J. & Karunarathna, H. (2015a), 'Impacts of storm chronology on the morphological changes of the formby beach and dune system, uk', *Natural Hazards and Earth System Sciences* **15**, pp. 1533–1543.

Dissanayake, P., Brown, J., Wisse, P. & Karunarathna, H. (2015b), 'Comparison of storm cluster vs isolated event impacts on beach/dune morphodynamics', *Estuarine, Coastal and Shelf Science* **164**, pp. 301–312.

Dobrynin, M., Murawsky, J. & Yang, S. (2012), 'Evolution of the global wind wave climate in cmip5 experiments', *Geophysical Research Letters* **39**, pp. 1–6.

Dodet, G., Bertin, X. & Taborda, R. (2010), 'Wave climate variability in the north-east atlantic ocean over the last six decades', *Ocean Modelling* **31**, pp. 120–131.

Dugan, J. P., Fetzer, G. J., Bowden, J., Farruggia, G. J., Williams, J. Z., Piotrowski, C. C., Vierra, K., Campion, D. & Sitter, D. N. (2001), 'Airborne optical system for remote sensing of ocean waves', *American Meteorological Society* **18**, pp. 1267–1276.

Dugan, J. P., Suzukawa, H. H., Forsyth, C. P. & Farber, M. S. (1996), 'Ocean wave dispersion surface measured with airborne ir imaging system', *IEEE Transactions on Geoscience and Remote Sensing* **34**, pp. 1282–1284.

Dyhr-Nielsen, M. & Sørensen, T. (1970), Some sand transport phenomena on coasts with bars, *in* 'Proceedings of the 12th International Conference on Coastal Engineering, Washington, D.C.'.

Ferreira, O. (2005), 'Storm groups versus extreme single storms: Predicted erosion and management consequences', *Journal of Coastal Research* **42**, pp. 221–227.

Gallagher, E. L., Elgar, S. & Guza, R. T. (1998), 'Observations of sand bar evolution on a natural beach', *Journal of Geophysical Research* **103**, pp. 1–13.

Garnier, R., Falqués, A., Calvete, D., Thiébot, J. & Ribas, R. (2013), 'A mechanism for sandbar straightening by oblique wave incidence', *Geophysical Research Letters* **40**, pp. 2726–2730.

Grilli, S. T. (1998), 'Depth inversion in shallow water based on nonlinear properties of shoaling periodic waves', *Coastal Engineering* **35**, pp. 185–209.

Hallmeier, R. J. (1981), 'A profile zonation for seasonal sand beaches from wave climate', *Coastal Engineering* **4**, pp. 253–277.

Hanson, H. (1989), 'Genesis: a generalized shoreline change model', *Journal of Coastal Research* **5(1)**, pp. 1–17.

Harley, M. D., Turner, I. L., Short, A. D. & Ranasinghe, R. (2009), An empirical model of beach response to storms-se australia, *in* 'Coasts and Ports 2009: In a Dynamic Environment'.

Harley, M. D., Turner, I. L., Short, A. D. & Ranasinghe, R. (2011), 'Assessment and integration of conventional, rtk-gps and image-derived beach survey methods for daily to decadal coastal monitoring', *Coastal Engineering* **58**, pp. 194–205.

Haxel, J. H. & Holman, R. A. (2007), 'The sediment response of a dissipative beach to variations in wave climate', *Marine Geology* **206**, pp. 73–99.

Hillen, R., Ruig, J. D., Roelse, P. & Hallie, F. (1991), De basiskustlijn: Een technisch/morfologische uitwerking, Technical report, Rijkswaterstaat.

Hino, M. (1974), Theory on formation of rip-current and cuspidal coast, *in* 'Proceedings of the 14th International Conference on Coastal Engineering'.

Holland, K. T., Holman, R. A. & Lippmann, T. C. (1997), 'Practical use of video imagery in nearshore oceanographic field studies', *IEEE Journal of Oceanic Engineering* **22**, pp. 81–92.

Holland, T. K. (2001), 'Application of the linear dispersion relation with respect to depth inversion and remotely sensed imagery', *IEEE Transactions on Geoscience and Remote Sensing* **39**, pp. 2060–2072.

Holman, R. A., Plant, N. & Holland, T. (2013), 'cbathy: A robust algorithm for estimating nearshore bathymetry', *J. Geophys. Res. Oceans* **118**, pp. 2595–2609.

Holman, R. A., Sallenger, A. H., Lippmann, T. C. & Haines, J. W. (1993), 'The application of video image processing to the study of nearshore processes', *Oceanography* **6(3)**, pp. 78–85.

Holman, R. & Bowen, A. J. (1982), 'Bar bumps and holes: models for the generation of complex beach topography', *Journal of Geophysical Research* **87(C1)**.

Holman, R. & Stanley, J. (2007), 'The history and technical capabilities of Argus', *Coastal Engineering* **54**(6-7), pp. 477–491.

Holthuijsen, L. H. (2007), *Waves in Oceanic and Coastal waters*, Cambridge University Press.

Horel, J. D. (1984), 'Complex principal component analysis: theory and examples', *Journal Climate Applied Meteorology* **23**, pp. 1660–1673.

Kalman, R. (1960), 'A new approach to linear filtering and prediction problems', *Journal of basic Engineering* **82**, pp. 35–45.

Kirby, J. T. & Dalrymple, R. A. (1986), 'An approximate model for nonlinear dispersion in monochromatic wave propagation models', *Coastal Engineering* **9(6)**, pp. 545–561.

Komar, P. (1999), *Beach processes and Sediment (2nd edition)*, Prentice Hall.

Kramer, J. (2005), Unibest cl+ 6.0, user manual, Technical report, wl— delft hydraulics-Deltares.

Kroon, A., Larson, M., , Möller, I., Yokoki, H., Rozynski, G., Cox, J. & Larroude, P. (2008), 'Statistical analysis of coastal morphological data sets over seasonal to decadal time scales', *Coastal Engineering* **55**, pp. 581–600.

Lacey, E. & Peck, J. (1998), 'Long-term beach profile variations along the south shore of rhode island', *Journal of Coastal Research* **14(4)**, pp. 1255–1264.

Larson, M. & Kraus, N. C. (1994), 'Temporal and spatial scales of beach profile change, duck, north carolina', *Marine Geology* **117**, pp. 75–94.

Leffler, K. E. & Jay, D. A. (2009), 'Enhancing tidal harmonic analysis: Robust (hybrid $l^1/l^2$) solutions', *Continental Shelf Research* **29**, pp. 78–88.

Lippmann, T. C. & Holman, R. A. (1989), 'Quantification of sand bar morphology: A video technique based on wave dissipation', *Journal of Geophysical Research* **94**, pp. 995–1011.

Lippmann, T. C. & Holman, R. A. (1990), 'The spatial and temporal variability of sand bar morphology', *Journal of Geophysical Research* **95**, pp. 11575–11590.

Lippmann, T. C. & Holman, R. A. (1991), Phase speed and angle of breaking waves measured with video techniques, *in* 'Kraus, N. (Ed.). Coastal Sediments '91'.

Lorenz, E. N. (1956), Empirical orthogonal functions and statistical weather prediction, Technical report, Massachusetts Institute of Technology.

Loureiro, C., Ferreira, O. & Cooper, J. A. G. (2012), 'Extreme erosion on high-energy embayed beaches: Influence of megarips and storm grouping', *Geomorphology* **139/140**, pp. 155–171.

Masselink, G., Castelle, B., Scott, T., Dodet, G., Suanez, S., Jackson, D. & Floch, F. (2016), 'Extreme wave activity during 2013/2014 winter and morphological impacts along the atlantic coast of europe', *Geophysical Research Letters* **43(5)**, pp. 2135–2143.

Masselink, G., Scott, T., Poate, T., Russell, P., Davidson, M. & Conley, D. (2015), 'The extreme 2013/2014 winter storms: hydrodynamic forcing and coastal response along

the southwest coast of england', *Earth Surface Processes and Landforms* **41(3)**, pp. 378–391.

Masselink, G. & Short, A. D. (1993), 'The effect of tide range on beach morphodynamics and morphology: A conceptual beach model', *Journal of Coastal Research* **9**, pp. 785–800.

Masselink, G. & van Heteren, S. (2014), 'Response of wave-dominated and mixed-energy barriers to storms', *Marine Geology* **352**, pp. 321–347.

Merrifield, M. A. & Guza, R. T. (1990), 'Detecting propagating signals with complex empirical orthogonal functions: A cautionary note', *J. Physical Oceanography* **20**, pp. 1628–1633.

Metoffice (2014), The recent storms and floods in the uk, Technical report, MetOffice.

Misra, S. K., Kennedy, A. B. & Kirby, J. T. (2003), 'An approach to determining nearshore bathymetry using remotely sensed ocean surface dynamics', *Coastal Engineering* **47**, pp. 265–293.

Morton, R. A., Gibeaut, J. C. & Paine, J. G. (1995), 'Meso-scale transfer of sand during and after storms: implications for prediction of shoreline movement', *Marine Geology* **126**, pp. 161–179.

Nayak, J. (1970), Equilibrium Profile of Model Beaches, PhD thesis, Univerisity of California.

Nieto, M. A., Garau, B., Balle, S., Simarro, G., Zarruk, G. A., Ortiz, A., Tintor, J., Álvarez-Ellacuría, A., Gmez-Pujol, L. & Orfila, A. (2010), 'An open source, low cost video-based coastal monitoring system', *Earth Surface Processes and Landforms* **35(14)**, pp. 1712–1719.

O'Hare, T. & Davies, A. (1993), 'Sand bar evolution beneath partially-standing waves: laboratory experiments and model simulations', *Continental Shelf Research* **13(11)**, pp. 1149–1181.

Pearson, K. (1901), 'On lines and planes of closest fit to systems of points in space', *Philosophical Magazine* **2**, pp. 559–572.

Plant, N. G., Holland, K. T. & Haller, M. C. (2008), 'Ocean Wavenumber Estimation From Wave-Resolving Time Series Imagery', *IEEE Transactions on Geosciences and Remote Sensing* **46**, pp. 2644–2658.

Plant, N. G., Holland, K. T. & Holman, R. A. (2006), 'A dynamical attractor governs beach response to storms', *Geophysical Research Letters* **33(17)**, pp. 1–6.

Plant, N. G. & Holman, R. A. (1997), 'Intertidal beach profile estimation using video images', *Marine Geology* **140**, pp. 1–24.

Plant, N. G., Holman, R. A. & Freilich, M. (1999), 'A simple model for interannual sandbar behavior', *Journal of Geophysical Research* **104(C7)**, pp. 1575515776.

Poate, T. (2011), Morphological Response of High Energy Macrotidal Beaches, PhD thesis, Plymouth University; Coastal Processes Research Group.

Poate, T., Kingston, K., Masselink, G. & Russell, P. (2009), 'Response of high-energy, macrotidal beaches to seasonal changes in wave conditions: Examples from north cornwall, uk', *Journal of Coastal Research, SI 56 (Proceedings of the 10th International Coastal Symposium)* **56**, pp. 747–751.

Poate, T., Masselink, G., Russell, P. & Austin, M. (2014), 'Morphodynamic variability of high-energy macrotidal beaches, cornwall, uk', *Marine Geology* **350**, pp. 97–111.

Price, T. D. (2013), Morphological coupling in a double sandbar system, PhD thesis, Utrecht University.

Price, T. & Ruessink, B. (2011), 'State dynamics of a double sandbar system', *Continental Shelf Research* **31**, pp. 659–674.

Prodger, S., Russell, P., Davidson, M., Miles, J. & Scott, T. (2016), 'Understanding and predicting the temporal variability of sediment grain size characteristics on high-energy beaches', *Marine Geology* **376**, pp. 109–117.

Ranasinghe, R., Callaghan, D. & Roelvink, D. (2013), Does a more sophisticated storm erosion model improve probabilistic erosion estimates?, *in* 'Coastal Dynamics 2013'.

Reniers, A., Roelvink, D. & Thornton, E. B. (2004), 'Morphodynamic modeling of an embayed beach under wave group forcing', *Journal of Geophysical Research* **109**, pp. 1–22.

Ruessink, B., van Enckevort, I., Kingston, K. & Davidson, M. (2000), 'Analysis of observed two- and three-dimensional nearshore bar behaviour', *Marine Geology* **169**, pp. 161–183.

Rutten, J. (2014), Depth inversion including non-linear wave celerity. Argus Workshop, September 2014.

Scott, T., Masselink, G., Davidson, M. A., Conley, D. C., Russell, P. E., Saulter, A. & Siggery, E. (2015), Impact of extreme atlantic storms during 2013/1014 winter on the south-west coast of england, *in* 'Coastal Sediments 2015: The Proceedings of the Coastal Sediments 2015'.

Scott, T., Masselink, G. & Russell, P. (2011), 'Morphodynamic characteristics and classification of beaches in england and wales', *Marine Geology* **286**, pp. 1–20.

Scott, T., Masselink, G. & Russell, P. (2016), 'The extreme 2013/2014 winter storms: Beach recovery along the southwest coast of england', *Marine Geology* **382**, pp. 224–241.

Seiwell, H. (1946), 'Military oceanography in tactical operations of world war 2', *American Geophysical Union* **27(5)**, pp. 677–681.

Sénéchal, N., Gouriou, T., Castelle, B., Parisot, J., Capo, S., Bujan, S. & Howa, H. (2009), 'Morphodynamic response of a meso- to macro-tidal intermediate beach based on a long-term data set', *Geomorphology* **107**, pp. 263–274.

Shields, A. (1936), 'Anwendung der aehnlichkeitsmechanik und der turbulenzforschung auf die geschiebebewegung', *Mitteilungen der Preussischen Versuchsanstalt für Wasserbeu und Schiffbau, Berlin* .

Silva, A., Taborda, R., Catalão, J. & Freire, P. (2009), Dtm extraction using video-monitoring techniques: Application to a fetch limited beach, *in* 'Proceedings of the 10th International Coastal Symposium', pp. 203–207.

Smit, M., Reiniers, A., Ruessink, G. & Roelvink, D. (2008), 'The mophological response of a nearshore double sandbar system to constant wave forcing', *Coastal Engineering* **55**, pp. 761–770.

Southgate, H. N. (1995), 'The effect of wave chronology on medium and long term coastal morphology', *Coastal Engineering* **26(3)**, pp. 251–270.

Splinter, K. D., Carley, J. T., Golshani, A. & Tomlinson, R. (2014), 'A relationship to describe the cumulative impact of storm clusters on beach erosion', *Coastal Engineering* **83**, pp. 49–55.

Splinter, K. D., Holman, R. A. & Plant, N. G. (2011), 'A behavior-oriented dynamic model for sandbar migration and 2dh evolution', *Journal of Geophysical Research* **116(C1)**, pp. 1–21.

Stansby, P. & Feng, T. (2005), 'Kinematics and depth-integrated terms in surfzone waves from laboratory measurement', *Journal of Fluid Mechanics* **529**, pp. 279–310.

Stive, M. J. F. (1984), 'Energy dissipation in waves breaking on gentle slopes', *Coastal Engineering* **8(2)**, pp. 99–127.

Stockdon, H. F. & Holman, R. A. (2000), 'Estimation of wave phase speed and nearshore bathymetry from video imagery', *Journal of geophysical Research* **105**, pp. 22015–22033.

Stokes, C., Davidson, M. & Russell, P. (2015), 'Observation and prediction of three-dimensional morphology at a high energy macrotidal beach', *Geomorphology* **243**, pp. 1–13.

Svendsen, I. & Hansen, J. B. (1986), The interaction of waves and currents over a longshore bar, *in* 'ASCE Proceedings 20th International Conference Coastal Engineering'.

Svendsen, I., Madsen, P. & Hansen, J. B. (1979), Wave characteristics in the surf zone, *in* 'Proceedings of 16th International Conference on Coastal Engineering (Hamburg)'.

Taborda, R. & Silva, A. (2012), 'Cosmos: A lightweight coastal video monitoring system', *Computers & Geosciences* **49**, pp. 248–255.

TAW (2002), Leidraad zandige kust, Technical report, Technische Adviescommissie voor de Waterkeringen.

Tissier, M., Bonneton, P., Michallet, H. & Ruessink, G. (2015), 'Infragravity-wave modulation of short-wave celerity in the surf zone', *Journal of Geophysical Research* **120(10)**, pp. 67996814.

van Dongeren, A., Plant, N., Cohen, A., Roelvink, D., Haller, M. C. & Catalán, P. (2008), 'Beach wizard: Nearshore bathymetry estimation through assimilation of model computations and remote observations', *Coastal Engineering* **55**(12), pp. 1016–1027.

van Enckevort, I. & Ruessink, B. (2001), 'Effect of hydrodynamics and bathymetry on video estimates of nearshore sandbar position', *Journal of Geophysical Research* **106**, pp. 16969–16979.

van Enckevort, I. & Ruessink, B. (2003*a*), 'Video observations of nearshore bar behaviour. part 1: alongshore uniform variability', *Continental Shelf Research* **23(5)**, pp. 501–512.

van Enckevort, I. & Ruessink, B. (2003*b*), 'Video observations of nearshore bar behaviour. part 2: alongshore non-uniform variability', *Continental Shelf Research* **23(5)**, pp. 513–532.

van Enckevort, I., Ruessink, G., Coco, G., Suzuki, K., Turner, I. L., Plant, N. G. & Holman, R. A. (2004), 'Observations of nearshore crescentic sandbars', *Journal of Geophysical Research* **109**, pp. 1–17.

Vousdoukas, M. (2011), 'Erosion/accretion patterns and multiple beach cusp systems on a meso-tidal, steeply-sloping beach', *Geomorphology* **141-142**, pp. 34–46.

Wallace, J. M. & Dickinson, R. E. (1972), 'Empirical orthtogonal representation of time series in the frequency domain. part i: Theoretical considerations', *Journal of Applied Meteorology* **11**, pp. 887–892.

Wang, X. L., Feng, Y. & Swail, V. R. (2012), 'North atlantic wave height trends as reconstructedfrom the 20th century reanalysis', *Geophysical Research Letters* **39(18)**, pp. 1–6.

Wijnberg, K. M. & Kroon, A. (2002), 'Barred beaches', *Geomorphology* **48(1-3)**, pp. 103–120.

Wijnberg, K. M. & Terwindt, J. H. (1995), 'Extracting decadal morphological behaviour from high-resolution, long-term bathymetric surveys along the holland coast using eigenfunction analysis', *Marine Geology* **126**, pp. 301–330.

Williams, W. W. (1946), 'The determineation of gradients on enemy-held beaches', *The Geographical Journal* **109**, pp. 76–90.

Woolf, D. & Wolf, J. (2013), 'Impacts of climate change on storms and waves', *Marine climate change impacts partnership: Science review* pp. 20–26.

Wright, L. & Short, A. D. (1984), 'Morphodynamic variability of surf zones and beaches; a synthesis', *Marine Geology* **56**, pp. 93–118.

Wright, L., Short, A. & Green, M. (1985), 'Short-term changes in the morphodynamic states of beaches and surf zone: an empirical predictive model', *Marine Geology* **62**, pp. 339–364.

Marine Geology 374 (2016) 31–41

Contents lists available at ScienceDirect

Marine Geology

journal homepage: www.elsevier.com/locate/margo

# Video-based nearshore bathymetry estimation in macro-tidal environments

E.W.J. Bergsma *, D.C. Conley, M.A. Davidson, T.J. O'Hare

*School of Marine Science and Engineering, CPRG, Drake Circus, PL4 8AA Devon, Plymouth, United Kingdom*

ARTICLE INFO

*Article history:*
Received 4 September 2015
Received in revised form 30 January 2016
Accepted 7 February 2016
Available online 13 February 2016

*Keywords:*
Depth-inversion
Bathymetry estimation
Video beach monitoring
Macro-tidal
Floating pixel solution
Camera boundary solution

ABSTRACT

Video-based depth inversion through the linear dispersion relation for free surface waves using the cross spectral correlation analysis, cBathy (Holman et al., 2013), is applied for the first time in a highly energetic macro-tidal environment in the South West of England at Porthtowan. This application of cBathy reveals two main issues: 1) inaccurate depth estimations on inter camera boundaries when multiple cameras are used and 2) significantly less accurate depth estimates over the whole domain during spring tide compared to neap tide (inaccuracies of around 35% of the local depths are found during spring tide). These two issues are not only important in macro-tidal environments: the camera boundary issue has been reported in numerous video-camera sites and the deviation in accuracy during tidal levels is a function of the tidal range in combination of the vertical camera position. To overcome the two issues, a camera boundary solution and a floating pixel solution (meaning moving pixels in a horizontal plane as function of the tidal elevation) are proposed here. With the modifications, cBathy is capable of estimating depths in the sub-tidal zone with an accuracy in the order of 10% of the local depth irrespective to the local tidal regime. However, for the very upper part of the beach face less accurate results are found due to the reduced validity of the linear dispersion relation in that region due to the non-linear behaviour of breaking waves and wave–current interactions. The improvements persist across all bathymetry survey campaigns at Porthtowan and when compared to other well known Argus video-system sites the importance of the floating pixels is apparent.



## 1. Introduction

Nearshore bathymetric information is crucial in understanding vulnerability of the near-shore coastal region to e.g. flood risk exposure, long- and short-term erosion/accretion and beach user safety. Extreme storms, for example, can lead to severe erosion of the inter- and sub-tidal domain of the near-shore zone. The impact on, and recovery rate of, the sub- and inter-tidal zone varies greatly depending on location (Masselink et al., 2015). Our comprehension of driving processes behind storm impact and recovery is limited and largely constrained by the quality of the available datasets (Coco et al., 2013). At present, there is a gap in understanding of the sub-tidal bar morphology and the interaction with the inter-tidal beach (Coco and Murray, 2007). Attempts to increase the knowledge of the nearshore zone are mostly based on intermittent bathymetry surveys or numerical models (Smit et al., 2008). The lack of high spatio-temporal resolution bathymetry data has been identified as a weakness in relation to setting initial conditions and for calibration of numerical models (Castelle et al., 2010). However, there are remote sensing techniques which have the potential to deliver this data (e.g. for the storm impact/recovery and interaction between sub- and inter-tidal) on a high spatio-temporal scale.

Remote sensing techniques for marine and coastal environments take many forms, from satellite-based systems estimating wave fields to SONAR for estimating depths in the ocean. Camera systems have been used to estimate depth and obtain beach slope information for over half a century starting in a hostile environment of enemy held beaches (Williams, 1946). The mathematical relation between wave length, wave velocity and water depth (e.g. the linear dispersion relation) was applied to aerial photographs taken in preparation of the World War II landings. More recently video imagery has been applied in a research context such as for measurement of swash excursions (Guza et al., 1984). Since the 1980s, several video based tools have been developed within the Argus-camera system framework (Holman and Stanley, 2007). Examples of these tools include the estimation of the crossshore position of sub-tidal sandbars by taking mean pixel intensities over a confined time space (Lippmann and Holman, 1990) and estimation of beach width by determining the shoreline position (Plant and Holman, 1997) which was later modified into an inter-tidal shoreline mapper (Aarninkhof et al., 2003). These tools in combination with the camera systems have given the research community and coastal-zone managers a relatively inexpensive way of investigating and monitoring shorelines worldwide.

* Corresponding author.
*E-mail address:* erwin.bergsma@plymouth.ac.uk (E.W.J. Bergsma).

http://dx.doi.org/10.1016/j.margeo.2016.02.001
0025-3227/

Besides the qualitative crossshore position of the sub-tidal sandbars, much of the progress with video imagery over the last three decades has been focussed in the inter-tidal zone (Holman and Stanley, 2007). Although the inter-tidal area is important, Coastal Zone Management requires a more complete picture containing both the inter- and sub-tidal area as a basis for policy and decision making (Davidson et al., 2007). Accurate video camera-based sub- and inter-tidal depth information on a longer temporal scale provides data to enhance understanding about seasonal and inter-annual beach behaviour and storm recovery and gives the opportunity to adapt policies to local conditions. On a short time scale, up-to-date sub-tidal depth information is an important boundary condition for numerical models to improve the predictive capacity for short term computations such as the prediction of times and locations of highest risk for rip currents and hence provide lifeguards with accurate information to increase swimmer safety (Austin et al., 2013).

In the sub-tidal zone, remote sensing efforts have opened up the possibility to estimate depths accurately, primarily using video imagery or X-band radar. The most common approaches are depth-inversion methods, using the linear dispersion relation (Bell, 1999; Stockdon and Holman, 2000; Almar et al., 2008), non-linear depth inversion (Holland, 2001; Catálan and Haller, 2008) and extended Boussinesq equations (Misra et al., 2003). Another approach is the coupling of estimated dissipation rates with camera imagery and calculated rates with a numerical model (Aarninkhof et al., 2005). van Dongeren et al. (2008) brought these techniques (depth through dissipation rates and depth inversion) together in a data assimilation technique that combined the strong areas of both approaches. Wilson et al. (2010) shows that through data assimilation (wave and current measurements) using an ensemble Kalman filter, the accuracy of an updated, modelled, bathymetry can be enhanced. Remotely sensed (e.g. optical and radar) shore lines (Aarninkhof et al., 2005), wave celerity (Holman et al., 2013) and current fields (Chickadel, 2003) together can estimate morphology accurately through data assimilation without in-situ measurements (Birrien et al., 2013; Wilson et al., 2014). The focus in this study is on one of the parts of the data assimilation used in Wilson et al. (2014): sensing the wave celerity and, hence, the depth inversion technique (Holman et al., 2013).

Considering the first depth inversion technique mentioned above, the phase difference in pixel intensity between two pixels over a crossshore array gives a wave number from which the local depth can be found using the linear dispersion relation. This method of sensing the wave celerity between two pixels was limited in accuracy [O(10%)] on simple beaches (Holman and Stanley, 2007). A more robust method for determining the wave number in the coastal zone was recently developed using multiple pixels to fit a wave phase to an isolated frequency (Plant et al., 2008). The combination of the linear dispersion relation, wave phase fitting and a Kalman-like filter forms the latest, more robust version of cBathy (Holman et al., 2013). In (Holman et al., 2013), the cBathy system was tested in the micro/meso tidal regimes at Duck, Oregon and Washington State in the United States. Testing of the performance of cBathy in a highly energetic macro-tidal environment (with more complex (3D) bathymetries) has been recently carried out (Bergsma et al., 2014) showing the effect of the tide on the accuracy in a macro tidal domain.

The wave-phase fitting of an isolated frequency requires accurate knowledge of the pixel positions in the real-world to prevent over or underestimation of the depth by fitting an incorrect phase ramp (Bergsma et al., 2014). In addition, inaccurate depth estimation is a common issue on the camera boundaries when multiple cameras are used. Accurate estimation of the phase ramp between two cameras is a challenge as the wave propagates through the camera boundaries from one to the other camera. The objective of this paper is to highlight tide and camera boundary related inaccuracies that are observed during the application of cBathy in a macro-tidal environment and, ultimately, present solutions to overcome both issues.

In the Methodology section the cBathy routines are explained in more depth and the study site, site specific cBathy settings and field data are presented. The Results section presents the results of the application of cBathy as well as a diagnosis of the inaccurate depth estimations on the camera boundary and inaccuracies caused by imprecise pixel locations. In the same section solutions are introduced and renewed depth estimations are presented. The Discussion places the findings in perspective and examines the generality of the findings to locations which are not necessarily macro tidal.

## 2. Methodology

### 2.1. cBathy

The principle behind cBathy (Holman et al., 2013) is that wave-modulated time varying pixel intensities can be used in combination with the linear dispersion relation for free surface waves to estimate a depth. Details of the process can be found in Holman et al. (2013) but the general concept is that the linear dispersion relation can be rearranged so that a depth ($h$) can be found as a function of the wave frequency ($\sigma$) and wave number ($k$) (1).

$$h = \frac{\tanh^{-1}\left(\frac{\sigma^2}{kg}\right)}{k} \tag{1}$$

Where $g$ is the acceleration due to gravity. In order to apply (1) to estimate local depths, corresponding pairs of wave frequency and wave number values have to be determined. In cBathy, these parametres are estimated hourly using collection of pixel intensities recorded at 2 Hz. The time varying pixel intensities are decomposed by applying a Fast Fourier Transform from which the subsequent Fourier coefficients are normalised.

To calculate depth at a specific location, a subset of these normalised Fourier coefficients surrounding the point of interest $(x_m, y_m)$ are selected. Depending on the size of the sub-sampling domain (determined by smoothing scales $L_x$ and $L_y$), a subset contains typically 40–50 sub-samples with pixel coordinates $x_p$ and $y_p$. The cross spectral density matrix (2) is computed for all possible pixel pairs in this subset and averaged across each frequency.

$$C^{OBS}_{i,j,f} = \left\langle \widetilde{I}(x_i, y_i, f)\widetilde{I}^{*}\left(x_j, y_j, f\right)\right\rangle = \gamma_{i,j,f} e^{i\phi_{i,j,f}} \tag{2}$$

Where $\widetilde{I}$ represents the subset of the normalised Fourier coefficients and $\widetilde{I}^{*}$ is the complex conjugate, $\gamma$ represents the coherence and $\phi$ is the phase shift between pixel points. A selection (4 is the default) of the most coherent frequencies are identified (coherence is $\gamma_{i,j,f}$ in Eq. (2)) and these are then used through the remainder of the analysis. For each selected frequency the cross-spectral density matrix is kept while the rest is neglected. The cross-spectral density matrix essentially represents a noisy spatial (2D) wave pattern ($e^{i\phi_{i,j,f}}$) per selected frequency. (Holman et al., 2013) included a complex empirical orthogonal function analysis in order to filter different physical components from the observed spatial pattern ($C^{OBS}_{i,j,f}$) per selected frequency. The inverse tangent of the dominant complex mode [1st complex eigenvector, ($\upsilon_1(x_p, y_p, f)$) is assumed to represent a wave train pattern which contains a phase spatial pattern $\upsilon'_1(x_p, y_p)$ at the frequency of interest (Wallace and Dickinson, 1972). This spatial pattern with known angular frequency can be represented by a wave phase as a function of the wave number $k$, wave angle $\alpha$ and phase shift $\Phi$, as expressed in the right-hand side of (3). A Hanning filter is applied to the observed spatial pattern in order to give more importance to the values closer to the point of

interest. A non-linear Least Squares fitting procedure is then applied to identify optimal values of $k$, $\alpha$ and $\Phi$.

$$\underbrace{\upsilon'_1(x,y) = \tan^{-1}\left(\frac{Im(\upsilon_1(x,y))}{Re(\upsilon_1(x,y))}\right)}_{Observed spatial phase pattern} \cong \underbrace{k\cos(\alpha)x_p + k\sin(\alpha)y_p + \Phi}_{Spatial wave phase for known frequency} \quad (3)$$

The best-fit wave phase is determined for each selected frequency and results in a set of frequencies and corresponding wave numbers per point of interest where one wants to estimate a depth. This also means that multiple depth estimates are calculated at each point of interest. The set of depth estimates must be combined into a single depth, but simply averaging these depth estimates results in inaccuracies due to the non-linear character of the dispersion relation (1). Consequently a single depth is found yielding the best-fit relation between the selected frequencies and corresponding wave numbers to the linear dispersion relation. For each hourly dataset (or sampling period), this process is repeated throughout the field of view until depths have been estimated for a predetermined grid of points of interest ($x_m$,$y_m$).

Ultimately, the hourly estimated depths are combined through a Kalman Filter. The Kalman filter accounts for decay in faith in the depth estimate. Faith here means reliance upon the precision of the depth estimate that decreases over time due to the knowledge that morphological change will occur to a certain extent related to (in this case) changes in the wave height [$H_{m0}$] only. When a new depth is estimated the filter updates the depth points with new estimates when the faith in the new estimate is considered greater than the faith in the previous estimate. The decay in faith in the depth estimate is captured in a process variability function Q (Holman et al., 2013), presented in (4), where a crossshore Gaussian distribution is constructed such that:

$$Q(x, H_{mo}) = C_Q H_{mo}^n \exp\left\{-\left[\frac{(x-x_0)}{\sigma_x}\right]^2\right\} \quad (4)$$

In this relation, $C_Q$ represents a site specific constant, $\sigma_x$ is the crossshore standard deviation of the allowable area of change and $x_0$ the crossshore position where the highest level of morphological variability is allowed. The highest level of temporal variability in the depth estimates is allowed where the value for Q is maximum and so the decay in faith of the previous depth estimates is largest. This implies in practise that $x_0$ should be defined by the user as the cross-shore location where one expects the greatest morphological change, following (4), with the result that estimates in that region are updated most readily.

### 2.2. Study site

The aim of this paper is to identify issues that occur when cBathy is applied in a macro tidal environment, namely Porthtowan in Cornwall in the South-West of England. At Porthtowan, the mean spring tidal range is 6.0 m and, in addition, highly energetic waves may be present. For the present study, an offshore wave buoy at Perranporth (see Fig. 1, approximately 15 km North-East of Porthtowan in approximately 18 m water depth) was used to retrieve wave data, with the yearly averaged mean of the wave height being 1.6 m with an average direction of 281 °. During extreme events, wave heights of over 7 m have been recorded at this site (Masselink et al., 2015).

At Porthtowan beach, a single alongshore stretch of 2.5 km open beach at the foot of the rocky cliff appears during low tide reaching from Porthtowan to Chapel Porth. However, during mid to high tide the beaches are geologically constrained by the rocky cliffs creating 5 pocket beaches over the domain. The main and widest pocket beach (>300 m) is the entrance at Porthtowan and the other pocket beach widths ranges from 100 to 250 m. The orientation of the beach at Porthtowan is W-NW, in correspondence with the dominant wave direction. Reflection of the waves on the rocky cliff during high tide is a potential complication for the accuracy of cBathy (not considered in this paper). Typically, the lower beach face exhibits a slope of approximately 0.015 whereas the upper beach face is steeper with a slope of 0.045. At the lower and upper part of the beach a grain size ($D_{50}$) of respectively 380 $\mu$m and 410 $\mu$m is found (Buscombe and Scott, 2008; Poate et al., 2014).

### 2.3. Implementation of cBathy at Porthtowan

cBathy requires model specific settings (Table 1) and boundary conditions such as domain settings, depth truncation, frequency domain

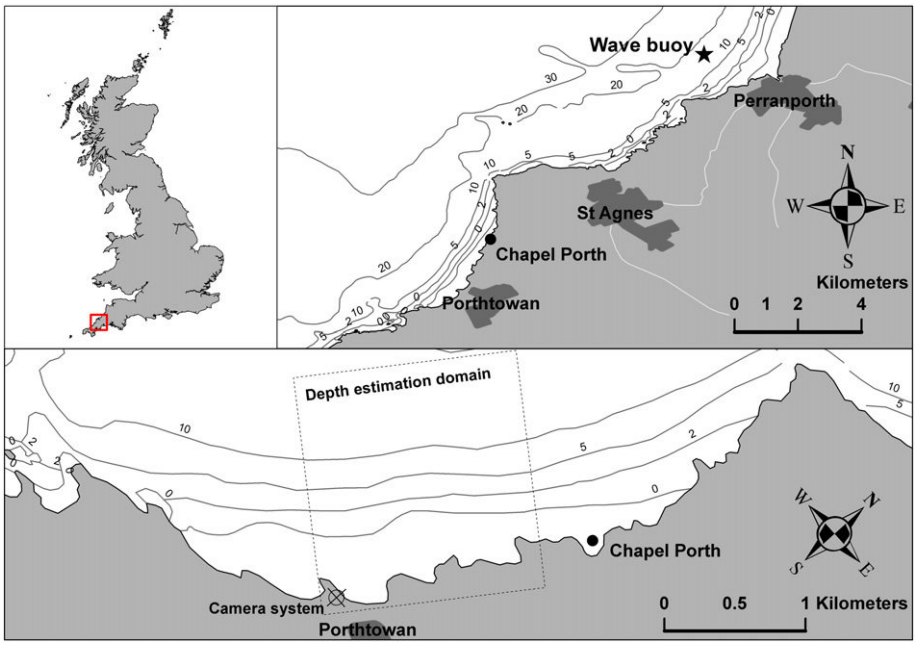


**Fig. 1.** Map showing the study site (Porthtowan) in the South-West of England, Chapel Porth being the Northern boundary of the study site and the wave buoy at Perranporth. The lower panel shows a close up on the bay in the vicinity of Porthtowan.

**Table 1**
Overview of Porthtowan specific settings for cBathy.

| Description | Value(s) | Units |
|---|---|---|
| Pixel collection spacing ($\Delta x_p$) | 4.0 | m |
| Pixel collection spacing ($\Delta y_p$) | 10.0 | m |
| Depth analysis spacing ($\Delta x_m$) | 10.0 | m |
| Depth analysis spacing ($\Delta y_m$) | 25.0 | m |
| Allowable depth range [$h_{min}$ to $h_{max}$] | 0.25 to 20.0 | m |
| Frequency domain [$f_{min}$ to $f_{max}$] | 1/18 to 1/4 | 1/s |
| $\Delta f$ | 1/100 | 1/s |
| Smoothing scales (in depth analysis) | $\Delta x_m$, $\Delta y_m$ | |

and smoothing length scales. The camera system at Porthtowan is mounted on the Southern cliff and the cameras are looking alongshore in a Northerly direction, as shown in Fig. 2a. Considering the spatial domain for the pixel intensity collections, the strategy used is to create the largest possible spatial domain stretching as far offshore as the method will allow. Practical limits to the offshore boundary are imposed by the depth controlled wave dispersion and the pixel resolution of the cameras. A reasonable offshore boundary for the domain is typically determined using the footprint of the pixel and occurring wave periods. The combination of wave periods and pixel footprint determines, at the same time, the spatial resolution ($\Delta x$ and $\Delta y$) of the pixel collection ($x_p$ and $y_p$). Following this procedure, the offshore boundary for the application of cBathy at Porthtowan was chosen to be 1.2 km offshore with $\Delta x$ (crossshore) of 4 m and $\Delta y$ (alongshore) of 10 m.

Points of interest on a (sub) grid are introduced ($x_m$,$y_m$) where the depth is estimated. The spacing between the gridded points for depth estimation is typically larger than the pixel intensity collection grid because for every depth estimate a set of sub-sampled pixel intensities around the depth estimation point is required. At Porthtowan the spacing for the depth estimation points is 10 m in the crossshore direction and 25 m in the alongshore direction.

Depth estimation values are filtered in cBathy by allowing depths within a reasonable site specific depth range. For this application of cBathy the depth truncation is set to a minimum depth of 0.25 m and maximum depth of 20 m. Besides the depth truncation, a frequency range controls the depth estimations. Based on wave data a typical frequency range is determined. Considering the prevailing swell-dominated wave climate at Porthtowan, a range up to 18 s wave period is used. $\Delta f$ was chosen as $100s^{-1}$ to create enough resolution around the longer wave periods.

The dimensions of the pixel sub-sampling domain are determined by the smoothing length scales. Smoothing takes place such that the contribution of the pixels to the final depth estimate is weighted through a Hanning filter. More weight is assigned to the pixels close to a depth analysis point when the sub-sampling domain is smaller while more spreading of the weighted contribution occurs if the sub-sampling domain is larger. The sub-sampling domain around the depth analysis point for Porthtowan has a width of $\Delta x_m$ and a length of $\Delta y_m$ (10 m and 25 m respectively). (See Table 1.)

### 2.4. Field data

Bed level data for ground truthing cBathy was collected in two ways. Following the work of Poate et al. (2009) in relation to the WAVEHUB (UK's wave energy array test site), monthly (inter-tidal) topographic surveys at Porthtowan have been carried out at spring low tide since 2008. Bathymetry measurements at neap tide have been periodically taken in addition to the topographic surveys since the application of cBathy at Porthtowan started (late 2012).

The monthly topography surveys are conducted using a GPS receiver mounted on an all-terrain vehicle(ATV) using real time kinematic (RTK) Global Positioning System (GPS). Alongshore lines are followed by the ATV-driver with a cross-shore spacing of between 7 and 10 m. Every metre or every second (depending on which occurs first) the GPS receiver stores a XYZ point in OSGB36 coordinates with an accuracy of O (5 cm). Two bathymetry surveys have been conducted with a single beam echo-sounder on a small rigid-hull inflatable boat (RIB) or inflatable rescue boat (IRB). The echo-sounder estimates a depth by using the principle of measuring the double way transit time of an acoustic signal reflected by the seabed. A RTK-GPS receiver is mounted on top of the echo-sounder in order to couple the depth estimate with a real-world position and elevation in OSGB36 coordinates. The elevation together with the depth gives the bed level elevation. Both, topography and bathymetry are combined into one dataset and the data is subsequently interpolated on a grid using a local regression (LOESs) model (Plant et al., 2008).

Fig. 2b shows a final result of the combined topographic and bathymetric data. For the following analysis, e.g. to determine RMS errors on a regional basis, we consider three areas in the bathymetric domain. The inter-tidal area (blue lines in Fig. 2b) is the area where the quad bike surveys are carried out. In the sub-tidal zone an area around the sub-tidal bars (yellow lines in Fig. 2b) is distinguished stretching from its boundary with the inter-tidal domain to well beyond the offshore extent of the bar. Further offshore of the bar an offshore region is defined (red lines in Fig. 2b).

The one bathymetric survey used in this work was conducted during relatively calm wave conditions and during neap tide on the 10th of April, as presented in Table 2. Since the aim is to investigate the impact under macro-tidal conditions we assume that limited morphological change took place between the neap tidal survey and the next spring

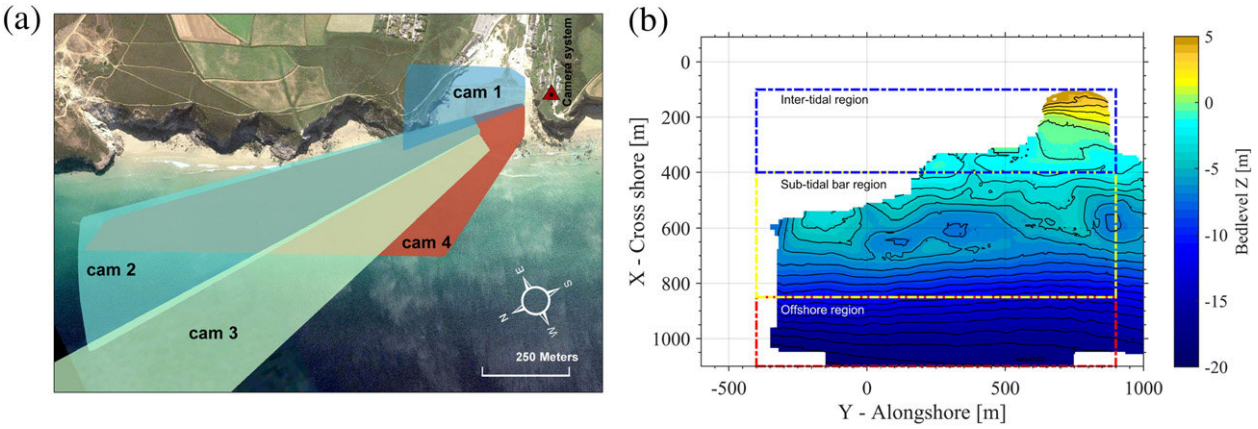


**Fig. 2.** a) Camera layout at Porthtowan, four cameras are located on the Southern cliff looking Northwards alongshore [satellite image from Google Earth]. b) Measured bathymetry (10 April 2014) with the overlaying lines indicate the different regions for the further analysis; inter-tidal (blue), sub-tidal bar region (yellow) and offshore region (red).

tide (17 April 2014). A comparison between the survey (Fig. 2b), a depth estimate with cBathy on the survey day and an estimate with cBathy during the next spring tide is presented in Section 3 and provides a picture of the behaviour of cBathy estimates under varying tidal ranges. (Holman et al., 2013) shows that the accuracy of the depth estimates during mild wave conditions is typically distinguishably better than when more energetic wave conditions occur. Taking this into account, and considering the wave conditions during the bathymetric survey (Tables 2–10 April 2014), one would expect that cBathy would work well for the day of bathymetric measurements (10 April 2014) and even better for the lower wave conditions experienced during the next spring tide (17 April 2014).

## 3. Results

### 3.1. Performance under macro tidal conditions

A bathymetry is estimated for all available hourly stack collections collected during daylight using the unmodified version of cBathy as presented in Holman et al. (2013). These hourly bathymetries (in the order of 12 per day around 10th of April) are combined into one bathymetry for the whole day through the Kalman filter. These filtered bathymetries are subsequently used for comparison with the bathymetric survey. Fig. 3a shows the bathymetry estimates for the 10th of April (neap tide and survey day), and results for the 17th of April (spring tide) are presented in Fig. 3b. The coast is in the upper part of the figures and offshore corresponds to the higher values along the X-axis (as Fig. 2b). Similar features at corresponding locations are observed in the bathymetric survey (Fig. 2b) and the estimate on the survey day (Fig. 3a,b), for example, the sub-tidal bar at approximately 700 m crossshore position in the survey can also be found in the depth estimate and the trough at the onshore side of the sub-tidal bar shows a similar shape. In contrast to this performance are the estimates during the next spring tide (17th of April). The shape of a bar in both estimates is recognisable but it seems that the bar shape is more smeared out in the crossshore direction over the complete alongshore domain.

The difference between the bathymetry survey which was collected on 10 April 2014 and the cBathy depth estimates calculated for 10 April 2014 and 17 April 2014 are presented in Fig. 3c and d respectively. The $17^{th}$ represents spring tide conditions. Although only a single realisation is presented here, a considerable difference in accuracy exists for the neap and spring tide depth estimation. Over most of the domain values of $\pm 3$ m are found during the spring tidal depth estimate while for the neap tidal depth estimate the difference is more in the order of $\pm 1.5$ m. Both difference plots show that cBathy underestimates the depth in most of the domain except for the shallowest parts of the domain. Holman et al. (2013) relates this overestimation of depth in shallow water to wave non-linearity due to breaking and hence poor correspondence with the linear dispersion relation in the surf zones. Tests including non-linear models have been carried out (Rutten, 2014) but significant improvements in estimating the depth in the shallower waters have not yet been achieved. Wave-induced currents to due wave breaking are a recognised source of error in the surfzone since the linear dispersion relation without currents is applied. Furthermore, Tissier et al. (2015) showed that the short-wave celerity depends largely on infragravity modulations (infragravity wave height and induced velocity) in the surf zone. However, depth estimations are found not to be significantly more accurate when these infragravity modulations are accounted for. Closer to shore, when the waves break, the linear dispersion relation does not relate to the more bore-like wave physics. The technique observes a rather coherent and relatively fast moving structure, this results in significant overestimation of the depth. Also, one can argue that the inter-tidal zone does not experience as much wet-time as the deeper areas. This means that the final estimates using the Kalman filter will be constructed with less depth estimates.

Two representative crossshore profiles, at respectively 100 m and 300 m alongshore, are presented for both dates in Fig. 3e,f. The estimate during neap tide on the 10th of April (Fig. 3e) shows a significant underestimation of the depth over the bar (at 700 m crossshore) in both cross sections (100 and 300 m). An underestimation of the depth is also observed over the sand bar at Duck, NC (Holman et al., 2013). However, the sandbar at Duck is smaller and less pronounced than the sand bar at Porthtowan. Similar ground truth tests have been carried out at Egmond aan Zee in the Netherlands (Sembiring, pers. comm.). The comparison between a survey and cBathy estimates at Egmond shows a similar pattern to those from Porthtowan - an underestimation of the depth over the sand bar followed by an overestimation of the depth at the bar trough. Fig. 3f shows the cross section during the next spring tide. The cross sections for the spring tidal estimate show that most of the domain experiences a significant underestimation of the depth. However, features are in approximately the right places but with a significant vertical offset. Differences between the survey and estimates up to 4.5 m can be found.

A Root-Mean-Square error was determined over the whole domain and per sub-domain (as indicated in Fig. 2b) for the neap and spring-tide estimates and presented in Table 3. Over the whole domain this analysis reveals an RMS-error that is almost doubled during the spring-tide (2.05 m) compared to the neap tide (1.06 m). Around the sub-tidal bar region the most accurate estimates (RMS-error of 0.77 m) can be found. However, for the same region during spring tide the RMS error increases to 2.03 m. The dramatic increases in RMS-errors in all the domains suggests that the tide related accuracy is clearly a factor and directly relates to the accuracy of cBathy. Especially taking into account the expected higher accuracy concerning the smaller waves during the spring tide estimates (larger waves = larger bias (Holman et al., 2013)).

An increase in RMS-error with tidal range is not only found during the test case above but it is observed consistently. Although many additional factors can play a role (for example, wave height and water on the camera lens), a systematic increase of the RMS-error over the whole domain with tidal range ($TR$) is found at Porthtowan as indicated in Fig. 4. For the lower tidal ranges (2 m$<TR<$4 m) a large spread of the RMS-error is found. One of the reasons for this is that wave heights up to 4 m were measured in the days before the survey. Larger waves show, in general, less accurate results with cBathy (Holman et al., 2013). For the larger tidal ranges ($TR>$4 m) the wave climate was relatively calm which results in a smaller range in RMS-error. Taking the context into account a slight trend of an increasing bias with increasing tidal range is observed.

### 3.2. Inaccuracies on camera boundaries

On the camera boundaries consistent inaccuracies in the depth estimates are found. The magnitude of this bias varies under different conditions. Although the bias varies in magnitude, the depth is consistently overestimated on the camera boundaries as shown in Fig. 5a,b which shows the final, single estimate (5a) and the Kalman-filtered(5b), depth estimation. For individual estimates (the whole domain at a single point in time) this camera boundary effect can be rather large O(1 m). However, the combination of numerous estimates in the Kalman filter process tends to smooth the effect. This can be observed in Fig. 5b, most of the domain experiences an underestimation but over most of the camera boundaries an overestimation is visible.

**Table 2**
Tide range and day-average wave conditions for the two estimate examples used here. The survey for this work has been carried out on the 10th of April 2014.

| | $TR_{max}$ [m] | Hs [m] | Tp [s] | Dir [°] |
|---|---|---|---|---|
| 10 April 2014 | 2.78 | 1.16 | 10.51 | 278.4 |
| 17 April 2014 | 6.03 | 0.52 | 10.38 | 278.9 |

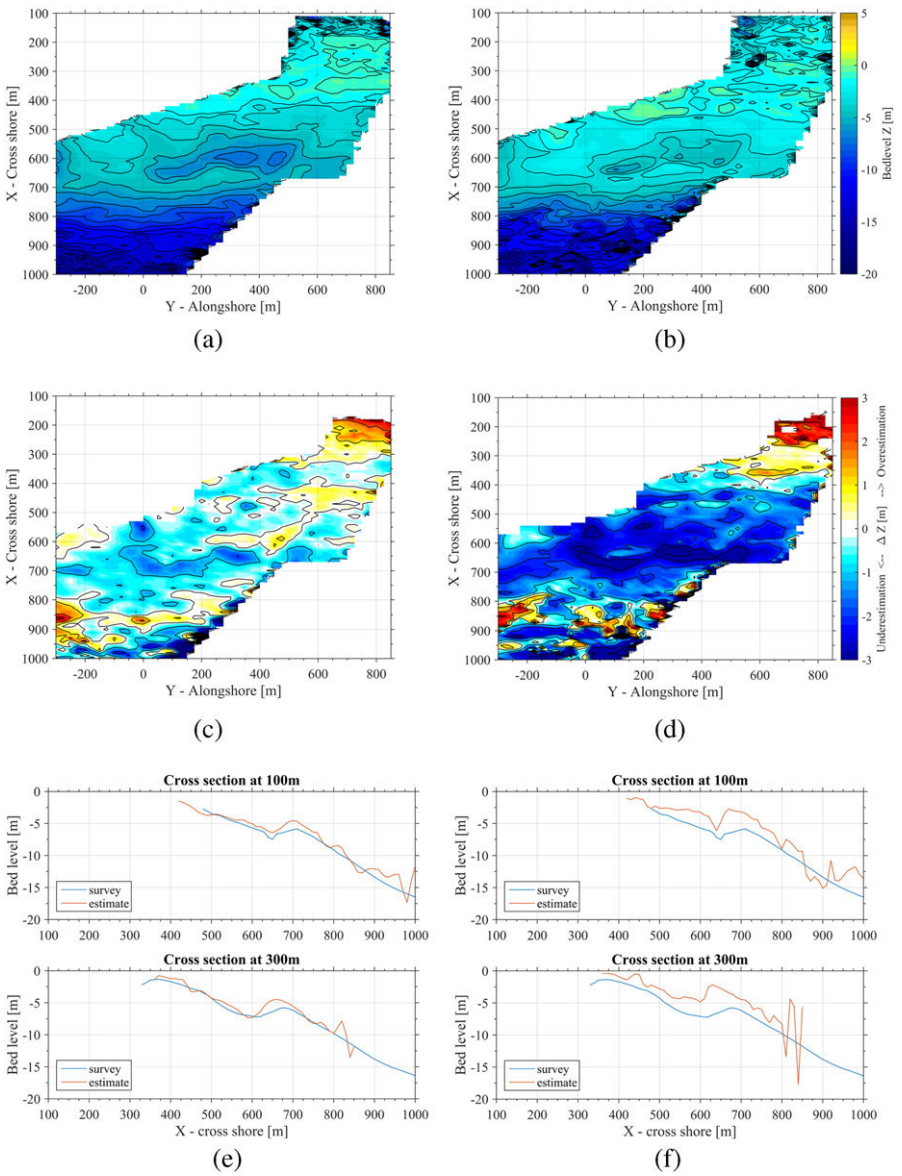


**Fig. 3.** On the left side respectively the bathymetry estimate on the 10th of April 2014 (a), the difference to the survey (c) and two cross sections (e) (at 100 m and 300 m) are shown. On the right side respectively the bathymetry estimate (b), the difference to the survey (d) and two cross sections (f) (at 100 m and 300 m) on 17 April 2014 are presented.

As the distance from the camera system increases the impact of the camera boundary issue increases.

### 3.3. Modifications

From the results above the two suspected issues are confirmed; 1) inaccurate depth estimation on the camera boundaries and 2) a significant tide dependent inaccuracy. The differences between survey and depth estimates are up to 3 m and in the same order of magnitude as the measured local depth. Considering the difference in RMS-error between the neap and spring tide estimates we can confidently state that the tidal elevation plays an important role in the accuracy of the depth estimates. In the following two sections, respective solutions for the camera boundary and tide dependent discrepancies are presented.

**Table 3**
The RMS errors are displayed here for cBathy (Holman et al., 2013). Results show the whole domain (All) and per area (inter-tidal, sub-tidal, sub-tidal bar and offshore) on the survey day (10 April 2014) and next spring-tide (17 April 2014). In brackets is the RMS error as percentage of the measured depth (mean over the (sub)domain).

| RMS error → | All [m] | inter-tidal [m] | sub-tidal [m] | sub-tidal Bar [m] | Offshore [m] |
|---|---|---|---|---|---|
| 10 April 2014 | 1.06 | 1.15 (350%) | 1.05 (14%) | 0.77 (14%) | 1.84 (13%) |
| 17 April 2014 | 2.05 | 1.77 (623%) | 2.12 (36%) | 2.03 (39%) | 2.43 (17%) |

#### 3.3.1. Camera boundary solution [cB]

Higher inaccuracies around the camera boundaries are identified when cBathy is compared to the surveys (e.g. see Fig. 5a,b). Such inter-camera differences are found at most of the sites where cBathy is applied [Duck (USA), Egmond aan Zee and the ZandMotor (Netherlands)]. A common work-around is to increase the spatial smoothing by enlarging the sub-sampling domain (Sembiring, pers com). Another approach seeks to derive perfect camera-geometries by adjusting individual camera geometry parametres in order to stitch the camera views perfectly together (Stanley, pers com). However, such approaches may not provide sufficiently accurate resolution or be practical, and so there is not yet a consensus about how to effectively overcome inaccuracies on the camera boundaries.

It is likely that even small errors in camera geometry solutions could lead to a significant difference between the estimated and real-world

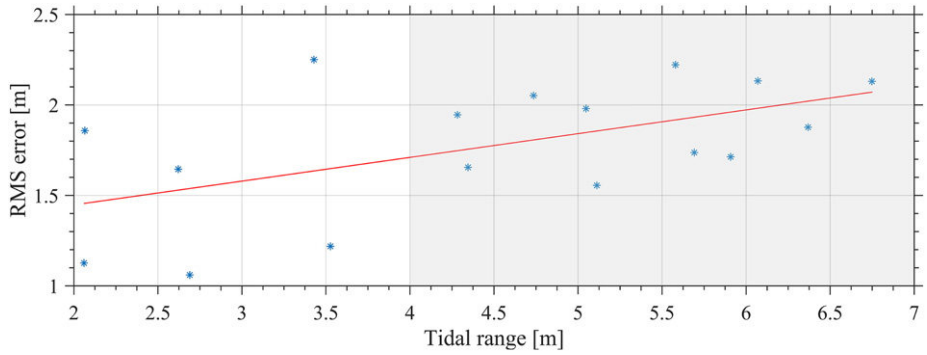


**Fig. 4.** RMS error compared to wave height and tidal range. Red line represents a linear regression with $r^2 = 0.295$ and is significant ($p = 0.024$) at the 95% confidence interval. Grey patch indicates the domain of the macro tidal range ($TR > 4$).

position of pixels. Such differences would result in a mismatch between the estimated phases across the camera boundary. Where the sub-sampling domain solely contains pixels from a single camera, depth is estimated independently from this phase shift, meaning that only wave number $k$ and wave angle $\alpha$ are used from Eq. (3). However, on the camera boundary, where the sub-sampling domain contains pixels from multiple cameras, the fitting procedure of a single wave phase is unable to incorporate a sudden apparent shift in the phase over the sub-samples. Nevertheless, the fitting procedure will seek to find the best fitting solution which in most cases means that the wave angle is increased. When the wave angle is larger, the estimated wavelength is larger and so the resulting wave number $k$ is smaller than it should be. Using this underestimated wave number in the linear dispersion relation then leads to an overestimation of the depth.

A new and effective solution to overcome this issue is presented here. If the sub-sampling domain contains pixels from multiple cameras the processing system automatically splits the depth estimation procedure into separate but parallel processes in which only pixels from single cameras are used. In this way any potential difference in phase is removed (Eq. (3)) as intended and only the wave number and wave angle are used. However, with this method, two wave numbers and two wave angles are found for the sub-sampling domain while only one depth estimate is desired. To counter this, the two separate depth estimates are combined through a weighted average based on the location of their centre of mass relative to the required location of the depth estimate. An accuracy measure is not incorporated in the weighting as the normal quality control within the cBathy routines determines whether a depth estimate is reliable or not. Fig. 6 illustrates the significant improvement that is achieved when the camera boundary solution is applied. Fig. 6a represents the bathymetry estimation without the camera solution. A clear overestimation of the depth on the camera boundaries is found between camera 2 and 3. Fig. 6b shows a depth estimation with the camera boundary solution implemented. Improved depth estimations on the camera boundaries are the result and, the camera boundary issue is no longer apparent.

### 3.3.2. Tide dependent floating pixels [TPix]

A significant variation in performance of cBathy with the tidal range is a consequence of the limited inclusion of tidal elevation in the code which results in fixed geographical pixel locations. The only use of tidal elevation is to transform depth estimates to an absolute reference level. Geographical pixel locations are determined once only when data collection is initially scheduled. However, the reference level, and hence the set of geographical pixel locations, changes as the water level rises and lowers with the tide. A set of pixels moves towards the camera system, and at the same time the spatial footprint of the set contracts, during a rising tide, while during a falling tide the opposite occurs, with pixels moving further from the camera and relative expansion of the pixel set footprint. Fig. 7 presents this process schematically, where the orange squares represent the pixel domain in the current version of cBathy and the blue and green squares represent the reality for low and high tide respectively. Incorrect pixel positions result in a shorter sensed wavelength than in reality at low tide which leads to an overestimation of the wave number and thus an underestimation of the depth, and vice versa for high tide.

The pixel shifting is not solely dependent on the tidal elevation but, rather, is a function of tidal elevation, vertical position of the camera system and distance to the camera. The maximum shift as a percentage of the distance between pixel and camera system can be found with the ratio $TR_{max}/z_{cam}$ where $TR_{max}$ is the maximum tidal range and $z_{cam}$ is the vertical position of the camera system. The instantaneous pixel shifting can be calculated using Eq. (5).

$$(dx(t), dy(t)) = \frac{\eta_{tide}(t)}{z_{cam}} \left(x_{ref} - x_{cam}, y_{ref} - y_{cam}\right) \tag{5}$$

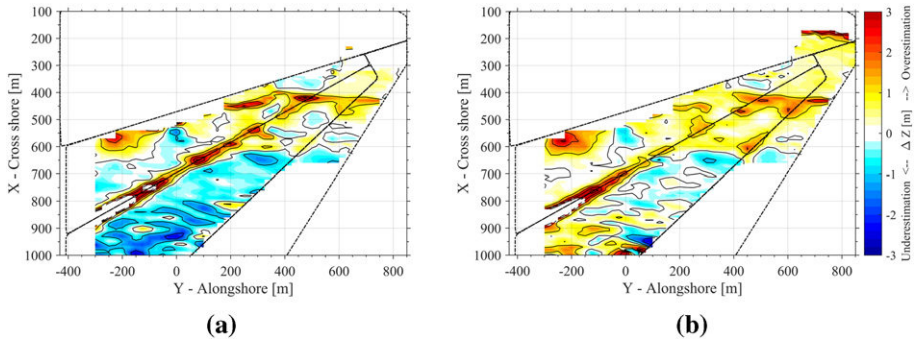


**Fig. 5.** Difference between the survey (10 April 2014) and estimates (9 April 2014). (a) represents the difference between the survey and a single estimate (18:00) and (b) is the difference between the survey and the daily Kalman filtered result. The black lines represent the camera boundaries.

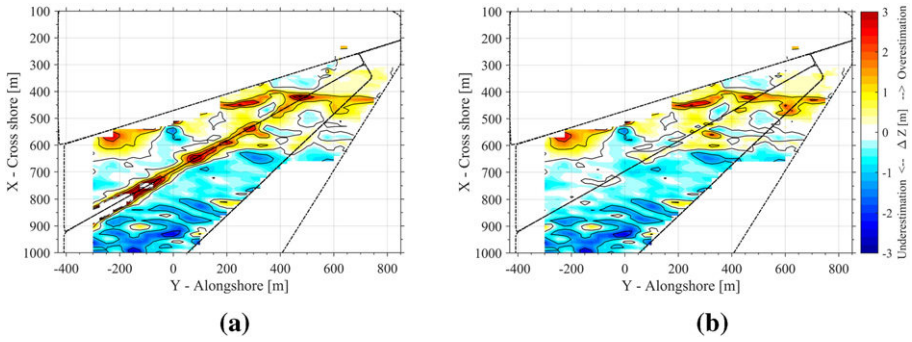


**Fig. 6.** Difference between the survey (10 April 2014) and estimates (9 April 2014). (a) represents the difference between the survey and a single estimate (18:00) without the solution and (b) shows the difference between the survey and the same single estimate (18:00) with the camera boundary solution. The black lines represent the camera boundaries.

Where *dx*, *dy* represent the shift in respectively *x* and *y* direction, $\eta_{tide}$ relates to the tidal elevation, $z_{cam}$ is the camera height and the subscripts ref. and cam refer respectively to the reference and camera position for x and y. For Porthtowan, a ratio of 15.9% is found using $z_{cam} = 44$ m and a $TR_{max} = 7$ m. This means that with a camera reach of around 1880 m in the far end of the domain the pixels move around 300 m back and forth between low and high spring tide. The horizontal shift of the pixel location is +/− half the total shift since the excursion that should be accounted for starts at the initial pixel location obtained using the vertical reference level (mid-tide at Porthtowan, $z = 0$ m). To overcome this issue an additional inclusion of the tide in the code was implemented following Eq. (5). For every stack collection the pixel location is recalculated according to the tidal elevation.

### 3.4. Performance with modifications

Bathymetry estimates for neap (left) and spring (right) tide including the floating pixels and camera boundary solution are presented in Fig. 8a-d. Unlike the estimates with the original version of cBathy (Fig. 3), estimates with the modifications show corresponding bar features in both spring and neap tidal estimates. Features like a rip channel (X = 600 m, Y = 0 m) and the sub-tidal bar are better resolved compared to the original version which indicates a clear improvement in performance. Inaccurate depth estimates are still found in the very shallow parts of the domain but as mentioned before this is likely due to the invalidity of the linear dispersion relation for that area.

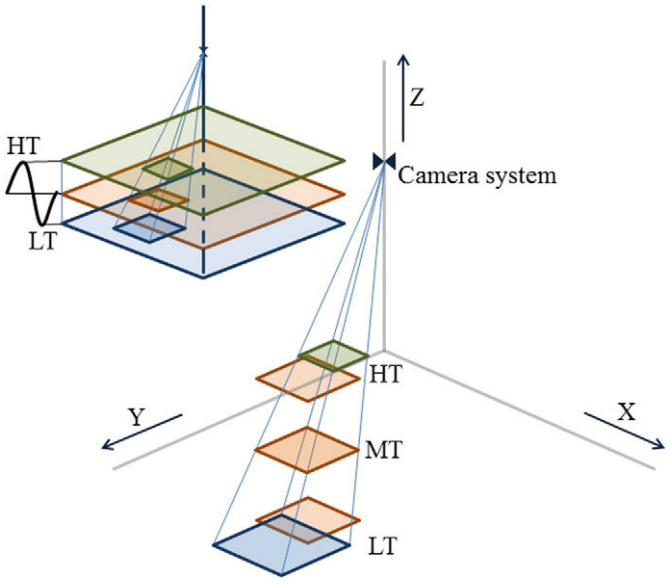


**Fig. 7.** The squares represent a selection of pixels moving up and down with the tidal elevation. The pixel set moves respectively towards the camera system and away from it. At the same time relative contraction and expansion between the pixels takes place.

Table 4 shows the calculated Root Mean Square (RMS) error and its percentage of the measured depth per step in the modifications for the whole domain and the specific regions indicated earlier in Fig. 2b. Considering the whole domain, a reduction of 8.5% with exclusively the floating pixel solution is found. If the floating pixel and camera boundary solution are applied simultaneously the RMS error is reduced by up to 19%. For the next spring tide a larger reduction is found with solely the floating pixel solution (49%). The combination of the floating pixels and camera boundary solution results in almost 53% reduction of RMS error. The improvement in accuracy was greatest for the sub-tidal bar area shifting from 2.03 m RMS error to 0.49 m. The RMS error as a percentage of the depth reduced in the sub-tidal bar region from 39% to 9%.

The overall RMS error is comparable (between 0.86 and 1.05 m) for all the new configurations. For the sub-tidal region a significant improvement is reached, the RMS error decreased from 2 m to 50 cm with the modifications. The difference between neap and spring tide depth estimates in the sub-tidal bar domain for the original version is 260%. When both the new camera boundary and floating pixel solutions are implemented simultaneously, the best performance occurs around the sub-tidal bar region (RMS-error of around 50 cm), around 9–10% of the local water depth.

## 4. Discussion

### 4.1. Improved performance at Porthtowan

The results, in particular Fig. 8 and Table 4, show a significant improvement using the two modifications compared to the estimates without the modifications. However, the data shown only comprises a single survey campaign and it remains a question whether the accuracy of the depth estimates is consistently ameliorated. Fig. 9 shows that an improvement in estimating depth is found when the modifications are applied to other arbitrary depth estimations around the time of the survey (Fig. 2b).

Fig. 9a and b show the RMS error over the whole domain against tidal range and wave height for the exact same points in time. Fig. 9c shows the reduction in percentage of the RMS error between cBathy (Holman et al., 2013) (9a) and cBathy with both corrections (9b). Depths estimated with the original cBathy code at a tidal range larger than 4.5 m seem to coincide with RMS errors larger than 1.5 m. With the inclusion of the floating pixels and the camera boundary solution the same estimates have a RMS error lower than 1.5 m. Fig. 9c shows that the largest improvement is achieved for the largest tidal ranges (as expected) during relatively calm wave conditions. At maximum, a reduction of 60% in RMS error over the whole domain is reached. The largest reductions in RMS error are found with limited wave heights (<1 m).

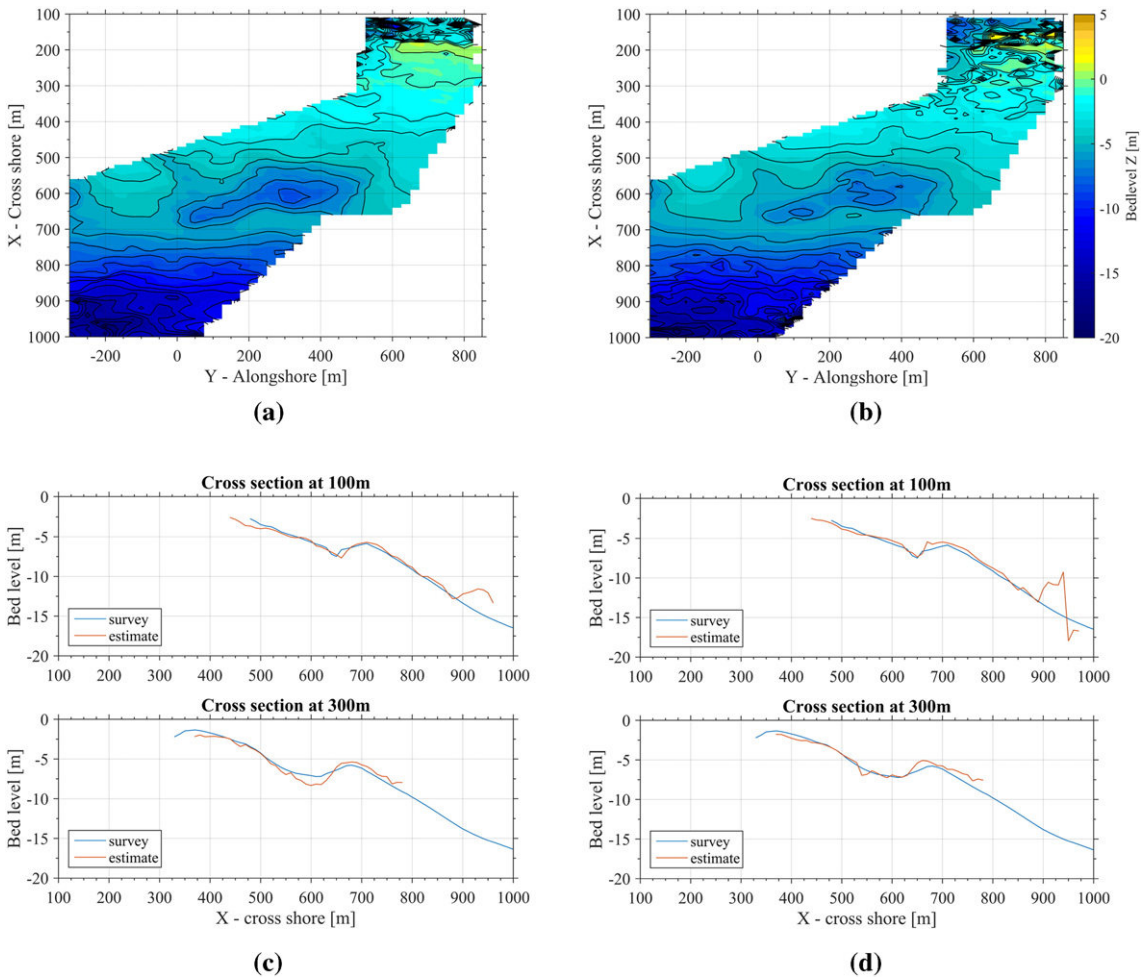


**Fig. 8.** On the left panel respectively a renewed bathymetry estimate using the modifications on the 10th of April 2014 (a) and two cross sections (c) at X = 100 m and X = 300 m. On the right is the renewed bathymetry estimate (b) on 17 April 2014 and the corresponding cross sections (d) at X = 100 and X = 300.

The depth estimates shown in Fig. 9 are representative for the day consisting of Kalman-filtered hourly depth estimates. Depending on the number of light hours per day, a certain amount of hourly depth estimates (maximum 16 h during the longest day) are combined together for a daily estimate. With more data the Kalman filtered depth estimates perform better. Furthermore, if the Kalman filtering starts with a measured bathymetry it starts from a relative accurate starting point. The Kalman like filter will keep the measured depth until the faith in the depth value has diminished over time or the cBathy estimates have a greater Kalman gain factor.

### 4.2. Potential effects at other sites

The issue on the camera boundaries is observed at other sites, for example at a recently installed video station near to the Sand Engine in the Netherlands (Holman, pers com). The camera boundary solution in its current form shows that the principle of estimating wave numbers per camera and combining them afterwards works at Porthtowan. This solution is easily transferable to other cBathy sites and collected data can be re-analysed with the solution implemented. Nevertheless, the camera boundary solution could be extended by incorporating cBathy's quality measure concerning the wave phase fitting.

The reduction in bias of the depth estimation related to the floating pixel solution is site specific. Eq. (5) suggests that tide-related inaccuracies in the cBathy depth estimates are not exclusively occurring at sites with a large tidal range. The vertical angle (ratio between tidal range and vertical camera position) is the key-factor and can potentially cause tide related inaccuracies in macro/meso tidal environments when the camera system is mounted relatively low. Fig. 10 shows the pixel displacement (presented on logarithmic scale) in relation to tidal

**Table 4**
The RMS errors are displayed here for cBathy (Holman et al., 2013) [Orig], cBathy with the floating pixel solution [TPix] and cBathy with the floating pixel and camera boundary solution [TPixcB]. Results show the whole domain (All) and per area (inter-tidal, sub-tidal, sub-tidal bar and offshore) on the survey day (10 April 2014) and next spring-tide (17 April 2014). In brackets is the RMS error as percentage of the measured depth (mean over the (sub)domain).

| RMS error → | All [m] | inter-tidal [m] | sub-tidal [m] | sub-tidal Bar [m] | Offshore [m] |
|---|---|---|---|---|---|
| 10 April 2014 [cBathy] | 1.06 | 1.15 (350%) | 1.05 (14%) | 0.77 (14%) | 1.84 (13%) |
| 17 April 2014 [cBathy] | 2.05 | 1.77 (623%) | 2.12 (36%) | 2.03 (39%) | 2.43 (17%) |
| 10 April 2014 [TPix] | 0.97 | 0.98 (160%) | 0.97 (13%) | 0.73 (14%) | 1.70 (12%) |
| 17 April 2014 [TPix] | 1.05 | 1.63 (610%) | 0.90 (11%) | 0.59 (10%) | 1.74 (12%) |
| 10 April 2014 [TPixcB] | 0.86 | 0.99 (160%) | 0.83 (10%) | 0.55 (9%) | 1.59 (11%) |
| 17 April 2014 [TPixcB] | 0.97 | 1.51 (600%) | 0.84 (10%) | 0.49 (9%) | 1.70 (12%) |

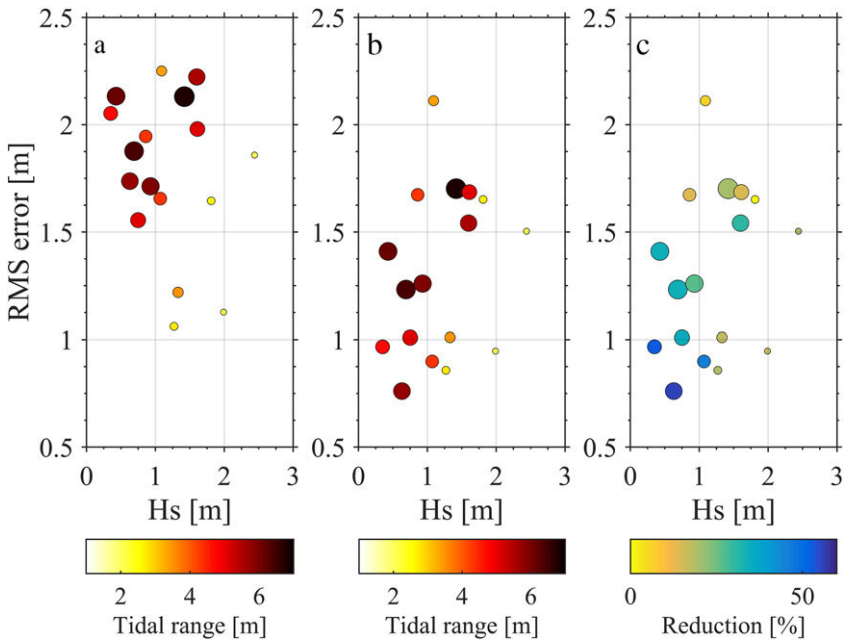


**Fig. 9.** RMS error versus significant wave height [Hs] over the whole domain where the marker size represents the tidal range at the time of the depth estimation. For the left and middle panel the colour corresponds to the tidal range while for the right panel the reduction of RMS-error in percentage is represented by the colour. The left panel represents the RMS error for cBathy as presented in (Holman et al., 2013), the middle panel shows the RMS error for cBathy with the floating pixel and camera boundary solutions together and the right panel shows the percentage reduction of the RMS error.

range and the ratio between the distance from the camera ($d$) and the camera height ($h$) for a range of sites. The greyed area in Fig. 10 shows the pixel displacement for all the pixels considered at Porthtowan. The pixels farthest away from the camera experience almost $10^{2.5} = 316$ m displacement.

Pixel displacement information for some other sites where video camera systems are sited but with smaller tidal ranges is also presented in Fig. 10. The chosen (most 'famous') Argus sites are Duck NC (USA), Palm Beach (AUS) and Egmond aan Zee (NL) and non-Argus sites are Biscarrosse (FRA) (Almar et al., 2008; Sénéchal et al., 2009) and Alfeite (PT) (Silva et al., 2009). Although the tidal range at all the sites is significantly lower compared to Porthtowan, the total pixel displacement between low and high tide due to the tidal elevation is up to 80 m in the outer edge of the domain at Egmond aan Zee. If this is not taken into account this displacement would mean that pixels are used to estimate a depth that are not around the point of interest but 40 m further away from the camera (if the vertical reference level is mid-tide).

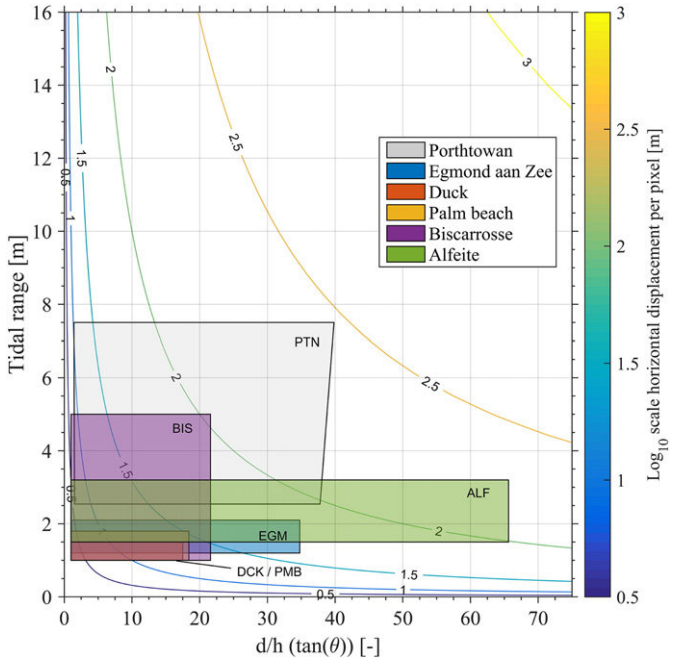


**Fig. 10.** Horizontal pixel displacement (log scale) as function of the tidal range and ratio d/h (d = distance from the camera and h = camera height).

## 5. Conclusions

Video-based bathymetry estimations are obtained at Porthtowan using an inverse method following linear dispersion relation of free surface elevations. Two areas of inaccurate depth estimation are identified: 1) inaccurate depth estimation on the camera boundaries and 2) tide dependent bias in depth estimation due to the lack of the exact position of the pixels in cBathy. On the boundary, where the camera field of view are overlapping or bordering, imprecise sensing of the propagation of the wave due to various reasons such as differences in distortion and independent camera movement result in an apparent abrupt phase shift and lead to errors in the depth estimation. A straightforward solution to diminish the observed systematic overestimation of depth on the camera boundary is proposed. The depth estimation analysis is performed independently for each camera to overcome these inaccuracies. The second identified source of inaccuracy is the tide dependent inaccuracy. Here, the formerly fixed positions of the pixels in the real-world have been changed to floating pixel positions depending on the instant tidal elevation and the camera height. Floating pixels are not only important in macro-tidal environments, since the magnitude of this effect depends on the tidal range and camera height. The two modifications to the unmodified cBathy version as presented in (Holman et al., 2013) lead to significant improvements over the whole domain at Porthtowan. Depending on multiple environmental variables, up to a 60% reduction in RMS-error over the whole domain (Fig. 9) and 75% reduction in RMS error in the sub-tidal bar domain has been demonstrated (Table 4) here. The video camera system at Porthtowan, with the inclusion of the modifications, is then shown to be capable of estimating the sub-tidal depths with a bias of around 10% of the local depth.

## Acknowledgement

This work is part of the PhD process of the first author. The PhD-project is funded by Quality Research/Research Excellence Framework CarePlan. The authors would like to thank Rob Holman for his comments on the work and especially the help to understand the cBathy coding and working in depth. We would like to thank Deltares for sharing the cBathy coding and implementation of stack collection at the Argus station in Porthtowan. The authors are thankful to all the help of members from the Coastal Processes Research Group during the different topography and bathymetry surveys, in particular Christopher Stokes and Sam Prodger. For the tidal elevation prediction and Kalman filter the offshore atmospheric pressure and wave data close to Porthtowan is used. The wave and atmospheric pressure data for the Perranporth wave buoy is courtesy of the South-West Regional Coastal Monitoring Programme and is available on www.channelcoast.org/southwest. The authors would like to thank the reviewers for their detailed comments that have undoubtedly helped to improve the paper.

## References

Aarninkhof, S.G., Turner, I.L., Dronkers, T.D., Caljouw, M., Nipius, L., 2003. A video-based technique for mapping intertidal beach bathymetry. Coastal Eng. 49, 275–289. http://dx.doi.org/10.1016/S0378-3839(03)00064-4.

Aarninkhof, S.G., Ruessink, B.G., Roelvink, J.A., 2005. Nearshore subtidal bathymetry from time-exposure video images. J. Geophys. Res. 110.

Almar, R., Bonneton, P., Roelvink, N.S.D., 2008. Wave celerity from video imaging: a new method. Proceedings of the 31st International Conference Coastal Engineering (pp. –).

Austin, M.J., Scott, T.M., Russell, P.E., Masselink, G., 2013. Rip current prediction: Development, validation, and evaluation of an operational tool. J. Coast. Res. 29, 300–383.

Bell, P.S., 1999. Shallow water bathymetry derived from an analysis of xband marine radar images of waves. Coastal 37, 513–527.

Bergsma, E.W.J., Conley, D.C., Davidson, M.A., O'Hare, T.J., Holman, R.A., 2014. An assesment of video-based bathymetry estimation in a macro-tidal environment. In: Lynett, P.J. (Ed.)Coastal Engineering, Proc. 34th Conference on Coastal Engineering vol. 34 (Seoul).

Birrien, F., Castelle, B., Marieu, V., Dubarbier, B., 2013. On a data-model assimilation method to inverse wave-dominated beach bathymetry using hetrogeneous video-derived observations. Ocean Eng.

Buscombe, D., Scott, T., 2008. Coastal geomorphology of North Cornwall: St. Ives to Trevose Head. Internal Report forWave Hub Impacts on Seabed and Shoreline Processes. Technical Report. University of Plymouth.

Castelle, B., Ruessink, B., Bonneton, P., Marieu, V., Bruneau, N., Price, T., 2010. Coupling mechanisms in double sandbar systems. part 1: patterns and physical explanation. Earth Surface Processes and Landforms 35, 476–486.

Catálan, P.A., Haller, M.C., 2008. Remote sensing of breaking wave phase speeds with application to non-linear depth inversions. Coastal Eng. 55, 93–111.

Chickadel, C.C., 2003. An optical technique for the measurement of longshore currents. J. Geophys. Res. 108, 3364. http://dx.doi.org/10.1029/2003JC001774.

Coco, G., Murray, A.B., 2007. Patterns in the sand: from forcing templates to self-organization. Geomorphology 91, 271–290.

Coco, G., Senechal, N., Rejas, A., Bryan, K., Capo, S., Parisot, J., Brown, J., MacMahan, J., 2013. Beach response to a sequence of extreme storms. Geomorphology.

Davidson, M., van Koningsveld, M., de Kruif, A., Rawson, J., Holman, R., Lamberti, A., Medina, R., Kroon, A., Aarninkhof, S., 2007. The coastview project: developing video-derived coastal state indicators in support of coastal zone management. Coastal Eng. 54, 463*–4475.

Guza, R.T., Thornton, E.R., Holman, R.A., 1984. Swash on steep and shallow beaches, in: Proceedings of the 9th International Conference on Coastal Engineering, edited by B.L. Edge.

Holland, T.K., 2001. Application of the linear dispersion relation with respect to depth inversion and remotely sensed imagery. Trans. Geosci. Remote Sens.

Holman, R., Stanley, J., 2007. The history and technical capabilities of Argus. Coastal Eng. 54, 477–491. http://dx.doi.org/10.1016/j.coastaleng.2007.01.003.

Holman, R.A., Plant, N., Holland, T., 2013. cBathy: a robust algorithm for estimating nearshore bathymetry. J. Geophys. Res. Oceans 118.

Lippmann, T.C., Holman, R.A., 1990. The spatial and temporal variability of sand bar morphology. J. Geophys. Res. 95, 11575–11590.

Masselink, G., Scott, T., Poate, T., Russell, P., Davidson, M., Conley, D., 2015. The extreme 2013/2014 winter storms: hydrodynamic forcing and coastal response along the southwest coast of england. Earth Surf. Processes Landforms 35, 476–486.

Misra, S.K., Kennedy, A.B., Kirby, J.T., 2003. An approach to determining nearshore bathymetry using remotely sensed ocean surface dynamics. Coastal Eng. 47, 265–293.

Plant, N.G., Holman, R.A., 1997. Intertidal beach profile estimation using video images. Mar. Geol. 140, 1–24.

Plant, N.G., Holland, K.T., Haller, M.C., 2008. Ocean wavenumber estimation from wave-resolving time series imagery. IEEE Trans. Geosci. Remote Sens. 46, 2644–2658.

Poate, T., Kingston, K., Masselink, G., Russell, P.E., 2009. Response of high-energy, macrotidal beaches to seasonal changes in wave conditions: examples from north cornwall, uk. J. Coast. Res. 56, 747–751 SI 56 (Proceedings of the 10th International Coastal Symposium).

Poate, T., Masselink, G., Russell, P., Austin, M., 2014. Morphodynamic variability of high-energy macrotidal beaches, cornwall, UK. Mar. Geol. 350, 97–111.

Rutten, J., 2014. Depth inversion including non-linear wave celerity. Argus Workshop (September 2014).

Sénéchal, N., Gouriou, T., Castelle, B., Parisot, J.P., Capo, S., Bujan, S., Howa, H., 2009. Morphodynamic response of a meso- to macro-tidal intermediate beach based on a long-term data set. Geomorphology 107, 263–274.

Silva, A., Taborda, R., Catalão, J., Freire, P., 2009. Dtm extraction using video-monitoring techniques: application to a fetch limited beach. Proceedings of the 10th International Coastal Symposium, pp. 203–207.

Smit, M., Reiniers, A., Ruessink, G., Roelvink, D., 2008. The mophological response of a nearshore double sandbar system to constant wave forcing. Coastal Eng. 55, 761–770.

Stockdon, H.F., Holman, R.A., 2000. Estimation of wave phase speed and nearshore bathymetry from video imagery. J. Geophys. Res. 105, 22015–22033.

Tissier, M., Bonneton, P., Michallet, H., Ruessink, G., 2015. Infragravitywave modulation of short-wave celerity in the surf zone. J. Geophys. Res.

van Dongeren, A., Plant, N., Cohen, A., Roelvink, D., Haller, M.C., Catalán, P., 2008. Beach wizard: nearshore bathymetry estimation through assimilation of model computations and remote observations. Coastal Eng. 55, 1016–1027. http://dx.doi.org/10.1016/j.coastaleng.2008.04.011.

Wallace, J.M., Dickinson, R.E., 1972. Empirical orthtogonal representation of time series in the frequency domain. part i: theoretical considerations. J. Appl. Meteorol. 11, 887–892.

Williams, W.W., 1946. The determineation of gradients on enemy-held beaches. Geogr. J. 109, 76–90.

Wilson, G., Özkan-Haller, H., Holman, R., 2010. Data assimilation and bathymetric inversion in a two-dimensional horizontal surf zone model. J. Geophys. Res.

Wilson, G., Özkan-Haller, H., Holman, R., Haller, M., Honegger, D., Chickadel, C., 2014. Surf zone bathymetry and circulation predictions via data assimilation of remote sensing observations. J. Geophys. Res. Oceans.